Development of Novel Molecules as Modulators of Amyloid-β Aggregation

by

Amy Trinh Pham

A thesis

presented to University of Waterloo

in fulfilment of the

thesis requirement for the degree of

Doctor of Philosophy

in

Pharmacy

Waterloo, Ontario, Canada, 2021

© Amy Trinh Pham 2021

EXAMINING COMMITTEE MEMBERSHIP

The following served on the Examining Committee for this thesis. The decision of the Examining Committee is by majority vote.

External Examiner	Dr. Richard Manderville
Supervisor	Dr. Praveen Nekkar P. Rao
Internal Members	Dr. Michael Beazely Dr. Eric Fillion
Internal-external Member	Dr. John Mielke

AUTHOR'S DECLARATION

I hereby declare that I am the sole author of this thesis. This is a true copy of the thesis, including any required final revisions, as accepted by my examiners.

I understand that my thesis may be made electronically available to the public.

ABSTRACT

Our brain is remarkably special and unique. It has billions of neurons that govern actions and reactions, and enables us to have thoughts, memories, and personality traits – outmost precious assets – that define who we are as individuals. What if we lose a certain part of the brain function? This is the case for the very first Alzheimer's patient – August Deter, who suffered from memory loss and psychological changes, and eventually succumbed to the devastating disease, known as Alzheimer's disease (AD). Indeed, it steals more than memory – it steals independence and breaks hearts. The two main culprits behind AD are the sticky amyloid beta (Aβ) plaques and neurofibrillary tangles (NFTs) nestled in the brain, which have been the main target for many researchers to chase them with hope to remove them directly so that they could conquer this disease. And finally, the first-of-its-kind therapy aducanumab directed at the underlying disease process of Alzheimer's just received its FDA approval, first new drug for AD in 17 years via the accelerated approval pathway, emphasizing the complexities in AD therapeutic design and concurrently suggesting that it requires more research and innovation.

As such, this thesis research presented here is to design and develop novel small molecules that can reduce and prevent the formation of two known Aβ peptides - Aβ40 and Aβ42 aggregation. A chemical library of ~47 derivatives, based on diphenylthiazolamine ring systems possessing a central thiazole-4-amine or thiazole-2-amines was designed, synthesized, and evaluated as inhibitors of both Aβ40 and Aβ42 aggregation. Specifically:

Chapter 1 guides the readers to the understanding of Alzheimer's background information and literature with an overview of key hypotheses such as cholinergic dysfunction, amyloid-β cascade and tauopathy and their disease pathology and therapies.

Chapter 2 provides a summary on the utility of the thiazole based derivatives in pharmaceutical industry and links them to the rationale, design, and development of the thiazole library that is capable of preventing Aβ40 and Aβ42 aggregation and their SAR studies based on in vitro fluorescence spectroscopy experiments, computational modeling studies, transmission electron microscopy (TEM) studies and cell viability assay.

Chapter 3 describes the design, development and evaluation of *N*,4-diphenylthiazol-4-amines. This section reports a series with 12 derivatives (**1a-j**, **2a**, **2b**) incorporating various EDG and EWG substituents demonstrating their significant inhibition toward Aβ40 and Aβ42 aggregation in vitro and their activity was translated from the solution based in vitro experiments to cell culture studies in HT22 hippocampal neuronal cells, where they were able to reduce the Aβ40 or Aβ42 induced cytotoxicity.

Chapter 4 describes the design, development and evaluation of *N*-methyl-*N*,4-dimethylthiazol-4-amines. This section reports a series with 11 derivatives (**3a-i**, **4a**, **4b**) incorporating similar substituents as those in Chapter 3. The outcomes show that some compounds in the series were able to show their inhibition activity profile toward both Aβ40 and Aβ42 in vitro although N-methylation reduced their activity profile compared to the corresponding *N*,4-diphenylthiazol-4-amine. However, compounds in this series were able to translate their anti-Aβ aggregation properties from the solution based in

vitro experiments to cell culture studies in HT22 cells to reduce both Aβ40 and Aβ42 cytotoxicity.

Chapter 5 describes the design, development and evaluation of alkylsulfonamide and sulfamide substituted *N*,4-diphenylthiazol-2-amines. This section reports a series of ten alkysulfonamide or sulfamide containing derivatives (**5a-j**), which was developed to assess their anti-Aβ40 and Aβ42 aggregation potential. The results demonstrated that they exhibited superior inhibition of Aβ40 aggregation compared to the *N*,4-diphenylthiazol-2-amine and *N*-methyl derivatives in Chapter 3 and 4. Several compounds in this series demonstrated neuroprotective effects against both Aβ40 and Aβ42-induced cytotoxicity in HT22 hippocampal cells.

Chapter 6 describes the design, development and evaluation of alkylsulfonamide and sulfamide substituted *N*-methyl-*N*-4,diphenylthiazol-2-amine derivatives. This was a series of ten derivatives (**6a-j**). The *N*-methylation was not a major factor in modulating their Aβ aggregation inhibition properties. Compounds in this series were able to exhibit excellent inhibition of Aβ40 and Aβ42-induced cytotoxicity in HT22 hippocampal neuronal cells.

Chapter 7 describes the design, development and evaluation of a mini library of four from *N*,2-diphenylthiazol-4-amine derivatives (**7a-d**), which are the regioisomers of *N*,4-diphenylthiazol-2-amine derivatives described in Chapter 3. The biochemical assay outcomes demonstrated their anti-aggregation properties toward Aβ40 and Aβ42, in addition to their ability to rescue HT22 cells from Aβ40 and Aβ42-induced cytotoxicity,

which further supports their development as novel class of agents to target the amyloid cascade in AD therapy.

Chapter 8 provides closing conclusions on the research findings related to the development of diphenylthiazolamines as a novel class of small molecules, which have the potential to reduce and or prevent the amyloid cascade of AD by, direct binding and outlines the next research directions.

ACKNOWLEDGEMENTS

I would like to thank to the University of Waterloo – School of Pharmacy for supporting the work I presented here. I also wish to thank the Ontario Graduate Scholarship (OGS) and the Graduate Studies Office for their funding of the project and conference expenses.

I owe my deepest gratitude to my supervisor, Dr. Praveen P. Nekkar Rao. His overall insights in this field have made this an inspiring experience for me. His motivation, guidance, understanding, and continuous support provided me with opportunities for growth. I am truly blessed and could not have asked for a better mentor. A special thank you also extends to my committee advisors, Dr. Michael Beazely and Dr. Eric Fillion, for their patience and insightful advice over these past five years. I gratefully acknowledge Jan Venn and Dr. Richard Smith for their help with spectral acquisitions throughout this project. Also, I would like to send my thanks to Melinda Recchia for her assistance with the administrative processes especially her friendly reminders.

I gratefully acknowledge Dr. Beazely's lab members – Morgan Robinson and Dr. Nyasha Gondora for providing training and on-going help with the cell culture studies. A special shout out goes to my lab members and fellow grad students for funny chats and texts, constant motivation and support, and happy memories throughout the course of my graduate program.

DEDICATION

"Anything is possible when you have the right people there to support you" – Misty Copeland

I dedicate this work as a token of my gratitude to my supervisor for helping me complete this journey.

Also, I dedicate this work as a token of my great love and gratitude to:

My parents

My brother in heaven

My niece and nephew

Last but not least, my husband and son.

Thank you for their unconditional love and support, and for giving me the opportunities to explore new directions in life and seek my own destiny because for me, everything is possible when they are here with me.

TABLE OF CONTENTS

List of Figures xviii

List of Tables xxix

List of Schemes xxxi

List of Abbreviations xxxii

CHAPTER 1 Background on Alzheimer's Disease 1

1.1 Introduction 1

1.2 The Cholinergic Dysfunction Hypothesis 6

1.3 Amyloid-β (Aβ) Hypothesis 11

1.3.1 Amyloid Precursor Protein (APP) 12

1.3.2 Amyloid Metabolism and Processing Pathways 12

1.3.3 The Aβ-Peptide: Structure, Aggregation and Clearance 17

1.3.4 Aβ Pathology and Physiology 21

1.3.5 Aβ Therapies 28

1.3.5.1 Upstream of Aβ Production 30

1.3.5.2 Downstream of Aβ Production 36

1.4 Tauopathy 41

CHAPTER 2 Hypothesis and Rationale in Using Thiazole Ring Scaffolds as Amyloid Aggregation Inhibitors 46

2.1 Thiazole Derivatives 46

2.2 Template Design 49

2.3 Synthesis of Thiazole Core Template 53

2.4 Target Thiazole Library 53

CHAPTER 3 Development of *N*,4-Diphenylthiazol-2-amines 55

3.1 Introduction 55

3.2 Hypothesis 56

3.3 Results and Discussion 56

3.3.1 Synthesis 56

3.3.2 Amyloid-β Aggregation Inhibition Studies 59

3.3.2.1 Correlating the ClogP Values, HBDs, and HBAs with Anti-Aβ Aggregation Properties 65

3.3.3 Computational Modeling Studies 68

3.3.4 Transmission Electron Microscopy (TEM) Studies 71

3.3.5 Cell Viability Assay 72

3.4 Summary 75

3.5 Experimental 76

3.5.1 Chemistry 76

3.5.1.1 Materials and Methods 76

3.5.1.2 General procedure for the synthesis of 2-bromo-3',4'-dimethoxyacetophenone or 2-bromo-3',4'-difluoroacetophenone.[217] 77

3.5.1.3 General procedure for the synthesis of N,4-diphenylthiazol-2-amine derivatives (1a-j and 2a-b).[209] 78

3.5.1.4 General Procedure for the synthesis of N,4-diphenylthiazol-2-amine derivatives (2a and 2b).[210] 81

3.5.2 Biological Screening 82

3.5.2.1 Amyloid-β (Aβ) Aggregation Assay 82

3.5.2.2 Transmission Electron Microscopy (TEM).....83
3.5.2.3 Computational Modeling Studies.....84
3.5.2.4 Cell Viability Assay.....85
CHAPTER 4 Development of *N*-Methyl-*N*,4-Diphenylthiazol-2-amines.....87
4.1 Introduction.....87
4.2 Hypothesis.....88
4.3 Results and Discussion.....88
4.3.1 Synthesis.....88
4.3.2 Amyloid-β Aggregation Inhibition Studies.....90
4.3.2.1 Correlating the ClogP Values, HBDs, and HBAs with Anti-Aβ Aggregation Properties.....95
4.3.3 Computational Modeling Studies.....98
4.3.4 Transmission Electron Microscopy (TEM) Studies.....101
4.3.5 Cell Viability Assay.....102
4.4 Summary.....104
4.5 Experimental.....106
4.5.1 Chemistry.....106
4.5.1.1 Materials and Methods.....106
4.5.1.2 General Procedure for the synthesis of N-methyl-N,4-diphenylthiazol-2-amine derivatives (3a-i).....107
4.5.1.3 General procedure for the synthesis of N-methyl-N,4-diphenylthiazol-2-amine derivatives (4a-b).....109
4.5.2 Biological Screening.....110

4.5.2.1 Amyloid-β (Aβ) Aggregation Assay....110
4.5.2.2 Transmission Electron Microscopy (TEM) Studies....111
4.5.2.3 Computational Modeling Studies....112
4.5.2.4 Cell Viability Assay....113
CHAPTER 5 Development of (Alkylsulfonyl-azaneylphenyl)-*N*-Phenylthiazol-2-amines 115
5.1 Introduction....115
5.2 Hypothesis....116
5.3 Results and Discussion....116
5.3.1 Synthesis....116
5.3.2 Amyloid-β Aggregation Inhibition Studies....118
5.3.2.1 Correlating the ClogP Values, HBDs, and HBAs with Anti-Aβ Aggregation Properties....124
5.3.3 Computational Modeling Studies....126
5.3.4 Transmission Electron Microscopy (TEM) Studies....129
5.3.5 Cell Viability Assay....130
5.4 Summary....132
5.5 Experimental....134
5.5.1 Chemistry....134
5.5.1.1 Materials and Methods....134
5.5.1.2 General procedure for the synthesis of N-methyl-N,4-diphenylthiazol-2-amine derivatives (5a-j).[230]....135
5.5.2 Biological Screening....138

5.5.2.1 Amyloid-β (Aβ) Aggregation Assay 138
5.5.2.2 Transmission Electron Microscopy (TEM) Studies 139
5.5.2.3 Computational Modeling Studies 140
5.5.2.4 Cell Viability Assay 141
CHAPTER 6 Development of *N*-Methyl-*N*,4-diphenylthiazol-2-amines 143
6.1 Introduction 143
6.2 Hypothesis 143
6.3 Results and Discussion 144
6.3.1 Synthesis 144
6.3.2 Amyloid-β Aggregation Inhibition Studies 145
6.3.3 Computational Modeling Studies 149
6.3.4 Transmission Electron Microscopy (TEM) Studies 152
6.3.5 Cell Viability Assay 153
6.4 Summary 155
6.5 Experimental 156
6.5.1 Chemistry 156
6.5.1.1 Materials and Methods 156
6.5.1.2 General procedure for the synthesis of N-methyl-N,4-diphenylthiazol-2-amine derivatives (6a-j).[230] 157
6.5.2 Biological Screening 160
6.5.2.1 Amyloid-β (Aβ) Aggregation Assay 160
6.5.2.2 Transmission Electron Microscopy (TEM) Studies 161
6.5.2.3 Computation Modeling 162

6.5.2.4 Cell Viability Assay 163

CHAPTER 7 Development of *N*,2-Diphenylthiazol-4-amines 164

7.1 Introduction 164

7.2 Hypothesis 164

7.3 Results and Discussion 165

7.3.1 Synthesis 165

7.3.2 Amyloid-β (Aβ) Aggregation Inhibition Studies 167

7.3.3 Computational Modeling Studies 171

7.3.4 Transmission Electron Microscopy (TEM) Studies 173

7.3.5 Cell Viability Assay 174

7.4 Summary 176

7.5 Experimental 177

7.5.1 Chemistry 177

7.5.1.1 Materials and Methods 177

7.5.1.2 General procedure for the synthesis of N,2-diphenylthiazol-4-amine derivatives (7a-d).[231] 178

7.5.2 Biological Screening 179

7.5.2.1 Amyloid-β (Aβ) Aggregation Assay 179

7.5.2.2 Transmission Electron Microscopy (TEM) Studies 180

7.5.2.3 Computational Modeling Studies 181

7.5.2.4 Cell Viability Assay 182

CHAPTER 8 Conclusions and Future Directions 184

8.1 Introduction 184

8.2 *N*,4-Diphenylthiazol-2-Amine Derivatives (Chapter 3) 185

8.3 *N*-Methyl-*N*,4-Diphenylthiazol-2-Amine Derivative (Chapter 4) 187

8.4 Alkysulfonamide and Sulfamide Substituted *N*,4-Diphenylthiazol-2-Amine Derivatives (Chapter 5) 188

8.5 Alkylfulfonamide and Sulfamide Substituted *N*-Methyl-*N*,4-Diphenylthiazol-2-Amine Derivative (Chapter 6) 189

8.6 *N*,2-Diphenylthiazol-4-Amine Derivatives (Chapter 7) 190

8.7 Limitations 191

8.8 Future Directions 192

Letters of Copyright Permission 196

Letter of Copyright Permission for Figure 9 196

Letter of Copyright Permission for Figure 12 197

References 198

Appendices 229

Appendix 1: Sample Spectra for Chapter 3 229

4-(3,4-Dimethoxyphenyl)-*N*-phenylthiazol-2-amine (1d) 229

4-(3-Nitrophenyl)-*N*-phenylthiazol-2-amine (1f) 233

4-(3,4-Difluorophenyl)-*N*-phenylthiazol-2-amine (1j) 237

4-(4-Aminophenyl)-*N*-phenylthiazol-2-amine (2a) 241

Appendix 2: Sample Spectra for Chapter 4 245

N-Methyl-*N*-diphenylthiazol-2-amine (3a) 245

4-(4-Methoxyphenyl)-*N*-methyl-*N*-phenylthiazol-2-amine (3c) 248

4-(4-Chlorophenyl)-*N*-methyl-*N*-phenylthiazol-2-amine (3g) 252

4-(3-Aminophenyl)-*N*-methyl-*N*-phenylthiazol-2-amine (4b) 256

Appendix 3: Sample Spectra for Chapter 5 260

N-(4-(2-Phenylamino)thiazol-4-yl)phenyl)ethanesulfonamide (5c).....260

2,2,2-Trifluoro-*N*-(4-(2-(phenylamino)thiazole-4-yl)phenyl)-2-ethane-1-sulfonamide (5g) 264

(4-(2-(Phenyl)amino)thiazole-4-yl)benzenesulfamide (5i) 268

Appendix 4: Sample Spectra for Chapter 6 272

N-(4-(2-(Methyl(phenyl)amino)thiazol-4-yl)phenyl)methanesulfonamide (6a) 272

N-(3-(2-(Methyl(phenylamino)thiazol-4-yl)phenyl)methanesulfonamide (6b) 276

N-(4-(2-(Methyl(phenylamino)thiazol-4-yl)phenyl)propane-2-sulfonamide (6e) ..279

2,2,2-Trifluoro-*N*-(3-(2-(methyl(phenylamino)thiazol-4-yl)phenyl)ethane-1-sulfonamide (6h).....283

Appendix 5: Sample Spectra for Chapter 7 287

N,2-Diphenylthiazol-4-amine (7a) 287

N-(4-Fluorophenyl)-2-phenylthiazol-4-amine (7c) 290

N-(3,5-Difluorophenyl)-2-phenylthiazol-4-amine (7d) 293

Cytotoxicity at 10 μM 297

LIST OF FIGURES

Figure 1. Schematic outline of the pathology depicting the complexity of AD disease. ...6

Figure 2. Schematic representation of cholinergic neurotransmission mediated by acetylcholine (ACh).....7

Figure 3. Schematic representation of AChE binding sites.[23] Reproduced with permission from Ref [23]. 9

Figure 4. Schematic domain structure of APP.[37] Reproduced with permission from Ref [37]. 13

Figure 5. The Aβ sequence within APP and the main secretase cleavage positions.[39] Reproduced with permission from Ref [39]. 14

Figure 6. Schematic diagram showing the two proteolytic pathways of APP: non-amyloidogenic pathway (left) and amyloidogenic pathway (right).....14

Figure 7. The human γ-secretase structure.[8] Reproduced with permission from Ref [8].16

Figure 8. An illustration of self-induced Aβ aggregation pathway.....19

Figure 9. Mechanism of Aβ clearance.[55] Reproduced with permission from Ref [55]. ..20

Figure 10. ROS production by Aβ-Cu^{2+}. Catalytic hydrogen peroxide (H_2O_2) cycle with superoxide ($O_2\bullet^-$) dissociation pathway (right) and Fenton cycle (left). 23

Figure 11. Mitochondria damage in AD.[81] Reproduced with permission from Ref [81]. 24

Figure 12. Pathological events in AD and microglia priming.[92] Reproduced with permission from Ref [92]. 27

Figure 13. Schematic overview of upstream interventions.[110] Reproduced with permission from Ref [110]. 30

Figure 14. BACE1 active site.[105] Reproduced with permission from Ref [105]. 32

Figure 15. Structure of semagacestat (LY-450139) – a γ-secretase inhibitors.....33

Figure 16. Structure of tarenflurbil (*R*-flurbiprofen) – a γ-secretase inhibitor.....34

Figure 17. Structure of atorvastatin – an α-secretase activator.....35

Figure 18. Schematic overview of downstream interventions.[110] Reproduced with permission from Ref [110]. 36

Figure 19. Compounds with anti-aggregation properties that are commonly used as gold standards in Aβ assays. 39

Figure 20. Scheme of nucleated growth kinetics mechanism of Aβ aggregation process represented as a sigmoidal curve to depict three phase kinetics.....40

Figure 21. Mechanism of thioflavin-T (ThT) binding to Aβ aggregates. Blue arrows represent the cross-β structure of amyloid fibrils. Reproduced with permission from Ref [110].....41

Figure 22. Schematic representation of tau hypothesis and the aggregation process of tau protein.....43

Figure 23. Structure of ANAVEX2-73 – an anti-amyloid and anti-tau agent.....45

Figure 24. Structure of novel thiazole derivatives.....46

Figure 25. Biologically important thiazole.[170] 47

Figure 26. Thiazole skeleton containing FDA-approved drugs.[171,172] 47

Figure 27. Chemical structures of heterocyclic ring systems as potential anti-AD agents. 49

Figure 28. Structures of small molecules with neurogenesis-inducing activities.[202–205] ..50

Figure 29. Chemical structure of 4,5-diphenylthiazol-4-amine.....51

Figure 30. Chemical structure and molecular modeling of Neuropathiazol®. Molecular modeling of thiazole docked with the Aβ40-dimer model (pdb id: 2LMN) using the Discovery Studio Structure-based design software. Neuropathizol® undergoes a number of interactions in the hydrophobic region (orange) of Aβ40-dimer, such as hydrogen bonding with Val18 and Phe19, and π-π interactions with Phe20. 52

Figure 31. Retrosynthetic pathway to the synthesis of *N*-diphenylthiazoleamine derivatives.....53

Figure 32. Banner for Chapter 3 55

Figure 33. Proposed mechanism of cyclization reaction to synthesize *N*-4-diphenylthiazol-2-amine derivatives (**1-2**). 57

Figure 34. Mechanism of the catalytic reduction reaction to synthesize nitro-substituted 4-diphenylthiazol-2-amine derivatives. SET – Single electron transfer.....58

Figure 35. Chemical structures of reference compounds used in the ThT-based kinetic assay. 61

Figure 36. ThT-monitored 24 h aggregation kinetics of Aβ40 (5 μM) in the presence of 1, 5, 10, and 25 μM of *N*,4-diphenylthiazol-2-amine (**2a**) at pH 7.4, 37 °C in phosphate buffer. Aggregation kinetics were monitored by ThT-fluorescence spectroscopy (excitation = 440 nm, emission = 490 nm). Results are average ± SD of three independent experiments (n = 3).....62

Figure 37. ThT-monitored 24 h aggregation kinetics of Aβ42 (5 μM) in the presence of 1, 5, 10, and 25 μM of *N*,4-diphenylthiazol-2-amine (**1j**) at pH 7.4, 37 °C in phosphate buffer. Aggregation kinetics were monitored by ThT-fluorescence

spectroscopy (excitation = 440 nm, emission = 490 nm). Results are average ± SD of three independent experiments (n = 3). 65

Figure 38. Chemical structure of *N*,4-diphenylthiazol-2-amines described in Chapter 3 highlighting the C4-position of the thiazol-2-amine that was modified by SAR. HBD – Hydrogen Bond Donors, HBA – Hydrogen Bond Acceptors. 65

Figure 39. Correlation of Aβ40 aggregation inhibition properties of **1a–j**, **2a** and **2b** at 25 μM, with ClogP values. Blue line represents ClogP values. 66

Figure 40. Correlation of Aβ42 aggregation inhibition properties of **1a–j**, **2a** and **2b** at 10 μM, with ClogP values. Blue line represents ClogP values. 67

Figure 41. Panel A: Predicted binding mode of **2a** (ball and stick cartoon) in the Aβ40-dimer model (ribbon diagram, pdb id: 2LMN, CDOCKER energy = -9.47 kcal/mol; CDOCKER interaction energy = -19.65 kcal/mol). Panel B: Predicted binding mode of **1j** (ball and stick cartoon) in the Aβ42-dimer model (ribbon diagram, pdb id: 5KK3, CDOCKER energy = –7.97 kcal/mol; CDOCKER interaction energy = –21.09 kcal/mol). 70

Figure 42. TEM images of A**β**40 aggregation morphology. Panel A: A**β**40 control (5 **μ**M). Panel B: A**β**40 + **2a** (25 **μ**M). Panel C: A**β**40 + **2b** (25 **μ**M). Scale bars represent 100 nm. 71

Figure 43. TEM images of Aβ42 aggregation. Panels A: A**β**42 control (5 **μ**M). Panel B: A**β**42 + **1j** (5 **μ**M). Scale bars below the images represent 100 nm. 72

Figure 44. Percentage viability of the *N*,4-diphenylthiazol-2-amine derivatives **1a-j**, **2a-b**, and RES (10 **μ**M) in HT22 cells in the presence of A**β**40 was assessed by MTT

assay after 24 h incubation at 37 °C. The results were given as average of two independent experiments (n = 3). UC = untreated cells, RES = resveratrol. 74

Figure 45. Percentage viability of the *N*,4-diphenylthiazol-2-amine derivatives **1a-j**, **2a-b**, and RES (10 μM) in HT22 cells was assessed by MTT assay toward Aβ42 after 24 h incubation at 37 °C. The results were given as average of two independent experiments (n = 3). UC = untreated cells, RES = resveratrol. 74

Figure 46. Cummulative chapter summary of *N*,4-diphenylthiazol-2-amines (**1-2**). 75

Figure 47. Banner for Chapter 4 87

Figure 48. Mechanism of the *N*-alkylation of *N*,4-diphenylthiazol-2-amine derivatives **3a-i**. 89

Figure 49. Panels A and B show ThT-monitored 24 h aggregation kinetics of Aβ42 (5 μM) in the presence of 1, 5, 10, and 25 μM of *N*-methyl-*N*,4-diphenylthiazol-2-amines (**4a** and **4b**) at pH 7.4, 37 °C in phosphate buffer. Aggregation kinetics were monitored by ThT-fluorescence spectroscopy (excitation = 440 nm, emission = 490 nm). Results are average ± SD of three independent experiments (n = 3). 95

Figure 50. Chemical structure of *N*-methyl-*N*,4-diphenylthiazol-2-amines described in Chapter 4 highlighting the C4-position of the thiazol-2-amine that was modified by SAR. HBD – Hydrogen Bond Donors, HBA – Hydrogen Bond Acceptors. 96

Figure 51. Correlation of Aβ40 aggregation inhibition properties of **3a–h**, **4a** and **4b** at 1 μM, with ClogP values. Blue line represents ClogP values. 97

Figure 52. Correlation of Aβ42 aggregation inhibition properties of **3a–g**, **4a** and **4b** at 1 μM, with ClogP values. Blue line represents ClogP values. 98

Figure 53. Panel A: Predicted binding mode of **3f** (ball and stick cartoon) in the Aβ40-dimer model (ribbon diagram, pdb id: 2LMN, CDOCKER energy = –6.24 kcal/mol; CDOCKER interaction Energy = –21.09 kcal/mol). Panel B: Predicted binding mode of **4b** (ball and stick cartoon) in the Aβ42-dimer model (ribbon diagram, pdb id: 5KK3, CDOCKER energy = –14.20 kcal/mol; CDOCKER interaction energy = –24.44 kcal/mol). 100

Figure 54. TEM images of Aβ40 and Aβ42 aggregation. Top: Panel A: Aβ40 control (5 μM). Panel B: Aβ40 + **3f** (5 μM). Bottom: Panel A: Aβ42 control (5 μM). Panel B: Aβ42 + **4b** (5 μM). Scale bars represent 100 nm. 101

Figure 55. Percentage viability of the *N*-methyl-*N*,4-diphenylthiazol-2-amine derivatives **3c**, **3h**, and RES (10 μM) in HT22 cells was assessed by MTT assay toward Aβ40 after 24 h incubation at 37 °C. The results were given as average of two independent experiments (n = 3). UC = untreated cells, RES = resveratrol. 103

Figure 56. Percentage viability of the *N*-methyl-*N*,4-diphenylthiazol-2-amine derivatives **3a**, **3d**, **3g**, and RES (10 μM) in HT22 cells was assessed by MTT assay toward Aβ42 after 24 h incubation at 37 °C. The results were given as average of two independent experiments (n = 3). UC = untreated cells, RES = resveratrol. 103

Figure 57. Cumulative chapter summary of *N*-methyl-*N*,4-diphenylthiazol-2-amines (**3-4**). 104

Figure 58. Banner for Chapter 5 115

Figure 59. Mechanism of the sulfonylation reaction to synthesize sulfonyl-substituted 4-diphenylthiazol-2-amine derivatives. 117

Figure 60. ThT-monitored 24 h aggregation kinetics of Aβ40 (5 μM) in the presence of 1, 5, 10, and 25 μM of sulfonamide based *N*,4-diphenylthiazol-2-amine derivatives (**5c**, **5g**, and **5i**) at pH 7.4, 37 °C in phosphate buffer. Aggregation kinetics were monitored by ThT-fluorescence spectroscopy (excitation = 440 nm, emission = 490 nm). Results are average ± SD of three independent experiments (n = 3).....121

Figure 61. ThT-monitored 24 h aggregation kinetics of Aβ42 (5 μM) in the presence of 1, 5, 10, and 25 μM of *N*,4-diphenylthiazol-2-amine (**5g**) at pH 7.4, 37 °C in phosphate buffer. Aggregation kinetics were monitored by ThT-fluorescence spectroscopy (excitation = 440 nm, emission = 490 nm). Results are average ± SD of three independent experiments (n = 3).....123

Figure 62. Chemical structure of *N*,4-diphenylthiazol-2-amines possessing alkylsulfonamide and sulfamide moieties described in Chapter 5 highlighting the C4-position of the thiazole-2-amine that was modified by SAR. HBA – Hydrogen Bond Acceptors. 124

Figure 63. Correlation of Aβ40 aggregation inhibition properties of **5a–j** at 25 μM, with ClogP values. Blue line represents ClogP values. 125

Figure 64. Correlation of Aβ42 aggregation inhibition properties of **5a–j** at 10 μM, with ClogP values. Blue line represents ClogP values. 126

Figure 65. Panel A: Predicted binding mode of **5c** (ball and stick cartoon) in the Aβ40-dimer model (ribbon diagram, pdb id: 2LMN, CDOCKER energy = –10.89 kcal/mol; CDOCKER interaction Energy = –22.38 kcal/mol). Panel B: Predicted binding mode of **5g** (ball and stick cartoon) in the Aβ42-dimer model (ribbon

diagram, pdb id: 5KK3, CDOCKER energy = –16.48 kcal/mol; CDOCKER interaction energy = –26.63 kcal/mol).....128

Figure 66. TEM images of Aβ40 and Aβ42 aggregation. Top: Panel A: Aβ40 control (5 μM). Panel B: Aβ40 + **5c** (5 μM). Bottom: Panel A: Aβ42 control (5 μM). Panel B: Aβ42 + **5g** (5 μM).Scale bars represent 100 nm.....129

Figure 67. Percentage viability of the *N*,4-diphenylthiazol-2-amine derivatives **5a-j** and RES (10 μM) in HT22 cells was assessed by MTT assay toward Aβ40 after 24 h incubation at 37 °C. The results were given as average of two independent experiments (n = 3). UC = untreated cells, RES = resveratrol. 131

Figure 68. Percentage viability of the *N*,4-diphenylthiazol-2-amine derivatives **5a-j** and RES (10 μM) in HT22 cells was assessed by MTT assay toward Aβ42 after 24 h incubation at 37 °C. The results were given as average of two independent experiments (n = 3). UC = untreated cells, RES = resveratrol. 132

Figure 69. Cumulative chapter summary of *N*,4-diphenylthiazol-2-amines (**5**).....132

Figure 70. Banner for Chapter 6 143

Figure 71. ThT-monitored 24 h aggregation kinetics of Aβ42 (5 μM) in the presence of 1, 5, 10, and 25 μM of *N*-methyl-*N*,4-diphenylthiazol-2-amines (**6a**) at pH 7.4, 37 °C in phosphate buffer. Aggregation kinetics were monitored by ThT-fluorescence spectroscopy (excitation = 440 nm, emission = 490 nm). Results are average ± SD of three independent experiments (n = 3). 149

Figure 72. Panel A: Predicted binding mode of **6j** (ball and stick cartoon) in the Aβ40-dimer model (ribbon diagram, pdb id: 2LMN, CDOCKER energy = –18.03 kcal/mol; CDOCKER interaction Energy = –24.99 kcal/mol). Panel B: Predicted

binding mode of **6a** (ball and stick cartoon) in the Aβ42-dimer model (ribbon diagram, pdb id: 5KK3, CDOCKER energy = –14.79 kcal/mol; CDOCKER interaction energy = –26.93 kcal/mol).....151

Figure 73. TEM images of Aβ40 and Aβ42 aggregation. Top: Panel A: Aβ40 control (5 μM). Panel B: Aβ40 + **6j** (5 μM). Bottom: Panel A: Aβ42 control (5 μM). Panel B: Aβ42 + 6a (5 μM). Scale bars represent 100 nm.....152

Figure 74. Percentage viability of the *N*,4-diphenylthiazol-2-amine derivatives **6a-j** and RES (10 μM) in HT22 cells in the presence of Aβ40 was assessed by MTT assay after 24 h incubation at 37 °C. The results were given as average of two independent experiments (n = 3). UC = untreated cells, RES = resveratrol.....154

Figure 75. Percentage viability of the *N*,2-diphenylthiazol4-amine derivatives **6a-j** and RES (10 μM) in HT22 cells in the presence of Aβ42 was assessed by MTT assay after 24 h incubation at 37 °C. The results were given as average of two independent experiments (n = 3). UC = untreated cells, RES = resveratrol.....154

Figure 76. Cumulative chapter summary of *N*,4-diphenylthiazol-2-amines (**6**).....155

Figure 77. Banner for Chapter 7.....164

Figure 78. Synthetic mechanism of the *N*,2-diphenylthiazol-4-amine derivatives 7a-d.166

Figure 79. ThT-monitored 24 h aggregation kinetics of Aβ40 (5 μM) in the presence of 1, 5, 10, and 25 μM of *N*,4-diphenylthiazol-2-amines (**7a**) at pH 7.4, 37 °C in phosphate buffer. Aggregation kinetics were monitored by ThT-fluorescence spectroscopy (excitation = 440 nm, emission = 490 nm). Results are average ± SD of three independent experiments (n = 3).....169

Figure 80. ThT-monitored 24 h aggregation kinetics of Aβ42 (5 μM) in the presence of 1, 5, 10, and 25 μM of *N*,4-diphenylthiazol-2-amines (**7b**) at pH 7.4, 37 °C in phosphate buffer. Aggregation kinetics were monitored by ThT-fluorescence spectroscopy (excitation = 440 nm, emission = 490 nm). Results are average ± SD of three independent experiments (n = 3). 171

Figure 81. Panel A: Predicted binding mode of **7a** (ball and stick cartoon) in the Aβ40-dimer model (ribbon diagram, pdb id: 2LMN, CDOCKER energy = –8.90 kcal/mol; CDOCKER interaction Energy = –18.95 kcal/mol). Panel B: Predicted binding mode of **7b** (ball and stick cartoon) in the Aβ42-dimer model (ribbon diagram, pdb id: 5KK3, CDOCKER energy = –8.81 kcal/mol; CDOCKER interaction energy = –23.40 kcal/mol). 173

Figure 82. TEM images of Aβ40 and Aβ42 aggregation. Top: Panel A: Aβ40 control (5 μM). Panel B: Aβ40 + **7a** (5 μM). Bottom: Panel A: Aβ42 control (5 μM). Panel B: Aβ42 + **7b** (5 μM). Scale bars represent 100 nm. 174

Figure 83. Percentage viability of the *N*,2-diphenylthiazol-4-amine derivatives **7a-d** and RES (10 μM) in HT22 cells treated with Aβ40 was assessed by MTT assay after 24 h incubation at 37 °C. The results were given as average of two independent experiments (n = 3). UC = untreated cells, RES = resveratrol. 175

Figure 84. Percentage viability of the *N*,4-diphenylthiazol-2-amine derivatives **7a-d** and RES (10 μM) in HT22 cells treated with Aβ42 was assessed by MTT assay after 24 h incubation at 37 °C. The results were given as average of two independent experiments (n = 3). UC = untreated cells, RES = resveratrol. 176

Figure 85. Cumulative chapter summary of *N*,2-diphenylthiazol-4-amines (**7**)..... 176

Figure 86. General structure of *N*,4-diphenylthiazol-2-amine derivatives in Chapter 3.185

Figure 87. General structure of *N*-methyl-*N*,4-diphenylthiazol-2-amine derivatives in Chapter 4. 187

Figure 88. General structure of *N*,4-diphenylthiazol-2-amine derivatives in Chapter 5.188

Figure 89. General structure of *N*-methyl-*N*,4-diphenylthiazol-2-amine derivatives in Chapter 6. 189

Figure 90. General structure of *N*,2-diphenylthiazol-4-amine derivatives in Chapter 7.190

Figure 91. Suggested SAR strategies based on varying the central rings for future studies 194

Figure 92. Percentage viability of the *N*,4-diphenylthiazol-2-amines and regioisomer (10 μM) in HT22 cells in the absence of Aβ was assessed by MTT assay after 24 h incubation at 37 °C.....297

LIST OF TABLES

Table 1. Currently approved treatments of AD. 11

Table 2. BACE1 inhibitors in phase III clinical trials. 31

Table 3. Inhibition data for *N*,4-diphenylthiazol-2-amine derivatives **1a-j**, **2a-b** and reference compounds toward Aβ40 aggregation, and their ClogP values. 61

Table 4. Inhibition data for *N*,4-diphenylthiazol-2-amine derivatives **1a-j**, **2a-b**, and reference compounds toward Aβ42 aggregation, and their ClogP values. 64

Table 5. Inhibition data for *N*-methyl-*N*,4-diphenylthiazol-2-amine derivatives **3a-i**, **4a-b**, and reference compounds toward Aβ40 aggregation, and their ClogP values. 91

Table 6. Inhibition data for *N*-methyl-*N*,4-diphenylthiazol-2-amine derivatives **3a-i**, **4a-b**, and reference compounds toward Aβ42 aggregation, and their ClogP values. 93

Table 7. Inhibition data for sulfonamide based *N*,4-diphenylthiazol-2-amine derivatives **5a-j**, and reference compounds toward Aβ40 aggregation, and their ClogP values. 120

Table 8. Inhibition data for *N*-methyl-*N*,4-diphenylthiazol-2-amine derivatives **5a-j**, and reference compounds toward Aβ42 aggregation, and their ClogP values. 122

Table 9. Inhibition data for *N*-methyl-*N*,4-diphenylthiazol-2-amine derivatives **6a-j**, and reference compounds toward Aβ40 aggregation, and their ClogP values. 147

Table 10. Inhibition data for *N*-methyl-*N*,4-diphenylthiazol-2-amine derivatives **6a-j** and reference compounds toward Aβ42 aggregation, and their ClogP values. 148

Table 11. Inhibition data for *N*,2-diphenylthiazol-4-amine derivatives **7a-d**, and reference compounds toward Aβ40 aggregation, and their ClogP values. 168

Table 12. Inhibition data for *N*,2-diphenylthiazol-4-amine derivatives **7a-d**, and reference compounds toward Aβ42 aggregation, and their ClogP values. 170

LIST OF SCHEMES

Scheme 1. Synthetic route towards the *N*,4-diphenylthiazol-2-amine derivatives **1-2**. 58

Scheme 2. Synthetic route toward the *N*-methyl-*N*,4-diphenylthiazol-2-amines **3-4**. 89

Scheme 3. Synthetic route toward the (alkylsulfonyl-azaneylphenyl)-*N*-phenylthiazol-2-amines **5a-h** and (2-(phenylamino)thiazole-4-yl)phenyl)-azanesulfonamides **5i** and **5j**. 118

Scheme 4. Synthetic route toward the *N*-methyl-*N*,4-diphenylthiazol-2-amine derivatives **6a-j** possessing either sulfonamide or sulfamide substituents. 145

Scheme 5. Synthetic route toward the *N*,2-diphenylthiazol-4-amine derivatives **7a-d**. .166

LIST OF ABBREVIATIONS

Aβ = Amyloid-β

ACE = Angiotensin converting enzyme

ACh = Acetylcholine

AChE = Acetylcholinesterase

AChEI = Acetylcholinesterase inhibitor

ACID = APP intracellular domain

ACN = Acetonitrile

AD = Alzheimer's disease

ADAM = A disintegrin and metalloprotease

ADDLs = Amyloid-derived diffusible ligands

ALS = Amyotrophic lateral sclerosis

AMPAR = 2-Amino-3-(5-methyl-3-oxo-1,2-oxazol-4-yl)propaoic acid receptor

APH1 = Anterior pharynx-defective 1

APOE4 = Apolipoprotein ε4

APP = Amyloid precursor protein

BACE = β-site APP cleaving enzyme

BBB = Blood-brain barrier

BuChE = Butylrylcholinesterase

BuChEI = Butylrylcholineesterase inhibitor

cAMP = Cyclic adenosine monophosphate

CAPPD = Central APP domain

CD = Circular dichroism

CDK5 = Cyclin dependent kinase

ChAT = Choline acetyltransferase

ChE = Cholinesterase

ChEI = Cholinesterase inhibitor

ClogP = Partition coefficient

CNS = Central nervous system

CSF = Cerebrospinal fluid

CT83/99 = C-terminal fragment 83 or 99

DCM = Dichloromethane

DLB = Dementia with Lewy body

DMF = Dimethylformamide

DMSO = Dimethylsulfoxide

DMTs = Disease-modifying therapies

EDG = Electron-donating group

EOAD = Early-onset AD

ERK2 = extracellular signal-regulated kinase

EtOH = Ethanol

EWG = Electron-withdrawing group

FAD = Familial AD

FDA = Food and Drug Administration

FDG-PET = ^{18}F-fluorodeoxyglucose PET

FTD = Fronto-temporal dementia

GFLD = growth factor-like domain

GPCR = G-protein-coupled receptor

GSK3 = Glycogen synthase kinase 3

HBS = Heparin binding site

HMW = High molecular weight

HD = Huntington's disease

IDE = Insulin degrading enzyme

iGluR = Ionotropic receptor

IL = Interleukin

IVIG = Intravenous immunoglobulin

KPI = Kunitz protease inhibitor

LCMS = Liquid-chromatography coupled to a mass spectrometer

LMW = Low molecular weight

LOAD = Late-onset AD

LRP = Lipoprotein receptor-related protein

mAChR = Muscarinic acetylcholine receptor

MAP = Microtubule-associated protein

MAPK = Mitogen activated protein kinase

MARK = Microtubule-affinity regulating kinase

MB = Methylene blue

MCI = Mild cognitive impairment

mGluR = Metabotropic receptor

$MgSO_4$ = Magnesium sulfate

MOA = Mechanism of actions

MRI = Magnetic resonance imaging

MoCA = Montreal cognitive assessment

MT = Microtubule

MTT = 3-(4,5-Dimethylthiazol-2-yl)-2,5-diphenyltetrazolium bromide

nAChR = Nicotinic acetylcholine receptor

NaH = Sodium hydride

NCT = Nicastrin

NEP = Neprilysin

NFTs = Neurofibrillary tangles

NMDA = *N*-methyl-D-asparate

NMDAR = *N*-methyl-D-asparate receptor

NMJ = Neuromuscular junction

NMR = Nuclear magnetic resonance

OG = Orange G

PAS = Peripheral anionic site

PEN2 = Presenilin enhancer 2

PET = Positron emission tomography

P-gp = P-glycoprotein

PHFs = Paired helical filaments

PKA = protein kinase A

PS1 (or 2) = Presenilin 1 (or 2)

PTA = Phosphotungstic acid

RAGE = Receptor for advanced glycation end products

RES = Resveratrol

RFUs = Relative fluorescence units

ROS = Reactive oxygen species

RT = Room temperature

SAD = Sporadic AD

sAPPα = Soluble APP fragment α

sAPPβ = Soluble APP fragment β

SAR = Structure-activity relationship

TEM = Transmission electron microscopy

THF = Tetrahydrofuran

ThT = Thioflavin T

TLC = Thin layer chromatography

TNFα = Tumour necrosis factor

UC = Untreated cells

Va-D = Vascular dementia

CHAPTER 1 Background on Alzheimer's Disease

1.1 Introduction

We are living in this new world, which is filled up with mind-boggling creations and inventions beyond people's imaginations. These advancements conceivably promise to give us powers just like our superheroes that we adore as their lifelong fans. An old-age question, of course, popped up into our head: which superpower of all time would we wish for if we had the opportunity. The ultimate superpower that we are more likely to own is mind control. It might be really cool to wield mind control powers like Professor X in Marvel comics to manipulate opponents' abilities. So, you might be thinking, "How do I possess these powers?" Thanks to the advances in science and technology, our world is brought one step closer to that direction – being able to read out the brain activity from one person and transferring to another person telepathically. But what, exactly, makes our brains so special that many researchers have spent years and years diving into learning more about it? Our brain is remarkably unique. It has billions of neurons that govern actions and reactions, and enable us to have the thoughts, memories, and personality traits – our most precious assets – that define who we are as individuals; every one of us is unique and different. What if people have lost a certain part of their brain function – as in the case of Auguste Deter – the very first Alzheimer's patient, who suffered from memory loss, paranoia, and psychological changes. Eventually she became bedridden and succumbed to the devastating disease, known as Alzheimer's disease (AD).[1–3]

AD is a progressive neurodegenerative disorder that affects wide areas of the cerebral cortex and hippocampus causing the brain cells to degenerate and die, leading to

the depletion of brain mass, deficit in memory, loss of cognitive abilities, and interference with the patients' independence on a day-to-day basis, which substantially contribute to the morbidity and mortality that are associated with significant social and economic burden.[4,5] AD accounts for up to 70% of all dementia cases, with nearly 50 million people afflicted with AD or other related dementias worldwide. The Alzheimer's Society Canada (https://alzheimer.ca/en) estimates the number of Canadians age 65, and older living with Alzheimer's dementia may reach approximately one million by 2031. This represents a rapid escalation from 564,000 Canadians who are living with AD today. The annual direct and indirect costs of care for those having dementia were about $10.4 billion in 2008, which may rise to $153 billion by 2038. According to the Alzheimer's Association (www.alz.org), AD is the 6th leading cause of death in the United States and every 66 seconds, there is a new patient being diagnosed with AD. In coming years, when the first wave of baby boom generation will reach to the age of 85, it is anticipated that this illness will have a profound impact on the lives of many people – not only individuals but also society. It is paradoxical that prolonging life has traditionally been an explicit goal for science,[6] but until now advances in science have not resulted in finding a cure to slow the erosion of memory that mainly targets people in their old age. Stunningly, and only very recently, a new drug aducanumab, which targets the amyloid cascade of AD received accelerated FDA approval in June 2021 (www.fda.gov). This is the first new drug to come out nearly in the last two decades for treating AD. Only time will tell if this heralds a new beginning for AD treatment.

Putting aside the development of Alzheimer's drugs for now, let's briefly discuss how AD is diagnosed. Even though the word "Alzheimer's disease" has existed for

centuries, it has still been adopted interchangeably with dementia. As mentioned earlier, Alzheimer's is a particular disease that damages the brain and robs the patients' memory and cognitive abilities. Dementia, on the other hand, is a constellation of symptoms of cognitive impairment – thinking, remembering, reasoning – and interfering with a person's daily living activities regardless of cause.[7] Currently, there hasn't been a specific test that can be used to diagnose dementia, except for a combination of physical (*i.e.*, medical history, lab tests, and imaging techniques) and cognitive tests (*i.e.*, Montreal Cognitive Assessment (MoCA)). To rule out AD, one must meet all the criteria for dementia and have a history of worsening of cognition with no evidence of another concurrent neurological disease, such as dementia with Lewy bodies (DLB), vascular dementia (Va-D), and fronto-temporal dementia (FTD). Until now, the use of clinical cognitive assessments has become standard practice for "early" detection of Alzheimer's.

Alzheimer's disease (AD) is a multifactorial disorder apparently caused by a variety of risk factors such as genetic and environmental factors. AD can be classified in two distinct forms of AD: familial AD (FAD) and sporadic AD (SAD). The etiology of FAD develops as a result of autosomal dominant mutations in amyloid precursor protein (APP) and presenilin (PS1 on chromosome 14, or PS2 on chromosome 1)[8] genes in human that lead to early-onset AD (EOAD) at the age under 60 years old, which is said to account for up to 1% of AD cases. In contrast, the vast majority of AD patients at the age of 60 and older are attributed to SAD or late-onset AD (LOAD).

Individuals who carry the apolipoprotein E4 (APOE4) allele are commonly exposed to higher risk of developing AD.[9–12] Depending on the number of APOE4 they carry can determine how early the disease progresses although the mechanism of this

correlation still remains unclear.[10,13] In humans, there are three major subtypes of APOE (a cholesterol transport gene)[13] namely APOE2, APOE3, and APOE4, which differ from one another by the substitutions at residues 112 and 158. APOE2 has two cysteines at both positions, APOE3 has cysteine at 112 and arginine at 158 while APOE4 has two arginines at both positions.[11] Not only they are different structurally, but they also differ in their effects on brain function. For instance, the first two APOE proteins have protective effects while the latter has neurotoxic effects against AD.[11,12] Furthermore, epidemiological studies exploring the risk factors for SAD have shown that there is a disproportionate incidence of AD in women compared to men, with about two-thirds of female patients developing AD.[14] Explanations for the different incidence rates between sexes are unclear and current studies suggest the discrepancy may depend on several factors.[15–19] One reason for a higher prevalence of AD among women is greater life expectancy compared to men. Another reason for this is because when women reach the menopause phase, their estrogen declines. In fact, estrogen plays an important role as mitochondrial protectors against the Aβ toxicity by decreasing the production of reactive oxygen species (ROS) which reduces oxidative stress, a well-known factor in AD pathology.[14]

In a general sense, the journey of more than two decades for studying and developing the pharmacotherapies for AD was quite challenging and narrow due to the maddening complexity of this neurodegenerative disease. In 1906, after Auguste Deter passed away due to the advanced stage of AD at age 55, Dr. Alois Alzheimer performed an autopsy of her brain under a microscope and conclusively confirmed the presence of the extensive accumulation and deposition of an abnormal form of the amyloid β (Aβ)

proteins located outside of neurons (*a.k.a*. amyloid plaques) and tau (τ) proteins inside of neurons (*a.k.a.* intracellular neurofibrillary tangles NFT).[1–3] These clumps of sticky plaques and tangles, which became the major hallmarks of the disease named after him.[1–3]

Let's skip decades of discovery to fast-forward to the 1990s, when billions of dollars have gone into the mind-blowing idea of chasing these sticky proteins nestled in the brain with the hope that they could remove them directly. However, it did not turn out to be that easy due to the complexity of human brain. As a result, a number of other hypotheses have been proposed for explaining the pathogenesis of AD (Figure 1), including misfolding of proteins (amyloid β and tau hypotheses); synaptic failure and reduction of neurotransmitters (cholinergic dysfunction); and mitochondrial dysfunction (oxidative stress, impaired insulin signaling in the brain, inflammation, and depletion of calcium regulation).[13] That said, numerous studies have been published on the development of anti-AD therapies based on these hypotheses.

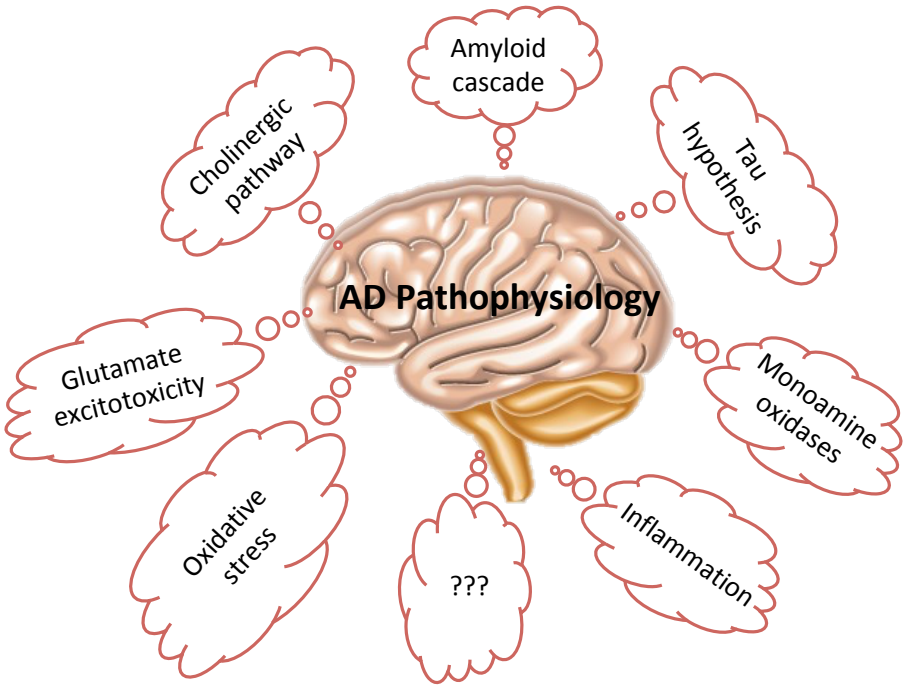

Figure 1. Schematic outline of the pathology depicting the complexity of AD disease**.**

1.2 The Cholinergic Dysfunction Hypothesis

In AD progression, neuronal damage and death are usually perceived as concomitants of the existence of amyloid plaques. One of the proteins interconnected with amyloid plaques is acetylcholinesterase (AChE), which is a pivotal enzyme in the cholinergic nervous system comprised of peripheral and central nervous systems (CNS).[20–23] In a normal cholinergic transmission, it acts as a catalyst in the hydrolysis of acetylcholine (ACh, a cholinergic neurotransmitter in the CNS) to afford acetate ions and choline, which can be recycled and reused for the synthesis of ACh in the presynaptic neuron *via* choline acetyltransferase (ChAT) by coupling recycled choline and acetyl coenzyme A.[20,21,23] After ACh is synthesized; it is transported to synaptic vesicles in the presynaptic neuron with the help of a vesicular ACh transporter (vAChT) and then released into the synaptic cleft. Upon its release, it briefly binds to post-synaptic

receptors: nicotinic (nAChR) and/or G-protein coupled muscarinic acetylcholine receptors (mAChR) to start off another neurotransmission cascade (Figure 2).[20,21,23] In the late stage of AD, in the basal forebrain of AD's patients, a remarkable loss of cholinergic neurons has been observed, causing havoc in the neurotransmission as well as significant reduction in ACh, ChAT, and AChE in the hippocampus and neocortex, which became one of the major pathologies in AD, and established a foundation for the cholinergic hypothesis.[22,24,25]

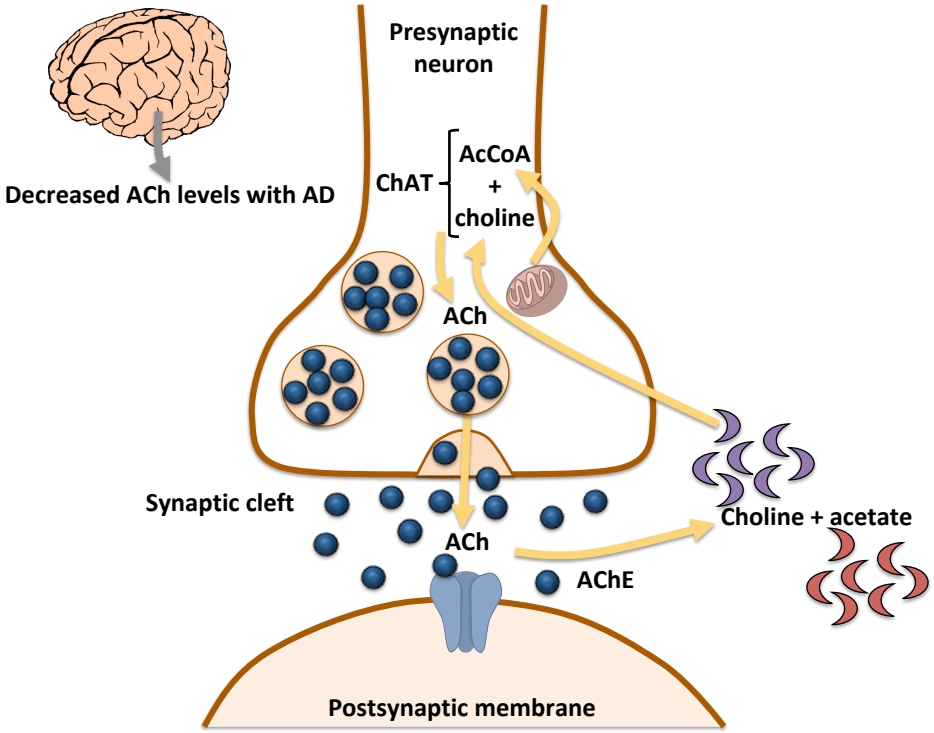

Figure 2. Schematic representation of cholinergic neurotransmission mediated by acetylcholine (ACh).

AChE is a serine hydrolase located at neuromuscular junction (NMJ) as well as in the cholinergic brain synapses, and generally referred to as the predominant cholinesterase (ChE) enzyme that is responsible for the dissociation of ACh so that it does not cause the over-stimulation at the post-synaptic neuron.[20–23] To maintain this

performance, AChE possesses such a high catalytic rate that it is able to break down up to 25,000 molecules of ACh within a second.[23] As a consequence, governing the rapid breakdown of ACh and increasing the ACh concentrations at the synapse have captivated the focus of intense research. Regarding its special structure, AChE has an active site situated deep down at the bottom of the gorge that is about 20 Å long and narrow (Figure 3).[20–23] There are various sub-sites within the gorge, comprising of the anionic site, to which the positive quaternary amine of choline scaffold of ACh binds, the esteratic site, which contains the catalytic triad: Ser200, His440, and Gln327 operates in tandem with the hydrolysis of ACh to generate acetate ions and choline; and the acyl pocket, which contributes to the enzyme's specificity and stability, particularly Phe295 and Phe297 residues.[20–23] About 15 Å above the active site close to the opening of the gorge containing Trp286, that is where a peripheral anionic site (PAS) positions. The PAS plays significant roles as a guide for the substrate entering the active site through stabilization of the cation from Trp82, as well as a neuropathological chaperone for Aβ proteins to develop into an extremely toxic complex of AChE-Aβ.[20–23]

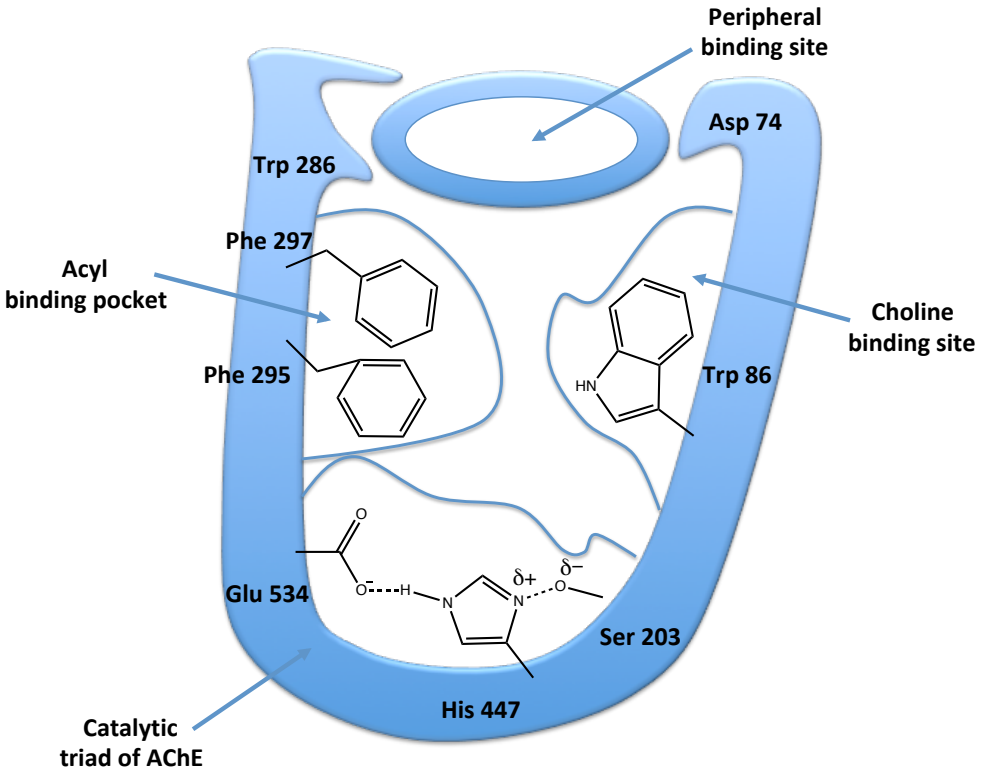

Figure 3. Schematic representation of AChE binding sites.[23] Reproduced with permission from Ref [23].

Another crucial ChE enzyme, butyrylcholinesterase (BuChE) is commonly found throughout the body – in plasma and in hippocampus and temporal neocortex, but not as abundant as AChE. Moreover, BuChE plays an essential supporting role for the AChE enzyme in hydrolyzing the metabolism of ACh similar to AChE, except for many differences in the structural arrangement of BuChE.[26,27] Both AChE and BuChE have similar 20 Å active site gorge embedded deep in the enzymes, as well as have the catalytic triad with three residues (Ser, His, and Gln). The differences between the two enzymes are the aromatic residues at the opening of the active site and at the acyl pocket, which are being arranged with smaller residues, giving rise to the better flexibility at the entrance and larger volume size of the active site for BuChE which is ~ 200 Å larger than that of AChE.[28] Interestingly, in the brain of AD's patients, the AChE activity is reported

to decline while that of BuChE rises, contributing to the variation in the ChE ratio that results in the deficiency of ACh, the loss of neurotransmission and ultimately the deterioration of cholinergic neurons.[26,29] Further studies revealed that BuChE is found to be masking the plaque areas, especially in the cerebral cortex, where a high level of BuChE in the cerebrospinal fluid (CSF) can be detected. This evidence suggests the BuChE may be associated with the progression of AD.[26,27]

All factors considered, these findings led to the development of AD pharmacotherapies with AChE inhibitors (AChEIs) or ChE inhibitors (ChEIs) by means of inhibiting the ChE from hydrolyzing ACh to increase the ACh concentrations, and thus recover the cholinergic neurotransmission.[22] To date, a few current marketed drugs, including ChEIs: donepezil, rivastigmine, galantamine and NMDA-receptor antagonist: memantine, only curtailed the symptoms – for a short term (Table 1).[23] These current approaches focus on managing patients (mild to moderate) to maintain their mental and behavioural functions, as well as slow down the disease progress.[22,24,25] The first-of-its-kind treatment aducanumab, which received the FDA's approval in June 2021, targets the underlying mechanism of disease initiation; however, the approval was controversial due to the question mark on its clinical efficacy and reported side effects, such as brain swelling and bleeding. Having said that, this will stimulate the development of the next generation of innovative AD therapies and a better understanding of the mechanism of proteinaceous deposits with hope to discover effective therapies.

Table 1. Currently approved treatments of AD.

Compound name Structure	Mechanism of Action	Indications	Formulations
Donepezil (Aricept, 1996) 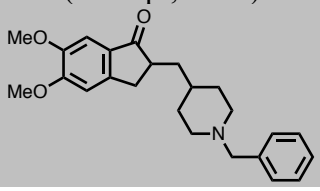	ChE inhibitor	Mild to moderate (5 – 10 mg) Moderate to severe (10 – 23 mg)	Tablet, disintegrating tablet
Galantamine (Razadyne, Reminyl, 2001) 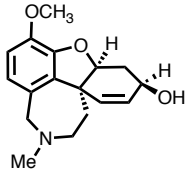	ChE inhibitor	Mild to moderate (8 – 24 mg)	Tablet, oral solution, transdermal patch
Rivastigmine (Exelon, 2000) 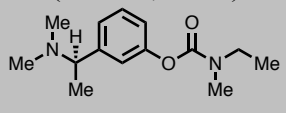	ChE inhibitor	Mild to moderate (1.5 – 6 mg)	Intermediate-release tablet, oral solution, extended-release tablet, transdermal patch
Memantine (Namenda, 2003) 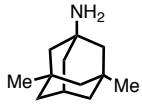	NMDA antagonist	Moderate to severe (5 – 10 mg)	Tablet, oral solution
Memantine/donepezil (Namzaric, 2014)	Combination	Moderate to severe (7/10 – 28/10 mg)	Extended-release capsule
Aducanumab (Aduhelm, 2021)	Anti-amyloid	(170 mg/1.7 mL or 300 mg/3 mL) – 100 mg/mL	Injection

1.3 Amyloid-β (Aβ) Hypothesis

The links between this amyloid cascade and AD pathogenesis are still vague in terms of how Aβ aggregation originally takes place and eventually leads to neurodegeneration. Such knowledge is crucial for depicting a map out of chaos for the complication of AD, which is neurophathologically characterized by a proteinaceous cocktail of amyloid plaques and tangles. In the neuritic plaques, amyloid β peptides (39 –

42 amino acids), which have been recognized as a central component of the plaques that extensively build up outside the neurons, stem from a large β-amyloid precursor protein (APP) *via* sequential proteolytic cleavages of the secretase enzymes, such as β and γ-secretases.[30–34] Despite APP being in conjunction with multiple implications including neurite outgrowth, cell adhesion,[35] and neuroprotection from injury, its normal physiological function of APP and its processing to convert APP into Aβ still remain unclear.[30]

1.3.1 Amyloid Precursor Protein (APP)

The human APP gene is located on the long arm of chromosome 21 with three main isoforms (APP_{695}, APP_{751}, and APP_{770}) derived from several alternative slicing of exons 7, 8 and 15, respectively.[30,31,36] The differences between these isoforms are that APP_{751} and APP_{770} isoforms are expressed by glial cells, platelets, and peripheral tissues,[31,36] and possess a Kunitz protease inhibitor (KPI) domain, while APP_{695} isoform is abundantly expressed in neurons but lacks the KPI domain.[33–36] KPI domain is an additional segment (57 amino acids) in the sequence of APP, which plays a significant role in communicating with other proteins.[34] Although KPI domain's function is not completely understood, numerous studies have shown that KPI-containing APP isoforms promote the deposits of Aβ aggregation, tightly linking to the pathogenesis of AD.[33,36]

1.3.2 Amyloid Metabolism and Processing Pathways

APP is comprised of two distinct domains: an extracellular glycosylated N-terminal domain and an intracellular cytoplasmic C-terminal domain. According to the sequence and structural analyses, N-terminal domain is larger than the C-terminal

domain.[35] Moreover, N-terminal domain shared two highly conserved domains: E1 and E2 (Figure 4).[36] E1 domain divides into several subdomains, including a growth factor-like domain (GFLD) known as heparin binding site (HBS), a metal binding domain, and acid domain.[36] E2 domain known as central APP domain (CAPPD), which is made up of six α-helices coiled tightly with each other, generating a dimerization motif.[36] Since the ends of N-terminal and C-terminal are located at the dimer's surface, they tend to undergo the dimerization of APP through the E2 domain, which suggests that APP has potential for cell-cell adhesion.[36] In fact, E2 can bind to itself in antiparallel dimers.[33,36] The E2 domain is followed by the Aβ region, wherein α and β-secretase cleavage sites are located. The γ-secretase cleavage site is found to situate within the transmembrane domain, which is followed by the APP intracellular cytoplasmic domain (AICD).[26] The AICD, which is generated from the sequential proteolytic processing of APP, is subsequently transported to cytoplasm.[26] Note that the AICD is generated at the same time as Aβ.[37]

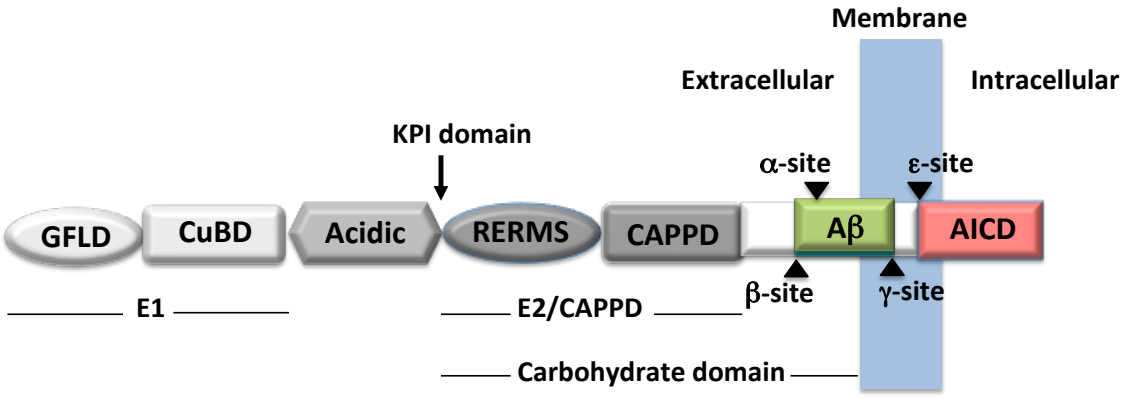

Figure 4. Schematic domain structure of APP.[37] Reproduced with permission from Ref [37].

As mentioned earlier, the mechanism of APP processing to Aβ in humans has not been fully understood yet due to the complex proteolytic process of pro- and anti-APP involving three types of secretase enzymes (α, β, γ) (Figure 5).[36,38] There are two major metabolic routes: the non-amyloidogenic and amyloidogenic pathways (Figure 6).

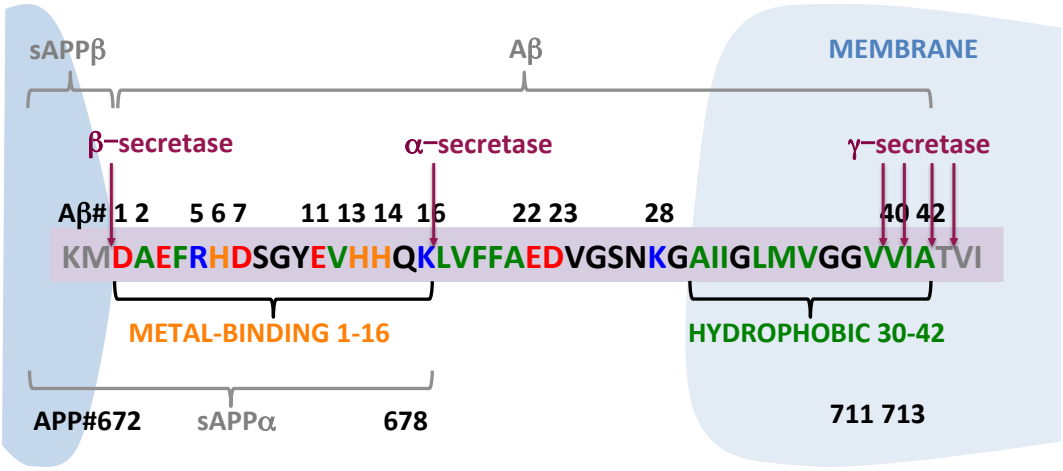

Figure 5. The Aβ sequence within APP and the main secretase cleavage positions.[39] Reproduced with permission from Ref [39].

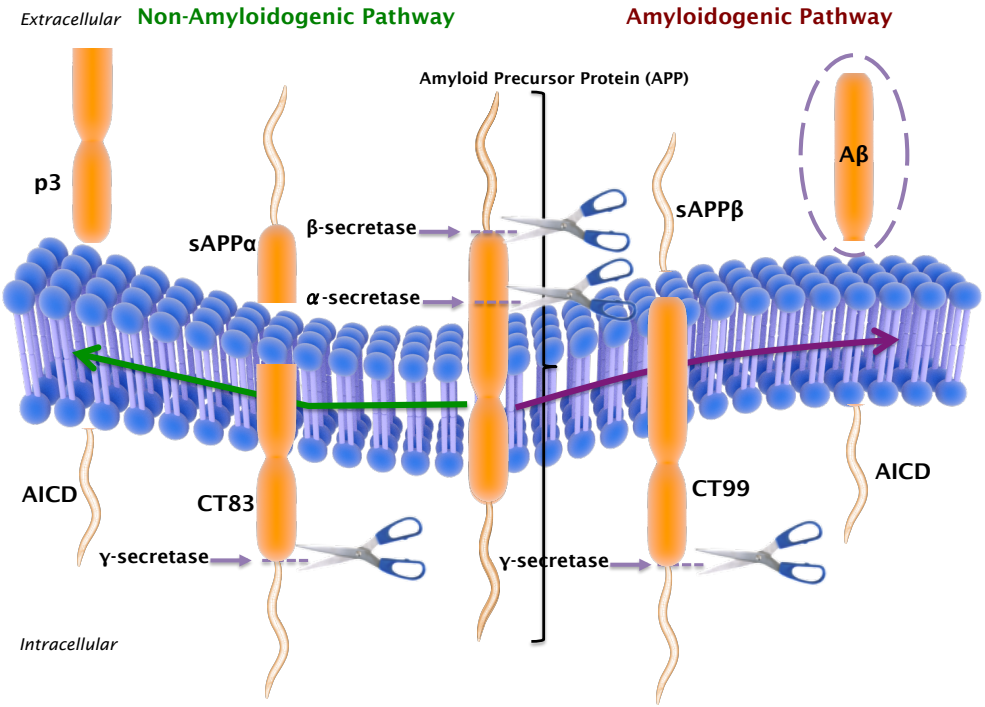

Figure 6. Schematic diagram showing the two proteolytic pathways of APP: non-amyloidogenic pathway (left) and amyloidogenic pathway (right).

In the non-amyloidogenic (benign) pathway, α-secretase – a disintegrin and metalloprotease (ADAM) family of zinc-metalloproteinase with ADAM9, ADAM10, and ADAM17 is involved in the cleavage of the APP molecule between amino acids 687 and 688 (APP751 numbering). [33,34,40] This cleavage of APP within the Aβ domain (at the Lys16 – Leu17 bond)[33] results in the release of the secreted form of a soluble ectodomain of N-terminal APP fragment (sAPPα) that has an essential role in neuronal survival and neurite growth,[33,40] and a membrane-bound-C-terminal fragment CT83. This fragment holds the carboxyl half of Aβ peptide, which subsequently becomes a substrate for γ-secretase to form AICD fragment and liberate an extracellular truncated Aβ fragment, termed p3 (3 kDa, also referred to as Aβ17-40/42).[40] Although Aβ17-40/42 has been recently reported to be directly involved in the pathogenesis of both AD and Down syndrome, their biological impact on neuronal function is yet to be fully elucidated.[33,41]

In the series of cleavages of membrane proteins, γ-secretase is known to be an intramembrane aspartyl protease that is composed of four subunits: anterior pharynx-defective 1 (APH1), presenilin enhancer 2 (PEN2), nicastrin (NCT), and presenilin (PS1 or PS2), all of these give rise to the function of the entire γ-secretase complex in the endoplasmic reticulum (Figure 7).[8,42,43] Even though the specific roles of each subunit are not yet fully defined, it has been suggested that PS is the active site of γ-secretase located at the interface between N-terminal and C-terminal fragments.[43] In fact, one of the catalytic aspartates of the active site is made up by each of PS components, and NCT plays a role of a substrate since it binds to the aminoterminal fragment of previously cleaved transmembrane proteins.[8,42–44] It is interesting that the cleavage by γ-secretase to release a large ectodomain region can only take place when the substrates are first

cleaved by another protease, such as α-secretase or β-secretase within the transmembrane domain of APP in the production of Aβ.[42,43]

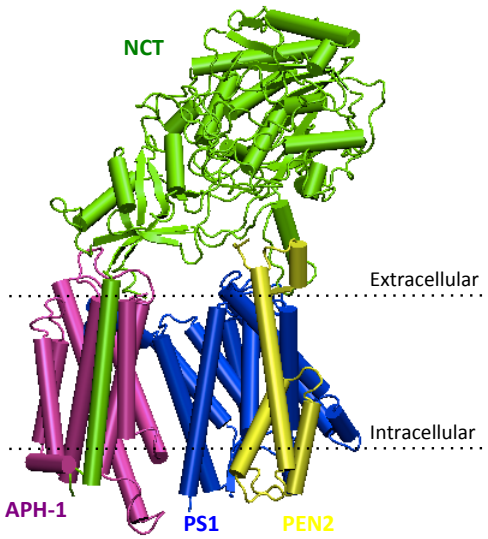

Figure 7. The human γ-secretase structure.[8] Reproduced with permission from Ref [8].

In the amyloidogenic (harmful) pathway, β-secretase is a 501 amino acid membrane-bound aspartyl protease β-site APP-cleaving enzyme 1 (BACE1, also known as Asp2 or memapsin 2)[33,45] that is overexpressed in cells and cleaves the APP molecule at the β-site (Asp1) between amino acids 671 and 672 (APP770 numbering),[33] generating a soluble ectodomain of N-terminal APP fragment (sAPPβ), which is 16 residues shorter than sAPPα at its C-terminus,[34] and does not offer the neuroprotection, as seen in sAPPα,[40] and a membrane-bound-C-terminal fragment CT99. Similarly to CTF83, CTF99 becomes a substrate for γ-secretase to cleave between amino acids 713/714 or 711/712, releasing the AICD fragment with the full Aβ fragment sequence, ranging from 36 to 42 amino acid residues in length owing to the various transmembrane cleavage sites of γ-secretase.[42] It is noteworthy that the functions of these intermediate products CTF83/99 have not been fully understood.[33]

Besides BACE1, which is involved in the rate-determining step in the APP cleavage process, BACE2 homologue has up to 64% similarity compared with BACE1, suggesting that it may have a β-secretase function. However, this function does not easily happen because BACE2 is only expressed and active in peripheral tissues, such as pancreas, stomach and placenta.[40,46,47]

Although Aβ40 and Aβ42 are the dominant species, Aβ40 is the most abundant isoform (~80-90%) compared to Aβ42 (~5-10%).[42] The Aβ42 has been reported to be more pathogenic due to its C-terminal residues being much more hydrophobic and more prone to aggregate into toxic species at a faster rate than Aβ40.[42,48] Within the Aβ40/42 peptide, a sequence of six amino acids (residues 16 to 21), denoted as KLVFFA gives rise to a steric zipper formation and the hydrophobic core that plays a key role in gluing the monomers together through intermolecular interactions and thus, promoting the Aβ aggregation.[41,49-50] On that account, this central hydrophobic KLVFFA segment has become a main therapeutic target for the development of AD treatment *via* the inhibition of Aβ hypothesis, which has been traditionally considered as the basis of amyloid cascade mechanism, causing the onset and progression of AD.[41,49] Noteworthy, the hexapeptide KLVFFA have many properties in common with the full-length Aβ peptides, and therefore they are often used as models of Aβ aggregation.[40]

1.3.3 The Aβ-Peptide: Structure, Aggregation and Clearance

In order to design therapeutics that can target the amyloidogenic core at an early stage of the disease, it is essential to understand how the formation and transition of Aβ to fibrils actually takes place. The structures of Aβ peptides can be evaluated using

nuclear magnetic resonance (NMR) spectroscopy, molecular dynamic (MD) techniques, and X-ray crystallography.[35]

In aqueous solution, Aβ primarily exists as β-sheet structure on aggregation and forms of fibrils.[51] In the self-aggregating pathway of Aβ peptides, the soluble monomers spontaneously polymerize into various types of low molecular weight (LMW) oligomers, ranging from dimers to heptamers (< 8 Aβ subunits).[51,52] These LMW oligomers are soluble and may spread through the brain; consequently, they tend to bind to the receptors on the nearby cells and synapses that interrupt their normal functionality and cause neurotoxicity. [35,53] The heptamers then convert from these aggregates to higher molecular weight (HMW) oligomers with various size (up to 24 Aβ-aggregate subunits ~42 kDa – 1 mDa)[52] and morphology. Depending on their morphology, some oligomers are defined as follows: Aβ-derived diffusible ligands (ADDLs; spherical aggregates), Aβ-annular oligomers (doughnut-shaped structure), and protofibrils (curvilinear structure).[51,52] The latter is a result of the next process of aggregation, and followed by the stabilization to form into the insoluble fibrils of different length,[50] as anti-parallel and cross-β-sheet structures, composed of 2-6 protofibril subunits with dimension of more than 1 μm in length and 8-12 nm in thickness,[51,52] which cannot be degraded and cleared up through the substantial catabolism within the brain.[42] Regardless of their various morphologies, these fibrils have similar cross-sectional areas.[50] In order to examine structural details (e.g. dihedral torsional angles, distances between specific atoms) of these reconstructed fibrils, there are several biophysical and biochemical techniques that can be used to analyze the fibrils, including solid-state nuclear magnetic resonance (NMR) spectroscopy, solution-state NMR spectroscopy coupled with deuterium

exchange, circular dichroism (CD) spectroscopy, and transmission electron microscopy (TEM).[50] These fibrils combine with other forms of aggregates to form into highly insoluble senile plaques that are the major hallmarks of AD (Figure 8).

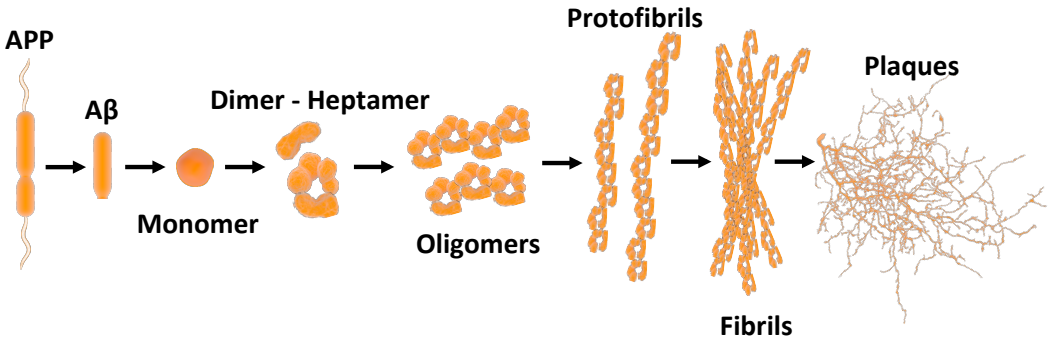

Figure 8. An illustration of self-induced Aβ aggregation pathway.

As discussed previously, Aβ is the primary component of amyloid plaque, which is commonly believed to be a prime suspect of AD pathogenesis. However, it has been reported that Aβ is not toxic when it is still in a non-aggregate form such as monomer.[48] In fact, the production of Aβ from APP has been observed even in non-AD patients under normal physiological conditions at the steady-state (or homeostatic) levels of Aβ, which is controlled and balanced by other processes such as enzymatic degradation, and receptor-mediated clearance that are primarily responsible for degrading Aβ peptides and transport Aβ out of the brain, across the blood brain barrier (BBB), or out into the blood circulation.[35,42,54] The exchange of soluble Aβ peptides across the BBB follows a bidirectional influx/efflux mechanisms (Figure 9), including the low-density lipoprotein receptor-related protein (LRP) on the abluminal (brain) side, and the receptor for advanced glycation end products (RAGE) on the luminal (blood) side.[42,55] It has been reported that LRP expression reduces during aging, leading to the disruption of Aβ oligomers efflux, which ultimately makes them to stay in the brain longer. In addition to

the impairments in the efflux mechanism, high affinity of Aβ oligomers to RAGE receptor entails Aβ oligomers to enter into the extracellular space of the brain from the blood stream.[56] In general, impairments in these influx/efflux mechanisms of Aβ results in a significant amount of Aβ deposition within the brain, leading to the development of amyloid pathology.[27,33,54–56]

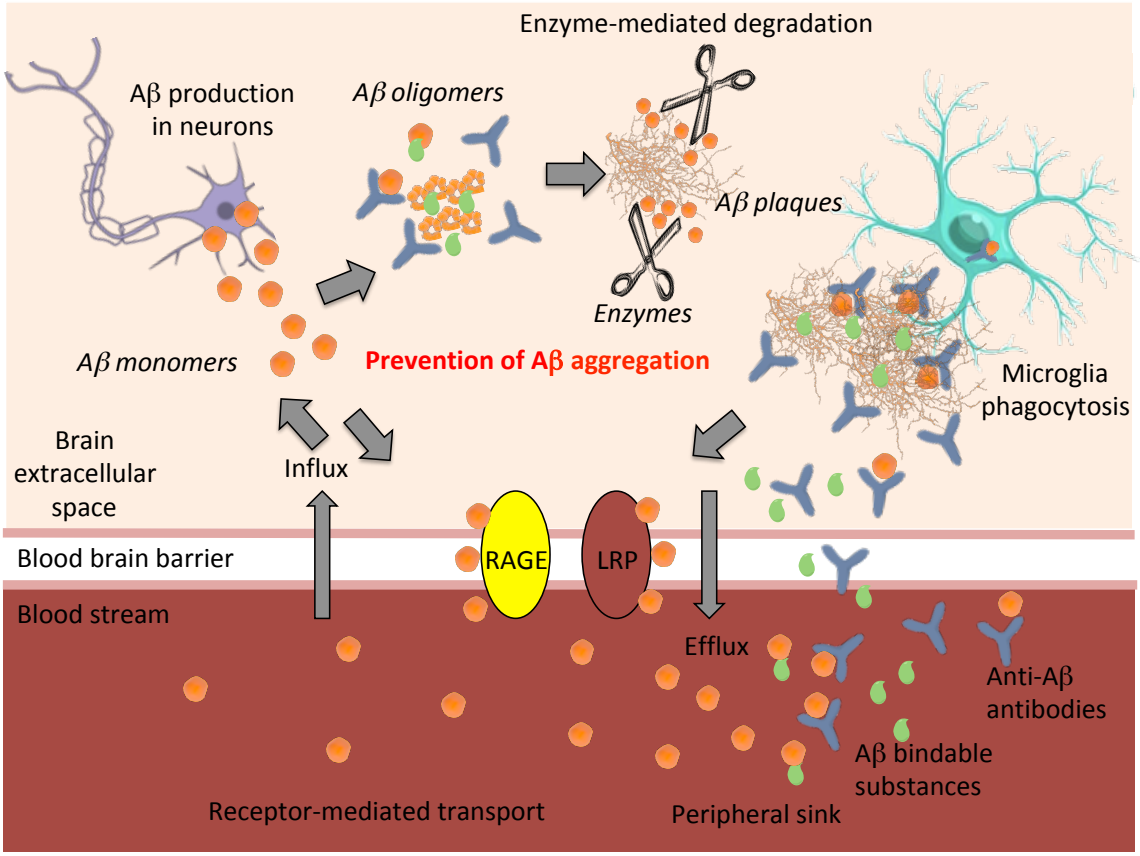

Figure 9. Mechanism of Aβ clearance.[55] Reproduced with permission from Ref [55].

With respect to enzymatic degradation, there are several Aβ-degrading enzymes: neprilysin (NEP), insulin degrading enzyme (IDE), endothelin converting enzyme (ECE1 or ECE2), cathepsin B, and angiotensin converting enzyme (ACE). Of these degrading enzymes, NEP appears to be the major key regulator of Aβ degradation and determinant of AD pathology.[35,42,54,55]

In this regard, NEP is a 93kDa type-II transmembrane zinc metallo-endopeptidase, whose active site situated in both intraluminal and extracellular space, into where it has been shown to degrade Aβ peptides.[35,42,54] This glycoprotein has a strong connection with many brain functions, one of which is memory.[35,42,54] NEP is capable of cleaving variety of peptides. Indeed, a number of studies have demonstrated that inhibition of NEP activity/expression results in the overload of Aβ that is linked to the accumulation of plaques and cognitive impairment.[35,42,54] In fact, it has been shown that NEP expression reduces in the cortex and hippocampus with age and in the early stages of AD, especially even more pronounced in AD patients with APOE4.[35,42,54,55]

1.3.4 Aβ Pathology and Physiology

As mentioned previously, the only cholinergic dysfunction theory alone cannot explain the complexity of AD pathophysiology,[57] which results in many functional consequences through multiple mechanisms, consisting of oxidative stress,[58–65] synaptic dysfunction,[51,52,66–69] excitotoxicity *via* interacting with neurotransmitters receptors, mitochondrial diffusion, inflammation, *ect*.[70] In fact, for many years, the aggregation of the mature amyloid fibrils was originally thought to account for pathogenesis of AD. As a matter of fact, some evidences based on recent studies on the toxicity levels of different Aβ oligomers revealed that the soluble oligomers ADDLs and protofibrils are the most neurotoxic species.[39,70–76] Moreover, an imbalance between Aβ production and Aβ clearance is one of the main culprits of early onset of AD.[57,60] This Aβ imbalance does not just limit to the disease process, but it has also been observed that oxidative stress is induced by the imbalance in the oxygen production and consumption of reactive oxygen

species (ROS) – a group of free radicals that are formed as a result of dysfunctional aerobic mitochondrial respiration.[58,64] Mitochondria is responsible for producing the necessary energy for metabolic cell processes *via* adenosine triphosphate (ATP) generation during oxidative phosphorylation, as well as generating ROS during respiration.[65] For instance, superoxide radicals ($O_2^{\bullet -}$) that are produced as by-product of reducing oxygen molecules and then reduced to hydrogen peroxide (H_2O_2) can react with the reduced metals (Cu^{1+}, Zn^{2+}, Fe^{2+}) to form the hydroxyl radicals ($^{\bullet}OH$) through Fenton reaction[77,78] in the presence of sulfur atom of amino acid methionine (M35) in the Aβ sequence, that acts as a electron donor (Figure 10) and *via* Haber-Weiss chemistry.[58,60,79,80] In fact, the excessive concentrations of these metal ions (*e.g.* copper and zinc) have been reported to deposit extensively in the brains of patients with AD.[60,59] Once ROS are produced in excess, these free radicals trigger severe cell damage in AD brain, by damaging proteins, DNA, and cell membranes through oxidation, as well as by facilitate Aβ aggregation in the CNS.[58–65] Oxidative stress is found to be elevated during normal aging and thus contributes to the primary cause of neurotoxicity owing to an overproduction of ROS or a reduction in antioxidant defenses, or both; however, it is exacerbated in neurodegenerative diseases, including AD, Parkinson's disease (PD), amyotrophic lateral sclerosis (ALS), and Huntington's disease (HD).[58,59,61,62,65]

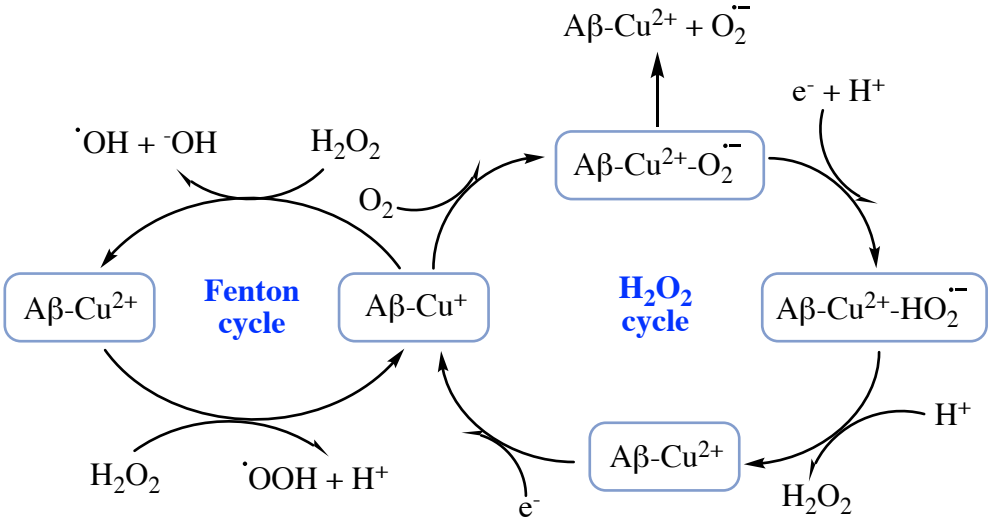

Figure 10. ROS production by Aβ-Cu^{2+}. Catalytic hydrogen peroxide (H_2O_2) cycle with superoxide ($O_2^{\bullet -}$) dissociation pathway (right) and Fenton cycle (left).

Mitochondrial dysfunction has been observed as a feature of normal aging and many neurodegenerative diseases, even in early stages.[60] Studies have shown that ROS has a connection with the amyloid hypothesis through mitochondrial dysfunction, in which mitochondrial complexes I (NADH dehydrogenase) and IV (cytochrome c oxidase) of mitochondria becomes deficient in transferring the electrons during oxidative phosphorylation, as Aβ overproduction reduces the expression of the electron transport chain enzymes, which results in the overproduction of ROS and the depletion of ATP (Figure 11).[59,61,70]

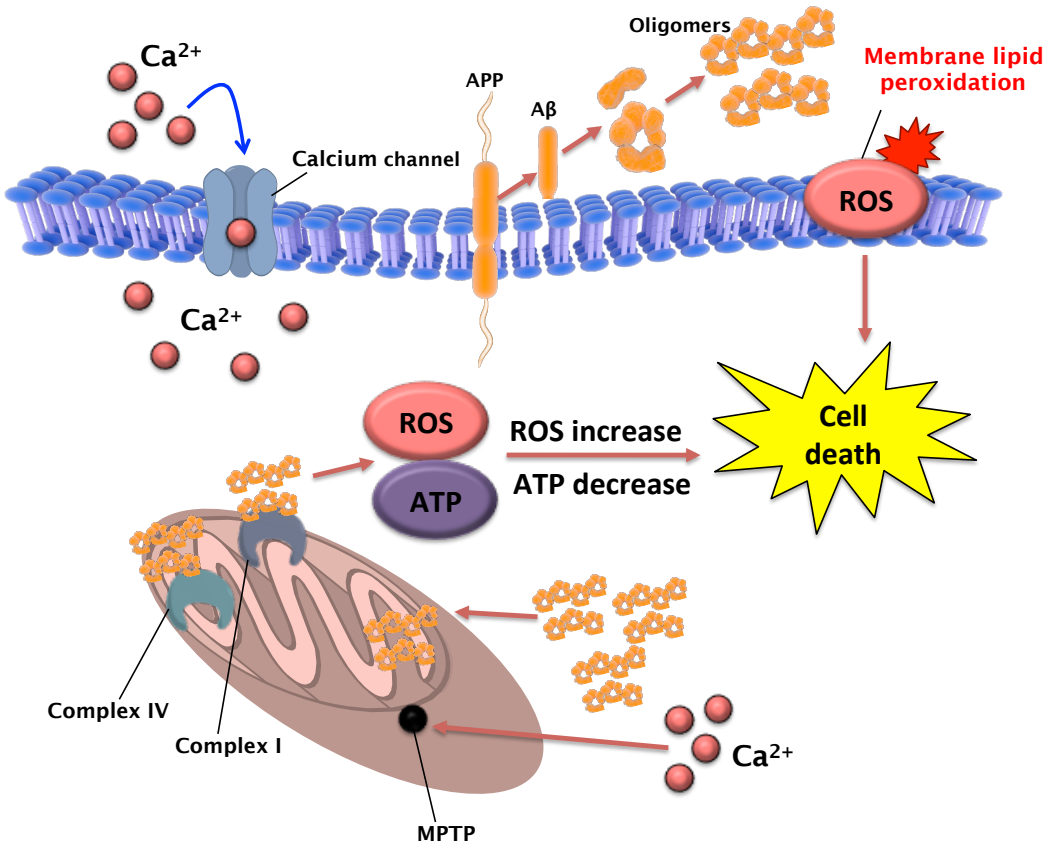

Figure 11. Mitochondria damage in AD.[81] Reproduced with permission from Ref [81].

The depletion of ATP and increased oxidative damage to synaptic proteins may be a consequence of the calcium (Ca^{2+}) dyshomeostasis, which significantly affects mitochondria that uses Ca^{2+} to activate some intracellular enzymes in the ATP generation, particularly pyruvate dehydrogenase, and ATP synthase, which are all regulated by Ca^{2+}.[82–87] With a prolonged increase in mitochondrial Ca^{2+}, the ROS production will be increased. In fact, this disturbance of Ca^{2+} homeostasis is further exacerbated by Aβ, which results in abnormally high levels of Ca^{2+} inside mitochondria and thus increases the generation of ROS, attributing to cell death (or apoptosis), synaptotoxicity, and associated with excitotoxicity.[82–87] Excitotoxicity is the overstimulation of *N*-methyl-D-aspartate (NMDA), or 2-amino-3-(5-methyl-3-oxo-1,2-oxazol-4-yl)propanoic acid

(AMPA) receptors, (NMDARs and AMPARs, respectively) expressed in the cerebral cortex and hippocampus by excessive neurotransmitter glutamate (predominantly) or aspartate and prolonged Ca^{2+} influx into the postsynaptic neuron through NMDARs, implicating in several neurological disorders, including AD, PD, HD, and ALS.[82–84,86–88] In particular, glutamatergic synaptic transmission is primarily affected. Glutamate is the excitatory neurotransmitter in CNS that takes a major part in synaptic plasticity, memory, and learning.[82–84,86–88] There are two groups of glutamate receptors: the ionotropic and the metabotropic receptors. The ionotropic receptor (iGluR) located in the postsynaptic sites is a group of transmembrane ion channels that respond to the binding of a chemical further divided into three subclasses: NMDA (NR1, NR2A-D, and NR3A-B), AMPA (Glu1-4), and kainate (GluR5-7) receptors. In this regard, NMDARs are much more permeable to Ca^{2+} compared to other iGluRs; in addition, the modulation of AMPARs and NMDARs induced by Aβ deposits overexpressed APP can result in cognitive deficits.[82–84,86–88] The metabotropic receptors (mGluRs) located in the presynaptic membrane which can be found in both neurons and glial cells in the brain that governs the release of glutamate and synaptic transmission.[83,86] mGluRs are also known as G-protein-coupled-glutamate receptors that are categorized into three subgroups according to their function and structure: GluN, GluA and GluK subunits.[83,86] The first group is capable of coupling to phosphatidylinositol (PI) hydrolysis and intracellular Ca^{2+} mobilization while the last two groups are able to negatively couple to adenylyl cyclase and play a key role as presynaptic autoreceptors.[83] A number of reports have suggested that the phospholipase C signaling of group I mGluR in the frontal cortex is down

regulated. Such dysfunction of mGluR aggravates the impairment of cognition in the pathogenesis of AD.[83]

With respect to AD pathology, it is also characterized by an inflammatory response, which is driven by the microglia (or myeloid cells) that maintains the healthy and normal conditions of homeostasis of the CNS and synaptic plasticity by securing and remodelling synapses.[89–93] For example, when there is a presence of Aβ oligomers and fibrils in the CNS, microglia automatically recognize the vicious signal triggered by Aβ, as Aβ aggregates are able to bind to microglia via several receptors such as CD14, CD36, CD47, α6β1 integrin, and RAGE; they respond to such changes by changing their function and morphological appearance or promoting the microglial activation (Figure 12).[92] These activated microglial cells are termed "reactive or primed" microglia, which can adopt a variety of functional microglia phenotypes.[92] In AD, during the transformation, microglia are observed to secrete pro-inflammatory cytokines[91] (*i.e.*, interleukin (IL-1β), IL-6, and tumour necrosis factor (TNFα)) and chemokines[91] (*i.e.*, chemokine (C-C motif) ligand (CCL)2/4/11), which actually prolong activation of the primed microglial cells.[92] Although this immune response is activated to protect the health of the CNS, this process ends up with a deterioration of microglia, which not only have an effect on their neighbour cells in the CNS including astrocytes,[91] oligodendrocytes and neurons, but also, exacerbate tau pathology,[92] as well as oxidative stress.[76] Ultimately, it leads to neurotoxicity, neurodegeneration, and neuronal death, which trigger neuroinflammation in AD.[89–93] In fact, there is evidence that microglia can phagocytize and degrade Aβ aggregates. However, such degradation or clearance of Aβ is clearly seen to be ineffective in AD.[89] Moreover, it has been shown that various states

of Aβ aggregates (monomers, oligomers, protofibrils, fibrils, and plaques) can dictate the pathogenic impact levels that may occur. For this reason, this knowledge has been used as a diagnostic measures to determine the neuropathological evaluation of AD brains.[92]

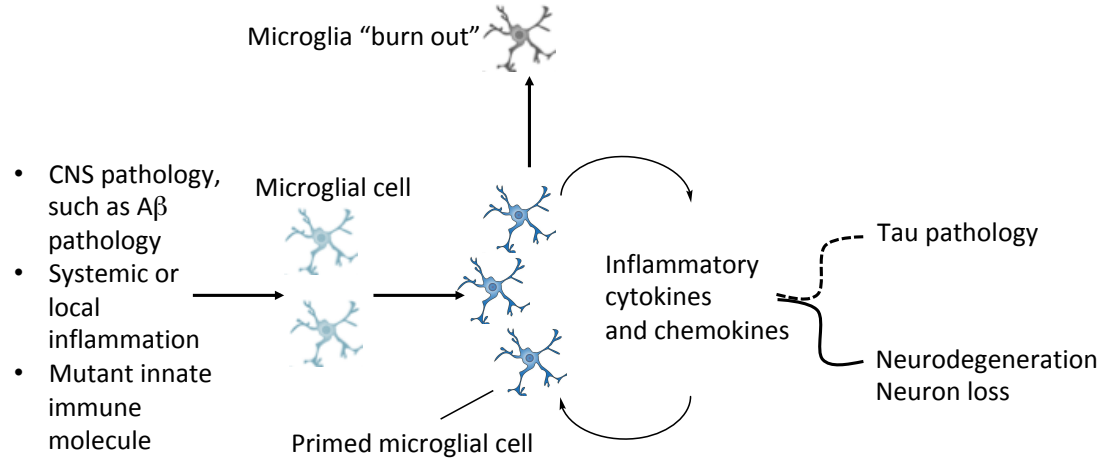

Figure 12. Pathological events in AD and microglia priming.[92] Reproduced with permission from Ref [92].

Besides the neuropsychological screenings to identify the mild cognitive impairment (MCI) patients *via* standard assessments such as the Mini-Mental State Examination (MMSE),[94] and Montreal Cognitive Assessment (MoCA),[94,95,96] in addition to the medical history regarding a dominant mutation within immediate family,[97] diagnosis of AD is commonly based on examining various AD biomarkers and neuroimaging techniques. Specifically, cerebrospinal fluid (CSF) markers[98] of Aβ and tau are reliable diagnostic tools to detect low Aβ42 levels in MCI patients as CSF Aβ42 is decreased in patients with AD due to the plaque deposits,[99] and for high tau levels, total tau, elevated phosphorylated tau – the prime component of NFTs that is more detailed than total tau.[99] It has been shown that a combination of these CSF markers have been used to provide more effective diagnosis in early stages of AD.[99] Moreover, Aβ aggregation processes can be examined by using amyloid positron emission tomography

(PET) to evaluate the surface area of amyloid plaques. In order to improve diagnostic accuracy, a non-invasive functional neuroimaging technique such as ^{18}F-fluorodeoxyglucose PET (FDG-PET) imaging[100,101] can be used to determine the loss of neuronal function in asymptomatic patients in early AD. This method measures the reduced cerebral metabolic rates of glucose metabolism (CMRglc) observed in temporo-parietal, frontal and posterior cingulate cortices of AD patients – a substitute marker for neuronal activities,[99] since the brain uses glucose as a primary source for energy generation. Therefore, brain has a complex regulatory system to preserve its glucose supply. In addition to maintaining normal brain glucose levels and normal cellular function, gluco-sensing neurons have been developed across the brain regions.[102] Another diagnostic technique – magnetic resonance imaging (MRI) is also widely used for the disproportionate atrophy in medial, basal, lateral, temporal lobe and medial parietal cortex.[97,103,104] In fact, recent advances in amyloid imaging have brought the potential for the Aβ amyloid deposits in the brain to be observed, even in normal patients.

1.3.5 Aβ Therapies

Taking these facts into account, it appears that amyloid cascade hypothesis has dominated the directions of basic science and research with hope to nail this long and unsolved mystery of Alzheimer's disease. However, recent research findings have also casted doubt on the amyloid cascade as the major culprit in AD, as hundreds of drugs developed based on this foundation have failed during the advanced stages of clinical trials. At this junction, it is clear that each of the pathologies discussed in the previous sections play crucial roles and thus, foster a possible therapeutic target for AD treatment. Nonetheless, a single approach based on a single therapeutic target, such as the amyloid

hypothesis alone is insufficient to explain the complexity that plays a key role in pathophysiology of AD. As a result, a multi-targeting approach towards AD therapies has been the focus of much attention. It is noteworthy that the amyloid cascade still remains the most studied and validated hypothesis when compared with other pathways involved in AD pathology.[105]

As of February 12, 2019, a review of AD drug development from Cummings and coworkers highlighted that AD therapies represented 28 candidates in 42 trials in phase III, 74 candidates in 83 trials in phase II, and 30 candidates in 31 trials in phase I.[106] The mechanisms of actions (MOA) of these agents includes 96 agents (73%) that act as disease-modifying therapies (DMTs), including tau-related mechanisms, or other mechanisms of action involving stem cell therapies, anti-inflammation, growth factors, or neuroprotective factors; 14% are enhancers for symptomatic cognition; 11% are symptomatic agents improving neuropsychiatric and behavioural symptoms; and 2% have undisclosed MOA.[106] Of these clinical trials, AD drug development is mainly driven by the amyloid cascade aiming to reduce Aβ aggregation in the brain, which might be attained by several strategies: (1) prevention or inhibition of Aβ production; (2) inhibition of the Aβ aggregation; (3) restriction of Aβ neurotoxicity; (4) promotion of Aβ clearance (immunotherapy).[105,107] These four strategies are divided into upstream and downstream approaches, which are designed to target Aβ. The upstream approach directly blocks either β- or γ-secretase enzymes involved in APP processing *via* the amyloidogenic pathways (see section 1.1.2); while the downstream approach targets the modulation of Aβ aggregation.

1.3.5.1 Upstream of Aβ Production

Looking back on the APP processing by both β- or γ-secretases laying groundwork for the production of neurotoxic Aβ, inhibiting or modulating BACE-1 and/or γ-secretase is one of the attractive upstream approaches for controlling the speed of Aβ production and thus slowing the AD progression (Figure 13).[105,108,109]

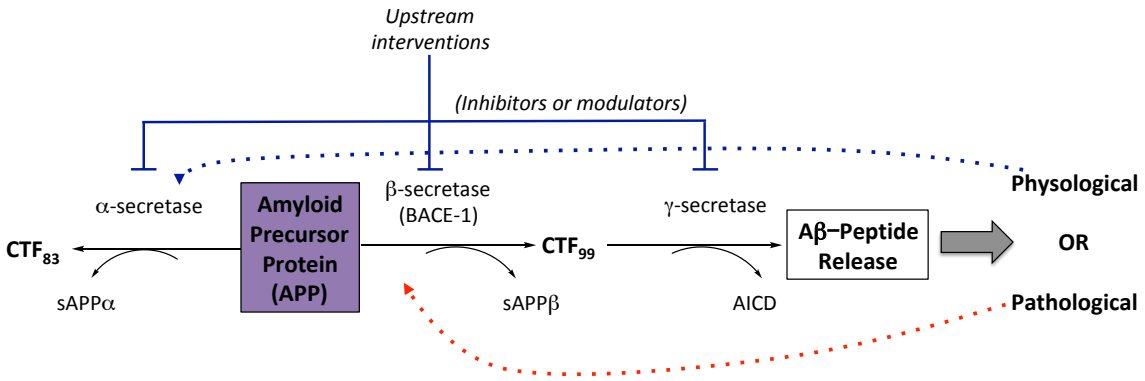

Figure 13. Schematic overview of upstream interventions.[110] Reproduced with permission from Ref [110].

In fact, over the years, these targets have taken a central stage in the AD drug development with selective, potent and bioavailable BACE1 inhibitors that have passed all stages of clinical trials, except for the late stages in clinical trials. Nonetheless, many of drug candidates targeting BACE1 ended up failing due to a variety of reasons besides safety issues, which could possibly stem from the understanding of BACE1 inhibition itself and the role of BACE1 in a healthy brain.[46,105] Among drugs in the 2019 AD drug development review article,[106] there were five BACE1 inhibitors (MK-8931, JNJ-54861911, AZD3293, E2609, and CNP520) to progress to clinical phase III (Table 2), in which MK-8931 was the first lead drug candidate that was terminated.[101,106]

Table 2. BACE1 inhibitors in phase III clinical trials.

Compound name Structure	Code	Mechanism of Action	Sponsor
Verubecestat 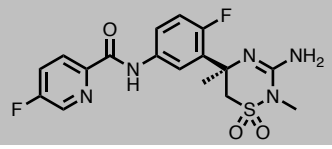	MK-8931	Anti-amyloid, BACE1 inhibitor	Merck
Atabecestat 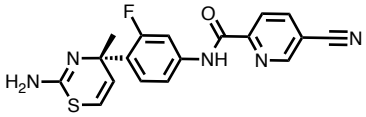	JNJ-54861911	Anti-amyloid BACE1 inhibitor	Janssen
Lanabecestat 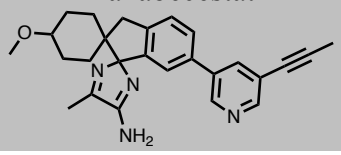	AZD3293	Anti-amyloid BACE1 inhibitor	Astra Zeneca, Eli Lilly
Elenbecestat 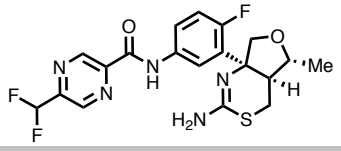	E2609	Anti-amyloid BACE1 inhibitor	Eisai, Biogen
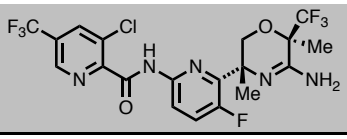	CNP520	BACE1 inhibitor	Novartis, Amgen

Overall, the road for these lead drug candidates to receive Food and Drug Administration (FDA, USA) approval and reach the market is challenging, as the structure of BACE1 protein is not simple. In fact, its structure is similar to many other aspartyl proteases (Memapsin 2), which are found to be available in different parts of the human body, such as BACE2, pepsin, renin, cathepsin D, and cathepsin E, which are involved in many physiological functions.[105] Hence, selectivity in BACE1 inhibition has posed a challenge in a battle of developing potent BACE1 inhibitors with minimal side effects, since it is unlikely to avoid the significant impact on other proteases.[105] Moreover, BACE1 active site (Figure 14), which is made up of catalytic aspartic acid

residues, flap, and 10 seconds loop, is considered being fairly large for the small molecule to bind to the active site. If it does, it may not be able to cross the BBB.[105,112] The last drawback from developing BACE1 inhibitors is P-glycoprotein (P-gp)[113] efflux may obstruct the entry of drug to the brain, as BACE1 inhibitors are incline to undergo efflux by P-gp – a member of ATP binding cassette superfamily of transmembrane transport proteins and also an important drug efflux transporter.[105]

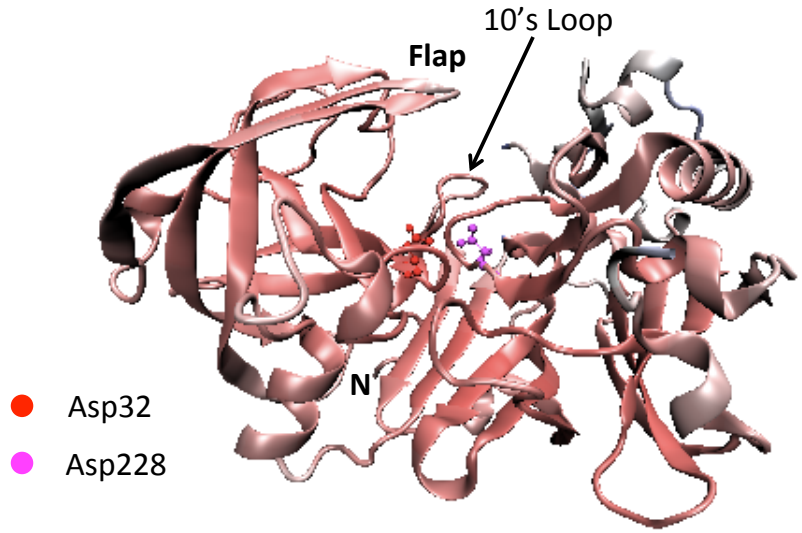

Figure 14. BACE1 active site.[105] Reproduced with permission from Ref [105].

Another rationale strategy for the treatment of AD has also been made efforts by targeting the γ-secretase that is involved in the last metabolic step of generating the neurotoxic Aβ peptides when interacting with CT99 (Figure 6). A small molecule γ-secretase inhibitor semagacestat (LY-450139, Eli Lilly, Figure 15) demonstrated the potential to reduce Aβ in blood and CSF in AD patients in phase III clinical trials. However, this drug was discontinued as a therapeutic option against AD owing to its severe adverse effects including alterations of immune cells, gastrointestinal symptoms, non-melanoma skin cancers, and skin reactions.[2,91,106,107,102–105] In addition, it did not

improve cognition and even showed significant worsening of functional ability in prodromal AD patients at higher doses compared to the placebo groups.[2,101–104]

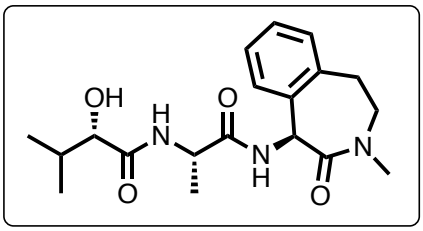

Figure 15. Structure of semagacestat (LY-450139) – a γ-secretase inhibitors.

Negative result of this γ-secretase inhibitor and its associated toxicity was primarily attributed to the inhibition of Notch signal processing.[106,107,115] Notch – a single-pass type I transmembrane receptor related to nuclear signaling and other functions is involved in cell-cell interactions and cell-surface receptors, which is processed similarly to CT99.[115] Recent study suggested that Notch and other proteins are all substrates for γ-secretase, leading to the limiting factor in selectivity in γ-secretase inhibitor, as it is prone to inhibit Notch processing more than APP processing itself. Hence, the generation of neurotoxic Aβ deposits originating in the suppression of the γ-secretase cleavage activity on APP persists to promote the neurotoxicity.[8,115,117] Building upon the lessons learned from these failures, the development of novel agents regarding Notch-sparing properties is currently underway.[106,107,117]

With a better understanding of the pathogenesis of AD, an alternate therapeutic approach based on as γ-secretase modulators arose regardless of the above potential hurdle in finding safer and more efficacious treatments for AD. Tarenflurbil (*R*-flurbiprofen or Flurizan™, licensed by Myriad Genetics, Figure 16),[8,99,117] the enantiomer of the NSAID flurbiprofen progressed to phase III clinical trials. This drug candidate was reported to be able to decrease Aβ42 peptides by modulating the γ-

secretase activity in a way that it shifts the production of Aβ42 to Aβ38 by binding to APP, instead of directly inhibiting γ-secretase.[8,117] In this regard, selectivity in γ-secretase inhibitors is not of importance, as it does not interfere the Notch cleavage or other APP processing pathways.[8,117] However, a vital 18-month phase III clinical trial was discontinued due to poor CNS penetration and no improvement in cognition and function.[8,99,107]

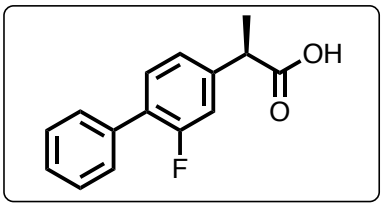

Figure 16. Structure of tarenflurbil (*R*-flurbiprofen) – a γ-secretase inhibitor.

While development of AD therapeutics targeting the amyloidogenic metabolism of APP and α-secretase enzyme on the non-amyloidogenic pathway has also attracted considerable interest as α-secretase activators, which may also inhibit the production of Aβ in the brain with the same efficiency.[118–122] Interestingly, such activation would confer neuroprotective levels of sAPPα, as well as suppress Aβ accumulation.[121] In fact, an indirect approach to activate α-secretase activity on APP cleavage by modulating hormones, statins, other neurotransmitters, and the signaling transduction pathways.[123] Such pathways are activated *via* several G protein-coupled receptors (GPCR) and receptor tyrosine kinases, consisting of of mitogen-activated protein kinases, phosphatidylinositol 3-kinases (PI3K), cAMP, tyrosin kinases, protein kinase C (PKC), and calcium.[118,120,123] A number of studies applying an indirect approach have demonstrated that the current drugs used to treat AD can induce the α-secretase activation.[121] For example, a repurposed drug – atorvastatin (cholesterol agent)[124] was

shown to induce activation of α-secretase. It has now progressed to phase III clinical trial (Figure 17).[121] Moreover, phase II clinical trials of bryostatin 1 (a PKC modulator) showed an increase in the production of sAPPα, improve cognition and reduce Aβ40/42 in transgenic mouse models.[111,107,120,121] In addition, etazolate (EHT-0202) – a selective $GABA_A$ receptor modulator was revealed to be capable of activating α-secretase activity and promoting sAPPα secretion.[107,125,121]

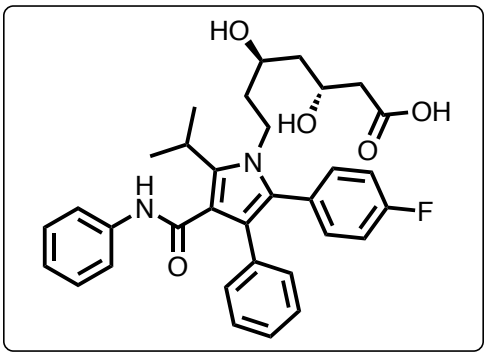

Figure 17. Structure of atorvastatin – an α-secretase activator.

At this point, the inhibition of BACE1 holds the greatest potential as a promising strategy in lowering the production of neurotoxic Aβ within the brain regardless the Aβ clearance production, as it can prevent of the formation of Aβ at an early stage of APP processing, leading to a significant downstream outcome on AD progression.[105]

Understanding the complexity of AD and previous failures of many experimental and clinical trials owing to lack of efficacy has been adapted greatly. Further analysis has also been called for regarding the possible inadequacies in our understanding of the AD pathogenesis and diagnosis, the selection of therapeutic targets as well as the design of drug development and clinical trials.[105,125]

1.3.5.2 Downstream of Aβ Production

One of the key solutions to AD is likely to develop the effective early diagnostic tools before neurodegeneration even occurs, since the process for the accumulation of Aβ aggregates and their conversion into plaques begins many years before the first symptom is perceived. Let's recall the primary cause of synaptic dysfunction and subsequent neurodegeneration characterized by the Aβ accumulation, in which soluble and highly toxic Aβ aggregates, known as oligomers and protofibrils and insoluble fibrils/plaques may be associated with AD pathogenesis.[126–132] In this regard, a large number of downstream interventions of anti-Aβ immunotherapy (active/passive) has currently been developed to directly address the clearance of Aβ formation with hope to prevent or reverse it, leading to an optimistic approach against AD (Figure 18).[126–132] Three different immune-mediated mechanisms that can elevate the Aβ aggregates have been postulated: (1) solubilisation by antibody binding to Aβ; (2) phagocytosis of opsonized Aβ by microglia; and (3) extraction of Aβ from the brain by plasma antibodies.[125]

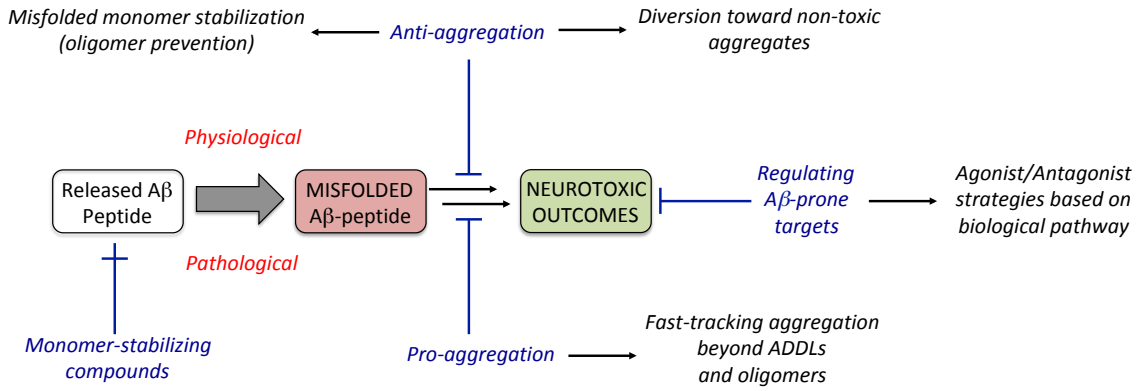

Figure 18. Schematic overview of downstream interventions.[110] Reproduced with permission from Ref [110].

The anti-Aβ immunotherapy has two different strategies to target Aβ aggregation intermediates: active or passive immunotherapy. Active immunotherapy employs the potential of the patient's immune system to produce polyclonal antibodies which target an Aβ-derived antigen or other stimuli designed to induce an immune response.[126,131] Whereas, passive immunotherapy strategy treats an AD patient with monoclonal antibodies, which come from a source, such as humanized-murine monoclonal antibodies, or donor-derived human polyclonal antibodies.[126,131,133] According to AD pipeline in 2019, there are six immunotherapies (monoclonal antibodies: aducanumab,[126] crenezumab,[133–135] gantenerumab,[136] solanezumab;[107] plasma exchange with albumin + immunoglobulin;[137,138] amyloid vaccine:[125] CAD106) currently ongoing in the phase III clinical trials that can remove Aβ ranging from monomers to oligomers and plaques.[106] Before these clinical trials, there were many candidates striving to prove their efficacy and treatment effect. AN-1792 was the initial agent undergoing the human clinical trials of active immunotherapy to remove Aβ, yet it was halted due to developed serious inflammatory reactions such as meningoencephalitis in patients in phase IIa AD trials.[99,107,139] A phase III clinical studies of passive immunotherapy with intravenous immunoglobulin (IVIG) plasma product (Gammagard) containing Aβ antibodies derived from prepared human plasma that was abandoned as a potential agent for prevention for AD because there was no progress in slowing the disease.[99,107,140]

In summary, both strategies offer advantages and disadvantages; however, the disadvantages of active immunotherapy are more of a problem than an improvement since elderly people may not be responsive to vaccines used in active immunization and long-term adverse effects may occur after vaccination. Because of this reason, the passive

immunotherapy became a more preferable and attractive treatment approach for AD.[106,125,128] The immunotherapy (or anti-aggregation) approach deems to prevent the process of oligomer formation by stabilizing the low-order of Aβ aggregates or elongating the lag phase, to reduce the neuronal exposure to the crucially toxic oligomer species which allows the non-toxic forms of Aβ to form, and to eliminate the end-stage amyloid fibrils built up in the brain.[141–143] The only pitfall in this strategy is that its therapeutic window of treatment, half-life, and long-term viability still pose a challenge. It should be noted that the current COVID-19 crisis led to rapid discovery and launch of mRNA-based vaccines at an astonishing pace. Lessons learned from these newer technologies could pave the way for novel anti-AD vaccines.

In addition to this strategy, instead of directing at fibrils or plaques, another potential method targeting Aβ – the pro-aggregation pathway utilizes small molecules that are capable of promoting the Aβ polymerization beyond the oligomer phase or accelerating the Aβ fribrillogenesis by enabling the small molecules to bind to the β-sheet structure characteristic of fibrils.[142,143] By doing so, the high-order of Aβ aggregates will form and eventually be removed by plaque-derived antibodies, leading to lower the concentration of oligomers present in the brain.[142,143] Even though this methodology seems to be useful for AD therapy development, it is still premature in the field, and has some challenges in terms of poor penetration of antibody to the brain, the increased plaque load at advanced stages could be too late to be treated, overloading the Aβ-clearance process.

Taken these together, owing to the myriad of AD's complexity, therapeutics targeting only one of these AD-related pathologies are less likely to succeed in the search

for a DMT. This approach may have to be combined with other strategies to simultaneously tackle several pathologies in order for the clinical effects to translate to an ideal treatment. These findings have paved the way for the rational design, synthesis, and development using the small molecules as Aβ aggregation modulators for AD. In this regard, methylene blue (MB) and orange G (OG) are well-established ligands that can inhibit Aβ aggregation (Figure 19).

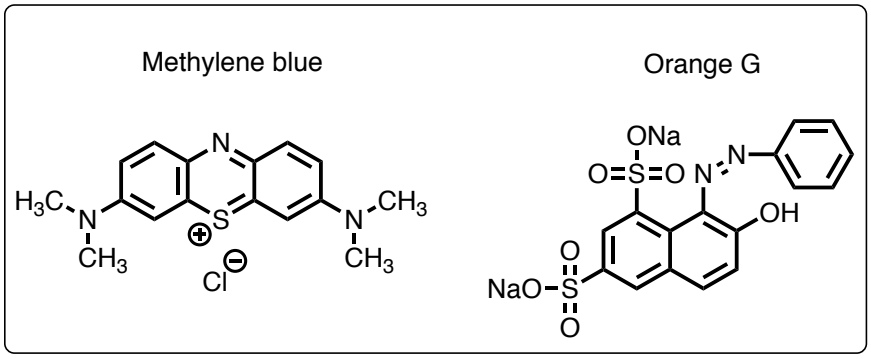

Figure 19. Compounds with anti-aggregation properties that are commonly used as gold standards in Aβ assays.

Particularly, MB – a cationic dye named tetramethylthionine chloride of phenothiazine class of compounds was investigated as a therapeutic agent for treating various brain disorders including AD.[144] MB demonstrated its potential in inhibiting Aβ42 oligomers with IC50 value of 12.4 μM *in vitro* by promoting fibril formation. Furthermore, another report shows that MB can also inhibit the Aβ40 fibril formation with IC50 value of 2.3 μM.[144] OG – a synthetic azo dye used in staining that can inhibit the Aβ aggregation by specifically binding and stabilizing the KLVFFA steric zipper (Aβ16-21), by binding between the pairs of anti-parallel β-sheets of amyloid fibers. While, the negatively charged sulfonic acid group of OG interacts with charged lysine side chain in the adjacent zipper forming salt links to further stabilize the amyloid/small

molecule complex.[49] Owing to their strong binding interactions to Aβ peptides, these small molecules are commonly used as "gold standards" for many *in vitro* Aβ assays, such as thioflavin-T-based assay. One of the most common methodologies to identify molecules capable of prevent Aβ aggregation is to utilize the dye thioflavin T (ThT) – a benzothiazole salt as an indicator to detect the presence of amyloid fibrils formation (Figure 20) *in vitro* by measuring the change in fluorescence intensity of ThT upon binding to amyloid fibrils.[145,146] Indeed, due to highly specific binding interactions of ThT with β-sheets of amyloid fibrils, it represents a versatile methodology for rapid screening of compound libraries to determine their anti-aggregation properties.[147]

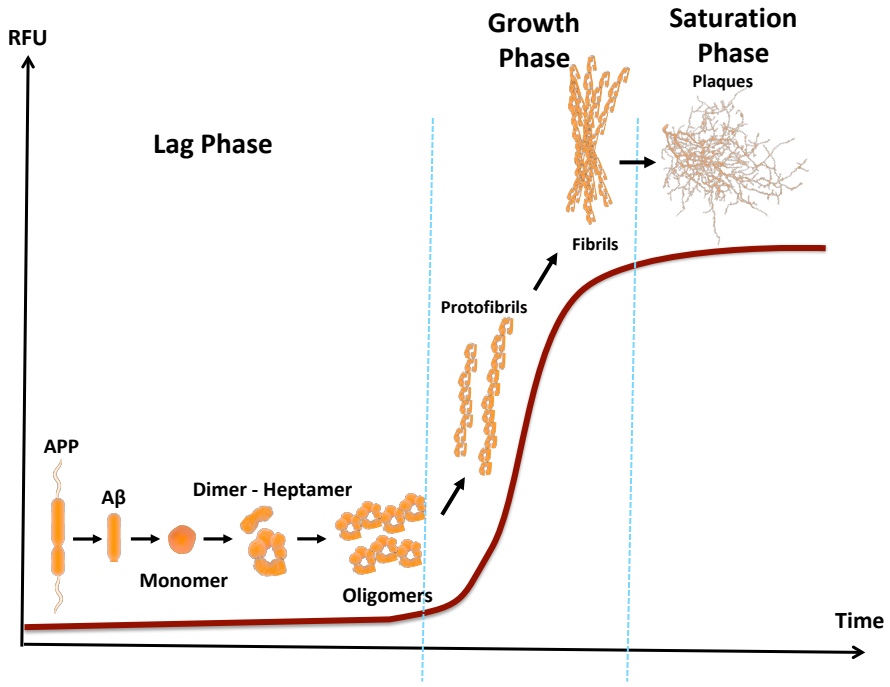

Figure 20. Scheme of nucleated growth kinetics mechanism of Aβ aggregation process represented as a sigmoidal curve to depict three phase kinetics.

Indeed, ThT is a well-established ligand that can bind to Aβ fibrils with modest affinity, which can serve as a medical probe in medical imaging of amyloid.[145,146] The mechanism of this methodology is that when ThT is unbound, the C-C bond of the

phenylamine and benzathiazole rings of ThT tends to freely rotate in solution.[145,146] The excited states generated by photon excitation are rapidly quenched by this steric rotation, resulting in low fluorescence emission for unbound ThT (excitation at 350 nm, emission at 450 nm).[145,146] Whereas, when ThT binds to the β-sheets of amyloid fibrils, it locks the rotation of ThT, causing the preservation of the excited state, which in turn causes the increase of fluorescence (excitation at 450 nm and emission at 482 nm) (Figure 21).[145,146] The change in fluorescence intensity can be measured by fluorescence spectroscopy (excitation at 440 nm and emission at 490 nm).[145,146] With this approach, the Aβ aggregation inhibitors can be detected.[145,146]

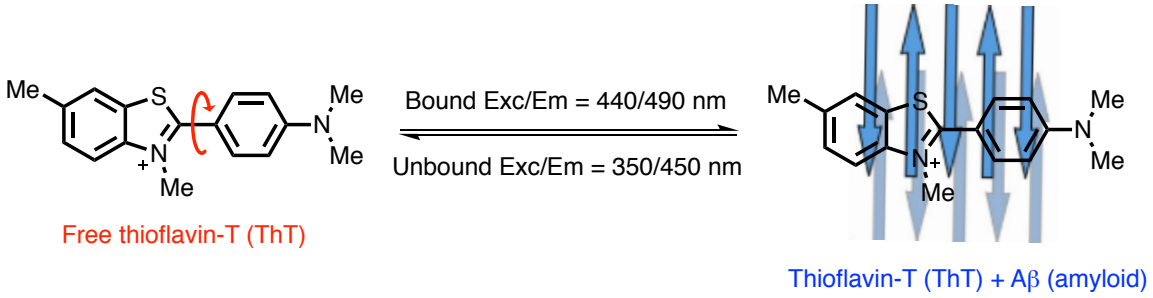

Figure 21. Mechanism of thioflavin-T (ThT) binding to **Aβ** aggregates. Blue arrows represent the cross-β structure of amyloid fibrils. Reproduced with permission from Ref [110].

1.4 Tauopathy

For many years, the aggregation of the mature amyloid fibrils was originally thought to account for the pathogenesis of AD. As a matter of fact, some evidence revealed that the toxicity levels of various forms of Aβ oligomers, which are responsible for synaptic dysfunction may be associated with the formation of neurofibrillary tangles (NFTs) due to the decreased phosphatase level observed in the AD patients.[148–152]

In parallel with senile plaques, the formation of NFTs displays another pathological hallmark of AD (Figure 22).[44,75,149,153,154] In fact, the tauopathy has been the

main competitor of the amyloid cascade hypothesis. Tau is a microtubule-associated protein (MAP) located in the axons of neurons and are generated by alternative mRNA splicing of a single gene,[148,155,156] from which six tau isoforms are expressed in an adult human brain, ranging between 352 and 441 amino acid residues.[149,155,157] Tau has various functions, one of which is to bind to tubulin (monomers of peptide) to form into microtubules (MTs) and stabilize MTs during its polymerization.[75,149,153,154] These are critical to the axonal growth and effective axonal transport.[149,158] Yet, the assembly and stabilization of MTs depends on tau isoforms and phosphorylation.[159,160] As one of the important components of the eukaryotic cellular cytoskeletal system, MTs take part as an internal transport system, which can assist with delivering nutrients and other cellular components, such as neurotransmitters containing vesicles.[53,161] When tau has a certain number of phosphate residues attached to it, this helps stabilize the MTs. However, in AD, when a large number of phosphate molecules adhere to tau, it gives rise to hyperphosphorylation (mutation).[44] When tau is hyperphosphorylated, the tubulin monomers of the MTs begin to lose their binding affinity; in addition, tau detaches from the MTs, causing them to unravel.[44,155] As a result, this process disturbs axonal transport and destructs the entire biochemical communication between the neurons, leading to neuronal death and synaptic impairment.[44,155] On the other hand, the hyperphosphorylated tau strands have a tendency to self-assemble and polymerize into paired helical filaments (PHFs), which then aggregate to form neurofibrillary tangles (NFTs) that are toxic to neurons.[44,155] During the process of aggregation, the normal tau and MAP are more likely to be sequestered by the hyperphosphorylated tau into the aggregation, which can damage the normal function of the MTs.[44,155]

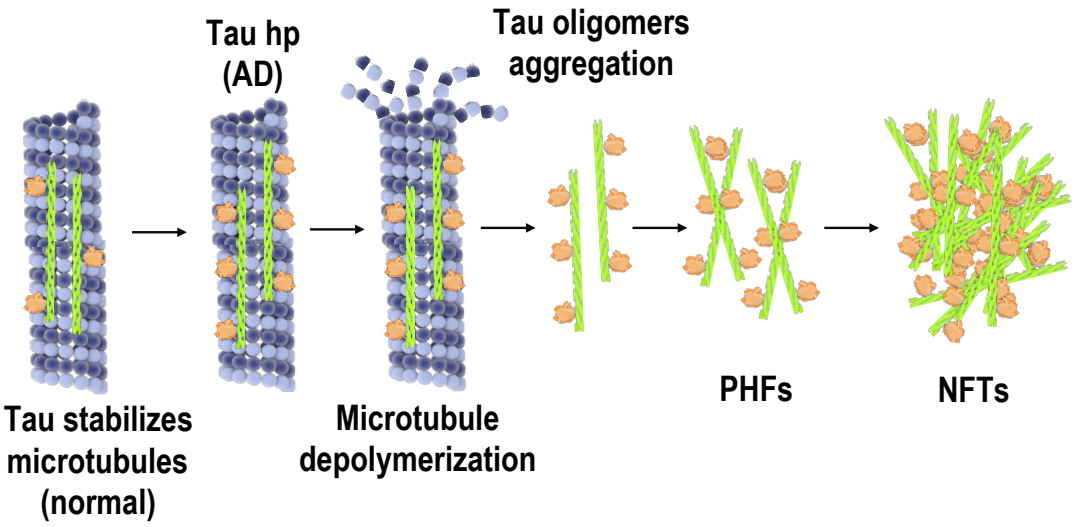

Figure 22. Schematic representation of tau hypothesis and the aggregation process of tau protein.

Tau has a large number of serine (S), threonine (T), and tyrosine (Y) sites, which can be phosphorylated easily. Tau activity is governed by various protein kinases and phosphatases.[161,162] Increased activity of the tau kinases (which are protein kinases) and phosphatases triggers hyperphosphorylation of tau.[147] The hyperphosphorylation of tau occurs on account of most of the protein kinases (known as tau kinases).[146] Normal tau phosphorylation takes place on both serine and threonine amino acids. These amino acids, which are directed by proline (P), are phosphorylated by cyclin-dependent kinase (CDK5 or tau protein kinase-II) and its activator subunit p25, glycogen synthase kinase 3 (GSK3), or mitogen activated protein kinase (MAPK, also known as ERK2 – extracellular signal-regulated kinase).[151,156] Nevertheless, the non-proline directed kinases include cyclic-AMP-dependent kinase (PKA) and microtubule-affinity regulating kinase (MARK).[151,156,146] Likewise, there are several phosphatases involved in reversing and dephosphorylating tau.[151,156,146] The protein phosphatase PP2A is the most active enzyme that is responsible for the tau dephosphorylation.[151,156,146] Some studies have reported that

the decreased expression and activities of the phosphatases were often observed in AD brain.[137] Similar to Aβ oligomers, the intermediate deposits of hyperphosphorylated tau such as soluble oligomeric tau are considered more cytotoxic than NFTs.[137] Experimental data in AD brain revealed that the Aβ deposits, indeed, pave the way for tau aggregation, which was found to be a mediator of Aβ toxicity as it gives rise to Aβ peptides binding to tau and forming a stable complex, promoting the phosphorylation of tau *via* tau protein kinase-I (GSK-3β).[137]

With this information in mind, numerous potential therapeutics have been developed focusing on tau kinase inhibitors using small molecules, as potential anti-AD therapies.[141,146,147] There are two main therapeutic approaches to target the tau protein: (1) tau kinase inhibitors help inhibit tau aggregation, preventing PHFs from forming into NFTs. An example of TRx0237, an anti-tau agent was observed to reduce tau-mediated neuronal damage in phase III clinical trials;[106] (2) tau kinase inhibitors promote the disassembly of tau aggregates, diminishing the NFTs formation.[125] Despite these advances, many challenges remain in the development of tau kinase inhibitors comprising of GSK-3β, CDK5, and MARK.[148] Interestingly, clinical studies showed significant improvement in cognition after GSK3 inhibitor administration in double blind, placebo-controlled, and randomized conditions.[148] Having said that, to a certain extent, many other inhibitors of GSK3 have evolved over the years.[148] For instance, ANAVEX2-73 has shown to enhance cognition, reduce tau phosphorylation and amyloid deposition in phase III clinical trials (Figure 23).[106,163]

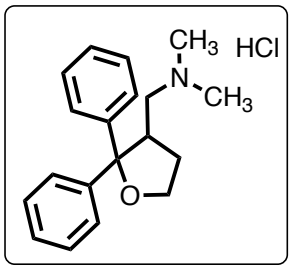

Figure 23. Structure of ANAVEX2-73 – an anti-amyloid and anti-tau agent.

Another study demonstrated that the tau hyperphosphorylation leading to the formation of NFTs could be inhibited by the use of phosphatase PP2A activator – sodium selenite in transgenic mouse models of AD.[148] These results have indicated that there are some symptomatic improvement in AD treatment, which may have wide-ranging benefits for the related phathological conditions. Using the same approach, a first generation tau aggregation inhibitor – methylene blue MB (Rember^{TM}) progressed to phase III clinical trials which enhanced cognition and inhibit tau aggregation, but then was abandoned due to the lack of efficacy.[164,165]

Recently, studies on immunization against tau have been reported. AADvac1 of active immunotherapy and ABBV-8E12 of passive immunotherapy have made to the furthest of the clinical trials since they both could remove tau and prevent tau aggregation.[166]

CHAPTER 2 Hypothesis and Rationale in Using Thiazole Ring Scaffolds as Amyloid Aggregation Inhibitors

2.1 Thiazole Derivatives

Small molecules containing heterocyclic rings are known to have a wide range of application in several fields including agriculture, pharmaceutical industry, polymer industry, and other areas.[167,168] Among the many possible heterocycles, thiazole (Figure 24) is an important class of heterocyclic compounds that have a five-membered ring structure, with a sulfur and nitrogen atom.[169] Furthermore, thiazole is aromatic on the basis of delocalization of a lone pair of electrons from the sulfur atom completing the 6π electrons to meet the criteria of Huckel's rule.[169]

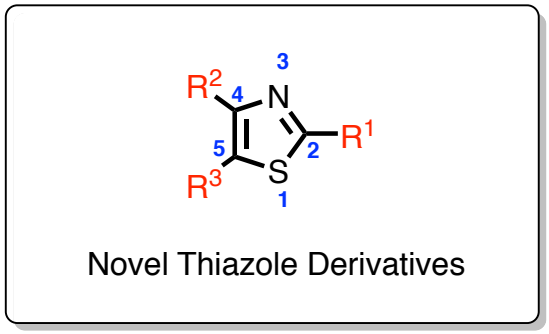

Figure 24. Structure of novel thiazole derivatives.

Thiazole was first described by Hantzsch and Weber in 1887 as the products obtained from reactions between thiourea and α-halo carbonyl compound.[170,171] The thiazole ring appears naturally in microbial and marine sources and thus, has been established in a number of natural products, including peptides, vitamins B1 (thiamine), alkaloids, epothilone, and chlorophyll (Figure 25).[170–172]

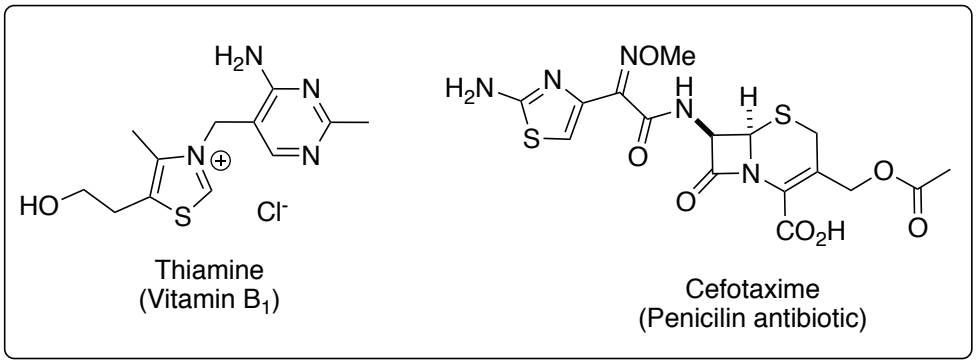

Figure 25. Biologically important thiazole.[170]

Moreover, thiazole is an effective and valuable scaffold in the field of medicinal chemistry due to its biological properties,[169] and has been incorporated into various chemical entities with a broad spectrum of pharmacological activities such as anti-allergic, anti-bacterial, anti-cancer, anti-convulsant, anti-fungal, anti-hypertension, anti-inflammatory, anti-malarial, anti-microbial, anti-psychotic, and anti-viral (Figure 26).[169–171,173–176]

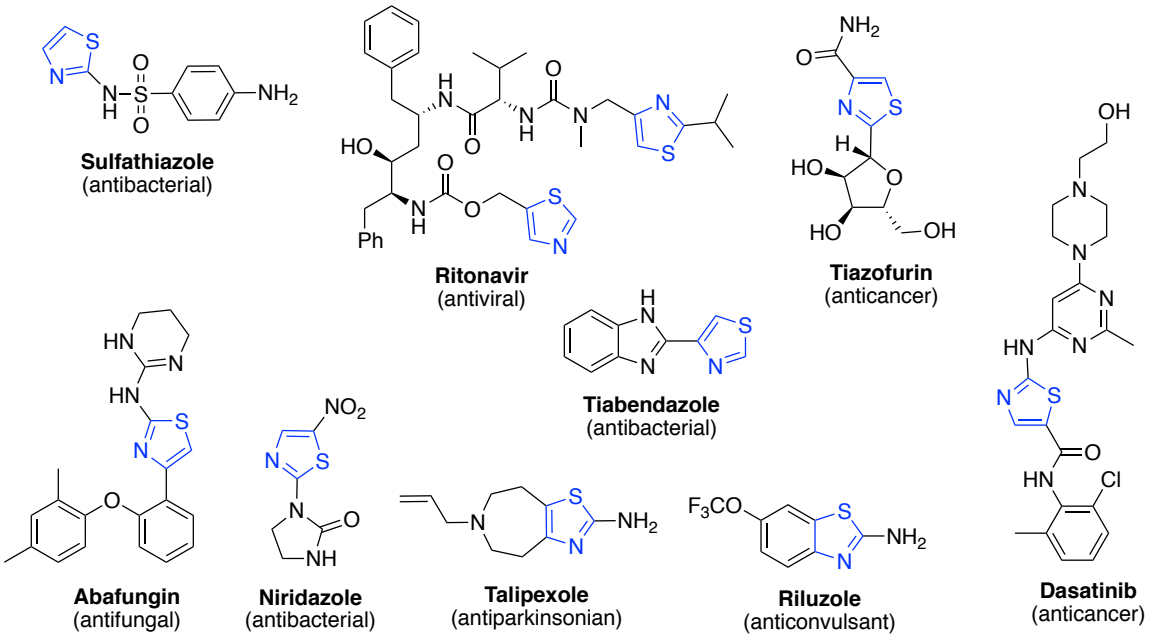

Figure 26. Thiazole skeleton containing FDA-approved drugs.[171,172]

By incorporating different substituents on different positions at the thiazole ring, the diversity and therapeutic potential of these thiazole derivatives have been reported in various diseases. In particular, those thiazoles containing an amine group have become exceptionally important. Recently, several thiazole analogs have been developed as anti-cholinesterase inhibitors.[168,175] For instance, acotiamide hydrochloride (Z-338) - a thiazole-based selective AChEI for the treatment in patients with functional dyspepsia has been reported, and evaluated in advance stages of clinical trials.[175,177] Pramipexole (Mirapex®, Pharmacia and Upjohn) incorporating with 2-aminothiazole fused with cyclohexane ring, in which aminothiazole moiety was used as a bisostere to the dopamine's catechol ring, demonstrating a potent dopamine D_2 agonist activity. This thiazole derivative is used in the treatment of both the motor and psychiatric symptoms of Parkinson's disease.[178] Another thiazole derivative – riluzole (2-amino-6-trifluoromethoxybenzothiazole) has been approved to treat patients by slowing down the progression of amyotrophic lateral sclerosis (ALS).[169,179,180] Moreover, benzothiazoles containing thiazole scaffolds have been demonstrated as promising neuroprotective agents, such as tetrahydrobenzothiazoles,[181] and benzothiazoles.[182] Several potent and selective glutamate receptor antagonists, such as ethynyl thiazole[183] and pyrimidyl thiazole[184] have been reported for the treatment of anxiety disorders. A group of thiazole derivatives including riluzole analogues,[180] thiazole-semicarbazides,[185] thiazolepyridons,[186] and thiazole-carboxamides[187] have been reported to have anticonvulsant properties in vitro. Butyl thiazoles as RAGE antagonists,[188] imidazolo thiazoles as AChE and BuChE inhibitors,[189] 2-aminothiazoles as inhibitors of tau-induced

neuronal toxicity,[190] and triazolyl thiazoles as cdk5/p25 inhibitors[191] have also been studied as potential treatments for AD.

2.2 Template Design

The last decade has been seen with an incremental increase in the design and development of novel small molecules as multi-target-directed ligands (MTDLs) to treat AD.[192] In this regard, Nekkar Rao's research group has focused on developing novel ring templates as MTDLs and their application in treating AD. Our group has worked on a number of heterocyclic ring templates as novel anti-AD agents (Figure 27).

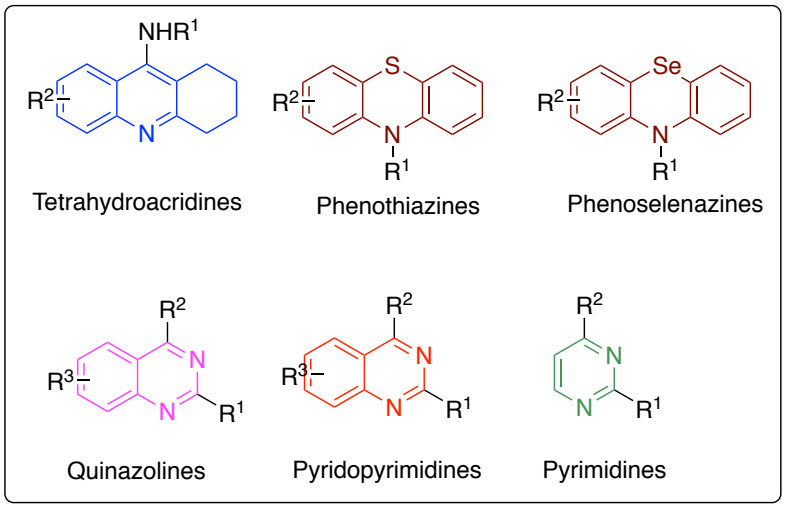

Figure 27. Chemical structures of heterocyclic ring systems as potential anti-AD agents.

For example, the fused tricyclic phenothiazine is an important ring scaffold present in CNS agents, which are used in therapy to treat psychotic disorders.[193] As such, phenothiazines are known to exhibit ChE inhibition and antioxidant activity.[194,195] Another example is the design and synthesis of planar, bicyclic ring systems such as quinazolines.[196] They exhibited dual ChE inhibition, human AChE induced Aβ aggregation inhibition, BACE-1 inhibition, and Aβ40 aggregation.[197] Furthermore,

Nekkar group has investigated 2,4-disubstituted pyrimidine derivatives as ChE and Aβ aggregation inhibitors.[198,199] In contribution of this line of research, in the current work, we have undertaken the design, synthesis, and evaluation of novel thiazole derivatives as inhibitors of neurotoxic Aβ aggregates. This study was inspired by a thiazole based small molecule, known as Neuropathiazol® (ethyl 4-(methyl(2-phenylthiazol-4-yl)amino)benzoate), which is an *N*,2-diphenylthiazole-4-amine.

Neuropathiazol® is a thiazole-4-amine, which was previously reported to selectively induce neuronal differentiation of multipotent adult hippocampal neural progenitor cells towards a neuronal phenotype.[200–202] For example, a series of 5-arylated *N*-arylthiazole-2-amines neurodzine and neurodazole (Figure 28) were studied for promoting the cell differentiation in skeletal muscle cells to enhance the healing process of muscles damaged by injury or disease,[202–205] which have the ability to induce neurogenesis in human neuroblastoma cells, such as SH-SY5Y cells. Furthermore, in another study, Shidore and coworkers reported the synthesis of 4,5-diphenylthiazole-4-amines as MTDLs in treating AD (Figure 29).[206] Their study demonstrated that these novel thiazole derivatives were able to inhibit cholinesterase enzymes and were able to reduce Aβ42-mediated toxicity.

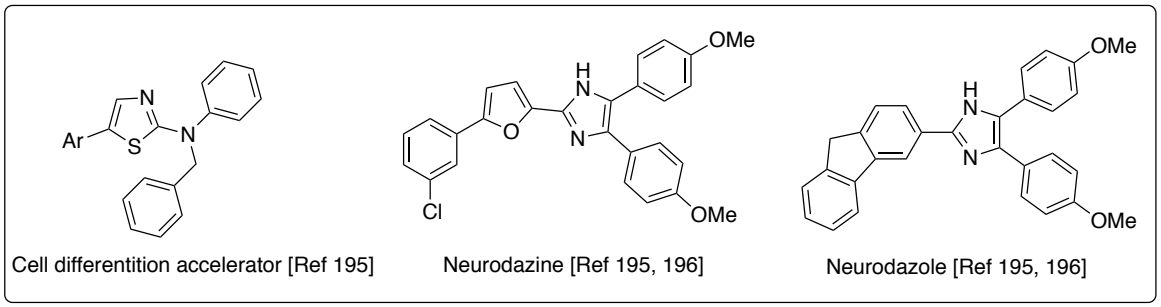

Figure 28. Structures of small molecules with neurogenesis-inducing activities.[202–205]

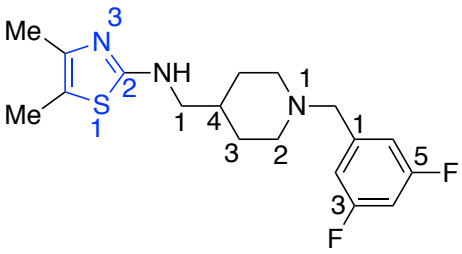

AChE inhibition IC50 = 0.30 mM; BuChE inhibition = 1.84 mM;
Aβ42 inhibition = 27.6%; BBB im, po

Figure 29. Chemical structure of 4,5-diphenylthiazol-4-amine.

These studies prompted us to investigate the potential of neuropathiazol® based *N*,2-diphenylthiazol-4-amines and the corresponding *N*,4-diphenylthiazol-2-amines in binding to Aβ and in preventing their toxicity forms. We conducted computational modeling studies using neuropathizol® and *N*,4-diphenylthiazol-2-amine (Figure 30). Molecular docking studies indicated that neuropathiazol® and *N*,4-diphenylthiazol-2-amines were able to interact at the KLVFFA region at the N- and C-terminals, respectively. The central thiazole ring was in contact with amino acids in the Aβ-turn region along with the amine substituent (N-Me), whereas the phenyl rings were in contact with amino acids in the C- and N-terminals. These studies suggest that either *N*,2-diphenylthiazol-4-amines or *N*,4-diphenylthiazol-2-amines possess the right structure and conformation required to bind and stabilize Aβ-aggregates and prevent their assembly into toxic forms. Past research has shown that KLVFFA segment is the key region involved in the nucleation dependent aggregation process and small molecules that bind to this particular regions can prevent Aβ aggregation and associated neurotoxicity.[207] While designing these *N*,2-diphenylthiazol-4-amines or *N*,4-diphenylthiazol-2-amines thiazole derivatives, it is extremely important to consider their physicochemical properties to cross the BBB. With this in mind, the 'Lipinski's rule of 5' was taken into

account to ensure the ClogP values of thiazole derivatives were in the range of 3-5, molecular weight under 500 Da, hydrogen-bonding acceptors under or equal to 10, and donors under or equal 5.[208] Individual thesis chapters will provide further rationale on the application of *N*-diphenylthiazoleamine derivatives as Aβ40 and Aβ42 aggregation inhibitors.

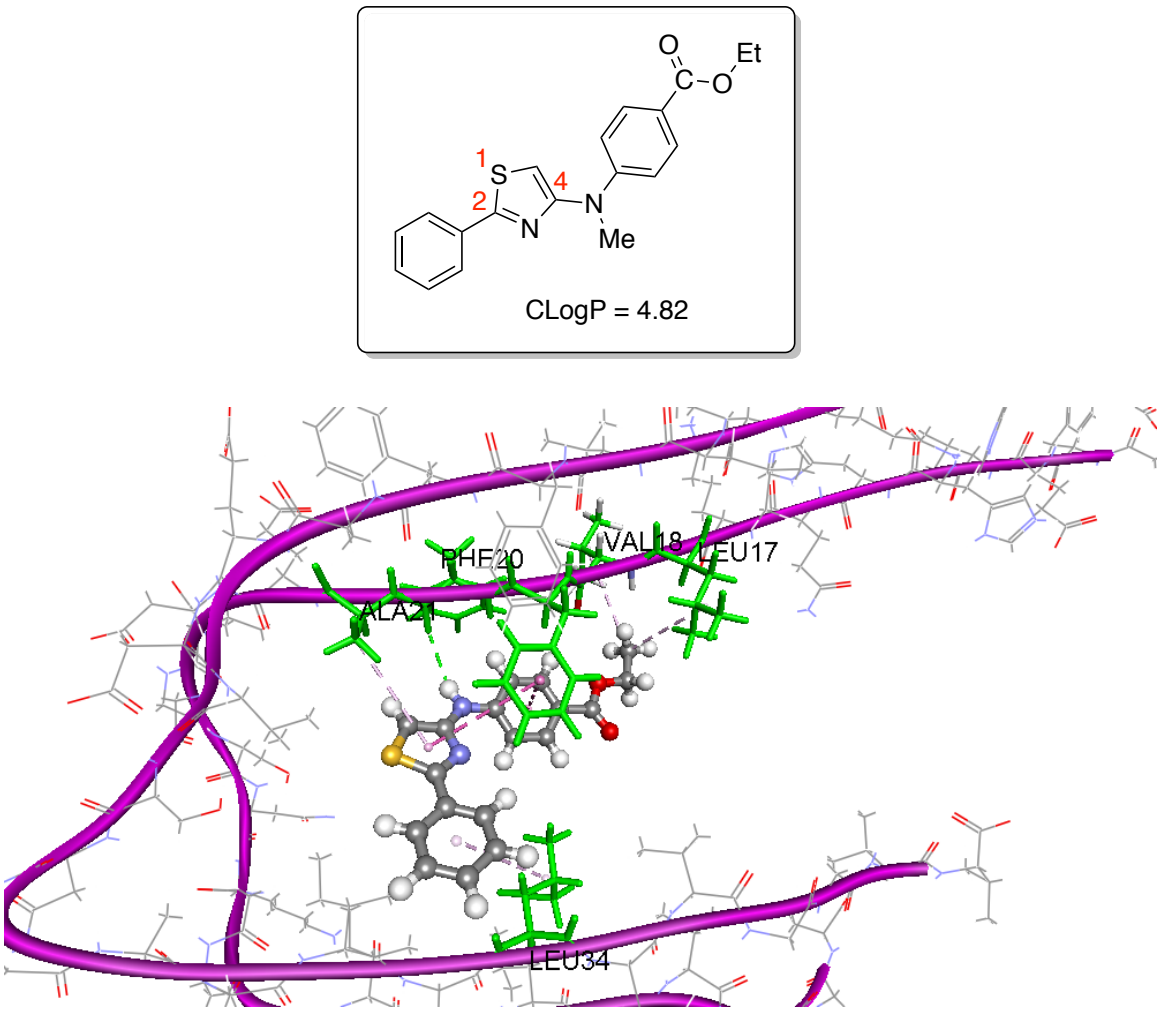

Figure 30. Chemical structure and molecular modeling of Neuropathiazol®. Molecular modeling of thiazole docked with the Aβ40-dimer model (pdb id: 2LMN) using the Discovery Studio Structure-based design software. Neuropathizol® undergoes a number of interactions in the hydrophobic region (orange) of Aβ40-dimer, such as hydrogen bonding with Val18 and Phe19, and π-π interactions with Phe20.

2.3 Synthesis of Thiazole Core Template

The retrosynthetic strategy used to synthesize *N*-diphenylthiazol-amine regioisomers is shown in Figure 31. The *N*,4-diphenylthiazol-amine was obtained by cyclization reaction[209] of commercially available and inexpensive *N*-phenylthiourea and 2-bromo-acetophenone (Hantzsch thiazole synthesis) while thiobenzamide was cyclized with 2-chloro-*N*-phenylacetamide to obtain *N*,2-diphenylthiazole-4-amine.

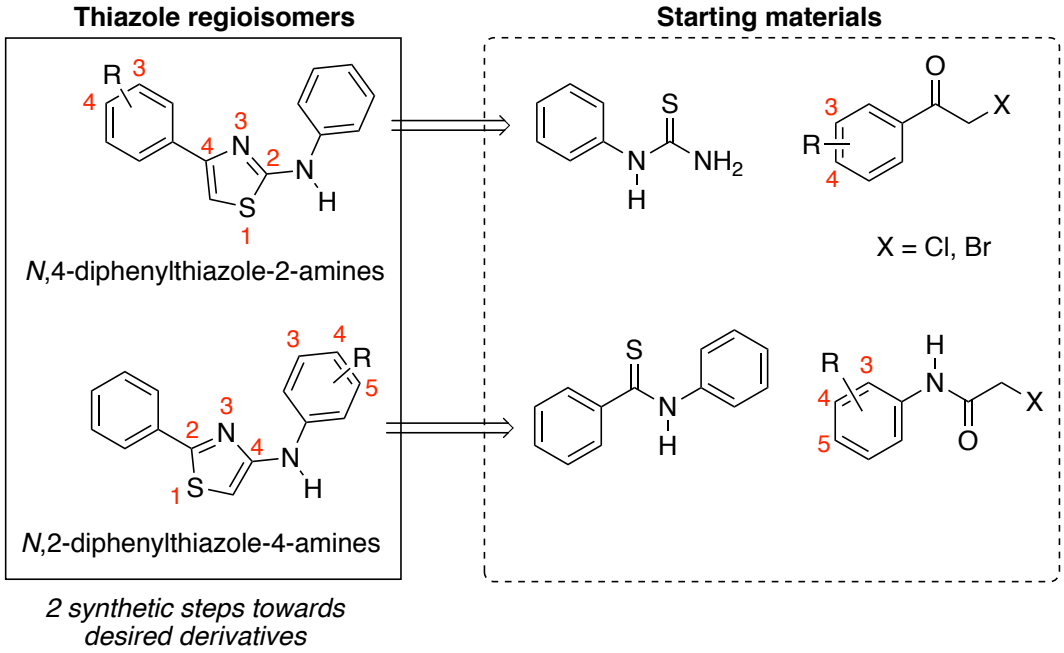

Figure 31. Retrosynthetic pathway to the synthesis of *N*-diphenylthiazoleamine derivatives.

2.4 Target Thiazole Library

In total, the thesis encompasses the design, development, and biological screening of **47** novel thiazole derivatives. Moreover, this study demonstrates that thiazole class of small molecules are capable of preventing the self-assembly of Aβ40 and Aβ42 peptides based on (i) in vitro fluorescence spectroscopy experiments and (ii) transmission electron microscopy (TEM) studies and are capable of preventing and reducing Aβ40 and Aβ42-induced neurotoxicity in HT22 hippocampal cells.

The following is the complete list of novel thiazole-based compound libraries synthesized and categorized into four chapters.

---

1. *N*,4-Diphenylthiazol-2-amines **(Chapter 3 – 12 derivatives)**
2. *N*-Methyl-*N*,4-diphenylthiazol-2-amines **(Chapter 4 – 11 derivatives)**
3. *N*,4-Diphenylthiazol-2-amines **(Chapter 5 – 10 derivatives)**
4. *N*-Methyl-*N*,4-diphenylthiazol-2-amines **(Chapter 6 – 10 derivatives)**
5. *N*,2-Diphenylthiazol-4-amines **(Chapter 7 – 4 derivatives)**

CHAPTER 3 Development of *N*,4-Diphenylthiazol-2-amines

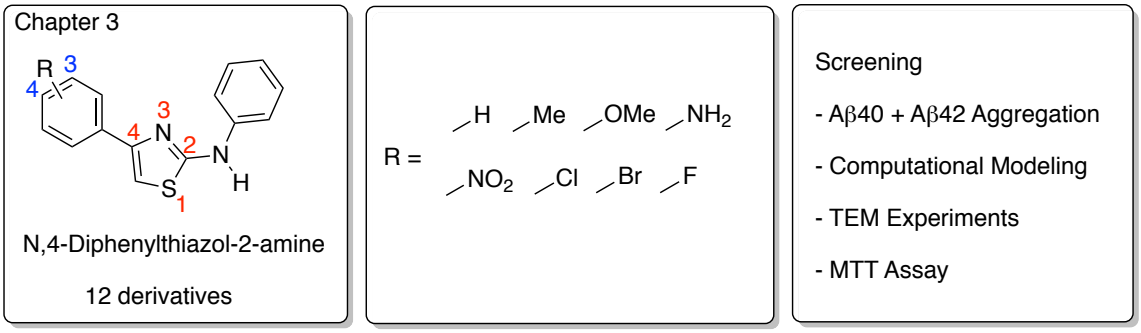

Figure 32. Banner for Chapter 3

3.1 Introduction

In this Chapter, we designed a library of novel class of diphenylthiazole-amine derivatives by focusing on the *N*,4-diphenylthiazol-2-amine derivatives possessing various electron-donating and electron-withdrawing groups (R = H, Me, OMe, NH_2, NO_2, Cl, Br, and F) at either the *para* (C4)- or *meta* (C3)- position of the 4-substituted phenyl ring (Figure 32) as inhibitors of Aβ40 and Aβ42 aggregation. The Chapter describes the synthetic methodology and analytical data for this series of compounds, their biological assay results based on ThT-based fluorescence aggregation kinetic studies and transmission electron microscopy (TEM) experiments, and their neuroprotective activity against Aβ40- or Aβ42-induced cytotoxicity in mouse hippocampal neuronal cells (HT22). In addition, results from computational modeling studies are included to understand the binding interactions of *N*,4-diphenylthiazol-2-amine derivatives in Aβ40 or Aβ42 aggregates.

3.2 Hypothesis

For this series of *N*,4-diphenylthiazol-2-amine derivatives, we hypothesize that (i) the diphenyl rings undergo nonpolar interactions with both the N- and C-terminal residues (Phe20 and Val36) in the Aβ40 dimer model, which can stabilize the dimer assembly and can reduce its aggregation propensity; (ii) interact in the KLVFFA and polar region of Aβ42 to prevent growth kinetics; and that (iii) incorporating substituted phenyl rings at the thiazole C4-position can enhance their binding toward Aβ40 and Aβ42, and their anti-aggregation properties. These hypotheses were addressed by synthesizing *N*,4-diphenylthiazole-2-amine derivatives with EDGs and EWGs (R = H, Me, OMe, NH_2, NO_2, Cl, Br, and F). All the derivatives designed exhibited ClogP values in the range of 3.8-4.7, which is suitable for transport into the CNS.[208]

3.3 Results and Discussion

3.3.1 Synthesis

The synthetic route for the target compound (**1-2**) is outlined in Scheme 1. As discussed earlier in Chapter 2, the synthesis of *N*,4-diphenylthiazol-2-amine derivatives (**1a-j** and **2a-b**, Scheme 1) was carried out by coupling *N*-phenylthiourea with 2-bromo-3' or 4'-substituted-acetophenone (R = H, *p*-Me, *p*-OMe, 3,4-diOMe, *p*-Cl, *p*-Br, *p*-F, 3,4-diF, *m*-NO_2, and *p*-NO_2) in ethanol via cyclization reaction (Figure 33).[209] The substituted bromoacetophenone precursors were synthesized from the respective *para* or *meta*-substituted acetophenone *via* copper bromide catalyzed bromination reaction as shown in Scheme 1. The purified *N*,4-diphenylthiazol-2-amine derivatives were characterized by ^{1}H and ^{13}C NMR, LCMS and HRMS analysis. The yields of the desired

target compounds (**1a-j**) ranged from 69-99%. The reaction mechanism pertaining to cyclization reaction is briefly outlined in Figure 33.

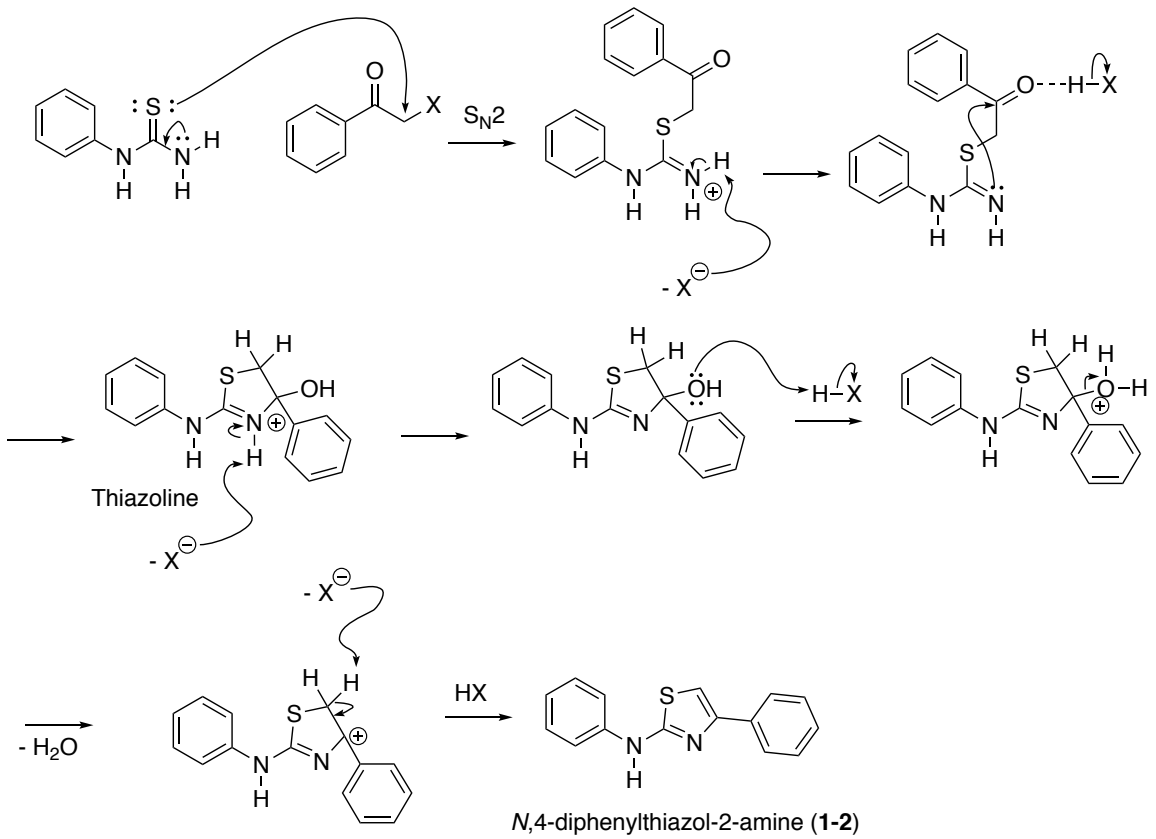

Figure 33. Proposed mechanism of cyclization reaction to synthesize *N*-4-diphenylthiazol-2-amine derivatives (**1-2**).

The corresponding amine derivatives (**2a** or **2b**) were obtained by hydrazine hydrate/palladium-carbon mediated catalytic hydrogen-transfer reduction of nitro-substituted *N*,4-diphenylthiazol-2-amines **1e** and **1f** (Figure 34), where hydrazine is the source of the hydrogen.[210] Their yields ranged from 78-83%. The reaction mechanism pertaining to the hydrazine hydrate:Pd/C catalyzed reduction is shown in Figure 34.[211] In total, a library of 12 *N*,4-diphenylthiazol-2-amine derivatives were synthesized using Scheme 1, which were evaluated as Aβ aggregation inhibitors.

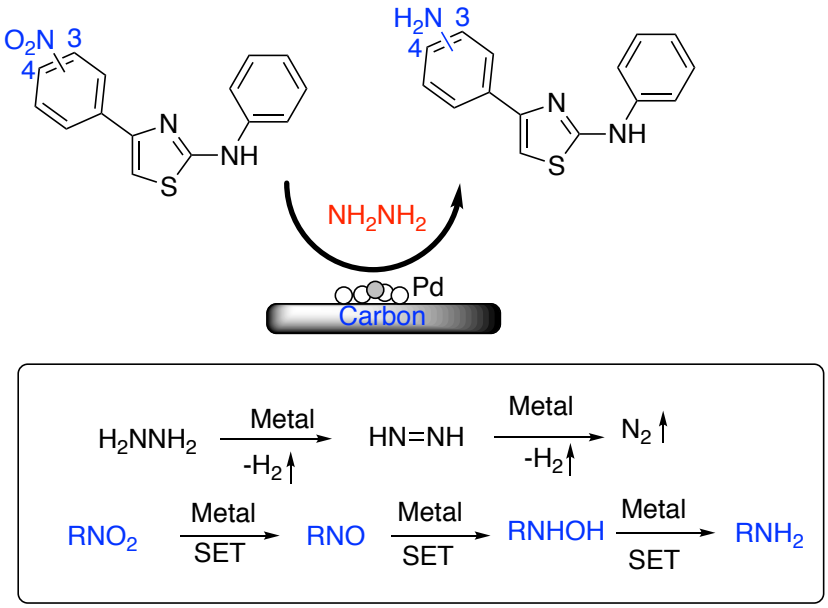

Figure 34. Mechanism of the catalytic reduction reaction to synthesize nitro-substituted 4-diphenylthiazol-2-amine derivatives. SET – Single electron transfer.

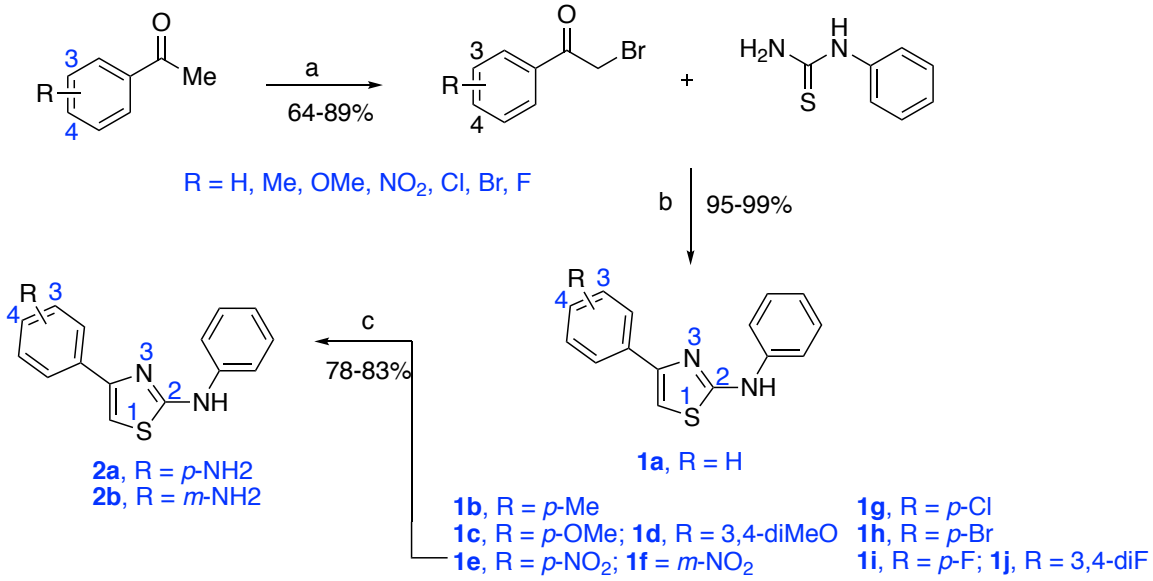

*Reagents and conditions: (a) $CuBr_2$, EtOAc, 70 °C, 15 h; (b) EtOH, 80 °C, 5 h; (c) Pd/C, hydrazine hydrate, EtOH, 85 °C, 3-5 h

Scheme 1. Synthetic route towards the *N*,4-diphenylthiazol-2-amine derivatives **1-2**.

3.3.2 Amyloid-β Aggregation Inhibition Studies

The anti-aggregation activity of the *N*,4-diphenylthiazol-2-amine derivatives **1a-j** and **2a-b** toward either Aβ40 or Aβ42 were evaluated at four different concentrations (1, 5, 10, and 25 μM). The results obtained were compared with known inhibitors methylene blue (MB) and resveratrol (Figure 35) using the ThT-based fluorescence assay (Table 3, Aβ40 assay results and Table 4, Aβ42 assay results) at pH 7.4,[145] 37 °C for 24 h. In Table 3 and Table 4, the results are presented as average % inhibition ± standard deviation (SD) in triplicates for three independent experiments. Structure-activity relationship (SAR) studies show that the unsubstituted *N*,4-diphenylthiazol-2-amine (**1a**, R = H) exhibited anti-aggregation properties against Aβ40 aggregation with inhibition ranging from 28-62% at various concentrations (Table 3). Adding an EDG (R = Me) at the *para*-position in compound **1b** did not enhance the anti-aggregation property with maximum inhibition of 56% seen at 25 μM. The anti-Aβ40 activity was reduced when *p*-Me was replaced with *p*-OMe group (34% inhibition at 25 μM, Table 3). Replacing the *p*-OMe with a 3,4-diOMe substituent (compound **1d**) restored the activity with the anti-aggregation properties ranging from 45-68% inhibition). Remarkably, addition of NH_2 substituent either at the *para*- or *meta*-position provided *N*,4-diphenylthiazole-2-amines (**2a** and **2b**) with superior anti-aggregation properties against Aβ40 aggregation (Table 3), with activity reaching up to 75% inhibition (compound **2b**). Both compounds **2a** and **2b** were not as effective as reference agents, methylene blue (MB, 98% inhibition at 25 μM) and resveratrol (RES, 92% inhibition at 25 μM) as inhibitors of Aβ40 aggregation. Replacing the NH_2 substituent with an EWG such as a NO_2 either at the *para*- or *meta*-

position provided similar anti-aggregation properties (compound **1e** and **1f**, 70% and 74% inhibition, respectively, Table 3). This suggests that polar functional groups either at the *para*- or *meta*-position provide superior anti-Aβ40 activities. The addition of other EWGs, such as Cl, Br, or F at the *para*-position (compound **1g-i**) provided anti-aggregation properties although they were not as effective as either NH_2 or NO_2 substituted compounds. Similarly, addition of 3,4-diF substituent (compound **1j**) provided good inhibition of Aβ40 aggregation (inhibition range 32-63%). However, it was not as effective as NH_2 or NO_2 substituted compounds **1e-f**. These studies demonstrate that *N*,4-diphenylthiazol-2-amines possess inherent anti-aggregation properties and the activity was sensitive to variations in substituents at the *para*- and *meta*-positions, and that the Aβ40 aggregation inhibition activity was of the order: $NH_2 \approx NO_2 > Me \approx Cl > 3,4\text{-diF} \approx 3,4\text{-diOMe} > OMe \approx H$ (at 25 μM).

The 24 h Aβ40 aggregation kinetic plot for *p*-NH_2 substituted *N*,4-diphenylthiazol-2-amines 2a is shown in diphenylthiazol-2-amines 2a is shown in

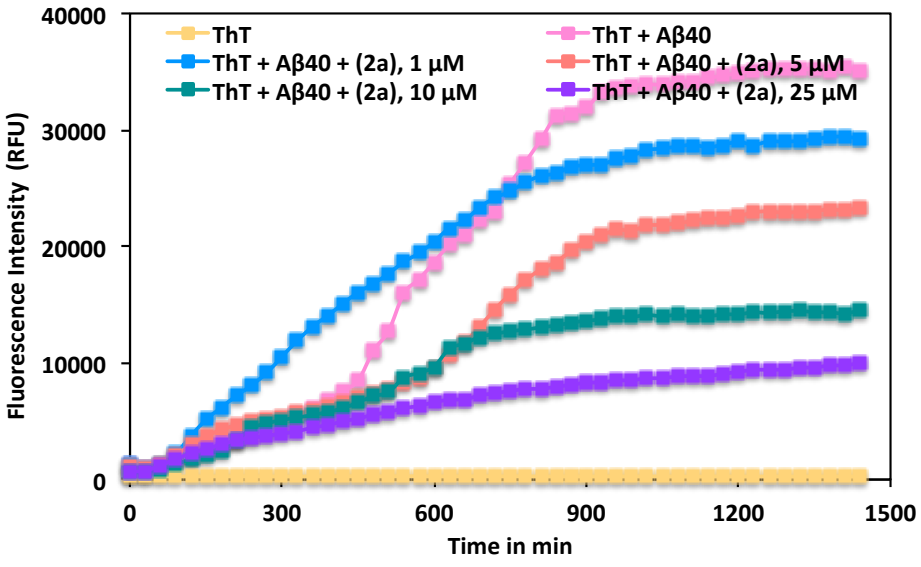

Figure 36. In the absence of test compound, Aβ40 (5 μM) shows a sigmoidal curve with a short lag phase, followed by quick and rapid growth phase which starts to plateau after ~15 h time point and a saturation phase which indicates the formation of Aβ40 fibrils. In the presence of **2a** at various concentrations (1-25 μM), the ThT fluorescence intensity declined gradually which indicates a reduction in the formation of Aβ40 aggregates. Compound **2a** was able to reduce the growth phase significantly and demonstrated maximum inhibition of Aβ40 aggregation at 25 μM (74% decline in ThT fluorescence intensity). This Aβ40 aggregation kinetic plot demonstrates the ability of *N*,4-diphenylthiazol-2-amine to perturb various phases of the nucleation dependent fibrillogenesis of Aβ40.

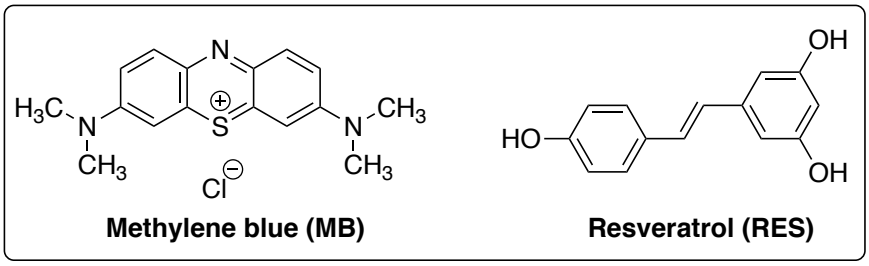

Figure 35. Chemical structures of reference compounds used in the ThT-based kinetic assay.

Table 3. Inhibition data for *N*,4-diphenylthiazol-2-amine derivatives **1a-j**, **2a-b** and reference compounds toward Aβ40 aggregation, and their ClogP values.

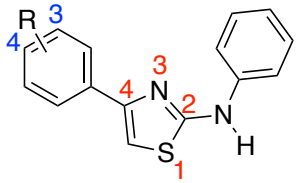

1-2

R = H, Me, OMe, NH_2, NO_2, Cl, Br, F

Compound	R-group	% Inhibition for Aβ40 [a]	ClogP [b]

		1 µM	5 µM	10 µM	25 µM	
1a	H	50	62	28	37	3.87
1b	*p*-Me	53	53	46	56	4.36
1c	*p*-OMe	15	20	24	34	3.78
1d	3,4-diOMe	68	53	56	45	3.35
1e	*p*-NO_2	45	52	34	70	3.61
1f	*m*-NO_2	55	63	72	74	3.61
1g	*p*-Cl	NA	NA	28	55	4.58
1h	*p*-Br	NA	NA	NA	30	4.73
1i	*p*-F	48	56	22	25	4.01
1j	3,4-diF	63	32	53	47	4.08
2a	*p*-NH_2	45	53	53	74	2.64
2b	*m*-NH_2	36	41	27	75	2.64
MB	-	90	95	97	98	3.62
RES	-	45	52	65	92	2.83

[a]Percent aggregation inhibition values were average ± SD < 10% (n = 3) for three experiments. NA – Not Active. [b]ClogP values were determined using ChemDraw 19.1.

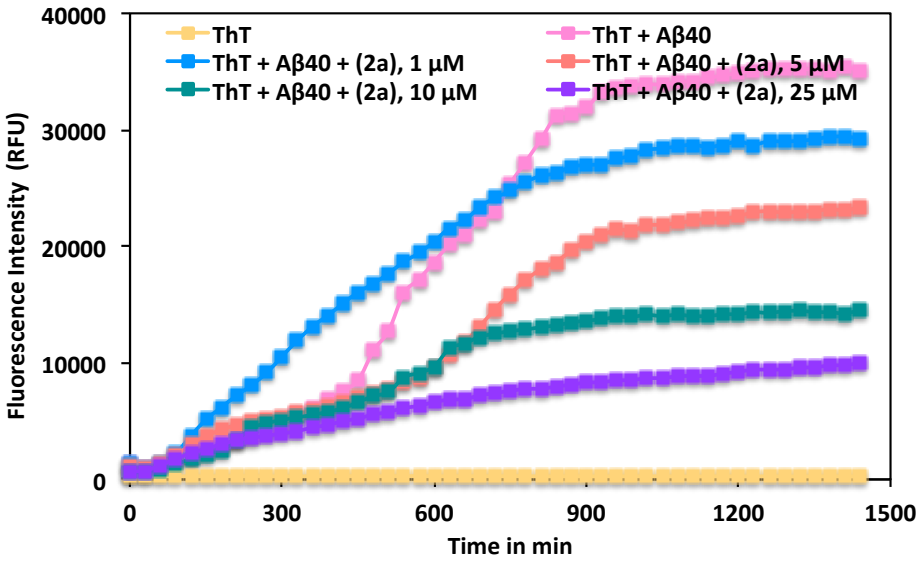

Figure 36. ThT-monitored 24 h aggregation kinetics of Aβ40 (5 µM) in the presence of 1, 5, 10, and 25 µM of *N*,4-diphenylthiazol-2-amine (**2a**) at pH 7.4, 37 °C in phosphate buffer. Aggregation kinetics were monitored by ThT-fluorescence spectroscopy (excitation = 440 nm, emission = 490 nm). Results are average ± SD of three independent experiments (n = 3).

The results of anti-aggregation properties of *N*,4-diphenylthiazol-2-amines **1a-j**, **2a** and **2b** toward Aβ42 aggregation is shown in Table 4. The SAR analysis shows that

the unsubstituted compound **1a** (R = H), exhibited excellent inhibition profile ranging from 75–90% inhibition (Table 4). Incorporating EDGs such as Me, or OMe at *para*- or *meta*-positions provided similar inhibition as the unsubstituted compound **1a** when tested at a concentration of 25 μM (inhibition range = 90–96%). However, they exhibited weaker inhibition at lower concentrations (1-10 μM) compared to the unsubstituted compound **1a**. Interestingly, presence of NH_2 substituent either at *para*- or *meta*-position exhibited lower inhibition of Aβ42 (~58%), compared to the unsubstituted compound **1a** (Table 4). Investigating the effect of disubstitution on Aβ42 aggregation properties shows that compounds **1d** (R = 3,4-diOMe) and **1j** (R = 3,4-diF) exhibited consistent and excellent inhibition of Aβ42 aggregation at all the tested concentration (inhibition range of 70–97%, Table 4) and exhibited comparable activity as the reference agents MB (99% inhibition) and RES (98% inhibition) at 25 M (Table 4). The presence of EWGs (R = NO_2, Cl, Br) was able to retain Aβ42 aggregation inhibition properties and demonstrated excellent inhibition at 25 μM (compounds **1e-h** 83–96% inhibition, Table 4) whereas the presence of a *p*-F substituent diminished the anti-aggregation property (compound **1i**, 83-96% inhibition, Table 4). The Aβ42 aggregation inhibition activity was of the order: 3,4-diF ≈ Me ≈ OMe ≈ Cl ≈ 3,4-diOMe > H > NO_2 > NH_2 > F (at 25 μM). These studies show that *N*,4-diphenylthiazol-2-amines derivatives exhibited superior inhibition of Aβ42 aggregation as compared to Aβ40 inhibition.

The 24 h aggregation kinetics data for Aβ42 (5 μM) in the presence of *N*,4-diphenylthiazol-2-amines derivatives **1j** is shown as representative example in Figure 37. In the absence of test compound, Aβ42 (5 μM) underwent rapid aggregation exhibiting characteristic features such as the lag phase, growth phase and saturation phase with

corresponding increase in ThT fluorescence intensity (Figure 37). In the presence of varying concentrations of **1j**, the ThT fluorescence declined rapidly with maximum reduction seen at 25 μM. These results show that *N*,4-diphenylthiazol-2-amines derivatives exhibit excellent inhibition of Aβ42 aggregation at all the tested concentration and can reduce Aβ42 fibrillogenesis.

Table 4. Inhibition data for *N*,4-diphenylthiazol-2-amine derivatives **1a-j**, **2a-b**, and reference compounds toward Aβ42 aggregation, and their ClogP values.

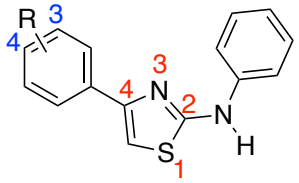

1-2

R = H, Me, OMe, NH_2, NO_2, Cl, Br, F

Compound	R-group	% Inhibition for Aβ42 [a]				ClogP [b]
		1 μM	5 μM	10 μM	25 μM	
1a	H	75	90	83	90	3.87
1b	*p*-Me	NA	34	52	96	4.36
1c	*p*-OMe	40	36	37	95	3.78
1d	3,4-diOMe	87	88	89	93	3.35
1e	*p*-NO_2	70	49	62	83	3.61
1f	*m*-NO_2	25	39	43	83	3.61
1g	*p*-Cl	11	NA	83	95	4.58
1h	*p*-Br	NA	55	68	92	4.73
1i	*p*-F	NA	41	40	51	4.01
1j	3,4-diF	80	95	78	97	4.08
2a	*p*-NH_2	40	36	60	57	2.64
2b	*m*-NH_2	25	30	52	58	2.64

MB	-	87	97	97	99	3.62
RES	-	81	94	95	98	2.83

[a]Percent aggregation inhibition values were average ± SD < 10% (n = 3) for three independent experiments. NA – Not Active. [b]ClogP values were determined using ChemDraw 19.1.

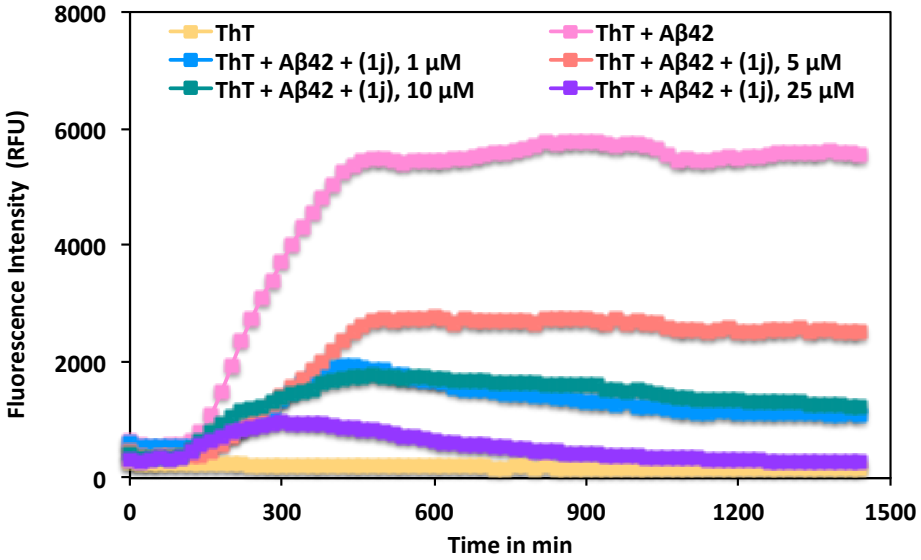

Figure 37. ThT-monitored 24 h aggregation kinetics of Aβ42 (5 µM) in the presence of 1, 5, 10, and 25 µM of *N*,4-diphenylthiazol-2-amine (**1j**) at pH 7.4, 37 °C in phosphate buffer. Aggregation kinetics were monitored by ThT-fluorescence spectroscopy (excitation = 440 nm, emission = 490 nm). Results are average ± SD of three independent experiments (n = 3).

3.3.2.1 Correlating the ClogP Values, HBDs, and HBAs with Anti-Aβ Aggregation Properties

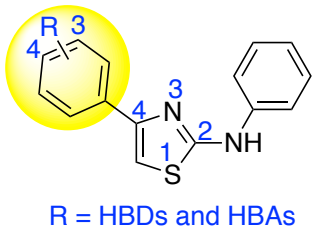

Figure 38. Chemical structure of *N*,4-diphenylthiazol-2-amines described in Chapter 3 highlighting the C4-position of the thiazol-2-amine that was modified by SAR. HBD – Hydrogen Bond Donors, HBA – Hydrogen Bond Acceptors.

The anti-aggregation activity data of *N*,4-diphenylthiazol-2-amines **1a–j**, **2a** and **2b** (at 25 μM each), toward Aβ40 obtained after conducting the in vitro ThT based fluorescence assay, was correlated with the ClogP values, number of hydrogen bond donors (HBD), and hydrogen bond acceptors (HBA) present in the phenyl ring at the C4-position of the thiazol-2-amine (Figure 38).

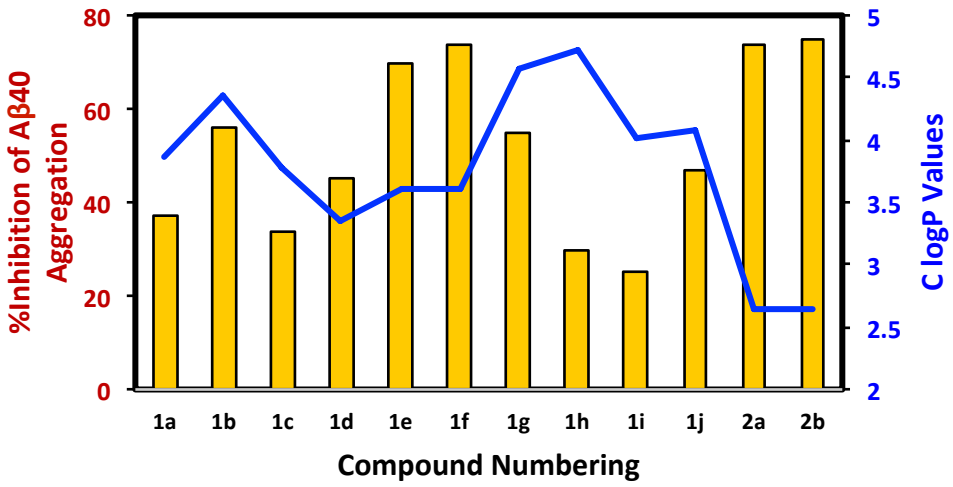

Figure 39. Correlation of Aβ40 aggregation inhibition properties of **1a–j**, **2a** and **2b** at 25 μM, with ClogP values. Blue line represents ClogP values.

This plot shows that the most potent inhibitors of Aβ40 aggregation (compounds **1e**, **1f**, **2a** and **2b**, 70–75% inhibition at 25 μM), had ClogP values of 3.61 and 2.64 respectively, Figure 39). Interestingly, all these compounds possess HBDs at the phenyl ring (C4-position of the thiazol-2-amine ring), with compounds **1e** and **1f** containing *p*- or *m*-NO_2-phenyl substituents and compounds **2a** and **2b** possessing a *p*- or *m*-NH_2-phenyl substituents. In contrast, *N*,4-diphenylthiazol-2-amine derivatives that possess HBAs such as compounds **1c** (*p*-OMe-phenyl), **1d** (3,4-diOMe-phenyl), **1i** (*p*-F-phenyl) and **1j** (3,4-diF-phenyl), were not as potent as compounds that possessed HBDs at the phenyl

ring and their anti-Aβ activity was in the range of 34–47% inhibition (Figure 39). This suggests that the presence of C4 phenyl ring possessing HBDs was enhancing the Aβ40 aggregation inhibition properties.

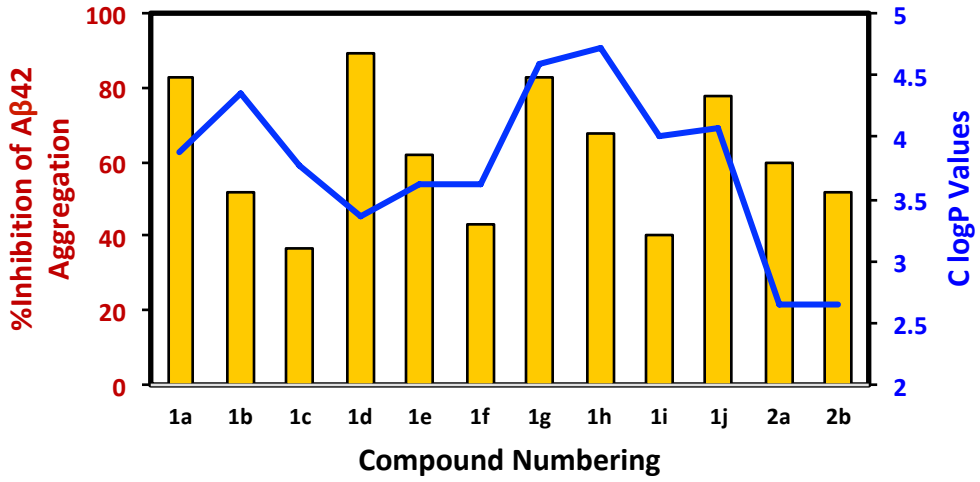

Figure 40. Correlation of Aβ42 aggregation inhibition properties of **1a–j**, **2a** and **2b** at 10 μM, with ClogP values. Blue line represents ClogP values.

A similar plot was obtained using the anti-aggregation data for the *N*,4-diphenylthiazol-2-amines **1a–j**, **2a** and **2b** toward Aβ42, and was correlated with the ClogP values, number of hydrogen bond donors (HBD) and hydrogen bond acceptors (HBA) present in the phenyl ring at the C4-position of the thiazole-2-amine (Figure 40). The anti-aggregation activity data at 10 μM was considered to assess the trend between activity, ClogP values, HBAs and HBDs, as there was no significance difference in the data obtained at 25 μM test compound concentration (Table 4). The correlation plot shown Figure 40 at 10 μM shows that *N*,4-diphenylthiazol-2-amines exhibiting maximum anti-aggregation properties (78–89% range, compounds **1a**, **1d**, **1g** and **1j**), had ClogP values ranging from 3.35–4.58. Compounds possessing two HBAs including **1d**

(3,4-diOMe-phenyl) and **1j** (3,4-diF-phenyl) exhibited superior inhibition of Aβ42 aggregation (89 and 78% inhibition respectively), whereas compounds containing HBDs such as **1c** (*p*-OMe-phenyl), **1e**, **1f** (either *p*- or *m*-NO_2), and **2a**, **2b** (either *p*- or *m*-NH_2) were not as potent (37–60% inhibition, Figure 40). One of the lipophilic compounds from this series, containing a *p*-chlorophenyl substituent (**1g**, ClogP = 4.58), was also a potent inhibitor of Aβ42 aggregation which suggests that both ClogP values and the presence of HBAs play an important role in enhancing the anti-aggregation properties.

3.3.3 Computational Modeling Studies

The binding interactions of most potent *N*,4-diphenylthiazol-2-amine derivatives was investigated by conducting molecular docking studies using the solved structures of Aβ40 and Aβ42 peptides.[212,213] Docking studies were carried out using the dimer assemblies of both Aβ40 and Aβ42 peptides as they represent the early forms of Aβ in solution. In the *N*,4-diphenylthiazol-2-amine series, compound **2a** (4-(4-aminophenyl)-*N*-phenylthiazol-2-amine) was identified as one of the most potent inhibitors of Aβ40 aggregation in the ThT-based fluorescence assay (74% inhibition at 25 μM). Figure 41 Panel A shows the predicted binding mode of **2a** in the Aβ40-dimer model. These studies show that the *N*-phenylthiazol-2-amine was oriented in the KLVFFA region closer to the N-terminal into where the 4-aminophenyl ring was situated. The central thiazole ring underwent couple of π-π T-shaped interactions with aromatic rings of Phe19 and Phe20 (distance ~ 5 Å). The secondary amine NH was in contact with backbone C=O of Lys16 via hydrogen bonding interaction (distance = 2.6 Å).

Panel B (Figure 41) shows interactions of **1j** in the Aβ42 dimer model. The diF substituent underwent hydrogen bonding interactions with backbone of Lys16 (distance = 2.2-2.6 Å). The 4-aminophenyl ring was in contact with Val18 and Ala21 via π-alkyl interaction with distance < 5 Å. The central thiazole ring underwent several π-alkyl interactions with side chain of Ala21 (distance < 5 Å). The *N*-phenyl ring underwent π-alkyl interaction with side chain of Ala21 (distance < 5 Å). These studies show that compound **1j** was in contact with amino acids present in the N-terminal, which can stabilize the dimer assembly and can reduce or prevent further aggregation into higher order structures.

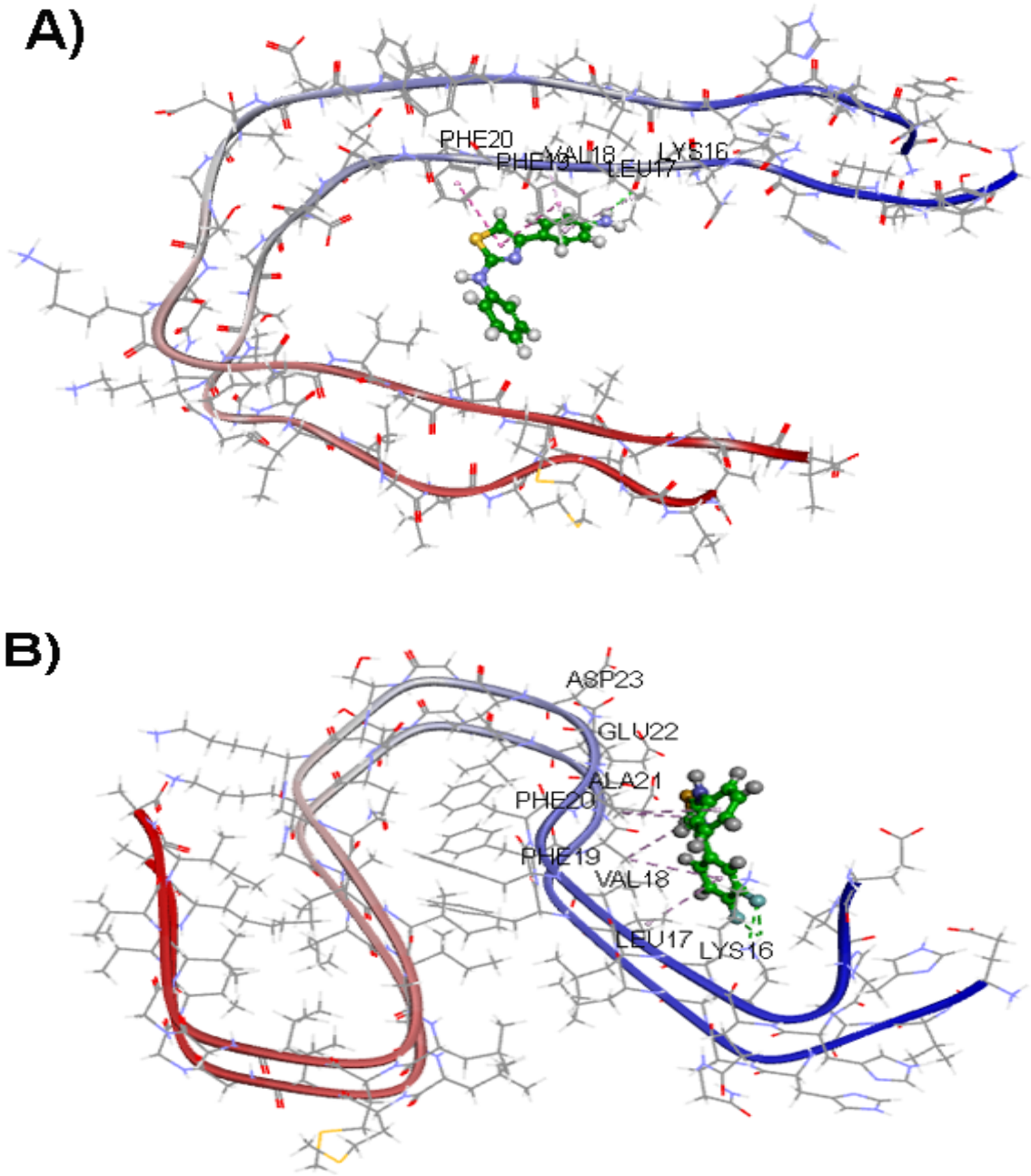

Figure 41. Panel A: Predicted binding mode of **2a** (ball and stick cartoon) in the Aβ40-dimer model (ribbon diagram, pdb id: 2LMN, CDOCKER energy = -9.47 kcal/mol; CDOCKER interaction energy = -19.65 kcal/mol). Panel B: Predicted binding mode of **1j** (ball and stick cartoon) in the Aβ42-dimer model (ribbon diagram, pdb id: 5KK3, CDOCKER energy = –7.97 kcal/mol; CDOCKER interaction energy = –21.09 kcal/mol).

3.3.4 Transmission Electron Microscopy (TEM) Studies

In order to validate and confirm the anti-aggregation properties of the *N*,4-diphenylthiazol-2-amine derivatives toward Aβ40 and Aβ42 aggregation observed in ThT-based fluorescence assay, transmission electron microscopy (TEM) experiments were carried out using representative *N*,4-diphenylthiazol-2-amine derivatives. The Aβ40 and Aβ42 aggregation morphologies were assessed in the presence and absence of the test compounds. Figure 42 shows the TEM morphologies of Aβ40 in the presence or absence of test compounds **2a** (25 μM) and **2b** (25 μM). Panel A shows the presence of dense and distinct fibrillar Aβ40 aggregates after 24 h incubation at 37 °C with phosphate buffer at pH 7.4. Co-incubation of Aβ40 with either **2a** or **2b** (25 μM) led to a significant reduction in Aβ40 aggregates, which further confirms the anti-aggregation properties of *N*,4-diphenylthiazol-2-amine derivatives (Figure 42).

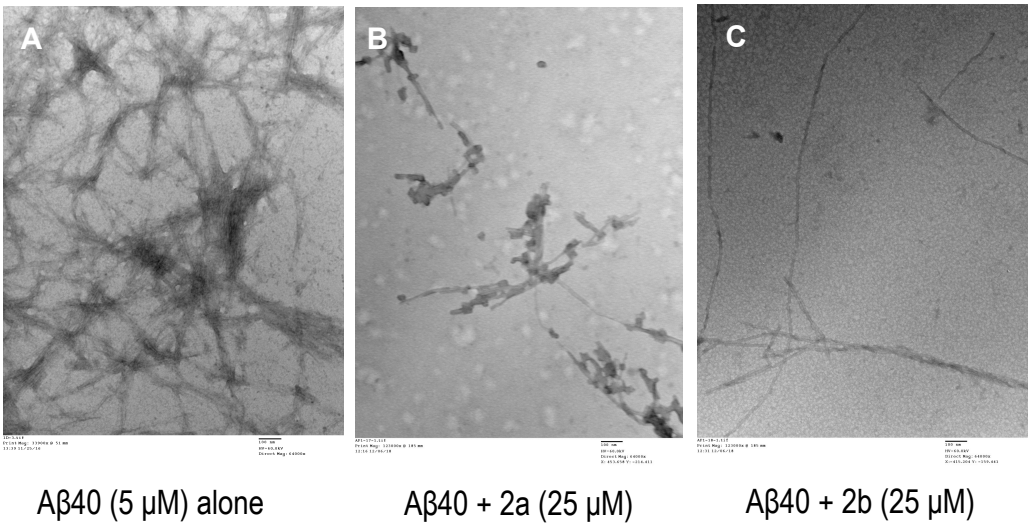

Figure 42. TEM images of Aβ40 aggregation morphology. Panel A: Aβ40 control (5 μM). Panel B: Aβ40 + **2a** (25 μM). Panel C: Aβ40 + **2b** (25 μM). Scale bars represent 100 nm.

Figure 43 shows TEM images of Aβ42 (5 μM) alone after 24 h incubation. This study shows the formation of densely formed Aβ42 fibrils. In the presence of **1j** (25 μM), the Aβ42 fibril load was reduced significantly, as observed in the panel B (Figure 43). These results further demonstrates the ability of *N*,4-diphenylthiazol-2-amine derivatives in reducing both Aβ40 and Aβ42 aggregation.

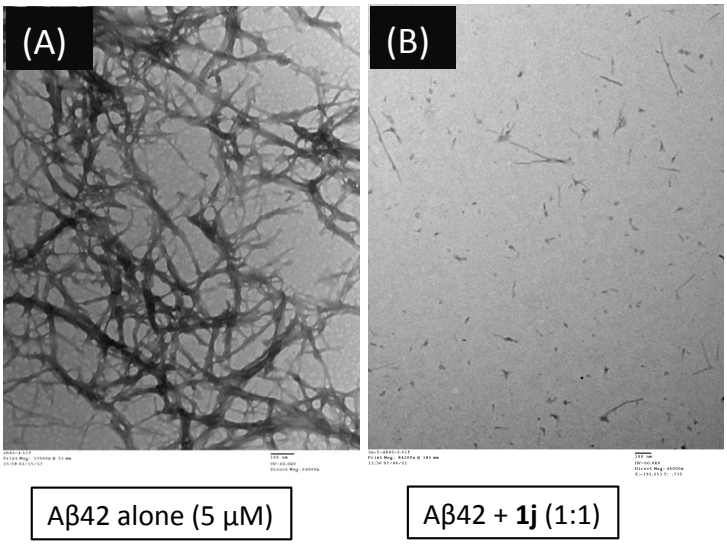

Figure 43. TEM images of Aβ42 aggregation. Panels A: Aβ42 control (5 μM). Panel B: Aβ42 + **1j** (5 μM). Scale bars below the images represent 100 nm.

3.3.5 Cell Viability Assay

The cell viability in the presence of the *N*,4-diphenylthiazol-2-amine derivatives **1a-j** and **2a-b** (10 μM), was evaluated in mouse hippocampal derived HT22 cells to investigate their ability to reduce cytotoxicity induced by either Aβ40 (Figure 44) or Aβ42 (Figure 45). This assay was carried out UV spectroscopy using the dye 3-(4,5-dimethylthiazol-2-yl)-2-5-diphenyltetrazolium bromide (MTT).[214,215]

Incubating Aβ40 (5 μM) in the presence of mouse hippocampal derived-cells (HT22) led to cytotoxicity and led to ~20% decline in cell viability compared to the untreated group (Figure 44). In the presence of 10 μM of *N*,4-diphenylthiazol-2-amine derivatives (**1a-j**, **2a** and **2b**), *N*,4-diphenylthiazol-2-amine derivatives (**1b**, **1c**, **1e**, **1f**, **1h**, and **2b**) exhibited maximum neuroprotection against Aβ40-induced cytotoxicity in HT22 with cell viability ranging from 80–86% (Figure 44); whereas, *N*,4-diphenylthiazol-2-amine derivatives (**1a**, **1f**, **1g** and **2a**) exhibited excellent neuroprotection against Aβ42-induced cytotoxicity in HT22 cells (Figure 45). For example, Aβ42 treated cells exhibited a drastic decline in cell viability (63%) which was restored in the presence *N*,4-diphenylthiazol-2-amine derivatives **1g** (Figure 45) which demonstrates their ability to provide neuroprotection against Aβ42-induced cytotoxicity. In this series, the unsubstituted compound **1**a (*N*,4-diphenylthiazol-2-amine) exhibited maximum neuroprotection, demonstrating 95% cell viability and was superior to the reference agent RES (72% cell viability, Figure 45). Overall, compounds in this series exhibited varying range of cell viability ranging from 59–95% with couple of compounds (**1a** and **1g)** exhibiting excellent neuroprotective activity against Aβ42-induced cytotoxicity (Figure 45).

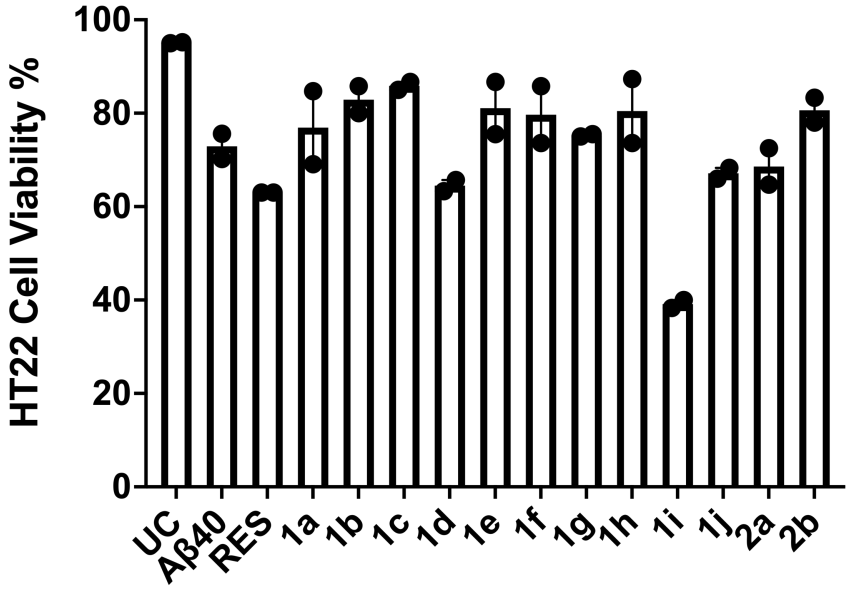

Figure 44. Percentage viability of the *N*,4-diphenylthiazol-2-amine derivatives **1a-j**, **2a-b**, and RES (10 μM) in HT22 cells in the presence of Aβ40 was assessed by MTT assay after 24 h incubation at 37 °C. The results were given as average of two independent experiments (n = 3). UC = untreated cells, RES = resveratrol.

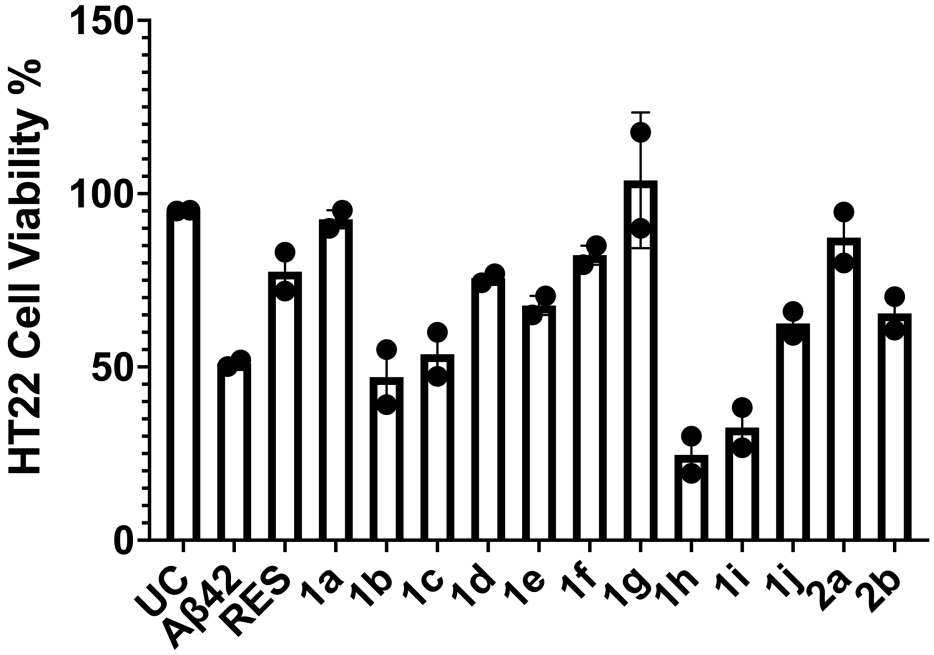

Figure 45. Percentage viability of the *N*,4-diphenylthiazol-2-amine derivatives **1a-j**, **2a-b**, and RES (10 μM) in HT22 cells was assessed by MTT assay toward Aβ42 after 24 h incubation at 37 °C. The results were given as average of two independent experiments (n = 3). UC = untreated cells, RES = resveratrol.

3.4 Summary

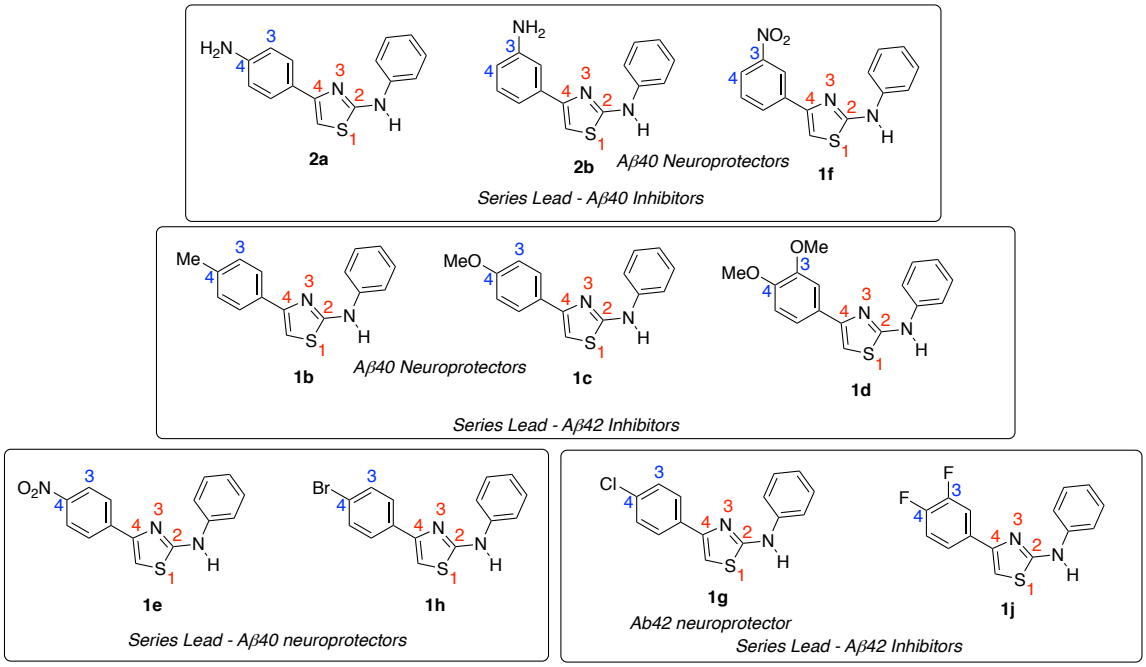

Figure 46. Cummulative chapter summary of *N*,4-diphenylthiazol-2-amines (**1-2**).

A library of twelve *N*,4-diphenylthiazol-2-amine derivatives (**1a-j** and **2a-b**) with various EDGs and EWGs either at the *para*- or *meta*-positions were synthesized, and evaluated to investigate their anti-aggregation properties toward Aβ40 and Aβ42 aggregation. The target compound libraries were obtained in good yields (range 64-99%) and were characterized by analytical methods such as NMR, LCMS, and HRMS. Biochemical experiments carried out included, ThT-based Aβ aggregation kinetics using fluorescence spectroscopy, TEM studies to assess aggregate morphology, cell culture experiments in mouse hippocampal derived HT22 cells to determine neuroprotection against Aβ40 and Aβ42 mediated cytotoxicity, and computational modeling studies to understand their binding interactions of *N*,4-diphenylthiazol-2-amine derivatives in Aβ40 and Aβ42 dimer model. These studies identified compounds **1f** (4-(3-nitrophenyl)-*N*-

phenylthiazol-2-amine), **2a** (4-(4-aminophenyl)-*N*-phenylthiazol-2-amine) and **2b** (4-(3-aminophenyl)-*N*-phenylthiazol-2-amine), as the best inhibitors of Aβ40 aggregation based on the ThT fluorescence assay (75% inhibition at 25 μM) and compounds **1b** (4-(4-methylphenyl)-*N*-phenylthiazol-2-amine), **1c** (4-(4-methoxyphenyl)-*N*-phenylthiazol-2-amine), **1d** (4-(3,4-dimethoxyphenyl)-*N*-phenylthiazol-2-amine), **1g** (4-(4-chlorophenyl)-*N*-phenylthiazol-2-amine, and **1j** (4-(3,4-difluorophenyl)-*N*-phenylthiazol-2-amine) with superior inhibition of Aβ42 aggregation (93-97% inhibition at 25 μM). In the HT22 cytotoxicity assay, several *N*,4-diphenylthiazol-2-amine derivatives (**1b**, **1c**, **1e**, **1f**, **1h**, and **2b**) exhibited excellent neuroprotection against Aβ40-induced cytotoxicity. Furthermore, several compounds (**1a**, **1d-f**, and **2a-b**) were able to reduce and/or prevent Aβ42 mediated cytotoxicity with compound **1a** (*N*,4-diphenylthiazol-2-amine) and **1g** (4-(4-chlorophenyl)-*N*-phenylthiazol-2-amine) exhibiting excellent protection (>95% cell viability). These SAR studies demonstrate that *N*,4-diphenylthiazol-2-amine derivatives represent a novel class of compounds which are capable of modulating Aβ aggregation kinetics and have potential for further development.

3.5 Experimental

3.5.1 Chemistry

3.5.1.1 Materials and Methods

All the reagents and solvents were purchased from various vendors (Sigma-Aldrich, Oakwood Chemical, Matrix Scientific, TCI Chemicals, AAblocks, and Ark Pharm Inc.) with a minimum purity of 95% and were used without further purification. Melting points (mp) were determined using a Fisher-Johns apparatus and are uncorrected.

Compound purification was carried out using Merck 230-400 mesh silica gel 60. All derivatives showed single spot on thin-layer chromatography (TLC) performed on Merck 60 F254 silica gel plates (0.2 mm) using variety of solvent systems and TLC spots were visualized with the handheld UV lamp 254/365 nm. ^{1}H NMR and ^{13}C NMR spectra were analyzed using a Bruker Avance 300 MHz series spectrometer in deuterated solvents. Data was analyzed using the Bruker TOPSPIN 3.6.1 software. Coupling constant (*J* values) were recorded in hertz (Hz) and the following abbreviations were used for multiplicity of NMR signals: s = singlet, d = doublet, t = triplet, m = multiplet, br = broad. Compound purity and low resolution mass (LRMS) were evaluated using an Agilent 6100 series single quad LCMS equipped with an Agilent 1.8 μM Zorbax Eclipse Plus C18 (2.1 x 50 mm) running 30:70 Water:ACN with 0.1% FA at a flow rate of 0.5 mL/min. All the final compounds were > 95% pure as determined by calculating the peak area by LCMS (UV detector, 254 nm). High-resolution mass spectrometry data were obtained by carrying out a positive ion electrospray (ESI) experiments on using a Thermo Scientific Q-Exactive hybrid mass spectrometer, Department of Chemistry, University of Waterloo. Accurate mass determinations were performed at a mass resolution of 70,000 (@m/z200) with lock mass correction. All samples were injected at 10 mL/min in a 1:1 MeOH/H_2O + 0.1% formic acid. *N*,4-diphenylthiazol-2-amines **1a**, **1b**, **1e**, **1g**, **1h**, **1i**, and **2b** are known in the literature.[176,216]

3.5.1.2 General procedure for the synthesis of 2-bromo-3',4'-dimethoxyacetophenone or 2-bromo-3',4'-difluoroacetophenone.[217]

$CuBr_2$ (10 g, 4.44 mmol) was added to the preheated EtOAc solution at 70 °C for 15 min. To this reaction mixture, 3',4'-dimethoxy- or 3',4'-difluoro- acetophenone was

added and refluxed at 70 °C for 15 h with stirring. In the next step, the reaction mixture was cooled and passed through cotton plug and then celite by washing with EtOAc (3 x 20 mL). The combined EtOAc fractions were extracted with saturated brine solution (2 x 20 mL). The resulting solution was dried over $MgSO_4$, filtered, evaporated *in vacuo*, and purified using silica gel column chromatography with EtOAc:MeOH (5:1) or EtOAc:Hex (1:1) as the eluent, respectively. Yield ranged from 64 – 92%. Analytical data for bromo-acetophenone derivatives are given below.

2-Bromo-3',4'-dimethoxyacetophenone. Yield: 89%. m.p. 60-62°C. ^{1}H NMR (300 MHz, DMSO-d_6) δ (ppm): 7.84-7.46 (m, 2H), 7.12-6.98 (m, 1H), 4.81 (s, 2H), 3.82 (s, 3H), 3.79 (s, 3H). Purity: 95%.

2-Bromo-3',4'-difluoroacetophenone. Yield: 64%. m.p. 30-31°C. ^{1}H NMR (300 MHz, DMSO-d_6) δ (ppm): 8.19-7.82 (m, 2H), 7.66-7.54 (m, 1H), 4.92 (s, 2H). Purity: 92%.

3.5.1.3 General procedure for the synthesis of N,4-diphenylthiazol-2-amine derivatives (1a-j and 2a-b).[209]

To a solution of N-phenylthiourea (0.62 g, 4.09-5.02 mmol) in ethanol in 50 mL RBF, α-haloacetophenone (1 g, 4.09-5.02 mmol) was added and refluxed at 80 °C for 5 h under a gentle flow of argon using a balloon. The resulting reaction mixture was poured into ice water (80 mL), with continuous stirring for further 30 min and at this point, the product started to precipitate. To this, aqueous 1N solution of Na_2CO_3 was added dropwise. The precipitate was filtered by vacuum filtration and washed with ice water (2 x 20 mL). The desired products *N*,4-diphenylthiazol-2-amine derivatives were obtained in

good purity and did not require further purification. Yield ranged from 69 – 99 %. The analytical data is given below:

N,4-Diphenylthiazol-2-amine (**1a**)[176] Yield: 69%. m.p. 134-136°C. ^{1}H NMR (300 MHz, DMSO-d_6) δ (ppm): 10.26 (s, 1H), 7.93 (d, J = 7.7 Hz, 2H), 7.75 (d, J = 7.9 Hz, 1H), 7.45-7.28 (m, 6H), 6.98 (t, J = 7.3 Hz, 1H). Purity: 95%.

4-(4-Methylphenyl)-N-phenylthiazol-2-amine (**1b**).[176,218] Yield: 89%. m.p. 95-97°C. ^{1}H NMR (300 MHz, DMSO-d_6) δ (ppm): 10.23 (s, 1H), 7.82 (d, J = 7.8 Hz, 2H), 7.73 (d, J = 8.1 Hz, 2H), 7.34 (t, J = 7.7 Hz, 2H), 7.24 (d, , J = 7.1 Hz, 3H), 6.98 (t, J = 7.3 Hz, 1H), 2.32 (s, 3H). Purity: 98%.

4-(4-Methoxyphenyl)-N-phenylthiazol-2-amine (**1c**).[176,218] Yield: 89%. m.p. 137-140°C. ^{1}H NMR (300 MHz, DMSO-d_6) δ (ppm): 10.21 (s, 1H), 7.86 (d, J = 8.6 Hz, 2H), 7.72 (d, J = 8.3 Hz, 2H), 7.33 (t, J = 7.8 Hz, 2H), 7.15 (s, 1H), 6.97 (m, 3H), 3.79 (s, 3H). HRMS (ESI) m/z calcd for $C_{16}H_{14}ON_2S$ $[M+H]^+$ 283.0905, found 283.0899. Purity: 97%.

4-(3,4-Dimethoxyphenyl)-N-phenylthiazol-2-amine (**1d**). Yield: 69%. m.p. 139-140 °C. ^{1}H NMR (300 MHz, DMSO-d_6) δ (ppm): 10.22 (s, 1H), 7.71 (d, J = 7.8 Hz, 2H), 7.50 (d, J = 1.6 Hz, 2H), 7.34 (t, J = 7.8 Hz, 2H), 7.21 (s, 1H), 7.02-6.93 (m, 2H), 3.83 (s, 3H), 3.78 (s, 3H). HRMS (ESI) m/z calcd for $C_{17}H_{17}O_2N_2S$ $[M+H]^+$ 313.1005, found 313.1013. Purity: 97%.

4-(4-Nitrophenyl)-N-phenylthiazol-2-amine (**1e**).[176] Yield: 93%. m.p. 208-209 °C. ^{1}H NMR (300 MHz, DMSO-d_6) δ (ppm): 10.38 (s, 1H), 8.30 (d, J = 8.8 Hz, 2H), 8.18 (d, J = 8.3 Hz, 2H), 7.72 (t, J = 3.7 Hz, 3H), 7.36 (t, J = 7.7 Hz, 2H), 6.99 (t, J = 7.3 Hz, 1H). Purity: 99%.

4-(3-Nitrophenyl)-N-phenylthiazol-2-amine (**1f**). Yield: 72%. m.p. 136-138 °C. ^{1}H NMR (300 MHz, DMSO-d_6) δ (ppm): 10.37 (s, 1H), 8.69 (s, 1H), 8.37 (d, J = 7.7 Hz, 1H), 8.17 (d, J = 8.4 Hz, 1H), 7.75-7.67 (m, 4H), 7.38 (t, J = 7.7 Hz, 2H), 6.99 (t, J = 7.4 Hz, 1H). HRMS (ESI) m/z calcd for $C_{15}H_{12}O_2N_3S$ $[M+H]^+$ 298.0644, found 298.0653. Purity: 100%.

4-(4-Chlorophenyl)-N-phenylthiazol-2-amine (**1g**).[176] Yield: 86%. m.p. 143-145 °C. ^{1}H NMR (300 MHz, DMSO-d_6) δ (ppm): 10.28 (s, 1H), 7.94 (d, J = 8.2 Hz, 2H), 7.72 (d, J = 7.8 Hz, 2H), 7.49 (d, J = 8.2 Hz, 2H), 7.39 (s, 1H), 7.34 (t, J = 7.6 Hz, 2H), 6.96 (t, J = 7.3, 1H). HRMS (ESI) m/z calcd for $C_{16}H_{15}ON_2S$ $[M+H]^+$ 283.0899, found 283.0905. Purity: 98%.

4-(4-Bromophenyl)-N-phenylthiazol-2-amine (**1h**).[176,218] Yield: 93%. m.p. 147-149 °C. ^{1}H NMR (300 MHz, DMSO-d_6) δ (ppm): 10.29 (s, 1H), 7.88 (d, J = 8.3 Hz, 2H), 7.72 (d, J = 8.3 Hz, 2H), 7.63 (t, J = 8.3 Hz, 2H), 7.40 (s, 1H), 7.34 (t, J = 7.5 Hz, 2H), 6.96 (t, J = 7.1 Hz, 1H). Purity: 98%.

4-(4-Fluorophenyl)-N-phenylthiazol-2-amine (**1i**).[176,218] Yield: 97%. m.p. 128-130 °C. ^{1}H NMR (300 MHz, DMSO-d_6) δ (ppm): 10.27 (s, 1H), 7.97-7.93 (m, 2H), 7.73 (d, J = 7.8 Hz, 2H), 7.36-7.22 (m, 5H), 6.96 (t, J = 7.3 Hz, 1H). Purity: 98%.

4-(3,4-Difluorophenyl)-N-phenylthiazol-2-amine (**1j**). Yield: 96%. m.p. 125-128 °C. ^{1}H NMR (300 MHz, DMSO-d_6) δ (ppm): 10.29 (s, 1H), 7.95-7.87 (m, 1H), 7.78-7.75 (m, 1H), 7.71 (d, J = 8.0 Hz, 2H), 7.53-7.43 (m, 2H), 7.34 (t, J = 7.4 Hz, 2H), 6.96 (t, J = 7.0 Hz, 1H). HRMS (ESI) m/z calcd for $C_{15}H_{11}N_2F_2S$ $[M+H]^+$ 289.0605, found 289.0611. Purity: 99%.

3.5.1.4 General Procedure for the synthesis of N,4-diphenylthiazol-2-amine derivatives (2a and 2b).[210]

3- or 4- (Nitrophenyl)-*N*-phenylthiazol-2-amines (2 g, 6.73 mmol) and Pd/C (10% weight, 0.7 g, 6.73 mmol) were dissolved in ethanol solution (100 mL) at 0 °C under gentle flow of argon in a 250 mL RBF. To this reaction mixture, hydrazine hydrate (2 mL, 67.3 mmol) was added dropwise. This resulting mixture was refluxed at 85 °C for 3 h and the reaction mixture was cooled to RT. Pd/C was filtered off by passing through cotton plug and celite column with ethanol wash (2 x 50 mL). The combined ethanol fractions were collected and concentrated *in vacuo* to obtain the crude product, which was purified using the silica gel column chromatography with EtOAc:Hex (1:1) as the eluent. Yield ranged from 78 – 83%.

4-(4-Aminophenyl)-N-phenylthiazol-2-amine (**2a**). Yield: 83%. m.p. 108-110 °C. ^{1}H NMR (300 MHz, DMSO-d_6) δ (ppm): 10.20 (s, 1H), 7.74 (d, J = 8.2 Hz, 2H), 7.33 (t, J =

7.8 Hz, 2H), 7.17 (s, 1H), 7.07 (t, J = 4.1 Hz, 3H), 6.95 (t, J = 7.2 Hz, 1H), 6.55-6.52 (m, 1H), 5.15 (s, 2H). HRMS (ESI) m/z calcd for $C_{15}H_{14}N_3S$ $[M+H]^+$ 268.0902, found 283.0901. Purity: 97%.

4-(3-Aminophenyl)-N-phenylthiazol-2-amine (**2b**).[219] Yield: 84%. m.p. 123-125 °C. ^{1}H NMR (300 MHz, DMSO-d_6) δ (ppm): 10.12 (s, 1H), 7.71 (d, J = 7.8 Hz, 2H), 7.59 (d, J = 7.3 Hz, 2H), 7.35 (t, J = 7.3 Hz, 2H), 6.93 (t, J = 8.6 Hz, 1H), 6.89 (s, 1H), 6.60 (d, J = 8.6 Hz, 2H), 5.22 (s, 2H). Purity: 100%.

3.5.2 Biological Screening

3.5.2.1 Amyloid-β (Aβ) Aggregation Assay

Thioflavin T (ThT) is a benzothiazole dye that was used to detect the formation of amyloid aggregates in solution. The excitation and emission properties of ThT changes when it binds to the β-sheet structures of Aβ40/Aβ42 oligomers and fibrils.[145] In this regard, the anti-Aβ aggregation activity of *N*,4-diphenylthiazol-2-amine based derivatives (**1a-j** and **2a**,**b**) was evaluated using ThT-based fluorescence assays. These assays were conducted in Costar, black, clear-bottomed 384-well plates with frequent shaking at 730 cpm under constant heating at 37 °C for 24 h. The excitation and emission of ThT were recorded at 440 and 490 nm, respectively. Readings were taken every 5 min using a BioTek Synergy H1 microplate reader. Test compounds were prepared in 215 mM phosphate buffer at pH 7.4. 0.5 mg of Aβ•HFIP samples (AnaSpec, CA, USA) was dissolved in 1% ammonium hydroxide solution for Aβ40 or 10% ammonium hydroxide for Aβ42, sonicated at RT for 5 min, and diluted to 50 μM in phosphate buffer. A 15 μM

ThT stock solution was prepared. To each ThT background well, 44 μL ThT, 35 μL phosphate buffer, and 1 μL DMSO were added. To the Aβ control wells, 44 μL ThT, 28 μL phosphate buffer, and 8 μL Aβ40/42 (5 μM final concentration) were added. To each test compound containing wells, 44 μL ThT, 20 μL phosphate buffer, 1 μL DMSO, and 8 μL test compound in various concentrations (1, 5, 10, and 25 μM), and 8 μL of Aβ were added. ThT interferences were taken before the addition of 8 μL of Aβ40 or Aβ42 stock solution (5 μM final concentration). Known Aβ40 and Aβ42 aggregation inhibitors MB and RES were also evaluated for comparison. Plates were sealed with a ThermoSeal film (Sigma Aldrich) before placing the plates in the reader. Data presented was an average of triplicate reading for two-three independent experiments.

3.5.2.2 Transmission Electron Microscopy (TEM)

The Aβ40 and Aβ42 aggregate morphology was examined by performing TEM experiment in the presence and absence of test compounds. TEM samples were prepared in Costar, round-bottomed 384-well plates with test compounds (25 μM). To the Aβ control wells, 44 μL ThT, 28 μL phosphate buffer, and 8 μL Aβ40/42 (5 μM final concentration) were added. To each test compound containing well, 44 μL ThT, 20 μL phosphate buffer, 1 μL DMSO, and 8 μL of test compound (25 μM), and 8 μL of Aβ40/42 were added. The plates were incubated on a BioTek Synergy H1 microplate reader at 37 °C and shaken at 730 cpm for 24 h.

TEM grids were prepared by adding 20 μL test compound over the formvar-coated copper grids (400 mesh) *via* the use of a Pasteur pipette, which were then air-dried for 3 h or longer before washing them with 20 μL of ultrapure water (UPW) to remove

any precipitated buffer salt. The sample grids were air-dried for 30 min. Once the grids were dry, they were stained with 20 μL of 2% phosphotungstic acid (PTA). The excess of PTA was removed by blotting with filter paper. The grids were allowed to dry overnight. Scanning of these grids was performed using a Philips CM10 TEM at 60 kV (Department of Biology, University of Waterloo), and micrographs were collected using a 14-megapixel AMT camera.

3.5.2.3 Computational Modeling Studies

Molecular docking studies of *N*,4-diphenylthiazol-2-amines derivatives with Aβ peptides were conducted *via* the computational chemistry Discovery Studio (DS) software – Structure-Based-Design (SBD), version 4.0 from BIOVA Inc. (San Diego, USA).[220] The *Small Molecules* module was used to build the *N*,4-diphenylthiazol-2-amine derivatives, which were in turn docked with Aβ40 and Aβ42 dimer models obtained from protein data bank (pdb id: 2LMN and 5KK3) using the CDOCKER algorithm in the *Receptor-Ligand Interactions* module in DS using CHARMm force field.[220,221] CDOCKER algorithm uses simulated annealing protocol to determine the best ligand binding modes. *N*,4-diphenylthiazol-2-amine derivatives were built in 3D using *Build Fragment* tool; energy minimization was applied for 1000 iterations using steepest descent and conjugate gradient minimizations, respectively. The ligands were minimized using the Smart Minimization protocol (200 steps, RMS gradient 0.1 kcal/mol), CHARMm force field and a distance depended dielectric constant. For the docking of *N*-diphenylthiazol-amine derivatives in Aβ40 and Aβ42 dimer models, the binding site was defined by a 20 Å radius sphere. Molecular docking was carried out by the CDOCKER algorithm, which includes 2000 heating steps, 700 K target temperature, 300 K cooling

temperature target with 5000 cooling steps. The docked poses obtained were ranked using the CDOCKER energy and CDOCKER interaction energy parameters (kcal/mol). The protein-ligand complexes were evaluated by examining various polar and nonpolar interactions, such as hydrogen bonding, electrostatic, *van der* Waal's, and hydrophobic interactions.

3.5.2.4 Cell Viability Assay

The HT22 hippocampal cells were plated at a density of 10,000 cells/100 μL in Nunclon Delta 96-well plates with complete growth media consisting of DMEM and Ham's F12 in a 1:1 ratio, supplemented with 10% fetal bovine serum (FBS) and 1% penicillin-streptomycin (10,000 U/mL) at 37 °C in 5% CO_2. The cells were incubated at 37 °C for 24 h. To each untreated well, 100 μL DMEM/F-12 was added. To the Aβ control wells, 85 μL DMEM/F-12, 10 μL PBS, and 5 μL Aβ40/42 (5 μM final concentration) were added. To each test compound containing wells, 85 μL DMEM/F-12, 10 μL filter-sterilized test compounds (**1a-j**, **2a-b**, and RES) in concentration of 10 μM in triplicates (n = 3), and 5 μL of Aβ40/42 were added. These cells were then incubated at 37 °C for 24 h. The MTT reagent solution[222] made of thiazolyl blue tetrazolium bromide powder (Sigma Aldrich) in PBS to 5 mg/mL and filter-sterilized through a 0.22 μm filter was added in 10% of the culture medium volume (DMEM/F-12, HEPES, no phenol red) to each well and the cells were cultured for an additional 2-3 h. After incubation, the resulting formazan crystals were solubilized with the solubilisation solution prepared from a mixture of IPA, 10% Triton X-100 and 1% HCl (12M). The absorbance was taken at 570 and 690 nm. All results were presented as a relative percent of (4,5-dimethylthiazol-2-yl)-2,5-diphenyl tetrazolium bromide (MTT) to untreated controls.

Known Aβ aggregation inhibitor resveratrol (RES) was used as a reference agent for comparison.

CHAPTER 4 Development of *N*-Methyl-*N*,4-Diphenylthiazol-2-amines

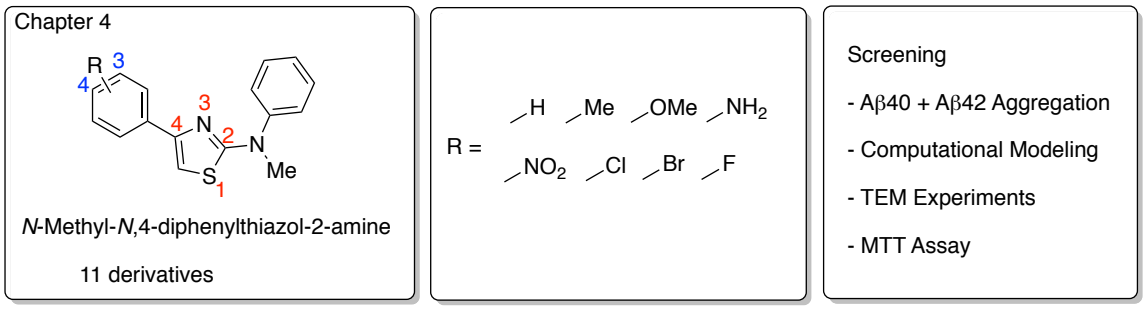

Figure 47. Banner for Chapter 4

4.1 Introduction

The investigation and subsequent confirmation of the anti-Aβ activity of *N*,4-diphenylthiazol-2-amine libraries in Chapter 3 encouraged us to conduct further SARs studies. This chapter describes our studies on the effect of *N*-alkylation of *N*,4-diphenylthiazol-2-amines, on Aβ40 and Aβ42 aggregation inhibition properties (Figure 47). A library of eleven *N*-methyl-*N*,4-diphenylthiazol-2-amines possessing EDG and EWGs at *para*- and or *meta*-position (R = H, Me, OMe, NH_2, NO_2, Cl, Br and F) were synthesized and evaluated to understand their inhibition properties toward Aβ40 and Aβ42 aggregation by conducting fluorescence aggregation kinetic studies, TEM experiments, computational modeling and cell culture studies in HT22 mouse hippocampal neuronal cells. The synthetic methodology, in vitro Aβ40/Aβ42 inhibition properties, and the results from the Aβ-induced cytotoxicity assay in HT22 neuronal cells, in the presence of *N*-methyl-*N*,4-diphenylthiazol-2-amine derivatives are discussed.

4.2 Hypothesis

For this series of *N*-methyl-*N*,4-diphenylthiazol-2-amine derivatives, we hypothesize that (i) the diphenyl rings undergo hydrophobic interactions with both the N- and C-terminal residues (Phe20 and Val36) in the Aβ40 dimer model, which can stabilize the dimer assembly and can reduce its aggregation propensity, and that loss of a hydrogen bond donor by *N*-methyl substitution, can reduce the anti-Aβ activity; (ii) in the Aβ42 dimer model, the *N*-methyl-*N*,4-diphenylthiazol-2-amine template interacts with the KLVFFA region at the N-terminal and the *N*-methyl substituent undergoes nonpolar contacts with nonpolar amino acids at the N-terminal; (iii) changing the electronic parameters at the thiazole C4-position by incorporating substituted phenyl rings can enhance their binding toward Aβ40/Aβ42 and their anti-Aβ aggregation properties.

4.3 Results and Discussion

4.3.1 Synthesis

The synthetic route for the *N*-methyl-*N*,4-diphenylthiazol-2-amine derivatives (**3-4**) is outlined in Scheme 2. Initially, the *N*,4-diphenylthiazol-2-amines were synthesized starting by coupling *N*-phenylthiourea with 2-bromo-3' or 4'-substituted-acetophenone (R = H, *p*-Me, *p*-OMe, 3,4-diOMe, *p*-Cl, *p*-Br, *p*-F, 3,4-diF, *m*-NO_2, and *p*-NO_2) in ethanol (Figure 48), as reported in Chapter 3 and as shown in Scheme 2. Then *N*-alkylation was carried out using MeI and NaH as base. The final yields of these target compounds (**3a-i**) ranged from 46-100% (Scheme 2). The amino-substituted *N*-methyl-*N*,4-diphenylthiazol-2-amines **4a** and **4b** (Scheme 2) were obtained via the Pd/C and hydrazine-driven reduction of the corresponding nitro derivatives as described in Chapter

3.[211] Their yields ranged from 78-83%. The purified *N*-methyl-*N*,4-diphenylthiazol-2-amine derivatives were characterized by ^{1}H and ^{13}C NMR, LCMS and HRMS analysis.

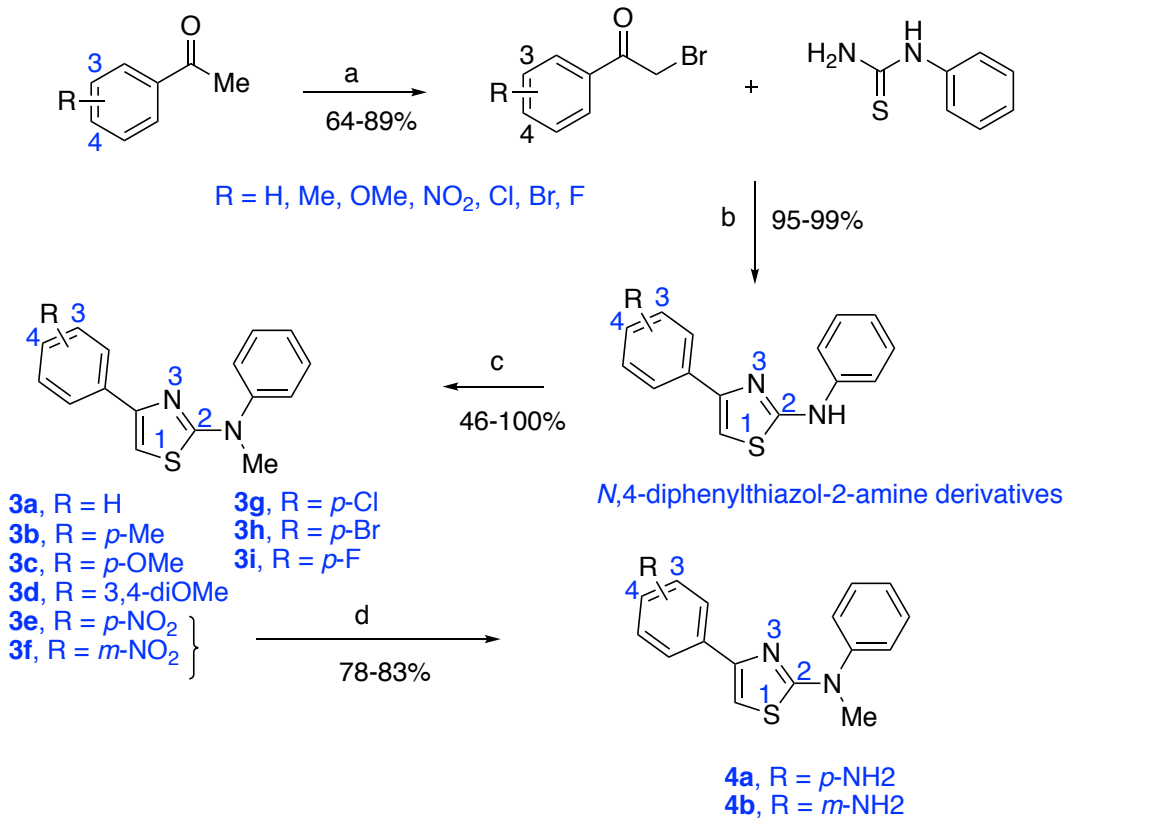

*Reagents and conditions: (a) $CuBr_2$, EtOAc, 70 °C, 15 h; (b) EtOH, 80 °C, 5 h; (c) MeI, NaH, THF, RT, 16 h; (d) Pd/C, hydrazine hydrate, EtOH, 85 °C, 3-5 h.

Scheme 2. Synthetic route toward the *N*-methyl-*N*,4-diphenylthiazol-2-amines **3-4**.

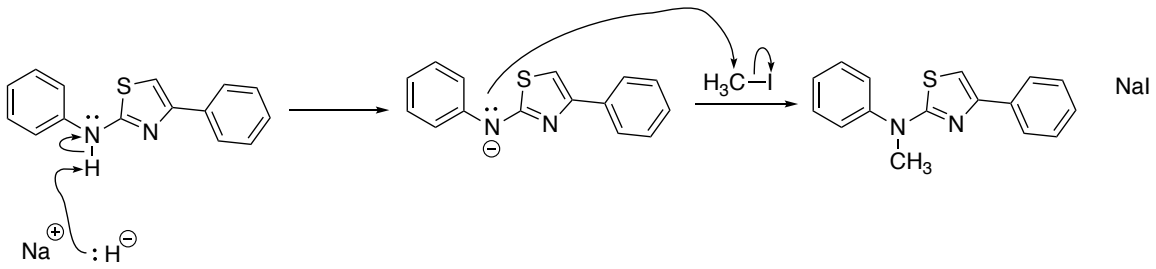

Figure 48. Mechanism of the *N*-alkylation of *N*,4-diphenylthiazol-2-amine derivatives **3a-i**.

4.3.2 Amyloid-β Aggregation Inhibition Studies

The inhibitory activity of *N*-methyl-*N*,4-diphenylthiazol-2-amine series toward Aβ40 aggregation was evaluated at different concentrations (1, 5, 10, and 25 μM). The results obtained show that their anti-aggregation properties against Aβ40 aggregation ranged from 11-46% inhibition at 25 μM (Table 5). Starting with the unsubstituted *N*-methyl-*N*,4-diphenylthiazol-2-amine (**3a**, R = H), it was observed to show moderate inhibitory activity ranging from 16-44% toward Aβ40 aggregation at various concentrations. Changing the substituents to EDGs such as *p*-Me and *p*-OMe (compounds **3b** and **3c**, Table 5) provided weak-to-moderate inhibition of Aβ40 aggregation (33% and 15% inhibition at 1 μM). Interestingly, these two compounds did not exhibit inhibition at other tested concentrations. Clearly *N*-methyl substitution led to weaker inhibition of Aβ40 aggregation compared to the corresponding *N*,4-diphenylthiazol-2-amine derivatives discussed in Chapter 3. Incorporating a 3,4-diOMe substituent in compound **3d** (R = 3,4-diOMe) did restore the anti-aggregation property with maximum inhibition of 32% at 25 μM. The presence of either a *para*- or *meta*-NH_2 substituent also provided weak-to-moderate inhibition (R = NH_2, compounds **4a** and **4b**, 14–38% inhibition). An addition of EWG group (R = NO_2) in compound **3e** and **3f** at the *para*- and *ortho*-positions, respectively, provided anti-Aβ40 activity at all the tested concentrations (11–46% inhibition, Table 5). Furthermore, addition halogens (R = Cl, Br, and F) at *para*-position in **3g**, **3h** and **3i** provided weak-to-moderate inhibition (11–41%, Table 5). Compared to the reference compounds MB and RES, none of the *N*-methyl derivatives were able to exhibit potent inhibition of Aβ40 aggregation. Nevertheless, all the tested compounds showed weak-to-moderate activity at 1 μM except for compound **3i**. The

activity order was: 3,4-diOMe > H ≈ Me ≈ NO_2 ≈ NH_2 > Br > Cl (at 1 μM). These studies clearly show that the presence of *N*-methyl substitution was detrimental to Aβ40 aggregation inhibition properties of *N*,4-diphenylthiazol-2-amines.

Table 5. Inhibition data for *N*-methyl-*N*,4-diphenylthiazol-2-amine derivatives **3a-i**, **4a-b**, and reference compounds toward Aβ40 aggregation, and their ClogP values.

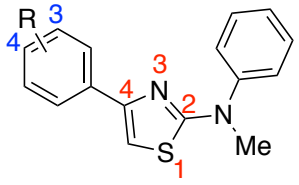

3-4

R = H, Me, OMe, NH_2, NO_2, Cl, Br, F

Compound	R-group	% Inhibition for Aβ40 [a]				ClogP [b]
		1 μM	5 μM	10 μM	25 μM	
3a	H	34	44	43	16	4.32
3b	*p*-Me	33	NA	NA	NA	4.82
3c	*p*-OMe	15	NA	NA	NA	4.24
3d	3,4-diOMe	44	41	NA	32	3.81
3e	*p*-NO_2	30	18	29	11	4.06
3f	*m*-NO_2	33	20	47	46	4.06
3g	*p*-Cl	19	NA	NA	NA	5.03
3h	*p*-Br	28	41	NA	NA	5.18
3i	*p*-F	NA	NA	NA	17	4.46
4a	*p*-NH_2	27	14	NA	14	3.09
4b	*m*-NH_2	32	17	16	38	3.09
MB	-	87	97	97	99	3.62
RES	-	81	94	95	98	2.83

[a]Percent aggregation inhibition values were average ± SD < 10% (n = 3) for three independent experiments. NA – Not Active. [b]ClogP values were determined using ChemDraw 19.1.

The results of anti-aggregation properties of *N*-methyl-*N*,4-diphenylthiazol-2-amines **3a-i** and **4a-b** toward Aβ42 aggregation are summarized in Table 6. These studies demonstrate that the presence of *N*-methyl substituent had a positive impact on Aβ42

inhibition properties with all the tested compounds exhibiting a concentration dependent inhibition of Aβ42 aggregation. These compounds exhibited excellent inhibition properties (49–96% inhibition at 25 μM), which were on par, or comparable to activity demonstrated by reference agents MB and RES (Table 6). The unsubstituted derivative **3a** exhibited excellent inhibition activity in preventing Aβ42 aggregation at all the tested concentration (82–95% inhibition). When adding the EDG (**3b**, R = Me) to the C4-phenyl ring, the inhibitory activity toward Aβ42 aggregation declined by about ~20% inhibition. However, the incorporation of EDGs such as OMe (compound **3c**) at either *para*- (**3d**, R = *p*-OMe) or 3,4-positions (**3d**, R = 3,4-diOMe) provided superior inhibitory activity against Aβ42 aggregation ranging from 93–96% inhibition. Addition of either a *para*- or *meta*-NH_2 substituent provided concentration dependent inhibition of Aβ42 aggregation with maximum inhibition seen at 25 μM (97% inhibition). The presence of EWGs such a NO_2 at either *para* or *meta*-position led to a reduction in Aβ42 inhibition properties compared compound **3a** (**3e** and **3f**, 73–74% inhibition, Table 6). Incorporating halogens R = Cl, Br and F at the *para*-position led to reduced inhibition activity in general compared to the unsubstituted (**3a**) and NH_2-substituted compounds (**4a** and **4b**, Table 6). In summary, these studies show that the presence of *N*-methyl substituents provided excellent inhibition of Aβ42 aggregation and the activity was of the order: NH_2 > 3,4-diOMe > H > OMe ≈ Cl > Me > NO_2 at 25 μM.

Table 6. Inhibition data for *N*-methyl-*N*,4-diphenylthiazol-2-amine derivatives **3a-i**, **4a-b**, and reference compounds toward Aβ42 aggregation, and their ClogP values.

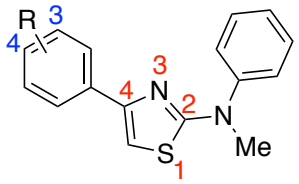

3-4

R = H, Me, OMe, NH_2, NO_2, Cl, Br, F

Compound	R-group	% Inhibition for Aβ42 [a]				ClogP [b]
		1 μM	5 μM	10 μM	25 μM	
3a	H	83	88	82	95	4.32
3b	*p*-Me	39	67	68	78	4.82
3c	*p*-OMe	32	58	84	93	4.24
3d	3,4-diOMe	78	94	94	96	3.81
3e	*p*-NO_2	38	42	52	73	4.06
3f	*m*-NO_2	36	66	70	74	4.06
3g	*p*-Cl	39	51	44	93	5.03
3h	*p*-Br	NA	NA	28	49	5.18
3i	*p*-F	NA	NA	NA	56	4.46
4a	*p*-NH_2	60	40	59	97	3.09
4b	*m*-NH_2	44	49	80	97	3.09
MB	-	87	97	97	99	3.62
RES	-	81	94	95	98	2.83

[a]Percent aggregation inhibition values were average ± SD < 10% (n = 3) for three independent experiments. NA – Not Active. [b]ClogP values were determined using ChemDraw 19.1.

The Aβ42 aggregation kinetics data in the presence and absence of compounds **4a** and **4b** at various concentrations (1–25 μM) is shown as representative examples (**Figure 49**). The kinetic plot for Aβ42 alone shows the lag phase lasting close to 1.3 h followed by rapid growth phase lasting for nearly 4 h, characterized by increase in ThT fluorescence intensity, followed by a saturation phase in a time-dependent fashion during the 24 h incubation period (pink curves, **Figure 49**). At a low concentration of 1 μM,

both **4a** and **4b** were able to reduce ThT fluorescence intensity, indicating the inhibition of Aβ42 aggregation. At a higher concentration (5, 10 and 25 μM) there was gradual decline in the fluorescence intensity with maximum inhibition observed 25 μM (Panels A and B, **Figure 49**). The presence of either **4a** or **4b** at higher concentrations led to an increase in lag phase period and also caused significant inhibition of the growth phase in the Aβ42 fibrillogenesis pathway. These results show that *N*-methyl-*N*,4-diphenylthiazol-2-amine derivatives **4a** and **4b** can reduce Aβ42 fibrillogenesis.

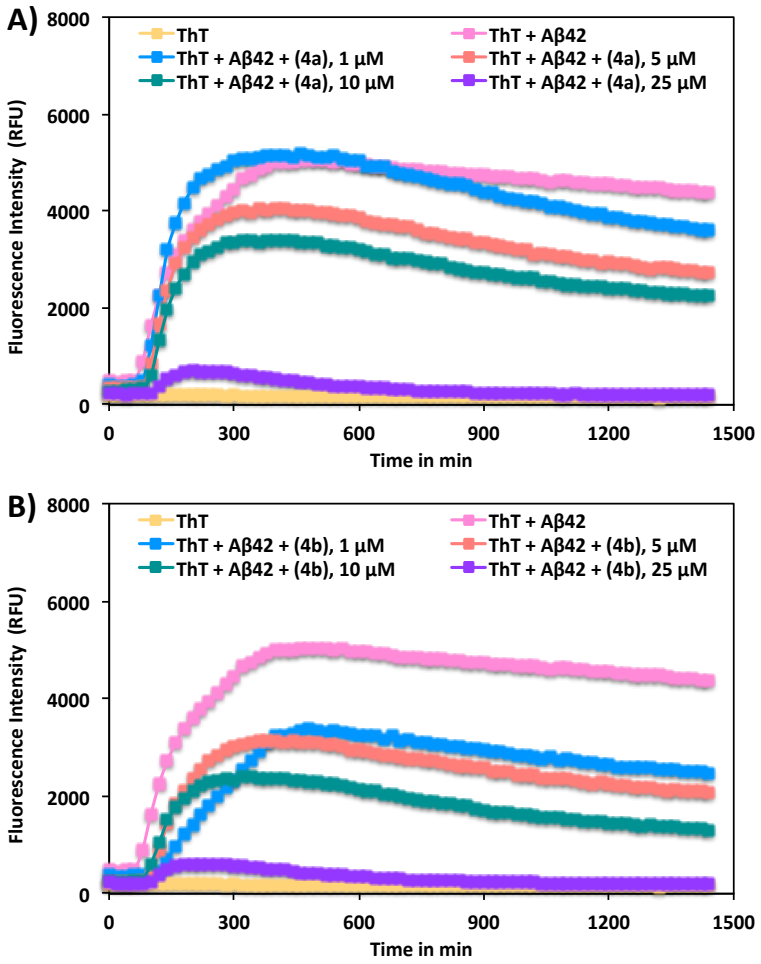

Figure 49. Panels A and B show ThT-monitored 24 h aggregation kinetics of Aβ42 (5 μM) in the presence of 1, 5, 10, and 25 μM of *N*-methyl-*N*,4-diphenylthiazol-2-amines (**4a** and **4b**) at pH 7.4, 37 °C in phosphate buffer. Aggregation kinetics were monitored by ThT-fluorescence spectroscopy (excitation = 440 nm, emission = 490 nm). Results are average ± SD of three independent experiments (n = 3).

4.3.2.1 Correlating the ClogP Values, HBDs, and HBAs with Anti-Aβ Aggregation Properties

The anti-aggregation activity data of *N*-methyl-*N*,4-diphenylthiazol-2-amines **3a**–**h**, **4a** and **4b** (at 25 μM each), toward Aβ40 obtained after conducting the in vitro ThT based fluorescence assay, was correlated with the ClogP values, number of hydrogen bond donors (HBD), and hydrogen bond acceptors (HBA) present in the phenyl ring at the C4-position of the thiazole-2-amine (Figure 50).

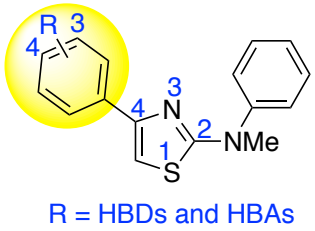

Figure 50. Chemical structure of *N*-methyl-*N*,4-diphenylthiazol-2-amines described in Chapter 4 highlighting the C4-position of the thiazol-2-amine that was modified by SAR. HBD – Hydrogen Bond Donors, HBA – Hydrogen Bond Acceptors.

The anti-aggregation activity data obtained at 1 μM test compound concentration was used for this comparison, as results obtained at other concentrations (5, 10 and 25 μM) showed that either compounds were not active or were not suitable for comparison due to similar activity profile. The *N*-methyl series of compounds were more lipophilic than the corresponding demethylated derivatives reported in Chapter 3 with their ClogP values ranging from 3.09 to 5.18 (Figure 51). The best compound in this series **3d** (44% inhibition at 1 μM) had a ClogP value of 3.81 (Figure 51). In addition, the presence of two HBAs in **3d** (3,4-diOMe-phenyl) was able to enhance its anti-aggregation property whereas presence of HBDs in compounds **3e**, **3f** (NO_2-phenyl) and **4a**, **4b** (NH_2-phenyl) led to weaker inhibition (27–33% inhibition, Figure 51).

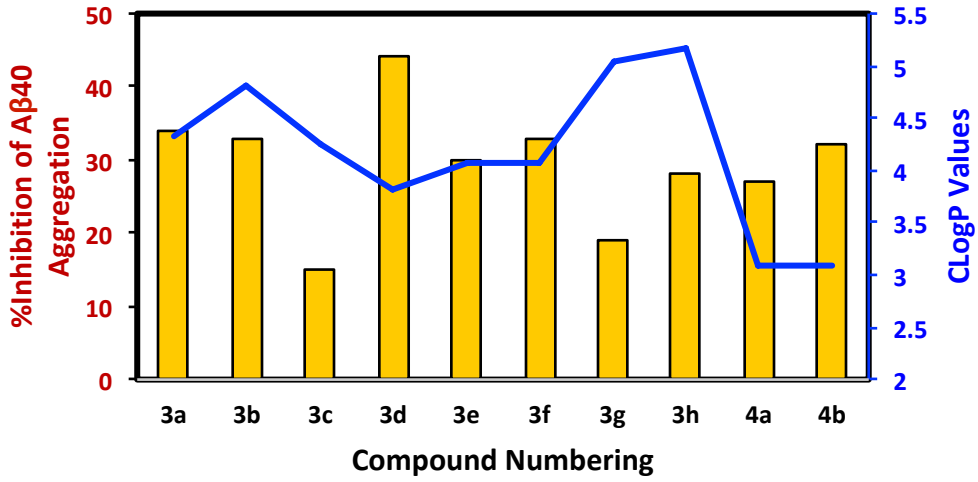

Figure 51. Correlation of Aβ40 aggregation inhibition properties of **3a–h**, **4a** and **4b** at 1 μM, with ClogP values. Blue line represents ClogP values.

A similar correlation plot was used to understand the role of ClogP values, HBDs and HBAs attached to the phenyl ring at the C4-position of the thiazole-2-amine toward Aβ42 aggregation (Figure 52). This shows that the unsubstituted *N*-methyl-*N*,4-diphenylthiazol-2-amine compound **3a** and the 3,4-diOMe-phenyl substituted compound **3d** with ClogP values of 4.32 and 3.81 respectively exhibited excellent inhibition (83% and 78% inhibition respectively, Figure 52). It appears that the presence of two HBAs was favouring superior inhibition of Aβ42 aggregation whereas the presence of single HBAs was not favourable (compound **3c**, *p*-OMe-phenyl, 32% inhibition). Among the *N*-methyl derivatives possessing HBDs, only did compound **4a** (*p*-NH_2-phenyl, ClogP = 3.09) exhibit good inhibition (60% inhibition at 1 μM). These studies suggest that the presence of two HBAs groups at the phenyl ring (compound **3d**) was directly correlating with enhanced activity in preventing both Aβ40 and Aβ42 aggregation whereas no major correlation was observed with changes in ClogP values by changing the substituents at the phenyl ring.

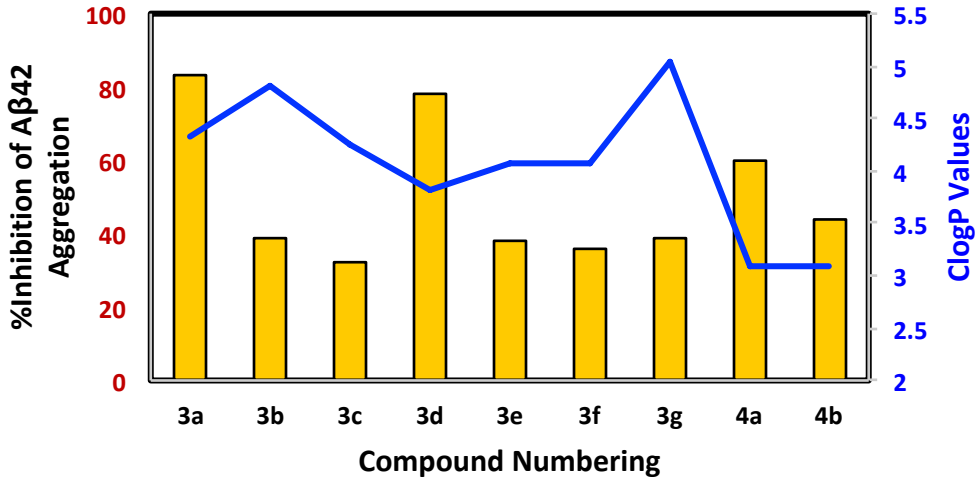

Figure 52. Correlation of Aβ42 aggregation inhibition properties of **3a–g**, **4a** and **4b** at 1 μM, with ClogP values. Blue line represents ClogP values.

4.3.3 Computational Modeling Studies

The binding interactions of most potent *N*-methyl-*N*,4-diphenylthiazol-2-amine derivatives was investigated by conducting molecular docking studies using the solved structures of Aβ40 and Aβ42 peptides.[212,213] Docking studies were carried out using the dimer assemblies of both Aβ40 and Aβ42 peptides as they represent the early forms of Aβ in solution. In the *N*-methyl-*N*,4-diphenylthiazol-2-amine series, compound **3f** (4-(3-nitrophenyl)-*N*-methyl-*N*-phenylthiazol-2-amine) was identified as the most potent inhibitor of Aβ40 aggregation in the ThT-based fluorescence assay (46% inhibition at 25 μM). Figure 53 Panel A, shows the predicted binding mode of **3f** in the Aβ40-dimer model. This compound was interacting at the N-terminal in the KLVFFA region, with the 3-nitrophenyl undergoing π-cation interactions with Phe19 and the C4 phenyl ring interacting at the C-terminal with Ile32. The *N*-Me substituent was in contact with Val36 side chain at the C-terminal and the C2 phenyl ring was closer to Val18 and Phe19 in the

KLVFFA region. Interestingly, the weaker anti-aggregation properties exhibited by this compound (46% inhibition of Aβ40 aggregation at 25 μM), compared to the rest of *N*,4-diphenylthiazol-2-amine series, could be attributed to the lack of interaction of the central thiazole in the Aβ40-dimer model.

In the *N*-methyl-*N*,4-diphenylthiazol-2-amine series, compound **4b** (4-(3-aminophenyl)-*N*-methyl-*N*-phenylthiazol-2-amine) was identified as the most potent inhibitor of Aβ42 aggregation in the ThT-based fluorescence assay (97% inhibition at 25 μM). Figure 53 Panel B, shows the predicted binding mode of **4b** in the Aβ42-dimer model. This compound underwent a number of polar and nonpolar interactions in the KLVFFA region, which supports its excellent inhibition activity (Panel B Figure 53). The 3-aminophenyl formed hydrogen-bonding interactions with His13 (distance = 2.2 Å) whereas the aromatic ring underwent π-cation interaction with side chain of Lys16 (distance ~2.5 Å). The central thiazole was in contact with Val18 side chain (distance < 5 Å) whereas the *N*-Me underwent hydrophobic interactions with Ala21 (distance < 5 Å). The unsubstituted phenyl ring formed π-cation interaction with side chain of Lys16 (distance ~2.5 Å). All these suggest that compound **4b** is able to exhibit effective binding in the Aβ42 dimer assembly, which can reduce or prevent Aβ42 aggregation.

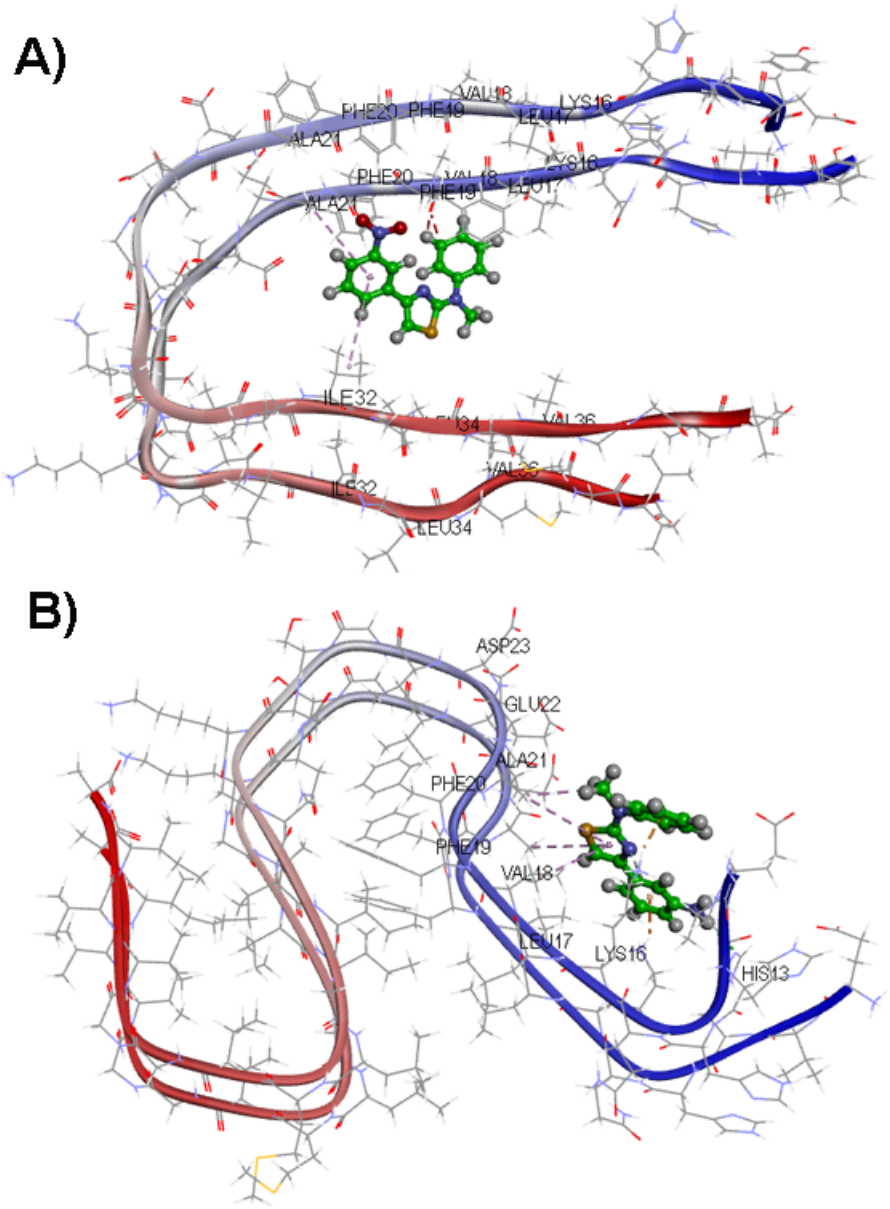

Figure 53. Panel A: Predicted binding mode of **3f** (ball and stick cartoon) in the Aβ40-dimer model (ribbon diagram, pdb id: 2LMN, CDOCKER energy = –6.24 kcal/mol; CDOCKER interaction Energy = –21.09 kcal/mol). Panel B: Predicted binding mode of **4b** (ball and stick cartoon) in the Aβ42-dimer model (ribbon diagram, pdb id: 5KK3, CDOCKER energy = –14.20 kcal/mol; CDOCKER interaction energy = –24.44 kcal/mol).

4.3.4 Transmission Electron Microscopy (TEM) Studies

The transmission electron microscopy (TEM) experiments for representative *N*-methyl-*N*,4-diphenylthiazol-2-amine derivatives (**3f** and **4b**) were carried out to validate and confirm the anti-aggregation properties. The morphology of both Aβ40 and Aβ42 aggregates were studied. Panel A (top and bottom in Figure 54) shows dense Aβ40 and Aβ42 aggregates, respectively. In the presence of 5 μM of either **3f** or **4b**, there was almost complete inhibition of Aβ40/42 aggregates (Figure 54). These results further confirm the Aβ40 and Aβ42 aggregation inhibition properties of *N*-methyl-*N*,4-diphenylthiazol-2-amine derivatives.

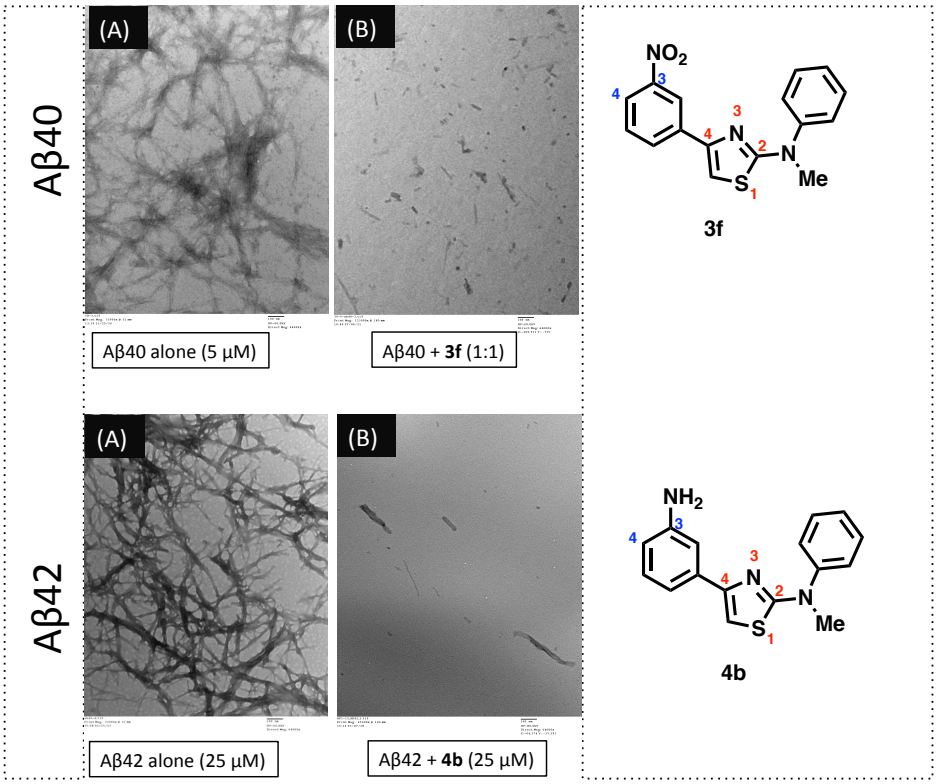

Figure 54. TEM images of Aβ40 and Aβ42 aggregation. Top: Panel A: Aβ40 control (5 μM). Panel B: Aβ40 + **3f** (5 μM). Bottom: Panel A: Aβ42 control (5 μM). Panel B: Aβ42 + **4b** (5 μM). Scale bars represent 100 nm.

4.3.5 Cell Viability Assay

The cell viability in the presence of the *N*-methyl-*N*,4-diphenylthiazol-2-amine derivatives **3a-i** and **4a-b** (10 μM) was evaluated in HT22 cells to investigate their ability to reduce cytotoxicity induced by Aβ40 (**Figure 55**). In the presence of Aβ40 (5 μM), the cell viability was reduced to 70% compared to untreated control. Interestingly all the tested *N*-methyl-*N*,4-diphenylthiazol-2-amine derivatives were able to reduce cytotoxicity compared to Aβ40-treated group with cell viability ranging from 69–97% (**Figure 55**), suggesting their neuroprotective effect against Aβ40-induced cytotoxicity. In this series, compounds **3c** and **3h** exhibited excellent inhibition of Aβ40-induced cytotoxicity (cell viability range: 90-95%, Figure 55) and better neuroprotection than the reference agent RES (63% cell viability, Figure 55).

Figure 56 shows the cell viability data in HT22 hippocampal neuronal cells in the presence of Aβ42 (5 μM) and *N*-methyl-*N*,4-diphenylthiazol-2-amine derivatives (10 μM). Treating HT22 cells with Aβ42 alone led to cytotoxicity (cell viability = 50%) compared to untreated group (cell viability = 95%). In the presence of *N*-methyl-*N*,4-diphenylthiazol-2-amine derivatives **3a-i**, **4a** and **4b**, the cell viability ranged from 45-95% (Figure 56). A number of compounds in this series (**3a**, **3d**–**g**, **4a** and **4b**) exhibited statistically significant reduction in Aβ42-induced cytotoxicity indicating their ability to translate their demonstrated in vitro anti-Aβ42 inhibition activity in ThT based assays to cell culture assays. In this series, the *para*-substituted compounds containing *p*-OMe (**3c**) or *p*-Br (**3h**) exhibited excellent neuroprotection activity (95% cell viability) against Aβ42-induced cytotoxicity (Figure 56). Several *N*-methyl derivatives demonstrated

superior neuroprotective activity against Aβ42-induced cytotoxicity compared to the reference agent RES (72% cell viability).

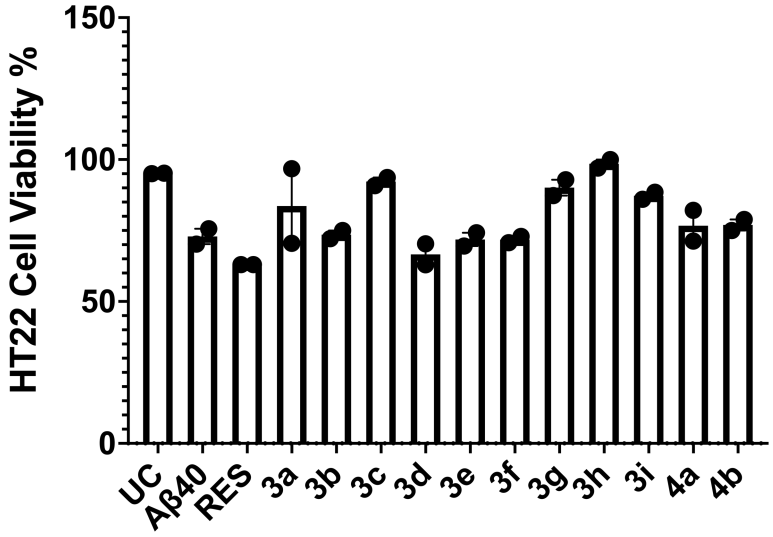

Figure 55. Percentage viability of the *N*-methyl-*N*,4-diphenylthiazol-2-amine derivatives **3c**, **3h**, and RES (10 μM) in HT22 cells was assessed by MTT assay toward Aβ40 after 24 h incubation at 37 °C. The results were given as average of two independent experiments (n = 3). UC = untreated cells, RES = resveratrol.

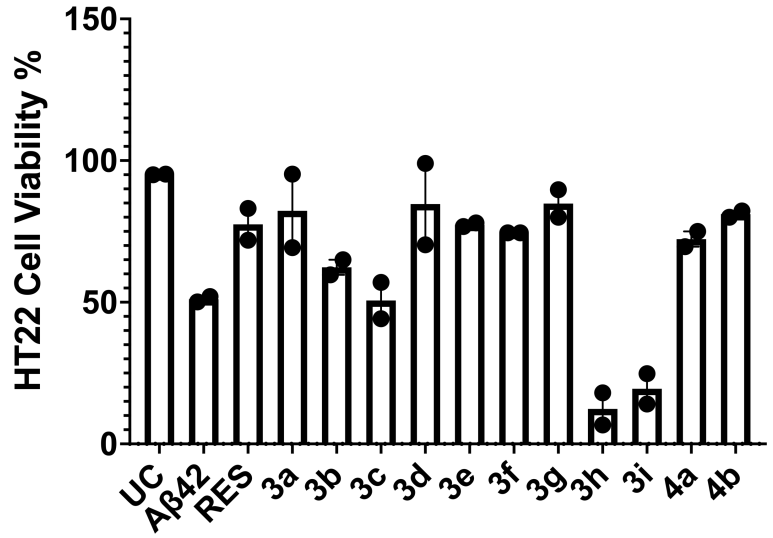

Figure 56. Percentage viability of the *N*-methyl-*N*,4-diphenylthiazol-2-amine derivatives **3a**, **3d**, **3g**, and RES (10 μM) in HT22 cells was assessed by MTT assay toward Aβ42 after 24 h incubation at 37 °C. The results were given as average of two independent experiments (n = 3). UC = untreated cells, RES = resveratrol.

4.4 Summary

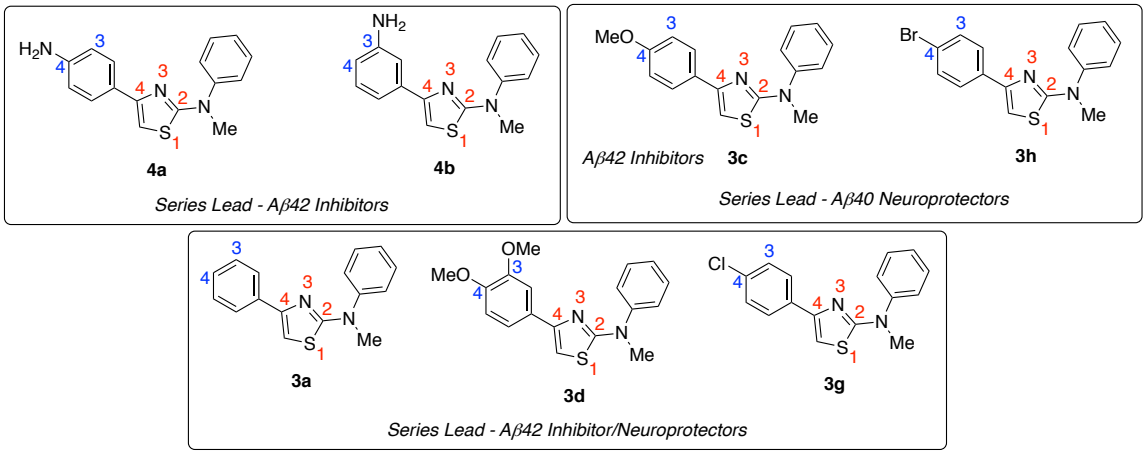

Figure 57. Cumulative chapter summary of *N*-methyl-*N*,4-diphenylthiazol-2-amines (**3-4**).

In this chapter, a total of 11 *N*-methyl-*N*,4-diphenylthiazol-2-amine derivatives were synthesized by alkylating the corresponding *N*,4-diphenylthiazol-2-amines and the compounds were characterized by analytical methods. Their anti-Aβ activity against both Aβ40 and Aβ42 aggregation was evaluated by ThT-based fluorescence assays, TEM studies, computational modeling and neuroprotective assay in Aβ40 or Aβ42-induced cytotoxicity assay in HT22 hippocampal derived-cells. These studies identified compound **3f** (4-(3-nitrophenyl)-*N*-phenylthiazol-2-amine) as the best inhibitor of Aβ40 aggregation based on the ThT fluorescence assay (46% inhibition at 25 μM); whereas, compounds **3a** (*N*-methyl-*N*-phenylthiazol-2-amine), **3c** (4-(3-methoxyphenyl)-*N*-methyl-*N*-phenylthiazol-2-amine), **3d** (4-(3,4-dimethoxyphenyl)-*N*-methyl-*N*-phenylthiazol-2-amine), **3g** (4-(4-chlorophenyl)-*N*-methyl-*N*-phenylthiazol-2-amine), **4a** (4-(4-aminophenyl)-*N*-methyl-*N*-phenylthiazol-2-amine), and **4b** (4-(3-aminophenyl)-*N*-methyl-*N*-phenylthiazol-2-amine) exhibit superior inhibition of Aβ42 aggregation (93–

97% inhibition at 25 μM). In the HT22 cytotoxicity assay, compounds **3c** (4-(4-methoxyphenyl)-*N*-methyl-*N*-phenylthiazol-2-amine) and **3h** (4-(4-bromophenyl)-*N*-methyl-*N*-phenylthiazol-2-amine) exhibited superior neuroprotection against Aβ40-induced cytotoxicity whereas compound **3a** (*N*-methyl-*N*-phenylthiazol-2-amine), **3d** (4-(3,4-dimethoxyphenyl)-*N*-methyl-*N*-phenylthiazol-2-amine), and **3g** (4-(4-chlorophenyl)-*N*-methyl-*N*-phenylthiazol-2-amine) exhibited superior neuroprotection against Aβ42-induced cytotoxicity. In general, the presence of *N*-methyl substituent led to a decrease in Aβ40 aggregation inhibition properties, which can be attributed to the loss of polar interaction of NH with Val18 backbone in the Aβ40-dimer model. In contrast the presence or absence of *N*-methyl substituent was not a major factor in exhibiting Aβ42 aggregation inhibition properties. Interestingly, in the cytotoxicity assay, the *N*-methyl-*N*,4-diphenylthiazole-2-amine derivatives were able to demonstrate neuroprotection against both Aβ40 and Aβ42-induced cytotoxicity, and were better than the corresponding *N*,4-diphenylthiazole-2-amine derivatives were effective only against Aβ42-induced cytotoxicity, suggesting that the increased lipophilicity of *N*-methyl-*N*,4-diphenylthiazole-2-amines (ClogP range = 3.09–5.18) could have contributed to better cell permeability and activity against Aβ40-induced cytotoxicity and be one of the reasons for their increased their cell permeability compared to the corresponding *N*,4-diphenylthiazole-2-amine derivatives (ClogP range = 2.64–4.73). In summary, *N*-methyl-*N*,4-diphenylthiazole-2-amines represent a novel class of compounds which are capable of inhibiting Aβ40 and Aβ42 aggregation.

4.5 Experimental

4.5.1 Chemistry

4.5.1.1 Materials and Methods

General information. All the reagents and solvents were purchased from various vendors (Sigma-Aldrich, Oakwood Chemical, Matrix Scientific, TCI Chemicals, AAblocks, and Ark Pharm Inc.) with a minimum purity of 95% and were used without further purification. Melting points (mp) were determined using a Fisher-Johns apparatus and are uncorrected. Compound purification was carried out using Merck 230-400 mesh silica gel 60. All derivatives showed single spot on thin-layer chromatography (TLC) performed on Merck 60 F254 silica gel plates (0.2 mm) using variety of solvent systems and TLC spots were visualized with the handheld UV lamp 254/365 nm. ^{1}H NMR and ^{13}C NMR spectra were analyzed using a Bruker Avance 300 MHz series spectrometer in deuterated solvents. Data was analyzed using the Bruker TOPSPIN 3.6.1 software. Coupling constant (*J* values) were recorded in hertz (Hz) and the following abbreviations were used for multiplicity of NMR signals: s = singlet, d = doublet, t = triplet, m = multiplet, br = broad. Compound purity and low resolution mass (LRMS) were evaluated using an Agilent 6100 series single quad LCMS equipped with an Agilent 1.8 μM Zorbax Eclipse Plus C18 (2.1 x 50 mm) running 30:70 Water:ACN with 0.1% FA at a flow rate of 0.5 mL/min. All the final compounds were > 95% pure as determined by calculating the peak area by LCMS (UV detector, 254 nm). High-resolution mass spectrometry data were obtained by carrying out a positive ion electrospray (ESI) experiments on using a Thermo Scientific Q-Exactive hybrid mass spectrometer, Department of Chemistry, University of Waterloo. Accurate mass determinations were performed at a mass

resolution of 70,000 (@m/z200) with lock mass correction. All samples were injected at 10 mL/min in a 1:1 MeOH/H_2O + 0.1% formic acid.

4.5.1.2 General Procedure for the synthesis of N-methyl-N,4-diphenylthiazol-2-amine derivatives (3a-i).

Compound **1e** or **1f** and NaH (0.097 g, 4.040 mmol) were added to the RBF, and stirred at 0 °C for 10 min. To this mixture, excess MeI (5.73 g, 40.40 mmol) was added and stirred at RT for 23 h. The solution was diluted with 20 mL DCM, washed three times with 20 mL brine solution; the aqueous layers were extracted with EtOAc (2 x 20 mL). The combined organic layers were dried over $MgSO_4$, filtered and concentrated *in vacuo* to obtain the crude product, which was purified using the silica gel column chromatography with Hex:EtOAc (7:1) as the eluent. Yield ranged from 46 – 100%. The analytical data is given below:

N-Methyl-N-diphenylthiazol-2-amine (**3a**)[218] Yield: 85%. m.p. 76-78 °C. ^{1}H NMR (300 MHz, DMSO-d_6) δ (ppm): 7.88 (d, J = 8.2 Hz, 2H), 7.54-7.26 (m, 8H), 7.19 (s, 1H), 3.54 (s, 3H). HRMS (ESI) m/z calcd for $C_{16}H_{15}N_2S$ $[M+H]^+$ 267.0950, found 298.0953. Purity: 100%.

N-Methyl-N-phenyl-4(p-tolyl)thiazol-2-amine (**3b**) Yield: 56%. m.p. 78-80 °C. ^{1}H NMR (300 MHz, DMSO-d_6) δ (ppm): 7.77 (d, J = 8.0 Hz, 2H), 7.53-7.44 (m, 4H), 7.28 (t, J = 7.1 Hz, 1H), 7.20 (d, J = 8.0 Hz, 2H), 7.11 (s, 1H), 3.53 (s, 3H), 2.31 (s, 3H). HRMS (ESI) m/z calcd for $C_{17}H_{17}N_2$ $[M+H]^+$ 281.1107, found 281.1117. Purity: 97%.

4-(4-Methoxyphenyl)-N-methyl-N-phenylthiazol-2-amine (**3c**) Yield: 46%. m.p. 87-89 °C. ^{1}H NMR (300 MHz, DMSO-d_6) δ (ppm): 7.81 (d, J = 8.4 Hz, 2H), 7.53-7.43 (m, 4H), 7.27 (t, J = 7.1 Hz, 1H), 7.01 (s, 1H), 6.96 (d, 2H), 3.77 (s, 3H), 3.52 (s, 3H). HRMS (ESI) m/z calcd for $C_{17}H_{17}ON_2S$ $[M+H]^+$ 297.1056, found 297.1056. Purity: 98%.

4-(3,4-Dimethoxyphenyl)-N-methyl-N-phenylthiazol-2-amine (**3d**) Yield: 84%. m.p. 112-114 °C. ^{1}H NMR (300 MHz, DMSO-d_6) δ (ppm): 7.53-7.42 (m, 6H) 7.28 (t, J = 8.4 Hz, 1H), 7.08 (s, 1H), 6.98 (d, J = 6.6 Hz, 1H), 3.80 (s, 3H), 3.77 (s, 3H), 3.53 (s, 3H). HRMS (ESI) m/z calcd for $C_{18}H_{19}O_2N_2S$ $[M+H]^+$ 327.1161, found 327.1155. Purity: 98%.

N-Methyl-4-(4-nitrophenyl)-N-phenylthiazol-2-amine (**3e**) Yield: 95%. m.p. 191-194 °C. ^{1}H NMR (300 MHz, DMSO-d_6) δ (ppm): 8.27 (d, J = 8.8 Hz, 2H) 8.13 (d, J = 8.1 Hz, 1H), 7.58 (s, 1H), 7.54-7.46 (m, 4H), 7.32 (t, J = 6.8 Hz, 1H), 3.55 (s, 3H). HRMS (ESI) m/z calcd for $C_{16}H_{14}O_2N_3S$ $[M+H]^+$ 312.0801, found 312.0805. Purity: 96%.

N-Methyl-4-(3-nitrophenyl)-N-phenylthiazol-2-amine (**3f**) Yield: 78%. m.p. 122-124 °C. ^{1}H NMR (300 MHz, DMSO-d_6) δ (ppm): 8.65 (s, 1H), 8.32 (d, J = 7.9 Hz, 1H), 8.15 (d, J = 8.6 Hz, 1H), 7.69 (t, J = 8.1 Hz, 1H), 7.55-7.46 (m, 5H), 7.32 (t, J = 7.0 Hz, 1H), 3.56 (s, 3H). HRMS (ESI) m/z calcd for $C_{16}H_{14}O_2N_3S$ $[M+H]^+$ 312.0801, found 312.0806. Purity: 98%.

4-(4-Chlorophenyl)-N-methyl-N-phenylthiazol-2-amine (**3g**) Yield: 100%. m.p. 107-110 °C. ^{1}H NMR (300 MHz, DMSO-d_6) δ (ppm): 7.90 (d, J = 8.3 Hz, 2H), 7.53-7.44 (m, 6H), 7.29 (m, 2H), 3.53 (s, 3H). HRMS (ESI) m/z calcd for $C_{16}H_{14}N_2ClS$ $[M+H]^+$ 301.0560, found 301.0569. Purity: 95%.

4-(4-Bromophenyl)-N-methyl-N-phenylthiazol-2-amine (**3h**) Yield: 100%. m.p. 113-115 °C. ^{1}H NMR (300 MHz, DMSO-d_6) δ (ppm): 7.83 (d, J = 8.3 Hz, 2H), 7.59 (d, J = 8.3 Hz, 2H), 7.53-7.44 (m, 4H), 7.29 (m, 2H), 3.53 (s, 3H). HRMS (ESI) m/z calcd for $C_{16}H_{14}O_2N_4BrS_2$ $[M+H]^+$ 345.0055, found 345.0049. Purity: 96%.

4-(4-Fluorophenyl)-N-methyl-N-phenylthiazol-2-amine (**3i**) Yield: 99%. m.p. 70-72 °C. ^{1}H NMR (300 MHz, DMSO-d_6) δ (ppm): 7.93-7.88 (m, 2H), 7.52-7.43 (m, 4H), 7.30-7.17 (m, 4H), 3.52 (s, 3H). HRMS (ESI) m/z calcd for $C_{16}H_{14}N_2FS$ $[M+H]^+$ 285.0856, found 285.0861. Purity: 95%.

4.5.1.3 General procedure for the synthesis of N-methyl-N,4-diphenylthiazol-2-amine derivatives (4a-b).

Compounds *N*-methyl-*N*,4-diphenylthiazol-2-amines **3e** or **3f** (1 g, 3.21 mmol) and Pd/C (10% weight, 0.34 g, 3.21 mmol) were dissolved in ethanol solution (100 mL) at 0 °C under gentle flow of argon in a 250 mL RBF. To this reaction mixture, hydrazine hydrate (1.0 mL, 32.1 mmol) was added dropwise. This resulting mixture refluxed with stirring at 85 °C for 3 h to the reaction was cooled to RT, Pd/C was filtered off by passing through cotton plug and celite column with ethanol wash (2 x 50 mL). The combined ethanol fractions were collected and concentrated *in vacuo* to obtain the crude product,

which was purified using the silica gel column chromatography with EtOAc:Hex (1:1) as the eluent. Yield ranged from 78 – 83%.

4-(4-Aminophenyl)-N-methyl-N-phenylthiazol-2-amine (**4a**) Yield: 83%. m.p. 91-94 °C. ^{1}H NMR (300 MHz, DMSO-d_6) δ (ppm): 7.52-7.43 (m, 4H), 7.27 (t, J = 6.8 Hz, 1H), 7.11 (s, 1H), 7.05-7.01 (m, 2H), 6.97 (s, 1H), 6.51 (s, 1H), 5.16 (s, 2H), 3.52 (1s, 3H). HRMS (ESI) m/z calcd for $C_{16}H_{16}N_3S$ $[M+H]^+$ 282.1059, found 282.1067. Purity: 99%.

4-(3-Aminophenyl)-N-methyl-N-phenylthiazol-2-amine (**4b**) Yield: 78%. m.p. 89-91 °C. ^{1}H NMR (300 MHz, DMSO-d_6) δ (ppm): 7.55-7.42 (m, 6H), 7.25 (t, J = 7.0 Hz, 1H), 6.77 (s, 1H), 6.57 (d, J = 7.8 Hz, 2H), 5.22 (s, 2H), 3.51 (s, 3H). HRMS (ESI) m/z calcd for $C_{16}H_{16}N_3S$ $[M+H]^+$ 282.1059, found 282.1061. Purity: 95%.

4.5.2 Biological Screening

4.5.2.1 Amyloid-β (Aβ) Aggregation Assay

Thioflavin T (ThT) is a benzothiazole dye that was used to detect the formation of amyloid aggregates in solution. The excitation and emission properties of ThT changes when it binds to the β-sheet structures of Aβ40/Aβ42 oligomers and fibrils.[145] In this regard, the anti-Aβ aggregation activity of *N*,4-diphenylthiazol-2-amine based derivatives (**3a-i** and **4a-b**) was evaluated using ThT-based fluorescence assays. These assays were conducted in Costar, black, clear-bottomed 384-well plates with frequent shaking at 730 cpm under constant heating at 37 °C for 24 h. The excitation and emission of ThT were recorded at 440 and 490 nm, respectively. Readings were taken every 5 min using a BioTek Synergy H1 microplate reader. Test compounds were prepared in 215 mM

phosphate buffer at pH 7.4. 0.5 mg of Aβ•HFIP samples (AnaSpec, CA, USA) was dissolved in 1% ammonium hydroxide solution for Aβ40 or 10% ammonium hydroxide for Aβ42, sonicated at RT for 5 min, and diluted to 50 μM in phosphate buffer. A 15 μM ThT stock solution was prepared. To each ThT background well, 44 μL ThT, 35 μL phosphate buffer, and 1 μL DMSO were added. To the Aβ control wells, 44 μL ThT, 28 μL phosphate buffer, and 8 μL Aβ40/42 (5 μM final concentration) were added. To each test compound containing wells, 44 μL ThT, 20 μL phosphate buffer, 1 μL DMSO, and 8 μL test compound in various concentrations (1, 5, 10, and 25 μM), and 8 μL of Aβ were added. ThT interferences were taken before the addition of 8 μL of Aβ40 or Aβ42 stock solution (5 μM final concentration). Known Aβ40 and Aβ42 aggregation inhibitors MB and RES were also evaluated for comparison. Plates were sealed with a ThermoSeal film (Sigma Aldrich) before placing the plates in the reader. Data presented was an average of triplicate reading for two-three independent experiments.

4.5.2.2 Transmission Electron Microscopy (TEM) Studies

The Aβ40 and Aβ42 aggregate morphology was examined by performing TEM experiment in the presence and absence of test compounds. TEM samples were prepared in Costar, round-bottomed 384-well plates with test compounds (25 μM). To the Aβ control wells, 44 μL ThT, 28 μL phosphate buffer, and 8 μL Aβ40/42 (5 μM final concentration) were added. To each test compound containing well, 44 μL ThT, 20 μL phosphate buffer, 1 μL DMSO, and 8 μL of test compound (25 μM), and 8 μL of Aβ40/42 were added. The plates were incubated on a BioTek Synergy H1 microplate reader at 37 °C and shaken at 730 cpm for 24 h.

TEM grids were prepared by adding 20 μL test compound over the formvar-coated copper grids (400 mesh) *via* the use of a Pasteur pipette, which were then air-dried for 3 h or longer before washing them with 20 μL of ultrapure water (UPW) to remove any precipitated buffer salt. The sample grids were air-dried for 30 min. Once the grids were dry, they were stained with 20 μL of 2% phosphotungstic acid (PTA). The excess of PTA was removed by blotting with filter paper. The grids were allowed to dry overnight. Scanning of these grids was performed using a Philips CM10 TEM at 60 kV (Department of Biology, University of Waterloo), and micrographs were collected using a 14-megapixel AMT camera.

4.5.2.3 Computational Modeling Studies

Molecular docking studies of *N*-methyl-*N*,4-diphenylthiazol-2-amine derivatives with Aβ peptides were conducted *via* the computational chemistry Discovery Studio (DS) software – Structure-Based-Design (SBD), version 4.0 from BIOVA Inc. (San Diego, USA).[220] The *Small Molecules* module was used to build the *N*-methyl-*N*,4-diphenylthiazol-2-amine derivatives, which were in turn docked with Aβ40 and Aβ42 dimer models obtained from protein data bank (pdb id: 2LMN and 5KK3) using the CDOCKER algorithm in the *Receptor-Ligand Interactions* module in DS using CHARMm force field.[220,221] CDOCKER algorithm uses simulated annealing protocol to determine the best ligand binding modes. *N*-Methyl-*N*,4-diphenylthiazol-2-amine derivatives were built in 3D using *Build Fragment* tool; energy minimization was applied for 1000 iterations using steepest descent and conjugate gradient minimizations, respectively. The ligands were minimized using the Smart Minimization protocol (200

steps, RMS gradient 0.1 kcal/mol), CHARMm force field and a distance depended dielectric constant. For the docking of *N*-Methyl-*N*-diphenylthiazol-amine derivatives in Aβ40 and Aβ42 dimer models, the binding site was defined by a 20 Å radius sphere. Molecular docking was carried out by the CDOCKER algorithm, which includes 2000 heating steps, 700 K target temperature, 300 K cooling temperature target with 5000 cooling steps. The docked poses obtained were ranked using the CDOCKER energy and CDOCKER interaction energy parameters (kcal/mol). The protein-ligand complexes were evaluated by examining various polar and nonpolar interactions, such as hydrogen bonding, electrostatic, *van der* Waal's, and hydrophobic interactions.

4.5.2.4 Cell Viability Assay

The HT22 hippocampal cells were plated at a density of 10,000 cells/100 μL in Nunclon Delta 96-well plates with complete growth media consisting of DMEM and Ham's F12 in a 1:1 ratio, supplemented with 10% fetal bovine serum (FBS) and 1% penicillin-streptomycin (10,000 U/mL) at 37 °C in 5% CO_2. The cells were incubated at 37 °C for 24 h. To each untreated well, 100 μL DMEM/F-12 was added. To the Aβ control wells, 85 μL DMEM/F-12, 10 μL PBS, and 5 μL Aβ40/42 (5 μM final concentration) were added. To each test compound containing wells, 85 μL DMEM/F-12, 10 μL filter-sterilized test compounds (**3a-i**, **4a-b**, and RES) in concentration of 10 μM in triplicates (n = 3), and 5 μL of Aβ40/42 were added. These cells were then incubated at 37 °C for 24 h. The MTT reagent solution[222] made of thiazolyl blue tetrazolium bromide powder (Sigma Aldrich) in PBS to 5 mg/mL and filter-sterilized through a 0.22 μm filter was added in 10% of the culture medium volume (DMEM/F-12, HEPES, no phenol red)

to each well and the cells were cultured for an additional 2-3 h. After incubation, the resulting formazan crystals were solubilized with the solubilisation solution prepared from a mixture of IPA, 10% Triton X-100 and 1% HCl (12M). The absorbance was taken at 570 and 690 nm. All results were presented as a relative percent of (4,5-dimethylthiazol-2-yl)-2,5-diphenyl tetrazolium bromide (MTT) to untreated controls. Known Aβ aggregation inhibitor resveratrol (RES) was used as a reference agent for comparison

CHAPTER 5 Development of (Alkylsulfonyl-azaneylphenyl)-*N*-Phenylthiazol-2-amines

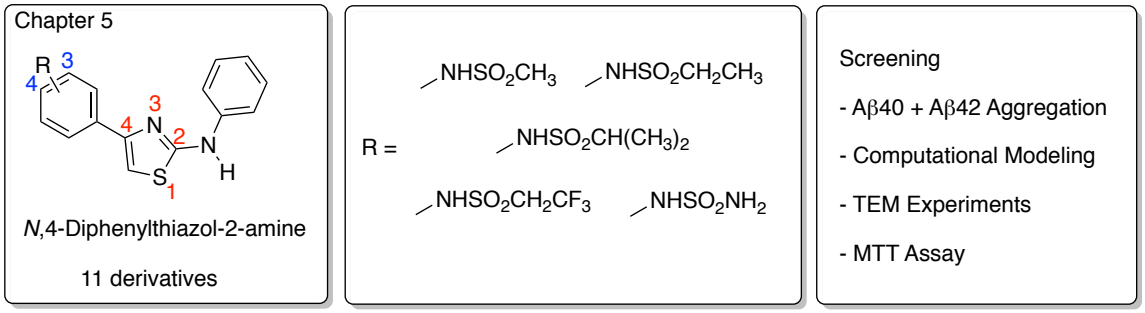

Figure 58. Banner for Chapter 5

5.1 Introduction

Many sulfonyl group containing compounds including sulfonamides have been widely used in the form of antibiotics, diuretics, antidiabetic agents and anticancer agents.[223–225] Several drugs possess sulfonyl (-SO_2R), sulfonamide (-SO_2NH_2) and alkylsulfonamide (-$NHSO_2R$) pharmacophores which are known to enhance their biological activity, oral absorption and cell penetration.[226,227] Moreover, sulfonamide group was incorporated in the design of the novel anti-AD agents such as β- and γ-secretase inhibitors,[228] as well to design neurogenesis promoters.[229] In light of their widespread utility, in this chapter we investigated a library of novel class of *N*,4-diphenylthiazol-2-amine derivatives possessing various alkylsufonyl-azaneylphenyl substituents (alkylsulfonamides, R = $NHSO_2CH_3$, $NHSO_2CH_2CH_3$, $NHSO_2CH(CH_3)_2$, $NHSO_2CH_2CF_3$) and ((phenylaminothiazol-4-yl)phenyl-azanesulfonamide, R = $NHSO_2NH_2$ or sulfamide) substituents either at the *para*- or *meta*-position of the thiazole C4-position (Figure 58) as inhibitors of Aβ40 and Aβ42 aggregation. The synthetic methodology, analytical data, and their biological assay results based on ThT-based

assay, transmission electron microscopy (TEM) experiments, computational modeling studies and their neuroprotective activity against Aβ40- and Aβ42-induced cytotoxicity are described.

5.2 Hypothesis

For this series of *N*,4-diphenylthiazol-2-amine derivatives, we hypothesize that (i) incorporating alkylsulfonamide (R = $NHSO_2CH_3$, $NHSO_2CH_2CH_3$, $NHSO_2CH(CH_3)_2$, $NHSO_2CH_2CF_3$) and $NHSO_2NH_2$ (sulfamide) substituents at the *para*- or *meta*-position of the phenyl ring at the C4-thiazole would enhance Aβ aggregation inhibition properties due to their ability to interact with both N- and C-terminal amino acids in the Aβ40 dimer model; (ii) the thiazol-2-amines with alkylsulfonamide and sulfamide substituents exhibit better Aβ-aggregation inhibition due to the interaction of these substituents in the turn region of Aβ40 dimer model (Asp23-Gly29) and in the KLVFFAE region of Aβ42 dimer model; (iii) the presence of alkylsulfonamide and sulfamide substituents results in greater cell permeation and activity in cell culture experiments.

5.3 Results and Discussion

5.3.1 Synthesis

The synthetic route for the target compounds (**5a-j**) is outlined in Scheme 3. The alkylsulfonamide and sulfamide substituted *N*,4-diphenylthiazol-2-amine derivatives (**5a-j**, Scheme 3) were synthesized via the sulfonylation using either alkylsulfonyl chlorides or sulfamoyl chloride to afford either *para*- or *meta*-amino substituted *N*,4-diphenylthiazol-2-amine derivatives using pyridine as a base (Scheme 3) to afford them in 13–88% yield. The 3- or 4-aminophenyl-*N*-phenylthiazol-2-amines were synthesized

by coupling *N*-phenylthiourea with 2-bromo-3' or 4'-nitroacetophenones, followed by their reduction over Pd/C and hydrazine hydrate as reported in Chapter 3 (Scheme 3). The reaction mechanism pertaining to sulfonylation reaction is briefly described in Figure 59. The purified sulfonamide and sulfamide based *N*,4-diphenylthiazol-2-amine derivatives were characterized by ^{1}H and ^{13}C NMR, LCMS and HRMS analysis.

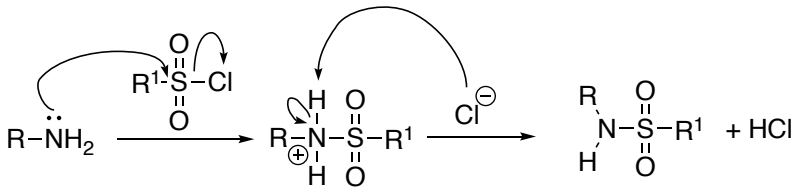

Figure 59. Mechanism of the sulfonylation reaction to synthesize sulfonyl-substituted 4-diphenylthiazol-2-amine derivatives.

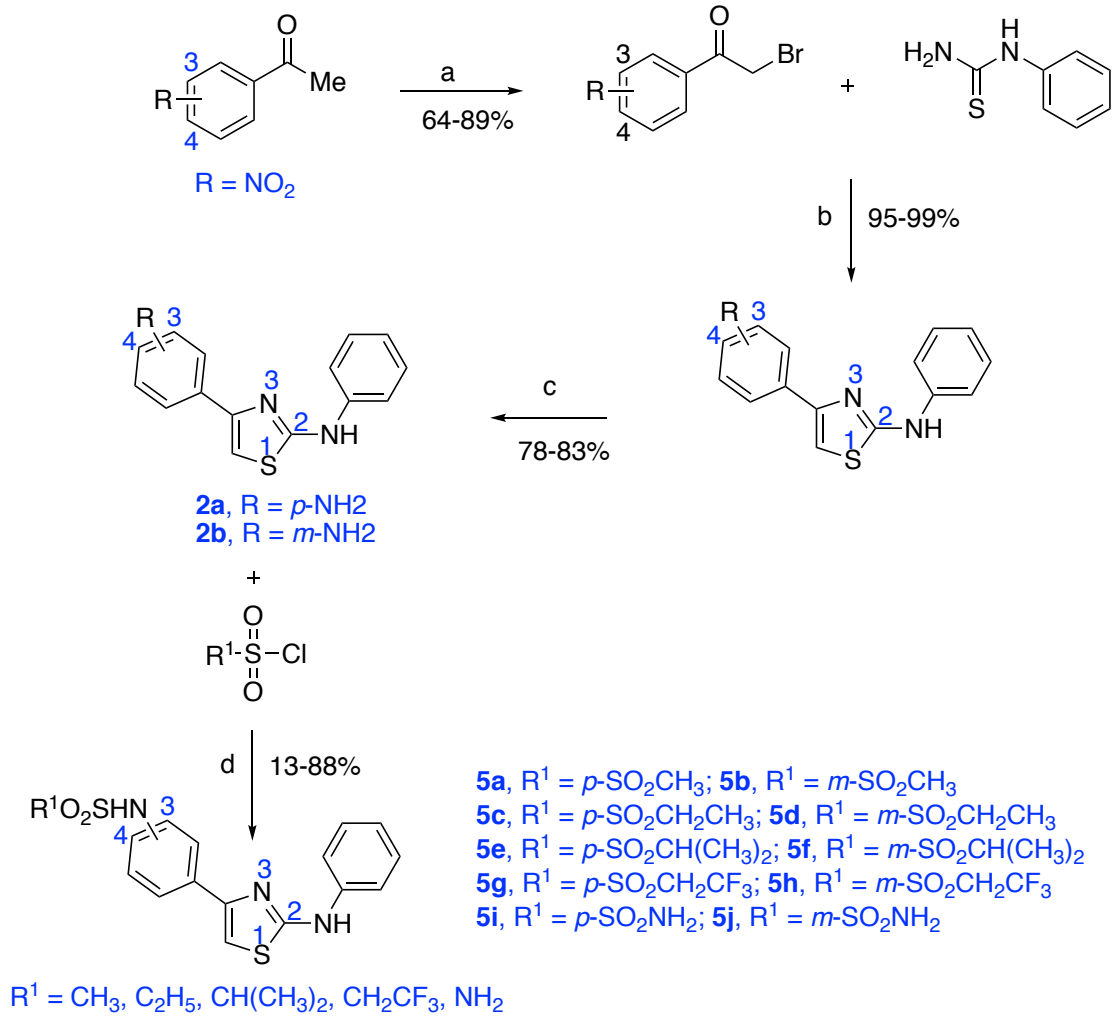

*Reagents and conditions: (a) $CuBr_2$, EtOAc, 70 °C, 15 h; (b) EtOH, 80 °C, 5 h; (c) Pd/C, hydrazine hydrate, EtOH, 85 °C, 3-5 h; (d) py, DCM, RT, 23 h.

Scheme 3. Synthetic route toward the (alkylsulfonyl-azaneylphenyl)-*N*-phenylthiazol-2-amines **5a-h** and (2-(phenylamino)thiazole-4-yl)phenyl)-azanesulfonamides **5i** and **5j**.

5.3.2 Amyloid-β Aggregation Inhibition Studies

The anti-aggregation properties of sulfonamide and sulfamide based *N*,4-diphenylthiazol-2-amine derivatives **5a-j** and reference compounds MB and RES against Aβ40 aggregation in the ThT-based fluorescence assay is shown in **Table 7**. Incorporation of a *para*-methanesulfonamide substituent (compound **5a**, R = $NHSO_2CH_3$) exhibited inhibition of Aβ40 aggregation at all the tested concentrations

(44–58% inhibition at 1–25 μM concentration range, **Table 7**). Moving the *p*-$NHSO_2CH_3$ to *meta*-position retained its anti-Aβ40 activity at all the tested concentration (compound **5b,** 43–70% inhibition**)**). Increasing the alkyl chain length from CH_3 to C_2H_5 or $CH(CH_3)_2$ led to enhancements in Aβ40 aggregation inhibition properties in compounds **5c**, **5d** and **5e** respectively (89, 84, and 71% inhibition at 25 μM, **Table 7**). Adding a terminal CF_3 substituent in compounds **5i** and **5j** did not increase their anti-aggregation properties (47% and 56% inhibition respectively). However, they exhibited similar activity as the *p*-and *m*-$NHSO_2CH_3$ derivatives **5a** and **5b** (**Table 7**). Replacing the methanesulfonamide moiety with a corresponding sulfamide bioisostere (-$NHSO_2NH_2$) did enhance their anti-aggregation properties toward Aβ40 aggregation with compounds **5i** and **5j** exhibiting ~70% inhibition at 25 μM (**Table 7**). Among these derivatives, the *para*- and *meta*-substituted $NHSO_2CH_2CH_3$ containing compounds **5c** and **5d** exhibited superior inhibition of Aβ40 fibrillogenesis with **5c** exhibiting maximum inhibition of 89% at 25 μM. In fact, compound **5c** was identified as the most potent inhibitor of Aβ40 aggregation among all the *N*,4-diphenylthiazol-2-amine derivatives evaluated (Chapters 3, 4 and 5). The 24 h Aβ40 aggregation kinetics in the presence and absence of compound **5c** is shown in Figure 60. This kinetic curve showed that compound **5c** exhibited a concentration dependent increase in its anti-aggregation properties. At 1 μM, it exhibited weak inhibition with slightly greater inhibition seen at 5 μM and 10 μM. However at 25 μM, there was a drastic increase in its anti-aggregation activity with a rapid decline in the ThT fluorescence intensity. Compound **5c** was able to exhibit almost complete inhibition of growth phase in the Aβ40 fibrillogenesis pathway at 25 μM

demonstrating its ability to prevent the conversion of lower order Aβ40 species into higher order structures effectively (**Figure 60**).

Table 7. Inhibition data for sulfonamide based *N*,4-diphenylthiazol-2-amine derivatives **5a-j**, and reference compounds toward Aβ40 aggregation, and their ClogP values.

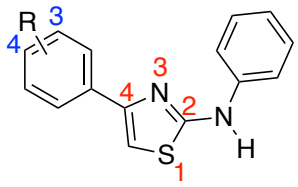

5

R = $NHSO_2CH_3$, $NHSO_2CH_2CH_3$, $NHSO_2CH(CH_3)_2$, $NHSO_2CH_2CF_3$, $NHSO_2NH_2$

Compound	R-group	% Inhibition for Aβ40 [a]				ClogP [b]
		1 μM	5 μM	10 μM	25 μM	
5a	*p*-$NHSO_2Me$	44	58	49	56	3.13
5b	*m*-$NHSO_2Me$	43	70	62	50	3.13
5c	*p*-$NHSO_2CH_2CH_3$	16	20	34	89	3.66
5d	*m*-$NHSO_2CH_2CH_3$	NA	NA	NA	84	3.66
5e	*p*-$NHSO_2CH(CH_3)_2$	NA	35	45	71	3.97
5f	*m*-$NHSO_2CH(CH_3)_2$	NA	NA	16	43	3.97
5g	*p*-$NHSO_2NH_2$	27	NA	NA	70	2.59
5h	*m*-$NHSO_2NH_2$	NA	NA	13	69	2.59
5i	*p*-$NHSO_2CH_2CF_3$	NA	NA	38	47	3.93
5j	*m*-$NHSO_2CH_2CF_3$	NA	NA	NA	56	3.93
MB	-	87	97	97	99	3.62
RES	-	81	94	95	98	2.83

[a]Percent aggregation inhibition values were average ± SD < 10% (n = 3) for three independent experiments. NA – Not Active. [b]ClogP values were determined using ChemDraw 19.1.

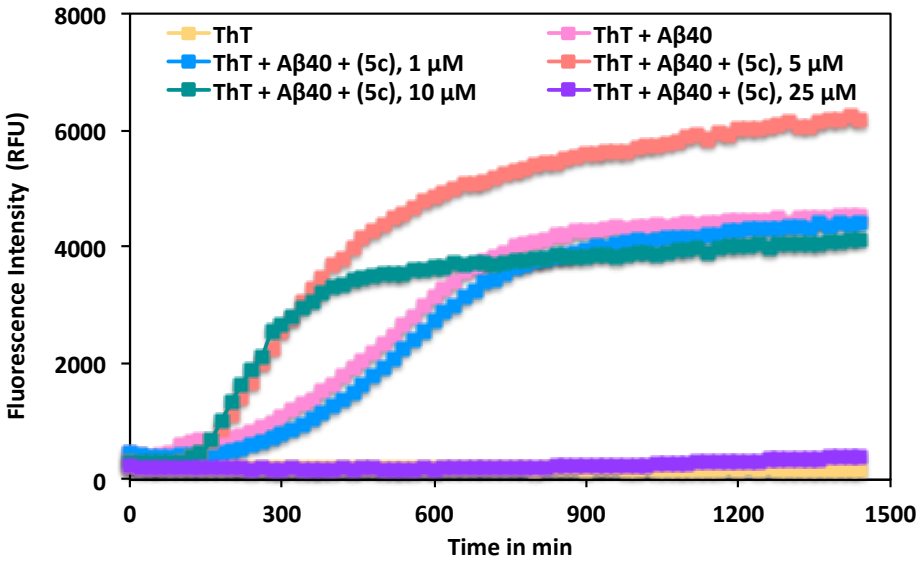

Figure 60. ThT-monitored 24 h aggregation kinetics of Aβ40 (5 μM) in the presence of 1, 5, 10, and 25 μM of sulfonamide based *N*,4-diphenylthiazol-2-amine derivatives (**5c, 5g**, and **5i**) at pH 7.4, 37 °C in phosphate buffer. Aggregation kinetics were monitored by ThT-fluorescence spectroscopy (excitation = 440 nm, emission = 490 nm). Results are average ± SD of three independent experiments (n = 3).

The results of the anti-aggregation properties of sulfonamide and sulfamide-based-*N*,4-diphenylthiazol-2-amines **5a-j** toward Aβ42 aggregation is shown in Table 8. Compounds in this series exhibited excellent inhibition activity in the range of 81–95% inhibition at 25 μM and demonstrated comparable activity with reference agents MB and RES (Table 8). Several compounds in this series exhibited concentration dependent increase in their anti-aggregation activity. For instance, at 1 μM, compound **5a** (R = *p*-$NHSO_2Me$) exhibited 58% inhibition. At 5 μM, the inhibitory activity increased (74% inhibition), which increased further at 10 and 25 μM, with inhibition ranging from 87–90%. Similarly compounds **5b**, **5c**, **5d**, **5f**, and **5g** exhibited ability to prevent the nucleation dependent Aβ42 aggregation process remarkably at all the tested concentrations (Table 8). It was satisfying to see that all the compounds in this series exhibited superior anti-aggregation properties toward Aβ42 aggregation ranging from

81–95%. In particular, adding the $NHSO_2CH_2CF_3$ substituent at the *para*-position in compound **5i** led to superior inhibition of Aβ42 aggregation 95% inhibition, which was comparable to the reference compounds MB (99% inhibition) and RES (98% inhibition) at 25 μM (Table 8).

Table 8. Inhibition data for *N*-methyl-*N*,4-diphenylthiazol-2-amine derivatives **5a-j**, and reference compounds toward Aβ42 aggregation, and their ClogP values.

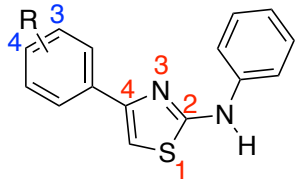

5

R = $NHSO_2CH_3$, $NHSO_2CH_2CH_3$, $NHSO_2CH(CH_3)_2$, $NHSO_2CH_2CF_3$, $NHSO_2NH_2$

Compound	R-group	% Inhibition for Aβ42 [a]				ClogP [b]
		1 μM	5 μM	10 μM	25 μM	
5a	*p*-$NHSO_2Me$	58	74	87	90	3.13
5b	*m*-$NHSO_2Me$	67	87	88	90	3.13
5c	*p*-$NHSO_2CH_2CH_3$	35	50	94	94	3.66
5d	*m*-$NHSO_2CH_2CH_3$	NA	NA	90	90	3.66
5e	*p*-$NHSO_2CH(CH_3)_2$	44	41	93	93	3.97
5f	*m*-$NHSO_2CH(CH_3)_2$	13	43	62	89	3.97
5g	*p*-$NHSO_2CH_2CF_3$	19	16	61	95	3.93
5h	*m*-$NHSO_2CH_2CF_3$	19	54	93	81	3.93
5i	*p*-$NHSO_2NH_2$	NA	72	75	94	2.59
5j	*m*-$NHSO_2NH_2$	46	NA	92	93	2.59
MB	-	87	97	97	99	3.62
RES	-	81	94	95	98	2.83

[a]Percent aggregation inhibition values were average ± SD < 10% (n = 3) for three independent experiments. NA – Not Active. [b]ClogP values were determined using ChemDraw 19.1.

The 24 h aggregation kinetic curve of Aβ42 in the presence of either compound **5g** shows that they are able to stabilize lower order species of Aβ42 in the lag phase

thereby reducing and or preventing the growth phase as indicated by reduction in the ThT fluorescence intensity **5g** (Figure 61). These compounds reduced ThT fluorescence intensity at 1, 5 and 10 μM with significant reduction in the ThT fluorescence intensity observed at 25 μM indicating their Aβ42 aggregation inhibition properties over a 24 h time period. At a higher concentration of 5 μM, the fluorescence intensity reduced to half and continued to decrease to a significantly low level observed in 25 μM. These results demonstrate that alkylsuflonamide-based *N*,4-diphenylthiazol-2-amine derivatives **5g** can reduce Aβ42 fibrillogenesis.

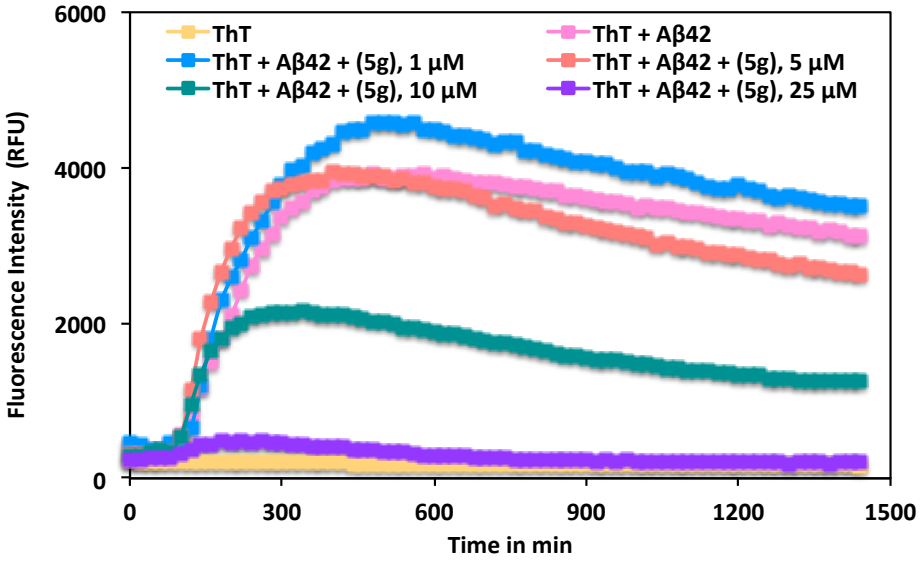

Figure 61. ThT-monitored 24 h aggregation kinetics of Aβ42 (5 μM) in the presence of 1, 5, 10, and 25 μM of *N*,4-diphenylthiazol-2-amine (**5g**) at pH 7.4, 37 °C in phosphate buffer. Aggregation kinetics were monitored by ThT-fluorescence spectroscopy (excitation = 440 nm, emission = 490 nm). Results are average ± SD of three independent experiments (n = 3).

5.3.2.1 Correlating the ClogP Values, HBDs, and HBAs with Anti-Aβ Aggregation Properties

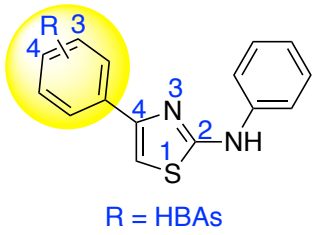

Figure 62. Chemical structure of *N*,4-diphenylthiazol-2-amines possessing alkylsulfonamide and sulfamide moieties described in Chapter 5 highlighting the C4-position of the thiazole-2-amine that was modified by SAR. HBA – Hydrogen Bond Acceptors.

The anti-aggregation properties of *N*,4-diphenylthiazol-2-amines possessing alkylsulfonamide and sulfamide moieties was correlated with their ClogP values and HBAs as shown in Figure 62. These derivatives were less lipophilic as compared to thiazole derivatives described in Chapter 3 and 4 and their ClogP values ranged from 2.59–3.97 (Figure 63) and the phenyl substituents explored are all known to act as HBAs. Compounds **5a**– **f**, **5i** and **5j** possessing alkylsulfonamide substituents are more lipophilic (ClogP range 3.13–3.97, Figure 63) compared to compounds **5g** and **5h** that possess sulfamide substituents (ClogP = 2.59). Activity data suggests that alkylsulfonamide substituted compounds **5c** (*p*-$NHSO_2Et$-phenyl), **5d** (*m*-$NHSO_2CH_2CH_3$-phenyl) and **5e** (*p*-$NHSO_2(Me)_2$) exhibited excellent inhibition of Aβ40 aggregation (71–89% inhibition at 25 μM, Figure 63). Increasing ClogP values led to a reduction in their anti-aggregation activity as seen with compounds **5i** and **5j** ($NHSO_2CH_2CF_3$-phenyl, ClogP = 3.97, 47% and 56% inhibition respectively, Figure 63). Polar compounds **5g** and **5h** (*p*-$NHSONH_2$-phenyl, ClogP value = 2.59) exhibited

good inhibition activity (~70% inhibition). These correlation studies suggest that both ClogP values and HBAs can contribute equally to inhibition of Aβ40 aggregation.

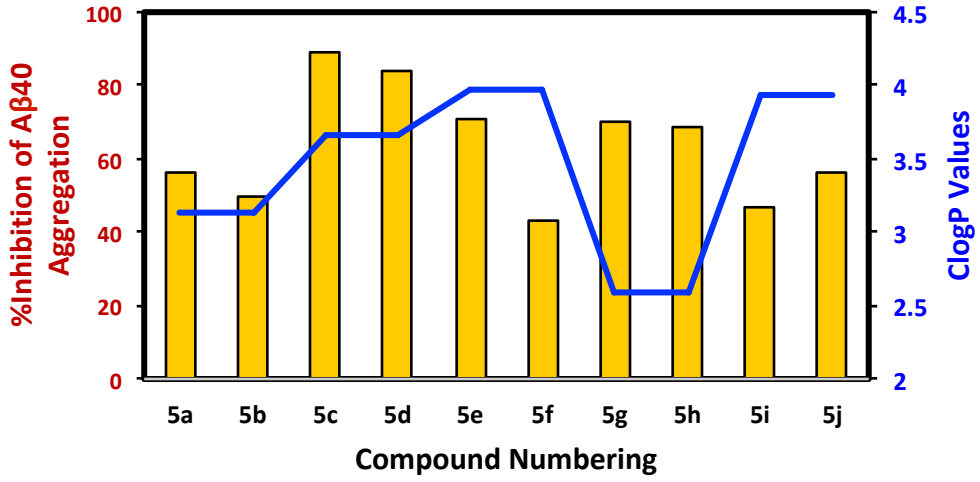

Figure 63. Correlation of Aβ40 aggregation inhibition properties of **5a–j** at 25 μM, with ClogP values. Blue line represents ClogP values.

The activity data toward Aβ42 aggregation was correlated with ClogP values and HBAs for compounds **5a–j** that possess either alkylsufonamides or sulfamides (Figure 64). Their activity data at 10 μM was compared as results obtained at other concentrations were shown to be similar. It was interesting to note that there was a direct correlation in the anti-aggregation properties and ClogP value for compounds **5a**, **5b**, **5c**, **5d** and **5e** (alkylsulfonamides, ClogP range = 3.13–3.97, 87–93% inhibition. Compounds **5g** and **5h** possessing HBAs such as sulfamides which are known to be better acceptors than alkylsulfonamides, also exhibited good inhibition despite being more polar (ClogP value = 2.59), compared to alkylsulfonamides (**5a** and **5b**, ClogP = 3.13), which suggests that both the phenyl substituents as well as ClogP values might contribute to their anti-aggregation properties.

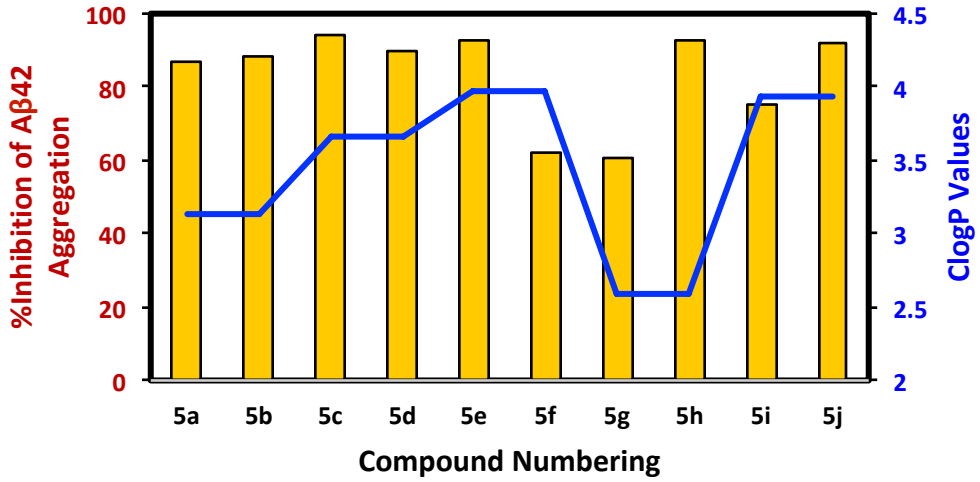

Figure 64. Correlation of Aβ42 aggregation inhibition properties of **5a–j** at 10 μM, with ClogP values. Blue line represents ClogP values.

5.3.3 Computational Modeling Studies

The binding interactions of most potent *N*,4-diphenylthiazol-2-amine derivatives containing either a sulfonamide or sulfamide substituents were investigated by conducting molecular docking studies using the solved structures of Aβ40 and Aβ42 peptides.[212,213] Docking studies were carried out using the dimer assemblies of both Aβ40 and Aβ42 peptides as they represent the early forms of Aβ in solution. In the *N*,4-diphenylthiazol-2-amine series, compound **5c** (*N*-(4-(2-(phenylamino)thiazol-4-yl)phenyl)ethanesulfonamide) was identified as the most potent inhibitor of Aβ40 aggregation in the ThT-based fluorescence assay (89% inhibition at 25 μM). Figure 65 Panel A, shows the predicted binding mode of **5c** in the Aβ40-dimer model. This compound also was able to interact with both N- and C-terminal amino acids and the entire thiazol-4-yl)phenyl)ethanesulfonamide moiety was interacting the in the KLVFFA region closer to the N-terminal (Panel A, Figure 65). Both the phenyl and thiazole rings

underwent T-shaped interactions with Phe19 and Phe20 respectively (distance < 5 Å). The unsubstituted phenyl ring was in contact with Leu34 at the C-terminal. These observations suggest the ability of compound **5c** in reducing Aβ40 aggregation.

In the sulfonamide and sulfamide containing *N*,4-diphenylthiazol-2-amine series, compound **5g** (2,2,2-trifluoro-*N*-(4-(2-(phenylamino)thiazol-4-yl)phenyl)ethane-1-sulfonamide) was identified as the most potent inhibitor of Aβ42 aggregation in the ThT-based fluorescence assay (95% inhibition at 25 μM). Figure 65 Panel B, shows the predicted binding mode of **5g** in the Aβ42-dimer model. This compound exhibited an extended conformation and was in binding in the KLVFFA region. The trifluoro-ethanesulfonamide group was in contact with polar amino acids His13 and Lys16 (distance < 5 Å) and sulfonyl oxygen formed hydrogen bond with Lys16 side chain, whereas the phenyl ring was in contact with Val18. The thiazole ring nitrogen formed a hydrogen bonding interaction with Lys16 side chain whereas the aromatic ring underwent π-alkyl interaction with Val18 and Ala21. These computational studies suggest that the presence of trifluoro-ethanesulfonamide group can increase the binding affinity of compound **5g**, which is also supported by the ligand-Aβ42 dimer complex energy (CDOCKER energy = –16.48 kcal/mol).

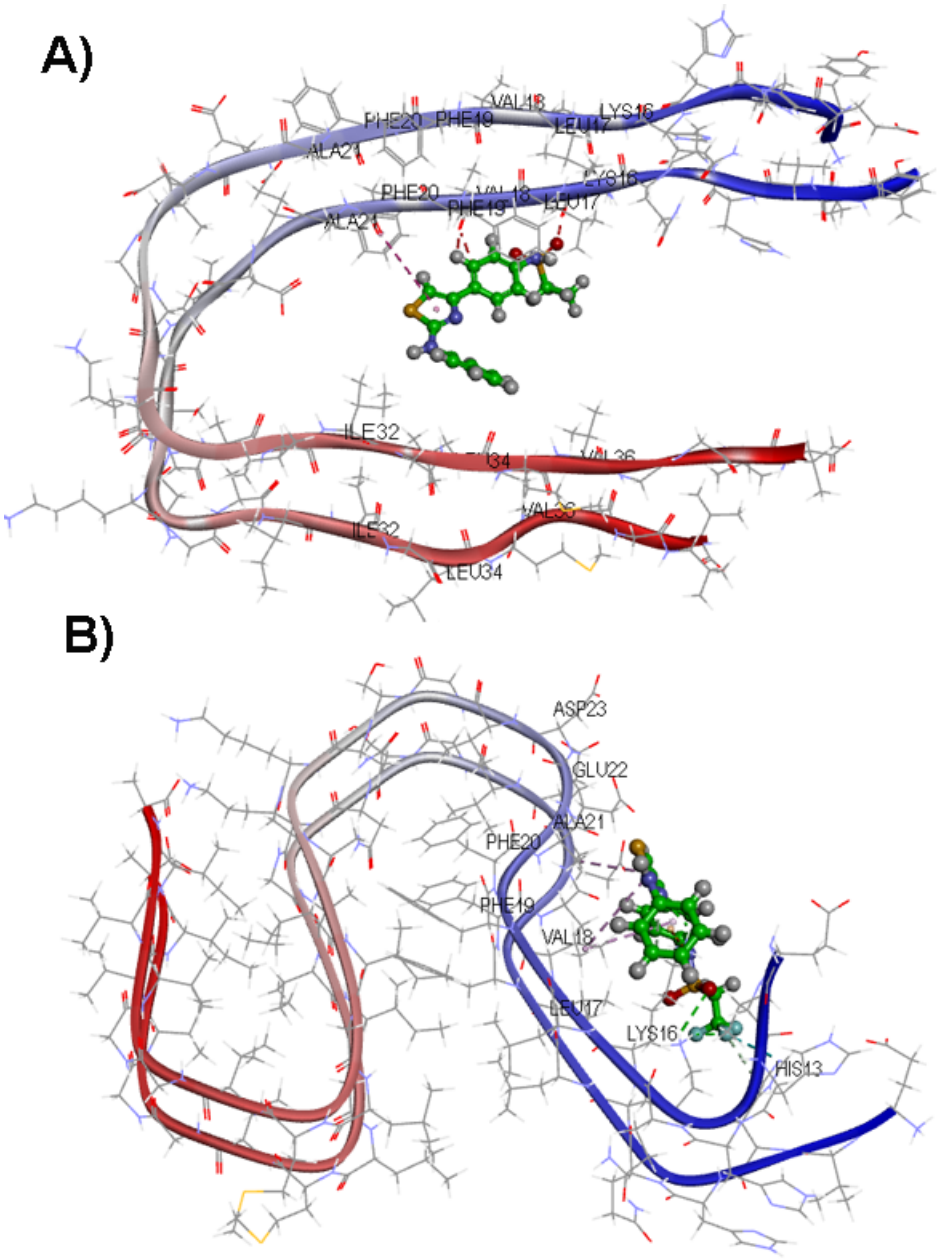

Figure 65. Panel A: Predicted binding mode of **5c** (ball and stick cartoon) in the Aβ40-dimer model (ribbon diagram, pdb id: 2LMN, CDOCKER energy = –10.89 kcal/mol; CDOCKER interaction Energy = –22.38 kcal/mol). Panel B: Predicted binding mode of **5g** (ball and stick cartoon) in the Aβ42-dimer model (ribbon diagram, pdb id: 5KK3, CDOCKER energy = –16.48 kcal/mol; CDOCKER interaction energy = –26.63 kcal/mol).

5.3.4 Transmission Electron Microscopy (TEM) Studies

The transmission electron microscopy (TEM) experiments were carried out for a representative sample compounds **5c** (R = *p*-$NHSO_2CH_2CH_3$) and **5g** (R = *p*-$NHSO_2CH_2CF_3$) from the sulfonamide and sulfamide-based *N*,4-diphenylthiazol-2-amine derivatives, to validate and confirm the anti-Aβ40 and anti-Aβ42 aggregation properties, respectively. Compounds **5c** and **5g** exhibited significant reduction in the formation of Aβ40 (top panels, Figure 66) and Aβ42 aggregates (bottom panels, Figure 66) at 25 μM. The results further demonstrate the ability of sulfonamide-based *N*,4-diphenylthiazol-2-amine derivatives to inhibit Aβ40/Aβ42 aggregation.

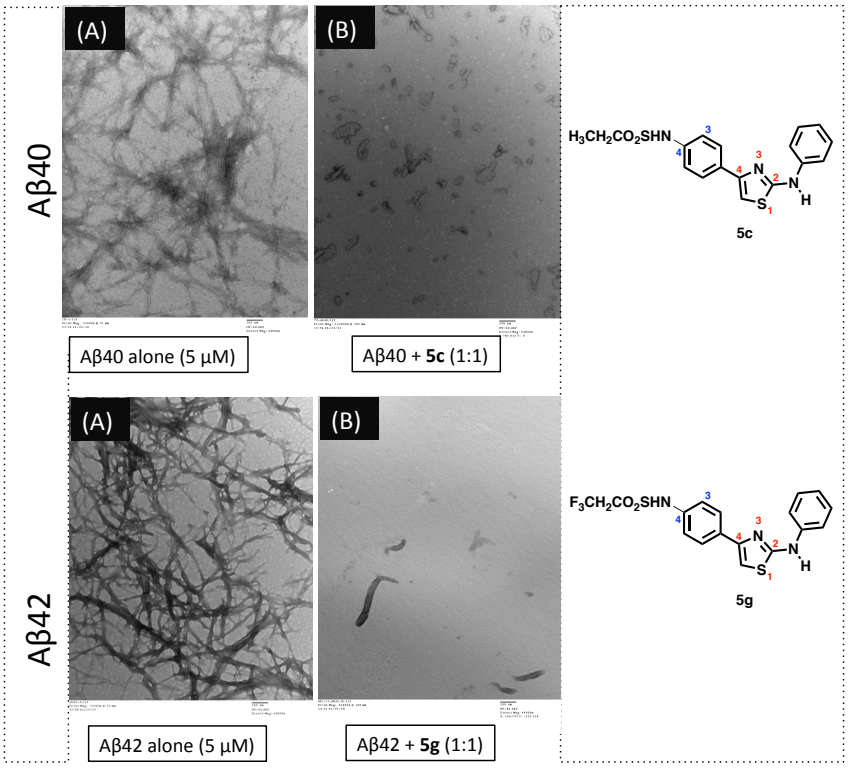

Figure 66. TEM images of Aβ40 and Aβ42 aggregation. Top: Panel A: Aβ40 control (5 μM). Panel B: Aβ40 + **5c** (5 μM). Bottom: Panel A: Aβ42 control (5 μM). Panel B: Aβ42 + **5g** (5 μM).Scale bars represent 100 nm.

5.3.5 Cell Viability Assay

The neuroprotective effect of sulfonamide and sulfamide-based *N*,4-diphenylthiazol-2-amine derivatives **5a-j** (10 μM), was evaluated in HT22 hippocampal derived-cells to investigate their potential in reducing the cytotoxicity induced by Aβ40. The results are shown in Figure 67. In untreated group, Aβ40 (5 μM) alone demonstrated cytotoxicity with cell viability of 63%. Strikingly, all the compounds tested exhibited excellent cell viability toward Aβ40-induced cytotoxicity in the range of 80-100% (Figure 67). This result directly correlates with the superior anti-aggregation properties demonstrated by this class of compounds in the ThT-based fluorescence assay. All compounds (**5a-j**) exhibited superior anti-aggregation activity in preventing Aβ40-induced cytotoxicity. In particular, compounds **5a** (R = *p*-$NHSO_2Me$), **5e** (R = *p*-$NHSO_2CH(CH_3)_2$), and **5h** (R = m-$NHSO_2CH_2CF_3$) exhibited excellent cell viability (>95%) (Figure 67). The reference agent RES failed to provide neuroprotection against Aβ40-induced cytotoxicity as seen in Figure 67.

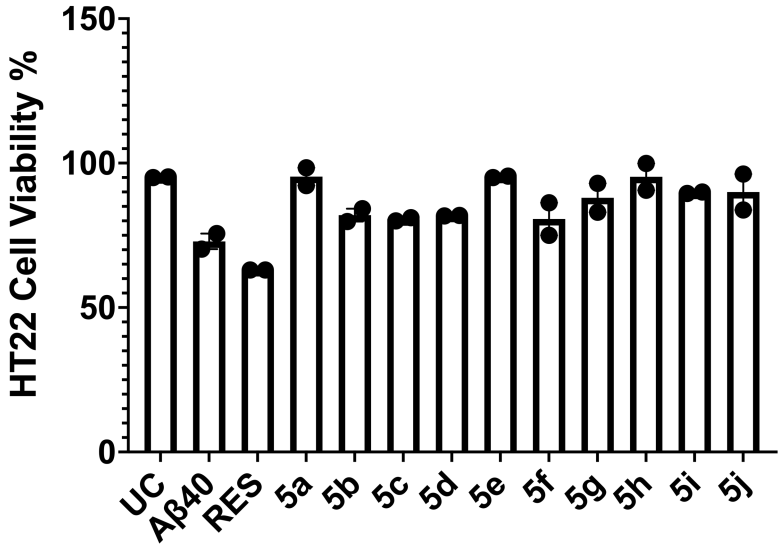

Figure 67. Percentage viability of the *N*,4-diphenylthiazol-2-amine derivatives **5a-j** and RES (10 μM) in HT22 cells was assessed by MTT assay toward Aβ40 after 24 h incubation at 37 °C. The results were given as average of two independent experiments (n = 3). UC = untreated cells, RES = resveratrol.

The neuroprotective effect of sulfonamide and sulfamide-based *N*,4-diphenylthiazol-2-amine derivatives **5a-j** (10 μM), was evaluated in HT22 hippocampal neuronal cells to investigate their potential in reducing the cytotoxicity induced by Aβ42. These studies led to the identification of a number of compounds that were able to provide neuroprotection by reducing Aβ42 induced cytotoxicity. Their cell viability ranged from 60-93%, which was greater than the cell viability observed in the presence of Aβ42 alone treated group (cell viability = 52%, Figure 68). Few compounds such as **5a**, **5b**, **5e**, **5f**, and **5h** exhibited statistically significant neuroprotection and surpassed the level of neuroprotection that was observed in the presence of reference compound RES (cell viability = 72%), ranging from 77-93% cell viability.

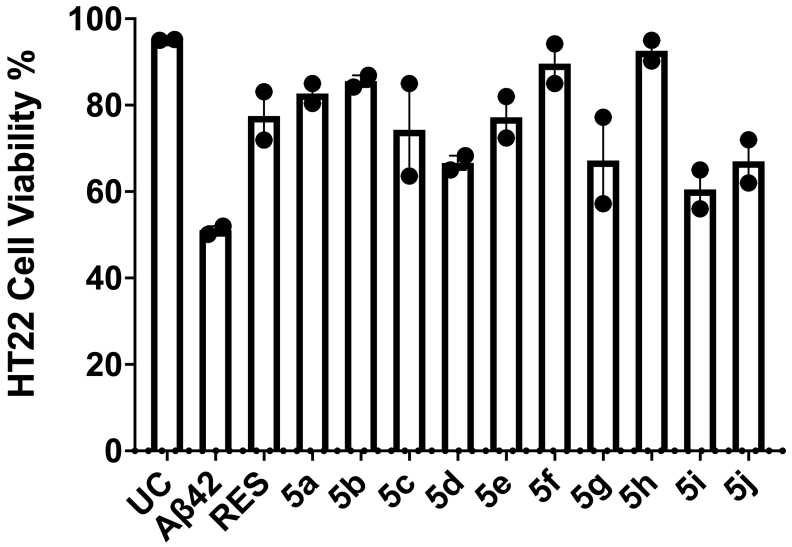

Figure 68. Percentage viability of the *N*,4-diphenylthiazol-2-amine derivatives **5a-j** and RES (10 μM) in HT22 cells was assessed by MTT assay toward Aβ42 after 24 h incubation at 37 °C. The results were given as average of two independent experiments (n = 3). UC = untreated cells, RES = resveratrol.

5.4 Summary

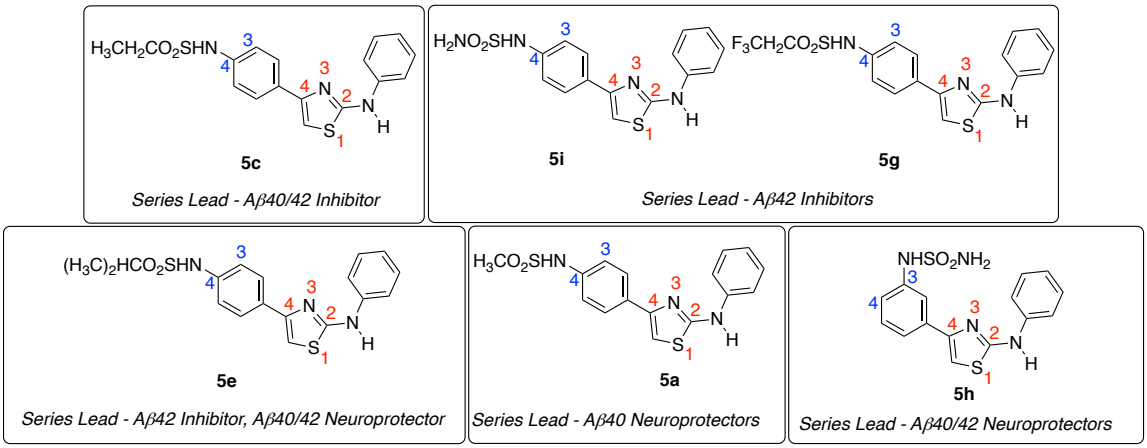

Figure 69. Cumulative chapter summary of *N*,4-diphenylthiazol-2-amines (**5**).

In this study, a class of eleven novel *N*,4-diphenylthiazole-2-amine derivatives possessing either an alkylsulfonamide (-$NHSO_2R$) or sulfamide (-$NHSO_2NH_2$) substituents were designed, synthesized and evaluated to assess their Aβ40 and Aβ42 aggregation inhibition potential. Their in vitro evaluation in ThT-based fluorescence

assay showed that these compounds were able to exhibit inhibition of both Aβ40 and Aβ42 aggregation with maximum inhibition observed at 25 μM (43–95% inhibition). Furthermore, the presence of either an alkylsulfonamide or sulfamide-substituents, provided superior inhibition of Aβ40 aggregation compared to either *N*-methyl or *N*,4-diphenylthiazole-2-amine derivatives possessing various electron-donating (R = Me, OMe, NH_2) or electron-withdrawing groups (R = NO_2, Cl, Br, F). This suggests that both alkylsulfonamide or sulfamide substituents can be considered as potential pharmacophores to design and develop novel molecules that can prevent the aggregation of Aβ40. Compounds in this series also exhibited excellent inhibition of Aβ42 aggregation and their activity was comparable to the *N*-methyl or *N*,4-diphenylthiazole-2-amine derivatives (Chapters 3 and 4) which shows that the Aβ42 inhibition property was not exclusive to *N*,4-diphenylthiazole-2-amine derivatives possessing either alkylsulfonamide or sulfamide-substituents. In this series, compound **5c** (*N*-(4-(2-(phenylamino)thiazol-4-yl)phenyl)ethanesulfonamide) was identified as an excellent inhibitor of Aβ40 and Aβ42 aggregation, while derivatives **5c**, **5e**, **5g** and **5i** were identified as excellent inhibitors of Aβ42 aggregation based on the data obtained from the ThT fluorescence assay with 93-95% inhibition respectively at 25 μM.

In the HT22 cell cytotoxicity assay, compounds **5a**, **5e**, **5h**, **5i** and **5j** from this series (**5a-j)** provided excellent neuroprotection against Aβ40-induced cytotoxicity while some compounds such as **5a**, **5b**, **5e**, **5f**, and **5h** had better neuroprotection against Aβ42-induced cytotoxicity than the reference compound RES. These SAR studies demonstrate that the sulfonamide and sulfamide containing *N*,4-diphenylthiazol-2-amine derivatives represent a novel class of compounds that are capable of inhibiting Aβ aggregation and

demonstrate neuroprotective property toward both Aβ40/Aβ42-induced cytotoxicity in HT22 hippocampal derived-cells. These discoveries can further advance the field of novel anti-AD drug development.

5.5 Experimental

5.5.1 Chemistry

5.5.1.1 Materials and Methods

General information. All the reagents and solvents were purchased from various vendors (Sigma-Aldrich, Oakwood Chemical, Matrix Scientific, TCI Chemicals, AAblocks, and Ark Pharm Inc.) with a minimum purity of 95% and were used without further purification. Melting points (mp) were determined using a Fisher-Johns apparatus and are uncorrected. Compound purification was carried out using Merck 230-400 mesh silica gel 60. All derivatives showed single spot on thin-layer chromatography (TLC) performed on Merck 60 F254 silica gel plates (0.2 mm) using variety of solvent systems and TLC spots were visualized with the handheld UV lamp 254/365 nm. ^{1}H NMR and ^{13}C NMR spectra were analyzed using a Bruker Avance 300 MHz series spectrometer in deuterated solvents. Data was analyzed using the Bruker TOPSPIN 3.6.1 software. Coupling constant (*J* values) were recorded in hertz (Hz) and the following abbreviations were used for multiplicity of NMR signals: s = singlet, d = doublet, t = triplet, m = multiplet, br = broad. Compound purity and low resolution mass (LRMS) were evaluated using an Agilent 6100 series single quad LCMS equipped with an Agilent 1.8 μM Zorbax Eclipse Plus C18 (2.1 x 50 mm) running 30:70 Water:ACN with 0.1% FA at a flow rate of 0.5 mL/min. All the final compounds were > 95% pure as determined by calculating the peak area by LCMS (UV detector, 254 nm). High-resolution mass spectrometry data

were obtained by carrying out a positive ion electrospray (ESI) experiments on using a Thermo Scientific Q-Exactive hybrid mass spectrometer, Department of Chemistry, University of Waterloo. Accurate mass determinations were performed at a mass resolution of 70,000 (@m/z200) with lock mass correction. All samples were injected at 10 mL/min in a 1:1 MeOH/H_2O + 0.1% formic acid.

5.5.1.2 *General procedure for the synthesis of N-methyl-N,4-diphenylthiazol-2-amine derivatives (5a-j).*[230]

Compound **2a** or **2b** and pyridine (0.38 mL, 1.87 mmol) were added in DCM solution. This resulting mixture was then stirred at 0 °C for 10 min. To the same mixture, alkylsulfonyl chloride or sulfamoyl chloride (0.23 mL, 2.06 mmol) was added at such a rate as to prevent the temperature from rising above 10 °C, and stirred at RT for 23 h. The reaction mixture was quenched with 10 mL NaHCO3 solution and washed three times with 20 mL brine solution. The aqueous layers were extracted with EtOAc (2 x 20 mL). The combined organic layers were dried over $MgSO_4$, filtered, and concentrated *in vacuo* to obtain the crude product, which was purified using the silica gel column chromatography with Hex:EtOAc (1:1) as the eluent. Yield ranged from 13 – 88%. The analytical data is given below:

*N-(4-(2-(Phenylamino)thiazol-4-yl)phenyl)methanesulfonamide (**5a**).* Yield: 79%. m.p. 210-212 °C. ^{1}H NMR (300 MHz, DMSO-d_6) δ (ppm): 10.24 (s, 1H), 9.81 (s, 1H), 7.89 (d, J = 8.8 Hz, 2H), 7.72 (d, J = 7.6 Hz, 2H), 7.33 (t, J = 8.0 Hz, 2H), 7.27 (s, 1H), 7.24 (d, J = 4.3 Hz, 2H), 6.95 (t, J = 7.0 Hz, 1H), 3.01 (s, 3H). HRMS (ESI) m/z calcd for $C_{16}H_{16}O_2N_3S_2$ $[M+H]^+$ 346.0678, found 346.0674. Purity: 97%.

*N-(3-(2-(Phenylamino)thiazol-4-yl)phenyl)methanesulfonamide (**5b**)*. Yield: 88%. m.p. 213-215 °C. ^{1}H NMR (300 MHz, DMSO-d_6) δ (ppm): 10.26 (s, 1H), 9.84 (s, 1H), 7.82 (s, 1H), 7.74-7.72 (m, 2H), 7.64 (d, J = 7.8 Hz, 1H), 7.55 (s, 1H), 7.40-7.28 (m, 3H), 7.18 (dd, J = 1.51, 1.68 Hz, 1H), 6.96 (t, J = 7.4 Hz, 1H), 3.02 (s, 3H). HRMS (ESI) m/z calcd for $C_{16}H_{16}O_2N_3S_2$ $[M+H]^+$ 346.0678, found 298.0678. Purity: 100%.

*N-(4-(2-(Phenylamino)thiazol-4-yl)phenyl)ethanesulfonamide (**5c**)*. Yield: 56%. m.p. 198-200 °C. ^{1}H NMR (300 MHz, DMSO-d_6) δ (ppm): 10.24 (s, 1H), 9.86 (s, 1H), 7.87 (d, J = 7.1 Hz, 2H), 7.72 (d, J = 9.6 Hz, 2H), 7.36-7.21 (m, 5H), 6.95 (t, J = 6.8 Hz, 1H), 3.12 (q, J = 7.5, 8.1 Hz, 2H), 1.20 (t, J = 7.1 Hz, 3H). HRMS (ESI) m/z calcd for $C_{17}H_{18}O_2N_3S_2$ $[M+H]^+$ 360.0834, found 360.0835. Purity: 98%.

*N-(3-(2-(Phenylamino)thiazol-4-yl)phenyl)ethanesulfonamide (**5d**)*. Yield: 65%. m.p. 86-89 °C. ^{1}H NMR (300 MHz, DMSO-d_6) δ (ppm): 10.27 (s, 1H), 9.88 (s, 1H), 7.84 (t, J = 3.4 Hz, 1H), 7.72 (d, J = 7.6 Hz, 2H), 7.59 (t, J = 7.8 Hz, 1H), 7.39-7.27 (m, 3H), 7.17 (dd, J = 1.20, 1.30 Hz, 1H), 6.97 (t, J = 7.3 Hz, 1H), 3.14 (q, J = 8.5, 7.5 Hz, 2H), 1.25-1.19 (t, J = 7.3 Hz, 3H). HRMS (ESI) m/z calcd for $C_{17}H_{18}O_2N_3S_2$ $[M+H]^+$ 360.0844, found 360.0844. Purity: 97%.

*N-(4-(2-(Phenylamino)thiazol-4-yl)phenyl)propane-2-sulfonamide (**5e**)*. Yield: 37%. m.p. 148-150 °C. ^{1}H NMR (300 MHz, DMSO-d_6) δ (ppm): 10.24 (s, 1H), 9.83 (s, 1H), 7.86 (d, J = 7.7 Hz, 2H), 7.72 (d, J = 7.7 Hz, 2H), 7.35-7.26 (m, 5H), 7.20 (s, 1H), 6.95 (t, J =

7.0 Hz, 1H), 3.32-3.21 (m, 1H), 1.25 (d, *J* = 6.9 Hz, 6H). HRMS (ESI) m/z calcd for $C_{18}H_{20}O_2N_3S_2$ $[M+H]^+$ 374.0991, found 374.0992. Purity: 98%.

*N-(3-(2-(Phenylamino)thiazol-4-yl)phenyl)propane-2-sulfonamide (**5f**)*. Yield: 49%. m.p. 88-100 °C. ^{1}H NMR (300 MHz, DMSO-d_6) δ (ppm): 10.27 (s, 1H), 9.84 (s, 1H), 7.87 (s, 1H), 7.75 (d, *J* = 7.8 Hz, 2H), 7.59 (d, *J* = 8.4 Hz, 1H), 7.37-7.29 (m, 3H), 7.26 (s, 1H), 7.18 (dd, *J* = 1.7, 1.7 Hz, 1H), 6.96 (t, *J* = 7.3 Hz, 1H), 3.31-3.22 (m, 1H), 1.28 (d, *J* = 6.8 Hz, 6H). HRMS (ESI) m/z calcd for $C_{18}H_{20}O_2N_3S_2$ $[M+H]^+$ 374.0991, found 374.0996. Purity: 97%.

*2,2,2-Trifluoro-N-(4-(2-(phenylamino)thiazol-4-yl)phenyl)-2-ethane-1-sulfonamide (**5g**)*. Yield: 70%. m.p. 189-191 °C. ^{1}H NMR (300 MHz, DMSO-d_6) δ (ppm): 10.51 (s, 1H), 10.25 (s, 1H), 7.90 (d, *J* = 8.1 Hz, 2H), 7.72 (d, *J* = 8.1 Hz, 2H), 7.36-7.25 (m, 5H), 6.95 (t, *J* = 7.0 Hz, 1H), 4.55 (q, *J* = 9.7 Hz, 2H). HRMS (ESI) m/z calcd for $C_{17}H_{15}O_2N_3F_3S_2$ $[M+H]^+$ 414.0552, found 414.0546. Purity: 100%.

*2,2,2-Trifluoro-N-(3-(2-(phenylamino)thiazol-4-yl)phenyl)ethane-1-sulfonamide (**5h**)*. Yield: 79%. m.p. 98-100 °C. ^{1}H NMR (300 MHz, DMSO-d_6) δ (ppm): 10.53 (s, 1H), 10.27 (s, 1H), 7.83 (s, 1H), 7.75-7.66 (m, 3H), 7.42-7.30 (m, 4H), 7.20 (dd, *J* = 0.8 Hz, 1H), 6.97 (t, *J* = 7.2 Hz, 1H), 4.55 (q, *J* = 9.7 Hz, 2H). HRMS (ESI) m/z calcd for $C_{17}H_{15}O_2N_3F_3S_2$ $[M+H]^+$ 414.05523, found 414.05515. Purity: 97%.

*(4-(2-(Phenyl)amino)thiazol-4-yl)benzenesulfamide (**5i**)*. Yield: 40%. m.p. 191-194 °C. ^{1}H NMR (300 MHz, DMSO-d_6) δ (ppm): 10.19 (s, 1H), 9.56 (s, 1H), 7.80 (d, J = 8.1 Hz, 2H), 7.69 (d, J = 7.6 Hz, 2H), 7.30 (t, J = 7.6 Hz, 2H), 7.16 (t, J = 7.4 Hz, 3H), 7.10 (s, 2H), 6.92 (t, J = 7.4 Hz, 1H). HRMS (ESI) m/z calcd for $C_{15}H_{15}O_2N_4S_2$ $[M+H]^+$ 347.06309, found 347.06292. Purity: 100%.

*(3-(2-(Phenyl)amino)thiazol-4-yl)benzenesulfamide (**5j**)*. Yield: 21%. m.p. 85-88 °C. ^{1}H NMR (300 MHz, DMSO-d_6) δ (ppm): 10.23 (s, 1H), 9.55 (s, 1H), 7.74 (d, J = 8.4 Hz, 3H), 7.52 (d, J = 7.7 Hz, 1H), 7.31 (q, J = 7.1, 7.4 Hz, 4H), 7.22 (s, 1H), 7.15 (d, J = 8.4 Hz, 1H), 7.10 (s, 2H), 6.95 (t, J = 7.2 Hz, 1H). HRMS (ESI) m/z calcd for $C_{15}H_{15}O_2N_4S_2$ $[M+H]^+$ 347.06309, found 347.06321. Purity: 96%.

5.5.2 Biological Screening

5.5.2.1 Amyloid-β (Aβ) Aggregation Assay

Thioflavin T (ThT) is a benzothiazole dye that was used to detect the formation of amyloid aggregates in solution. The excitation and emission properties of ThT changes when it binds to the β-sheet structures of Aβ40/Aβ42 oligomers and fibrils.[145] In this regard, the anti-Aβ aggregation activity of sulfonamide and sulfamide containing *N*,4-diphenylthiazol-2-amine based derivatives (**5a-j**) was evaluated using ThT-based fluorescence assays. These assays were conducted in Costar, black, clear-bottomed 384-well plates with frequent shaking at 730 cpm under constant heating at 37 °C for 24 h. The excitation and emission of ThT were recorded at 440 and 490 nm, respectively. Readings were taken every 5 min using a BioTek Synergy H1 microplate reader. Test compounds were prepared in 215 mM phosphate buffer at pH 7.4. 0.5 mg of Aβ•HFIP

samples (AnaSpec, CA, USA) was dissolved in 1% ammonium hydroxide solution for Aβ40 or 10% ammonium hydroxide for Aβ42, sonicated at RT for 5 min, and diluted to 50 μM in phosphate buffer. A 15 μM ThT stock solution was prepared. To each ThT background well, 44 μL ThT, 35 μL phosphate buffer, and 1 μL DMSO were added. To the Aβ control wells, 44 μL ThT, 28 μL phosphate buffer, and 8 μL Aβ40/42 (5 μM final concentration) were added. To each test compound containing wells, 44 μL ThT, 20 μL phosphate buffer, 1 μL DMSO, and 8 μL test compound in various concentrations (1, 5, 10, and 25 μM), and 8 μL of Aβ were added. ThT interferences were taken before the addition of 8 μL of Aβ40 or Aβ42 stock solution (5 μM final concentration). Known Aβ40 and Aβ42 aggregation inhibitors MB and RES were also evaluated for comparison. Plates were sealed with a ThermoSeal film (Sigma Aldrich) before placing the plates in the reader. Data presented was an average of triplicate reading for two-three independent experiments.

5.5.2.2 Transmission Electron Microscopy (TEM) Studies

The Aβ40 and Aβ42 aggregate morphology was examined by performing TEM experiment in the presence and absence of test compounds. TEM samples were prepared in Costar, round-bottomed 384-well plates with test compounds (25 μM). To the Aβ control wells, 44 μL ThT, 28 μL phosphate buffer, and 8 μL Aβ40/42 (5 μM final concentration) were added. To each test compound containing well, 44 μL ThT, 20 μL phosphate buffer, 1 μL DMSO, and 8 μL of test compound (25 μM), and 8 μL of Aβ40/42 were added. The plates were incubated on a BioTek Synergy H1 microplate reader at 37 °C and shaken at 730 cpm for 24 h.

TEM grids were prepared by adding 20 μL test compound over the formvar-coated copper grids (400 mesh) *via* the use of a Pasteur pipette, which were then air-dried for 3 h or longer before washing them with 20 μL of ultrapure water (UPW) to remove any precipitated buffer salt. The sample grids were air-dried for 30 min. Once the grids were dry, they were stained with 20 μL of 2% phosphotungstic acid (PTA). The excess of PTA was removed by blotting with filter paper. The grids were allowed to dry overnight. Scanning of these grids was performed using a Philips CM10 TEM at 60 kV (Department of Biology, University of Waterloo), and micrographs were collected using a 14-megapixel AMT camera.

5.5.2.3 Computational Modeling Studies

Molecular docking studies of *N*,4-diphenylthiazol-2-amines derivatives with Aβ peptides were conducted *via* the computational chemistry Discovery Studio (DS) software – Structure-Based-Design (SBD), version 4.0 from BIOVA Inc. (San Diego, USA).[220] The *Small Molecules* module was used to build the sulfonamide and sulfamide containing *N*,4-diphenylthiazol-2-amine derivatives, which were in turn docked with Aβ40 and Aβ42 dimer models obtained from protein data bank (pdb id: 2LMN and 5KK3) using the CDOCKER algorithm in the *Receptor-Ligand Interactions* module in DS using CHARMm force field.[220,221] CDOCKER algorithm uses simulated annealing protocol to determine the best ligand binding modes. The sulfonamide and sulfamide based *N*,4-diphenylthiazol-2-amine derivatives were built in 3D using *Build Fragment* tool; energy minimization was applied for 1000 iterations using steepest descent and conjugate gradient minimizations, respectively. The ligands were minimized using the

Smart Minimization protocol (200 steps, RMS gradient 0.1 kcal/mol), CHARMm force field and a distance depended dielectric constant. For the docking of sulfonamide and sulfami *N*-diphenylthiazol-amine derivatives in Aβ40 and Aβ42 dimer models, the binding site was defined by a 20 Å radius sphere. Molecular docking was carried out by the CDOCKER algorithm, which includes 2000 heating steps, 700 K target temperature, 300 K cooling temperature target with 5000 cooling steps. The docked poses obtained were ranked using the CDOCKER energy and CDOCKER interaction energy parameters (kcal/mol). The protein-ligand complexes were evaluated by examining various polar and nonpolar interactions, such as hydrogen bonding, electrostatic, *van der* Waal's, and hydrophobic interactions.

5.5.2.4 Cell Viability Assay

The HT22 hippocampal cells were plated at a density of 10,000 cells/100 μL in Nunclon Delta 96-well plates with complete growth media consisting of DMEM and Ham's F12 in a 1:1 ratio, supplemented with 10% fetal bovine serum (FBS) and 1% penicillin-streptomycin (10,000 U/mL) at 37 °C in 5% CO_2. The cells were incubated at 37 °C for 24 h. To each untreated well, 100 μL DMEM/F-12 was added. To the Aβ control wells, 85 μL DMEM/F-12, 10 μL PBS, and 5 μL Aβ40/42 (5 μM final concentration) were added. To each test compound containing wells, 85 μL DMEM/F-12, 10 μL filter-sterilized test compounds (**5a-j**, and RES) in concentration of 10 μM in triplicates (n = 3), and 5 μL of Aβ40/42 were added. These cells were then incubated at 37 °C for 24 h. The MTT reagent solution[222] made of thiazolyl blue tetrazolium bromide powder (Sigma Aldrich) in PBS to 5 mg/mL and filter-sterilized through a 0.22 μm filter

was added in 10% of the culture medium volume (DMEM/F-12, HEPES, no phenol red) to each well and the cells were cultured for an additional 2-3 h. After incubation, the resulting formazan crystals were solubilized with the solubilisation solution prepared from a mixture of IPA, 10% Triton X-100 and 1% HCl (12M). The absorbance was taken at 570 and 690 nm. All results were presented as a relative percent of (4,5-dimethylthiazol-2-yl)-2,5-diphenyl tetrazolium bromide (MTT) to untreated controls. Known Aβ aggregation inhibitor resveratrol (RES) was used as a reference agent for comparison.

CHAPTER 6 Development of *N*-Methyl-*N*,4-diphenylthiazol-2-amines

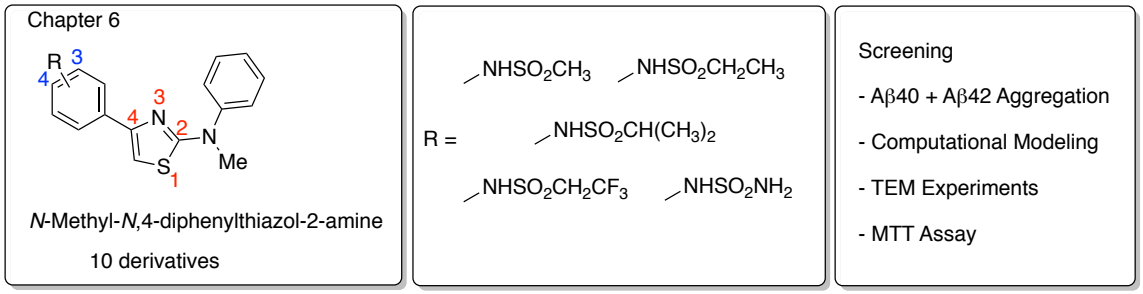

Figure 70. Banner for Chapter 6

6.1 Introduction

A library of *N*-methyl-*N*,4-diphenylthiazol-2-amines (**6a-j**) possessing either an alkylsufonamide (R = $NHSO_2CH_3$, $NHSO_2CH_2CH_3$, $NHSO_2CH(CH_3)_2$, $NHSO_2CH_2CF_3$) or sulfamide (R = $NHSO_2NH_2$) substituents (Figure 70), were designed and evaluated as Aβ aggregation inhibitors. These compounds were synthesized as an extension of the work in Chapter 5 to investigate the effect of incorporating *N*-methyl-substituent on Aβ40 and Aβ42 aggregation inhibition properties, in solution based ThT-fluorescence assay and in cell culture studies. This chapter highlights the synthetic methodology to prepare target derivatives along with their analytical characterization and their biological assay results based on ThT-fluorescence assay, transmission electron microscopy (TEM) experiments, and their neuroprotective activity toward Aβ40- and Aβ42-induced cytotoxicity in HT22 hippocampal neuronal cells.

6.2 Hypothesis

For this series of *N*-methyl-*N*,4-diphenylthiazol-2-amine derivatives, we hypothesize that (i) the diphenyl rings undergo hydrophobic interactions with both the N-

and C-terminal residues (Phe20 and Val36) in the Aβ40 dimer model which can stabilize the dimer assembly and can reduce its aggregation propensity, and that loss of a hydrogen bond donor by *N*-methyl substitution, will reduce the anti-Aβ activity compared to the corresponding *N*,4-diphenylthiazol-2-amine derivatives; (ii) *N*-methyl substitution will enhance their inhibition activity toward Aβ42 aggregation due to additional nonpolar contacts seen in the KLVFFA region in the Aβ42 dimer model; (iii) the presence of N-methyl group in addition to alkylsulfonamide (R = $NHSO_2CH_3$, $NHSO_2CH_2CH_3$, $NHSO_2CH(CH_3)_2$, $NHSO_2CH_2CF_3$) and $NHSO_2NH_2$ (sulfamide) substituents will enhance their cell permeation and neuroprotective activity in cell culture studies.

6.3 Results and Discussion

6.3.1 Synthesis

The synthetic route for the target compounds (**6a-j**) is outlined in Scheme 4. The sulfonamide or sulfamide containing *N*-methyl-*N*,4-diphenylthiazol-2-amine derivatives (**6a-j**) were synthesized starting from the reaction of precursors *N*-phenylthiourea with 2-bromo-3' or 4'-nitroacetophenones to obtain either *para*- or *meta*-substituted NO_2 derivatives of *N*,4-diphenylthiazol-2-amines (Scheme 4), which were further reduced to obtain the corresponding NH_2 derivatives using Pd/C and hydrazine hydrate as reported in Chapter 3. In the next step they were alkylated using CH_3I and NaH to afford the corresponding *N*-methyl derivatives which was further treated with alkylsufonyl chlorides or sulfamoyl chloride to obtain compounds **6a-j** containing alkylsulfonamide and sulfamide substituents (Scheme 4). They were characterized by ^{1}H and ^{13}C NMR,

LCMS and HRMS analysis. The yields of the desired compounds (**6a-j**) ranged from 3-93%.

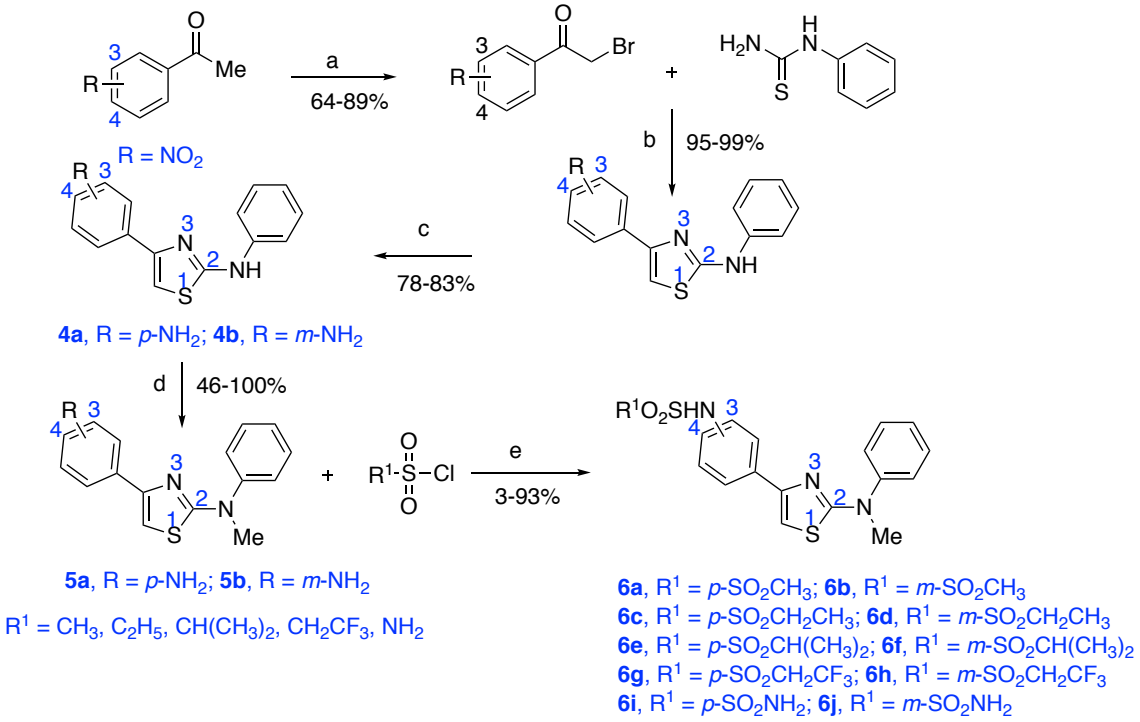

*Reagents and conditions: (a) $CuBr_2$, EtOAc, 70 °C, 15 h; (b) EtOH, 80 °C, 5 h; (c) Pd/C, hydrazine hydrate, EtOH, 85 °C, 3-5 h; (d) MeI, NaH, THF, RT; (e) py, DCM, RT, 23 h.

Scheme 4. Synthetic route toward the *N*-methyl-*N*,4-diphenylthiazol-2-amine derivatives **6a-j** possessing either sulfonamide or sulfamide substituents.

6.3.2 Amyloid-β Aggregation Inhibition Studies

The anti-aggregation activity of the *N*-methyl-*N*,4-diphenylthiazol-2-amine derivatives **6a-j** and reference compounds MB and RES at various concentrations (1, 5, 10, and 25 μM) toward Aβ40 is summarized in Table 9. These studies showed that the alkylsulfonamide and sulfamide substituted compounds inhibited Aβ40 aggregation ranging from 11–76% inhibition at 25 μM (Table 9). Most of the compounds tested were inactive at 1, 5, and 10 μM with only few compounds exhibited anti-aggregation properties at 25 μM. Compound **6f** (R = *m*-$NHSO_2CH(CH_3)_2$) and **6j** (R = *m*-

$NHSO_2NH_2$) were identified as inhibitors with superior anti-aggregation properties (~75% inhibition). The presence of methanesulfonamide group (R = $NHSO_2Me$, compounds **6a** and **6b**) was detrimental with very weak to loss of activity toward Aβ40 aggregation inhibition (inactive-16% inhibition). Overall compounds in this series exhibited reduced inhibition of Aβ40 aggregation compared to the corresponding *N*,4-diphenylthiazol-2-amine derivatives **5a-j** discussed in Chapter 5. This suggests that in general, the presence of *N*-methylation was not effective in enhancing the anti-aggregation properties toward Aβ40.

Table 9. Inhibition data for *N*-methyl-*N*,4-diphenylthiazol-2-amine derivatives **6a-j**, and reference compounds toward Aβ40 aggregation, and their ClogP values.

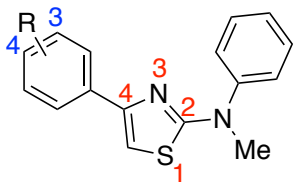

6

R = $NHSO_2CH_3$, $NHSO_2CH_2CH_3$, $NHSO_2CH(CH_3)_2$, $NHSO_2NH_2$, $NHSO_2CH_2CF_3$

Compound	R-group	% Inhibition for Aβ40 [a]				ClogP [b]
		1 μM	5 μM	10 μM	25 μM	
6a	*p*-$NHSO_2Me$	16	NA	NA	NA	3.13
6b	*m*-$NHSO_2Me$	NA	NA	NA	NA	3.13
6c	*p*-$NHSO_2CH_2CH_3$	NA	NA	NA	62	3.66
6d	*m*-$NHSO_2CH_2CH_3$	15	NA	NA	50	3.66
6e	*p*-$NHSO_2CH(CH_3)_2$	NA	NA	NA	67	3.97
6f	*m*-$NHSO_2CH(CH_3)_2$	NA	NA	NA	75	3.97
6g	*p*-$NHSO_2CH_2CF_3$	NA	NA	NA	55	3.93
6h	*m*-$NHSO_2CH_2CF_3$	NA	NA	NA	NA	3.93
6i	*p*-$NHSO_2NH_2$	NA	NA	NA	NA	2.59
6j	*m*-$NHSO_2NH_2$	NA	NA	NA	76	2.59
MB	-	87	97	97	99	3.62
RES	-	81	94	95	98	2.83

[a]Percent aggregation inhibition values were average ± SD < 10% (n = 3) for three independent experiments. NA – Not Active. [b]ClogP values were determined using ChemDraw 19.1.

N-Methylated *N*,4-diphenylthiazol-2-amine derivatives **6a-j** exhibited excellent anti-aggregation properties ranging from 68–96% inhibition toward Aβ42 aggregation (Table 10). Compound **6a** (R = *p*-$NHSO_2CH_3$) was the best compound in this series exhibiting 96% inhibition of Aβ42 aggregation at 25 μM and its activity was comparable to reference agents MB and RES (Table 10). The sulfonamide containing compounds **6i** and **6j** also exhibited excellent inhibition of Aβ42 aggregation (87-93% inhibition at 25

μM). In general all the compounds in the alkylsulfonamide and sulfamide series exhibited excellent inhibition of Aβ42 aggregation.

Table 10. Inhibition data for *N*-methyl-*N*,4-diphenylthiazol-2-amine derivatives **6a-j** and reference compounds toward Aβ42 aggregation, and their ClogP values.

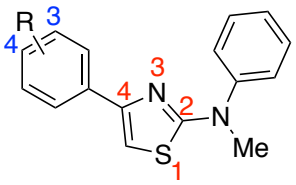

6

R = $NHSO_2CH_3$, $NHSO_2CH_2CH_3$, $NHSO_2CH(CH_3)_2$, $NHSO_2NH_2$, $NHSO_2CH_2CF_3$

Compound	R-group	% Inhibition for Aβ42 [a]				ClogP [b]
		1 μM	5 μM	10 μM	25 μM	
6a	*p*-$NHSO_2Me$	42	67	94	96	3.13
6b	*m*-$NHSO_2Me$	22	56	91	91	3.13
6c	*p*-$NHSO_2CH_2CH_3$	NA	NA	92	91	3.66
6d	*m*-$NHSO_2CH_2CH_3$	NA	NA	17	92	3.66
6e	*p*-$NHSO_2CH(CH_3)_2$	NA	50	90	94	3.97
6f	*m*-$NHSO_2CH(CH_3)_2$	NA	NA	93	93	3.97
6g	*p*-$NHSO_2CH_2CF_3$	NA	NA	NA	NA	3.93
6h	*m*-$NHSO_2CH_2CF_3$	NA	NA	12	92	3.93
6i	*p*-$NHSO_2NH_2$	NA	NA	73	87	2.59
6j	*m*-$NHSO_2NH_2$	NA	92	93	93	2.59
MB	-	87	97	97	99	3.62
RES	-	81	94	95	98	2.83

[a]Percent aggregation inhibition values were average ± SD < 10% (n = 3) for three independent experiments. NA – Not Active. [b]ClogP values were determined using ChemDraw 19.1.

The 24 h Aβ42 aggregation kinetics curve for compound **6a** is shown in Figure 71. In the presence of increasing concentrations of **6a**, there was a gradual decline in ThT fluorescence intensity indicating a reduction in Aβ42 fibrillogenesis. At 10 μM and 25 μM, there was a drastic and rapid decline in ThT fluorescence intensity, which indicates the ability of compound **6a** in increasing the lag phase and reducing the growth phase,

demonstrating its ability to prevent the formation of higher order Aβ42 species. In summary, this SAR study shows that the anti-aggregation properties did not vary to a great extent depending on the type of substituents present either at the *para*- or *meta*-position of the phenyl ring at the thiazole C4-position. *N*-methylation of *N*,4-diphenylthiazol-2-amines possessing either sulfonamide or sulfamide substituents led to decline in their Aβ40 aggregation inhibition properties whereas their inhibition properties toward Aβ42 aggregation was not affected.

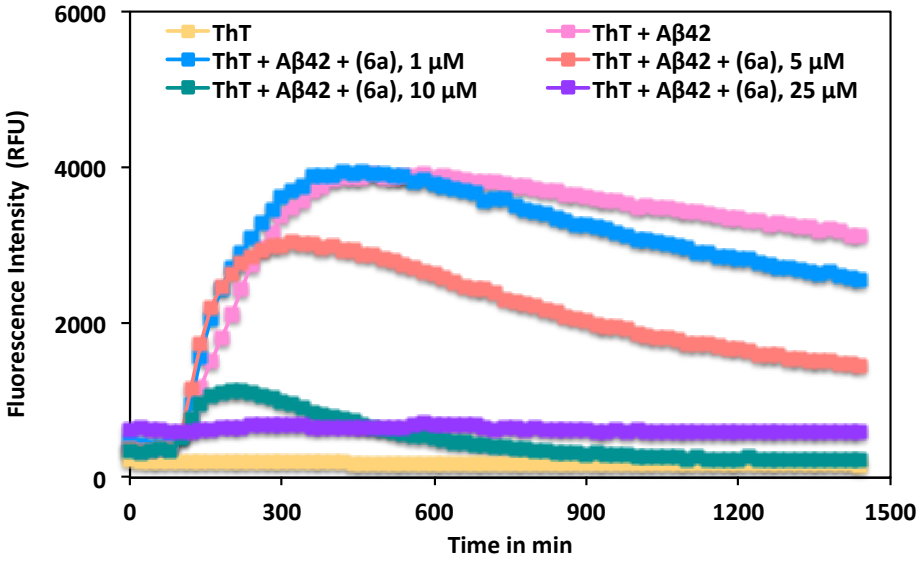

Figure 71. ThT-monitored 24 h aggregation kinetics of Aβ42 (5 µM) in the presence of 1, 5, 10, and 25 µM of *N*-methyl-*N*,4-diphenylthiazol-2-amines (**6a**) at pH 7.4, 37 °C in phosphate buffer. Aggregation kinetics were monitored by ThT-fluorescence spectroscopy (excitation = 440 nm, emission = 490 nm). Results are average ± SD of three independent experiments (n = 3).

6.3.3 Computational Modeling Studies

The binding interactions of most potent *N*-methyl-*N*,4-diphenylthiazol-2-amine derivatives containing either a sulfonamide or sulfamide substituents were investigated by conducting molecular docking studies using the solved structures of Aβ40 and Aβ42

peptides.[212,213] Docking studies were carried out using the dimer assemblies of both Aβ40 and Aβ42 peptides as they represent the early forms of Aβ in solution. In the *N*-methyl-*N*,4-diphenylthiazol-2-amine series, compound **6j** (4-(2-(methyl(phenyl)amino)thiazol-4-yl)benzenesulfamide) was identified as the most potent inhibitor of Aβ40 aggregation in the ThT-based fluorescence assay (76% inhibition at 25 μM). Figure 72 Panel A, shows the predicted binding mode of **6j** in the Aβ40-dimer model. Interestingly, this compound was interacting primarily at the N-terminal region without making any contacts with the C-terminal region. The *meta*-benzenesulfamide substituent underwent a number of contacts with backbone C=O of Phe20 and with Glu22 side chain. The central thiazole was in contact with aromatic rings of Phe19 and Phe20 via π-π T-shaped interactions (distance < 5 Å). Interestingly, the N-Me substituent underwent π-alkyl interactions with Leu17 and Val18 (distance < 5 Å). These studies suggest the ability of compound **6j** to stabilize the Aβ40-dimer assembly and reduce aggregation.

In the sulfonamide and sulfamide containing *N*-methyl-*N*,4-diphenylthiazol-2-amine series, compound **6a** (*N*-(4-(2-(methyl(phenyl)amino)thiazol-4-yl)phenyl)methanesulfonamide) was identified as the most potent inhibitor of Aβ42 aggregation in the ThT-based fluorescence assay (96% inhibition at 25 μM). Figure 72 Panel B, shows the predicted binding mode of **6a** in the Aβ42-dimer model. This methanesulfonamide derivative was bound in the KLVFFA region where the sulfonamide moiety was in contact with polar amino acids Glu11 and Lys16 (distance < 2.5 Å). The aromatic phenyl ring underwent π-cation interaction with Lys16 side chain. Furthermore, the thiazole ring underwent π-alkyl interaction with Ala21, the *N*-Me substituent was interacting with Ala21 and the unsubstituted phenyl ring was in contact with Val18.

These modeling studies show the ability of compound **6a** to bind in the KLVFFA pocket of Aβ42 dimer and prevent its aggregation.

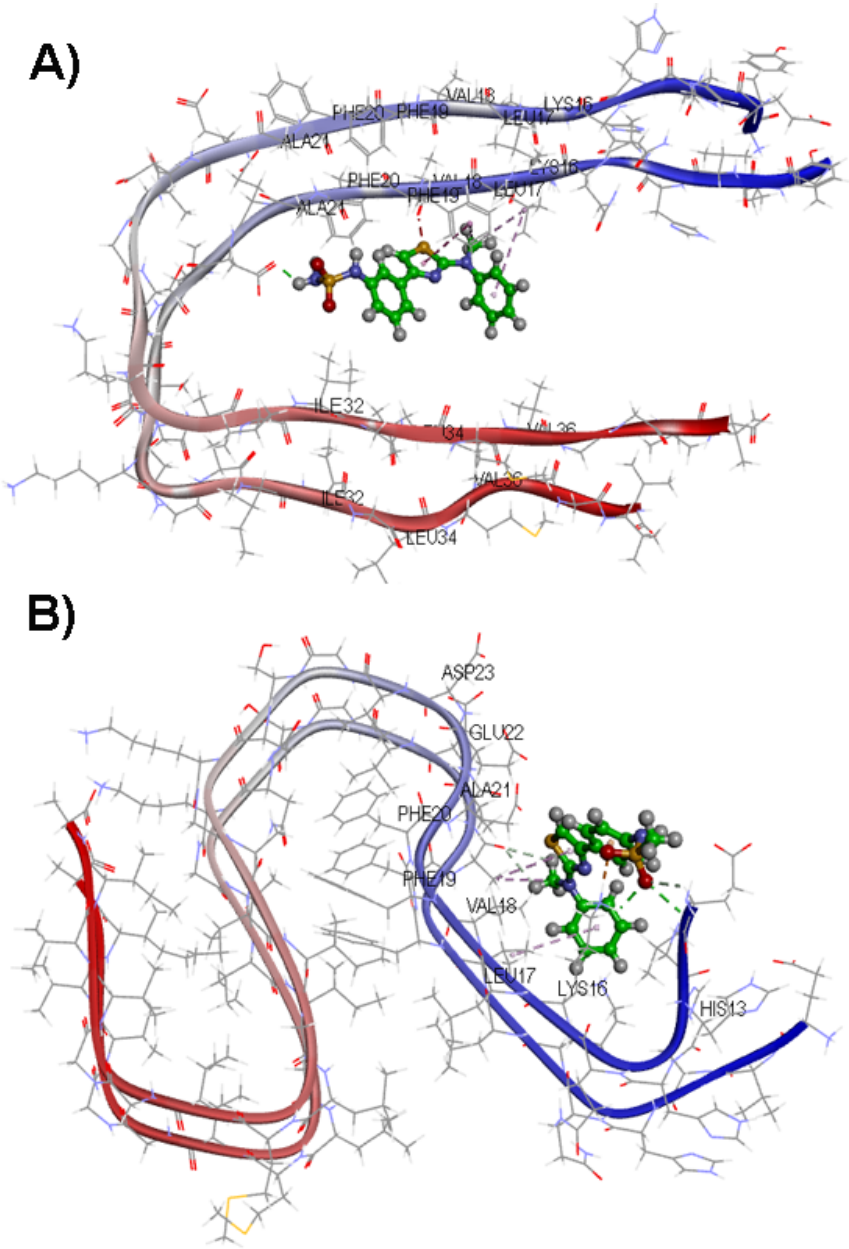

Figure 72. Panel A: Predicted binding mode of **6j** (ball and stick cartoon) in the Aβ40-dimer model (ribbon diagram, pdb id: 2LMN, CDOCKER energy = –18.03 kcal/mol; CDOCKER interaction Energy = –24.99 kcal/mol). Panel B: Predicted binding mode of **6a** (ball and stick cartoon) in the Aβ42-dimer model (ribbon diagram, pdb id: 5KK3, CDOCKER energy = –14.79 kcal/mol; CDOCKER interaction energy = –26.93 kcal/mol).

6.3.4 Transmission Electron Microscopy (TEM) Studies

The transmission electron microscopy (TEM) experiments for the *N*-methyl-*N*,4-diphenylthiazol-2-amine derivatives **6a** and **6j** were carried out to validate and confirm their anti-Aβ40/Aβ42 aggregation properties. It was observed that in the presence of compound **6j** (5 μM) led to drastic reduction in the formation of Aβ40 aggregates (Panel A, Figure 73). Similarly, in the presence of compound **6a** (5 μM), there was a dramatic reduction in the formation of Aβ42 aggregates (Panel B, Figure 73). The TEM results obtained were consistent with the results obtained from the in vitro Aβ40/Aβ42 aggregation kinetics experiments, which further confirmed the ability of compounds **6a** and **6j** in preventing Aβ40 and Aβ42 fibrillogenesis.

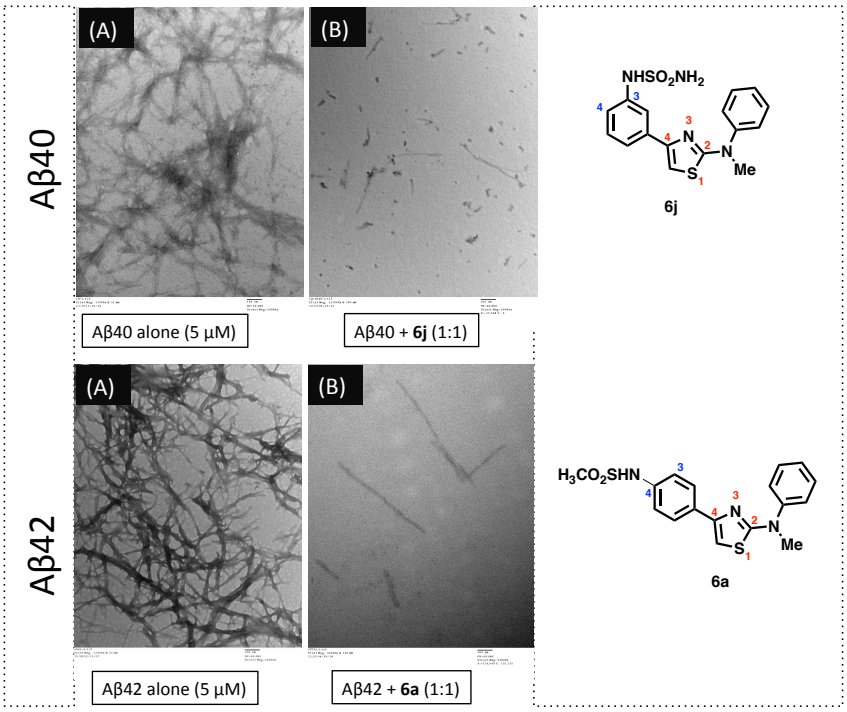

Figure 73. TEM images of Aβ40 and Aβ42 aggregation. Top: Panel A: Aβ40 control (5 μM). Panel B: Aβ40 + **6j** (5 μM). Bottom: Panel A: Aβ42 control (5 μM). Panel B: Aβ42 + **6a** (5 μM). Scale bars represent 100 nm.

6.3.5 Cell Viability Assay

The neuroprotective effect of *N*-methyl-*N*,4-diphenylthiazol-2-amine derivatives **6a-j** (10 μM) was investigated in mouse hippocampal derived-HT22 cells exposed to either Aβ40 (**Figure 74**) or Aβ42 (Figure 75). Incubating HT22 hippocampal neuronal cells with Aβ40 (5 μM) led to cytotoxicity with cell viability of ~64% (Figure 74). Interestingly, all the compounds in this series were able to demonstrate neuroprotective effect toward Aβ40 cytotoxicity. In the presence of 10 μM of *N*-methyl-*N*,4-diphenylthiazol-2-amine derivatives **6a-j**, statistically significant neuroprotection was seen with cell viability ranging from 75–98%. These results were similar to corresponding *N*,4-diphenylthiazol-2-amine derivatives **5a-j** discussed in Chapter 5. Among this series of compound **6h** (R = *m*-$NHSO_2CH_2CF_3$) was identified as the best compound (cell viability >98%, Figure 74). This shows that presence of either alkylsulfonamide or sulfamide substituent provides superior neuroprotection toward Aβ40-induced cytotoxicity.

Figure 75 shows the effect of compounds **6a-j** toward Aβ42-induced cytotoxicity in HT22 hippocampal neuronal cells. They exhibited cell viability ranging from 17-81%. Compound **6b** was identified as the best compound in this series (cell viability = 81%), but failed to prevent Aβ42-induced cytotoxicity compared to the reference agent RES (cell viability = 72%). Overall, these studies further demonstrate the neuroprotective effects of *N*,4-diphenylthiazol-2-amine derivatives in preventing Aβ-induced cytotoxicity.

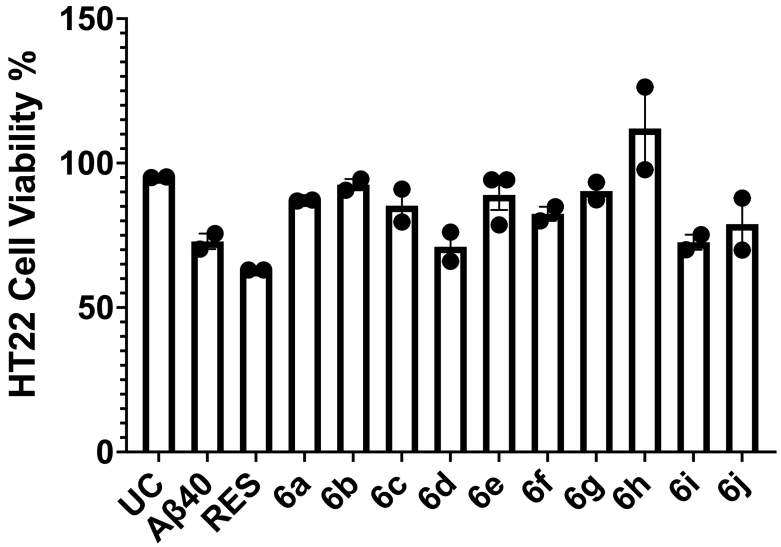

Figure 74. Percentage viability of the *N*,4-diphenylthiazol-2-amine derivatives **6a-j** and RES (10 μM) in HT22 cells in the presence of Aβ40 was assessed by MTT assay after 24 h incubation at 37 °C. The results were given as average of two independent experiments (n = 3). UC = untreated cells, RES = resveratrol.

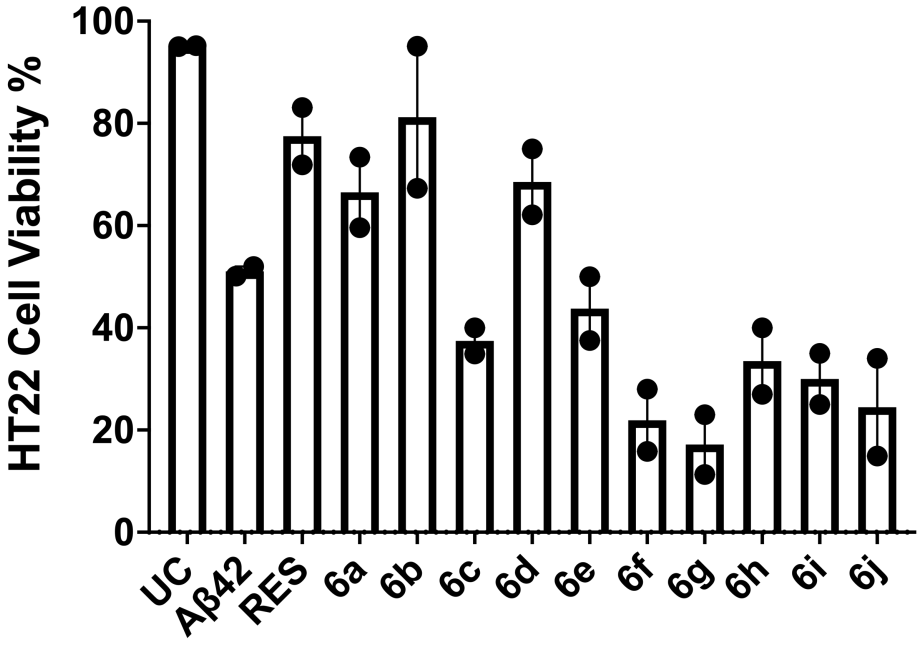

Figure 75. Percentage viability of the *N*,2-diphenylthiazol4-amine derivatives **6a-j** and RES (10 μM) in HT22 cells in the presence of Aβ42 was assessed by MTT assay after 24 h incubation at 37 °C. The results were given as average of two independent experiments (n = 3). UC = untreated cells, RES = resveratrol.

6.4 Summary

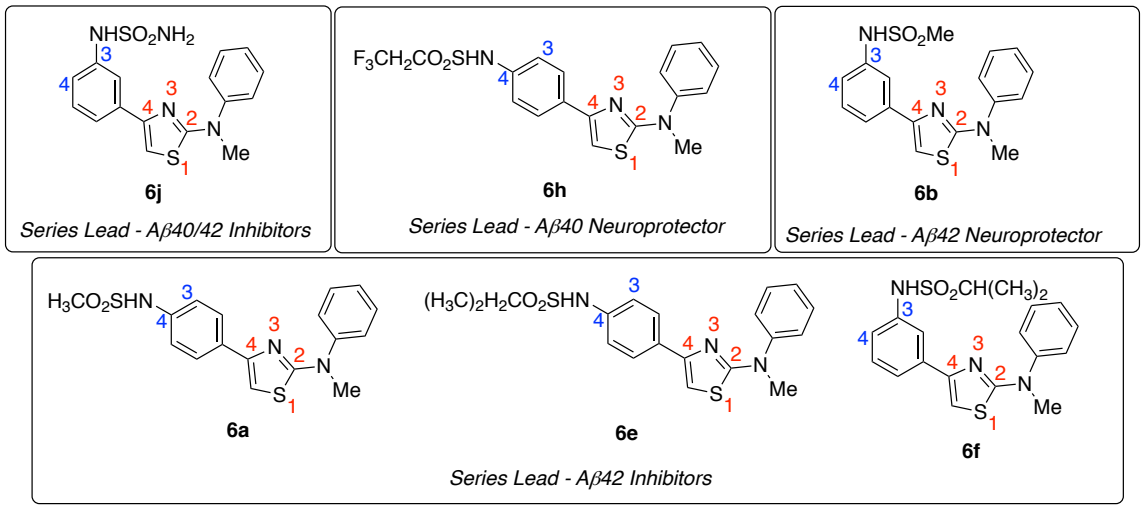

Figure 76. Cumulative chapter summary of *N*,4-diphenylthiazol-2-amines (**6**).

For this series of compounds, in vitro ThT-based Aβ40 aggregation kinetics assay results showed that *N*-methylation did not enhance their anti-aggregation properties compared to the corresponding *N*,4-diphenylthiazol-2-amine derivatives **5a-j** (Chapter 5). Compounds **6f** (R = *m*-$NHSO_2CH(CH_3)_2$) and **6j** (R = *m*-$NHSO_2NH_2$) were identified as top inhibitors (~75% inhibition) toward Aβ40. In the ThT-based Aβ42 aggregation kinetics assay, only couple of compounds (**6a** and **6b**) in this series exhibited inhibition of aggregation at all concentration tested, which shows that *N*-methylation was detrimental toward their Aβ42 aggregation. Compound **6a** (R = *p*-$NHSO_2CH_3$), **6e** (R = *p*-$NHSO_2CH(CH_3)_2$) and **6j** (R = *p*-$NHSO_2NH_2$) exhibited superior anti-aggregation activity profile toward Aβ42 aggregation based on the data obtained from the 24 h ThT kinetics experiment with 94–96% inhibition. In the HT22 cytotoxicity assay, all the compounds were able to exhibit neuroprotection with compound **6h** (R = *m*-$NHSO_2CH_2CF_3$) exhibiting excellent cell viability toward Aβ40-induced toxicity that was

identified as the top compound with cell viability >95% whereas in the Aβ42-induced cytotoxicity assay only compound **6a** was able to rescue HT22 from Aβ42-induced toxicity. These studies provide further evidence on developing *N*,4-diphenylthiazol-2-amine derivatives as novel class of anti-AD agents.

6.5 Experimental

6.5.1 Chemistry

6.5.1.1 Materials and Methods

General information. All the reagents and solvents were purchased from various vendors (Sigma-Aldrich, Oakwood Chemical, Matrix Scientific, TCI Chemicals, Aablocks, and Ark Pharm Inc.) with a minimum purity of 95% and were used without further purification. Melting points (mp) were determined using a Fisher-Johns apparatus and are uncorrected. Compound purification was carried out using Merck 230-400 mesh silica gel 60. All derivatives showed single spot on thin-layer chromatography (TLC) performed on Merck 60 F254 silica gel plates (0.2 mm) using variety of solvent systems and TLC spots were visualized with the handheld UV lamp 254/365 nm. ^{1}H NMR and ^{13}C NMR spectra were analyzed using a Bruker Avance 300 MHz series spectrometer in deuterated solvents. Data was analyzed using the Bruker TOPSPIN 3.6.1 software. Coupling constant (*J* values) were recorded in hertz (Hz) and the following abbreviations were used for multiplicity of NMR signals: s = singlet, d = doublet, t = triplet, m = multiplet, br = broad. Compound purity and low resolution mass (LRMS) were evaluated using an Agilent 6100 series single quad LCMS equipped with an Agilent 1.8 μM Zorbax Eclipse Plus C18 (2.1 x 50 mm) running 30:70 Water:ACN with 0.1% FA at a flow rate of 0.5 mL/min. All the final compounds were > 95% pure as determined by calculating

the peak area by LCMS (UV detector, 254 nm). High-resolution mass spectrometry data were obtained by carrying out a positive ion electrospray (ESI) experiments on using a Thermo Scientific Q-Exactive hybrid mass spectrometer, Department of Chemistry, University of Waterloo. Accurate mass determinations were performed at a mass resolution of 70,000 (@m/z200) with lock mass correction. All samples were injected at 10 mL/min in a 1:1 MeOH/H_2O + 0.1% formic acid.

6.5.1.2 General procedure for the synthesis of N-methyl-N,4-diphenylthiazol-2-amine derivatives (6a-j).[230]

Compound **5a** or **5b** and pyridine (0.38 mL, 1.87 mmol) were added in DCM solution. This resulting mixture was then stirred at 0 °C for 10 min. To the same mixture, alkylsulfonyl chloride or sulfamoyl chloride (0.23 mL, 2.06 mmol) was added at such a rate as to prevent the temperature from rising above 10 °C, and stirred at RT for 23 h. The reaction mixture was quenched with 10 mL $NaHCO_3$ solution and washed three times with 20 mL brine solution. The aqueous layers were extracted with EtOAc (2 x 20 mL). The combined organic layers were dried over $MgSO_4$, filtered, and concentrated *in vacuo* to obtain the crude product, which was purified using the silica gel column chromatography with Hex:EtOAc (1:1) as the eluent. Yield ranged from 13 – 88%. The analytical data is given below:

N-(4-(2-(Methyl(phenyl)amino)thiazol-4-yl)phenyl)methanesulfonamide ***(6a)***. Yield: 79%. m.p. 137-140 °C. ^{1}H NMR (300 MHz, DMSO-d_6) δ (ppm): 9.78 (s, 1H), 7.82 (d, J = 7.5 Hz, 2H), 7.53-7.43 (m, 4H), 7.30-7.21 (m, 3H), 7.09 (s, 1H), 3.52 (s, 3H), 2.99 (s, 3H). HRMS (ESI) m/z calcd for $C_{17}H_{18}O_2N_3S_2$ $[M+H]^+$ 360.0834, found 360.0837. Purity: 99%.

*N-(3-(2-(Methyl(phenylamino)thiazol-4-yl)phenyl)methanesulfonamide (**6b**)*. Yield: 93%. m.p. 65-68 °C. ^{1}H NMR (300 MHz, DMSO-d_6) δ (ppm): 9.76 (s, 1H), 7.73 (s, 1H), 7.60-7.45 (m, 5H), 7.37-7.27 (m, 2H), 7.17-7.15 (m, 2H), 3.54 (s, 3H), 3.00 (s, 3H). HRMS (ESI) m/z calcd for $C_{17}H_{18}O_2N_3S_2$ $[M+H]^+$ 360.0834, found 360.0837. Purity: 98%.

*N-(4-(2-(Methyl(phenylamino)thiazol-4-yl)phenyl)ethanesulfonamide (**6c**)*. Yield: 48%. m.p. 60-65 °C. ^{1}H NMR (300 MHz, DMSO-d_6) δ (ppm): 9.84 (s, 1H), 7.81 (d, J = 8.3 Hz, 2H), 7.53-7.44 (m, 4H), 7.31-7.21 (m, 3H), 7.09 (s, 1H), 3.53 (s, 3H) 3.11 (q, J = 7.2 Hz, 2H), 1.19 (t, J = 6.8 Hz, 3H). HRMS (ESI) m/z calcd for $C_{18}H_{20}O_2N_3S_2$ $[M+H]^+$ 374.0991, found 374.0998. Purity: 95%.

*N-(3-(2-(Methyl(phenylamino)thiazol-4-yl)phenyl)ethanesulfonamide (**6d**)*. Yield: 40%. m.p. 63-65 °C. ^{1}H NMR (300 MHz, DMSO-d_6) δ (ppm): 9.81 (s, 1H), 7.75 (t, J = 1.7 Hz, 1H), 7.57-7.44 (m, 5H), 7.36-7.26 (m, 2H), 7.16 (d, J = 1.2 Hz, 1H), 7.14 (s, 1H), 3.53 (s, 3H), 3.11 (q, J = 7.4 Hz, 2H), 1.20 (t, J = 7.4 Hz, 3H). HRMS (ESI) m/z calcd for $C_{18}H_{20}O_2N_3S_2$ $[M+H]^+$ 374.0991, found 374.0995. Purity: 96%.

*N-(4-(2-(Methyl(phenylamino)thiazol-4-yl)phenyl)propane-2-sulfonamide (**6e**)*. Yield: 4%. m.p. 160-163 °C. ^{1}H NMR (300 MHz, DMSO-d_6) δ (ppm): 9.80 (s, 1H), 7.80 (d, J = 8.5 Hz, 2H), 7.53-7.44 (m, 4H), 7.30-7.23 (m, 3H), 7.08 (s, 1H), 3.52 (s, 3H), 3.29-3.20 (m, 1H), 1.25 (d, J = 6.9 Hz, 6H). HRMS (ESI) m/z calcd for $C_{19}H_{22}O_2N_3S_2$ $[M+H]^+$ 388.1147, found 388.1151. Purity: 99%.

N-(3-(2-(Methyl(phenylamino)thiazol-4-yl)phenyl)propane-2-sulfonamide ***(6f)***. Yield: 3%. m.p. 62-64 °C. ^{1}H NMR (300 MHz, DMSO-d_6) δ (ppm): 9.78 (s, 1H), 7.77 (s, 1H), 7.55-7.44 (m, 5H), 7.32 (q, J = 7.9 Hz, 2H), 7.17 (dd, J = 1.3, 1.3 Hz, 1H), 7.13 (s, 1H), 3.53 (s, 3H), 3.24 (m, 1H), 1.26 (d, J = 7.0 Hz, 6H). HRMS (ESI) m/z calcd for $C_{19}H_{22}O_2N_3S_2$ $[M+H]^+$ 388.1147, found 388.1150. Purity: 95%.

2,2,2-Trifluoro-N-(4-(2-(methyl(phenylamino)thiazol-4-yl)phenyl)-2-ethane-1-sulfonamide ***(6g)***. Yield: 66%. m.p. 59-61 °C. ^{1}H NMR (300 MHz, DMSO-d_6) δ (ppm): 10.49 (s, 1H), 7.85 (d, J = 8.7 Hz, 2H), 7.54-7.44 (m, 4H), 7.31-7.23 (m, 3H), 7.13 (s, 1H), 4.54 (q, J = 9.5 Hz, 2H), 3.53 (s, 3H). HRMS (ESI) m/z calcd for $C_{18}H_{17}O_2N_3F_3S_2$ $[M+H]^+$ 428.0708, found 428.0709. Purity: 95%.

2,2,2-Trifluoro-N-(3-(2-(methyl(phenylamino)thiazol-4-yl)phenyl)ethane-1-sulfonamide ***(6h)***. Yield: 52%. m.p. 108-110 °C. ^{1}H NMR (300 MHz, DMSO-d_6) δ (ppm): 10.47 (s, 1H), 7.74 (s, 1H), 7.65 (d, J = 8.2 Hz, 1H), 7.58-7.45 (m, 5H), 7.40-7.27 (m, 2H), 7.17-7.16 (m, 1H), 4.53 (q, J = 9.7 Hz, 2H), 3.54 (s, 2H). HRMS (ESI) m/z calcd for $C_{18}H_{17}O_2N_3F_3S_2$ $[M+H]^+$ 428.0708, found 428.0709. Purity: 97%.

(3-(2-(Methyl(phenyl)amino)thiazol-4-yl)benzenesulfamide ***(6j)***. Yield: 21%. m.p. 191-194 °C. ^{1}H NMR (300 MHz, DMSO-d_6) δ (ppm): 9.56 (s, 1H), 7.77 (d, J = 8.3 Hz, 2H), 7.53-7.44 (m, 4H), 7.28 (t, J = 7.0 Hz, 1H), 7.18 (d, J = 8.6 Hz, 2H), 7.11 (s, 2H), 7.05

(s, 1H), 3.53 (s, 3H). HRMS (ESI) m/z calcd for $C_{16}H_{17}O_2N_4S_2$ $[M+H]^+$ 361.07874, found 361.07876. Purity: 95%.

6.5.2 Biological Screening

6.5.2.1 Amyloid-β (Aβ) Aggregation Assay

Thioflavin T (ThT) is a benzothiazole dye that was used to detect the formation of amyloid aggregates in solution. The excitation and emission properties of ThT changes when it binds to the β-sheet structures of Aβ40/Aβ42 oligomers and fibrils.[145] In this regard, the anti-Aβ aggregation activity sulfonamide and sulfamide based *N*,4-diphenylthiazol-2-amine based derivatives (**6a-j**) was evaluated using ThT-based fluorescence assays. These assays were conducted in Costar, black, clear-bottomed 384-well plates with frequent shaking at 730 cpm under constant heating at 37 °C for 24 h. The excitation and emission of ThT were recorded at 440 and 490 nm, respectively. Readings were taken every 5 min using a BioTek Synergy H1 microplate reader. Test compounds were prepared in 215 mM phosphate buffer at pH 7.4. 0.5 mg of Aβ•HFIP samples (AnaSpec, CA, USA) was dissolved in 1% ammonium hydroxide solution for Aβ40 or 10% ammonium hydroxide for Aβ42, sonicated at RT for 5 min, and diluted to 50 μM in phosphate buffer. A 15 μM ThT stock solution was prepared. To each ThT background well, 44 μL ThT, 35 μL phosphate buffer, and 1 μL DMSO were added. To the Aβ control wells, 44 μL ThT, 28 μL phosphate buffer, and 8 μL Aβ40/42 (5 μM final concentration) were added. To each test compound containing wells, 44 μL ThT, 20 μL phosphate buffer, 1 μL DMSO, and 8 μL test compound in various concentrations (1, 5, 10, and 25 μM), and 8 μL of Aβ were added. ThT interferences were taken before the

addition of 8 μL of Aβ40 or Aβ42 stock solution (5 μM final concentration). Known Aβ40 and Aβ42 aggregation inhibitors MB and RES were also evaluated for comparison. Plates were sealed with a ThermoSeal film (Sigma Aldrich) before placing the plates in the reader. Data presented was an average of triplicate reading for two-three independent experiments.

6.5.2.2 Transmission Electron Microscopy (TEM) Studies

The Aβ40 and Aβ42 aggregate morphology was examined by performing TEM experiment in the presence and absence of test compounds. TEM samples were prepared in Costar, round-bottomed 384-well plates with test compounds (25 μM). To the Aβ control wells, 44 μL ThT, 28 μL phosphate buffer, and 8 μL Aβ40/42 (5 μM final concentration) were added. To each test compound containing well, 44 μL ThT, 20 μL phosphate buffer, 1 μL DMSO, and 8 μL of test compound (25 μM), and 8 μL of Aβ40/42 were added. The plates were incubated on a BioTek Synergy H1 microplate reader at 37 °C and shaken at 730 cpm for 24 h.

TEM grids were prepared by adding 20 μL test compound over the formvar-coated copper grids (400 mesh) *via* the use of a Pasteur pipette, which were then air-dried for 3 h or longer before washing them with 20 μL of ultrapure water (UPW) to remove any precipitated buffer salt. The sample grids were air-dried for 30 min. Once the grids were dry, they were stained with 20 μL of 2% phosphotungstic acid (PTA). The excess of PTA was removed by blotting with filter paper. The grids were allowed to dry overnight. Scanning of these grids was performed using a Philips CM10 TEM at 60 kV (Department

of Biology, University of Waterloo), and micrographs were collected using a 14-megapixel AMT camera.

6.5.2.3 Computation Modeling

Molecular docking studies of sulfonamide and sulfamide based *N*,4-diphenylthiazol-2-amines derivatives with Aβ peptides were conducted *via* the computational chemistry Discovery Studio (DS) software – Structure-Based-Design (SBD), version 4.0 from BIOVA Inc. (San Diego, USA).[220] The *Small Molecules* module was used to build the sulfonamide and sulfamide based *N*,4-diphenylthiazol-2-amine derivatives, which were in turn docked with Aβ40 and Aβ42 dimer models obtained from protein data bank (pdb id: 2LMN and 5KK3) using the CDOCKER algorithm in the *Receptor-Ligand Interactions* module in DS using CHARMm force field.[220,221] CDOCKER algorithm uses simulated annealing protocol to determine the best ligand binding modes. The sulfonamide and sulfamide based *N*,4-diphenylthiazol-2-amine derivatives were built in 3D using *Build Fragment* tool; energy minimization was applied for 1000 iterations using steepest descent and conjugate gradient minimizations, respectively. The ligands were minimized using the Smart Minimization protocol (200 steps, RMS gradient 0.1 kcal/mol), CHARMm force field and a distance depended dielectric constant. For the docking of *N*-diphenylthiazol-amine derivatives in Aβ40 and Aβ42 dimer models, the binding site was defined by a 20 Å radius sphere. Molecular docking was carried out by the CDOCKER algorithm, which includes 2000 heating steps, 700 K target temperature, 300 K cooling temperature target with 5000 cooling steps. The docked poses obtained were ranked using the CDOCKER energy and CDOCKER interaction energy parameters (kcal/mol). The protein-ligand complexes were evaluated

by examining various polar and nonpolar interactions, such as hydrogen bonding, electrostatic, *van der* Waal's, and hydrophobic interactions.

6.5.2.4 Cell Viability Assay

The HT22 hippocampal cells were plated at a density of 10,000 cells/100 μL in Nunclon Delta 96-well plates with complete growth media consisting of DMEM and Ham's F12 in a 1:1 ratio, supplemented with 10% fetal bovine serum (FBS) and 1% penicillin-streptomycin (10,000 U/mL) at 37 °C in 5% CO_2. The cells were incubated at 37 °C for 24 h. To each untreated well, 100 μL DMEM/F-12 was added. To the Aβ control wells, 85 μL DMEM/F-12, 10 μL PBS, and 5 μL Aβ40/42 (5 μM final concentration) were added. To each test compound containing wells, 85 μL DMEM/F-12, 10 μL filter-sterilized test compounds (**6a-j** and RES) in concentration of 10 μM in triplicates (n = 3), and 5 μL of Aβ40/42 were added. These cells were then incubated at 37 °C for 24 h. The MTT reagent solution[222] made of thiazolyl blue tetrazolium bromide powder (Sigma Aldrich) in PBS to 5 mg/mL and filter-sterilized through a 0.22 μm filter was added in 10% of the culture medium volume (DMEM/F-12, HEPES, no phenol red) to each well and the cells were cultured for an additional 2-3 h. After incubation, the resulting formazan crystals were solubilized with the solubilisation solution prepared from a mixture of IPA, 10% Triton X-100 and 1% HCl (12M). The absorbance was taken at 570 and 690 nm. All results were presented as a relative percent of (4,5-dimethylthiazol-2-yl)-2,5-diphenyl tetrazolium bromide (MTT) to untreated controls. Known Aβ aggregation inhibitor resveratrol (RES) was used as a reference agent for comparison.

CHAPTER 7 Development of *N*,2-Diphenylthiazol-4-amines

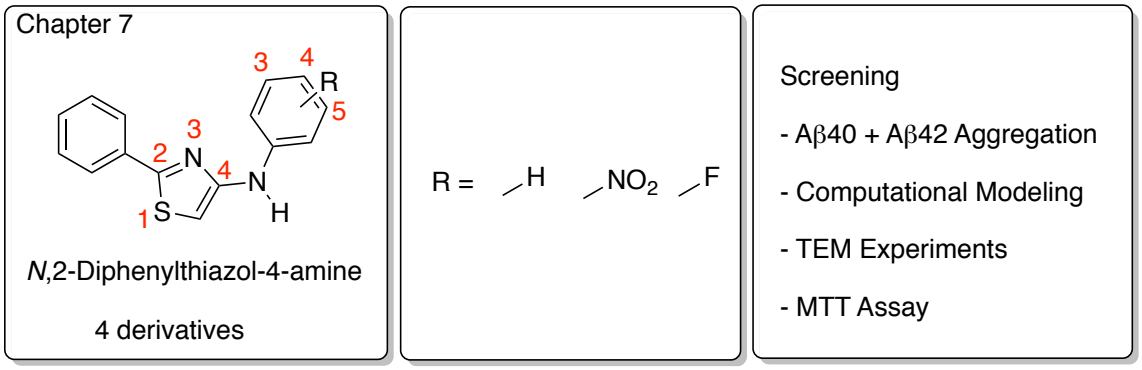

Figure 77. Banner for Chapter 7

7.1 Introduction

In this chapter, a small library of novel class of diphenylthiazole-amine derivatives were synthesized and evaluated to investigate their anti-aggregation properties. These compounds are regioisomers of *N*,4-diphenylthiazol-2-amines discussed in previous chapters (Chapters 3, 4, 5 and 6) and are the corresponding *N*,2-diphenylthiazol-4-amine isomers which possess a central thiazole-4-amine instead of a thiazole-2-amine. They contained H, NO_2, or F substituent at the *para*-position of the substituted phenyl ring (Figure 77). The synthetic methodology, analytical data, biological assay results based on ThT-based fluorescence aggregation kinetic studies, transmission electron microscopy (TEM) experiments, computational modeling and their neuroprotective activity toward Aβ40- or Aβ42-induced cytotoxicity in mouse hippocampal neuronal cells (HT22) are reported.

7.2 Hypothesis

For this series of *N*,2-diphenylthiazol-4-amine derivatives, we hypothesize that (i) the diphenyl rings undergo hydrophobic interactions only at the N-terminal region in the

Aβ40 dimer model and therefore exhibit reduced inhibition of Aβ40 aggregation compared to the corresponding *N*,4-diphenylthiazol-2-amine regioisomers; (ii) incorporating *para*- and *meta*-substituents at the thiazole C4 phenyl ring enhance their binding and inhibition toward both Aβ40 and Aβ42; (iii) *N*,2-diphenylthiazol-4-amine regioisomers are able to exhibit superior inhibition of Aβ42 aggregation compared to the corresponding *N*,4-diphenylthiazol-2-amines due to the interaction of the phenyl ring (thiazole C4) with polar amino acids Glu11 and Lys16.

7.3 Results and Discussion

7.3.1 Synthesis

The *N*,2-diphenylthiazol-4-amine derivatives **7a-d** were synthesized according to the synthetic route outlined in Scheme 5. They were synthesized via the cyclization of thiobenzamide with 2-chloro-*N*-phenylacetamide. Reaction mechanism is given in Figure 78. The purified *N*,2-diphenylthiazol-4-amine derivatives were characterized by ^{1}H and ^{13}C NMR, LCMS and HRMS analysis. The yields of the desired target compounds (**7a-d**) ranged from 3–55%.

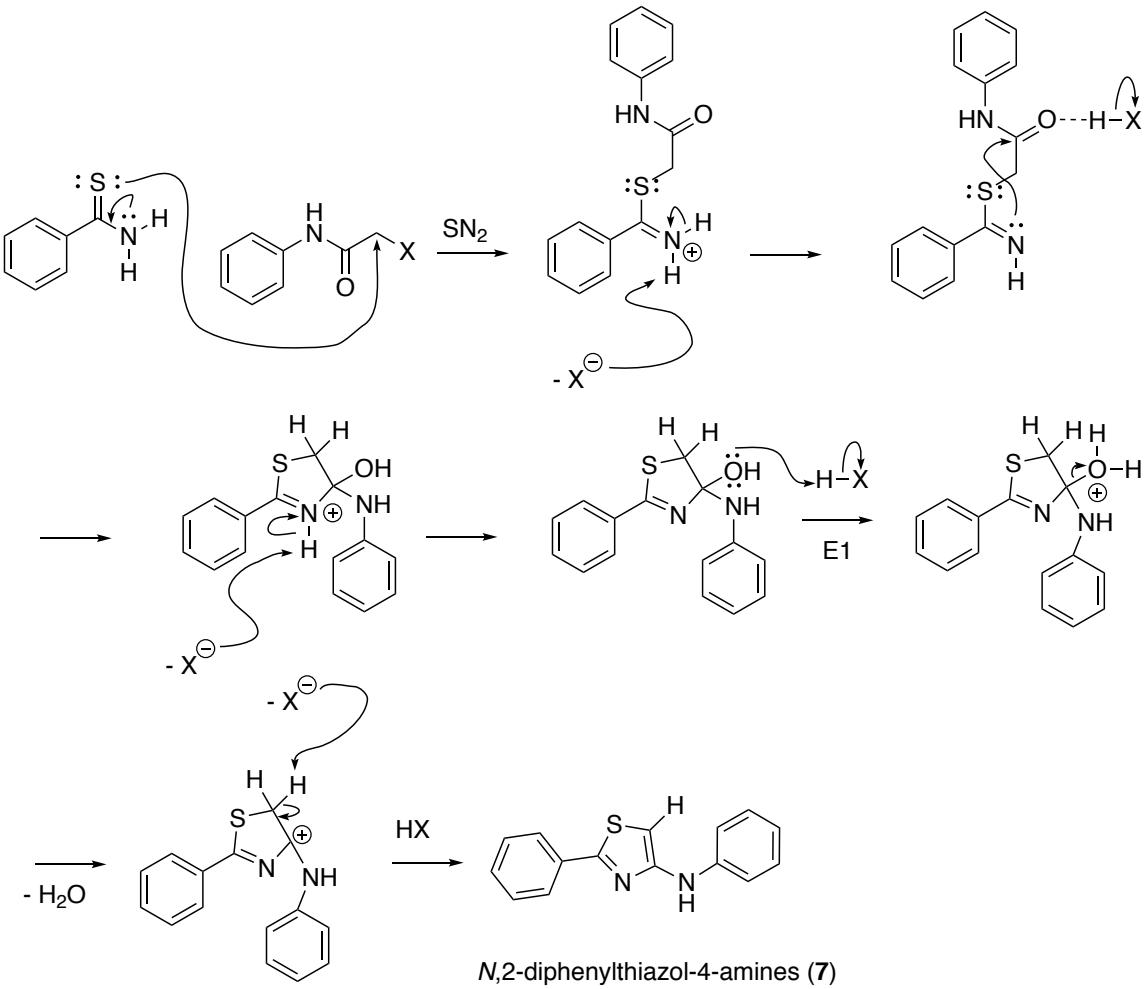

Figure 78. Synthetic mechanism of the *N*,2-diphenylthiazol-4-amine derivatives **7a-d**.

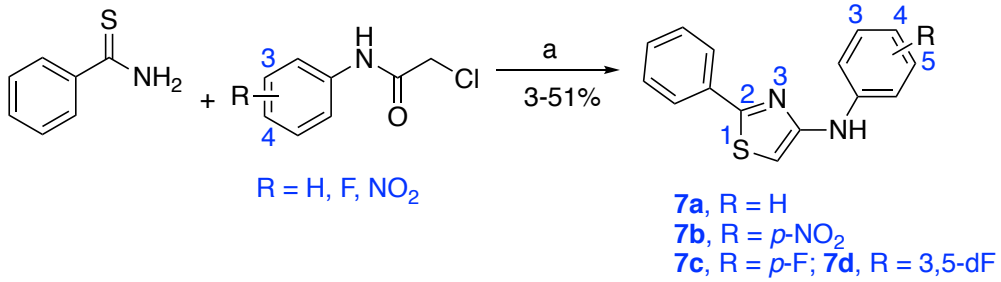

*Reagents and conditions: (a) DMF, 80 °C, 16 h.

Scheme 5. Synthetic route toward the *N*,2-diphenylthiazol-4-amine derivatives **7a-d**.

7.3.2 Amyloid-β (Aβ) Aggregation Inhibition Studies

The anti-aggregation properties of *N*,2-diphenylthiazol-4-amine derivatives **7a-d** toward Aβ40, was investigated using the ThT-based assay over a 24 h time period and the results are shown in Table 11. The unsubstituted compound **7a** exhibited a concentration dependent activity by inhibiting Aβ40 aggregation and showed 67% inhibition at the highest tested concentration of 25 μM. Presence of EWGs such as *p*-NO_2, *p*-F and 3,5-diF led to a reduction in their inhibition activity (18–45% inhibition range, Table 11). None of the compounds tested were as potent as the reference agents MB and RES. The 24 h aggregation kinetic for the best compound in this series **7a** is shown in Figure 79. This shows that **7a** was able to reduce the ThT fluorescence intensity along with increasing concentrations. The kinetic plots indicate that **7a** was primarily acting on the growth phase in the Aβ40 fibrillogenesis pathway and was able to reduce the formation of higher order aggregates. The anti-aggregation activity order for this set of *N*,2-diphenylthiazol-4-amine derivatives was of the order: H > *p*-F > *p*-NO_2 > 3,5-diF (at 25 μM). Due to the limited number of compounds, no clear SAR trend could be SAR obtained for this series of compounds. Therefore it is not possible to compare them with the corresponding *N*,4-diphenylthiazol-2-amine derivatives discussed in Chapter 3.

Table 11. Inhibition data for *N*,2-diphenylthiazol-4-amine derivatives **7a-d**, and reference compounds toward Aβ40 aggregation, and their ClogP values.

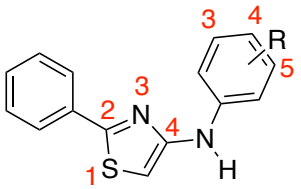

7

R = H, NO_2, F

Compound	R-group	% Inhibition for Aβ40 [a]				ClogP [b]
		1 μM	5 μM	10 μM	25 μM	
7a	*H*	24	40	49	67	3.87
7b	*p-NO_2*	NA	NA	NA	28	2.64
7c	*p*-F	NA	NA	NA	45	4.01
7d	*3,5-diF*	NA	NA	NA	18	4.15
MB	-	87	97	97	99	3.62
RES	-	81	94	95	98	2.83

[a]Percent aggregation inhibition values were average ± SD < 10% (n = 3) for three independent experiments. NA – Not Active. [b]ClogP values were determined using ChemDraw 19.1.

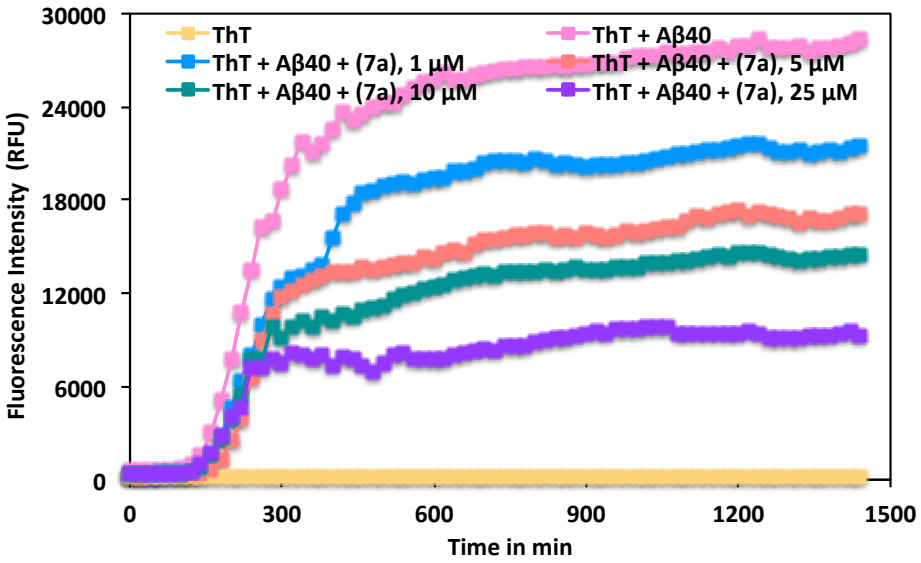

Figure 79. ThT-monitored 24 h aggregation kinetics of Aβ40 (5 μM) in the presence of 1, 5, 10, and 25 μM of *N*,4-diphenylthiazol-2-amines (**7a**) at pH 7.4, 37 °C in phosphate buffer. Aggregation kinetics were monitored by ThT-fluorescence spectroscopy (excitation = 440 nm, emission = 490 nm). Results are average ± SD of three independent experiments (n = 3).

The anti-aggregation properties of *N*,2-diphenylthiazol-4-amine derivatives **7a-d** toward Aβ42, was investigated using the ThT-based assay over a 24 h time period and the results are shown in Table 12. Interestingly, all these compounds exhibited excellent inhibition of Aβ42 aggregation and their activity was comparable to reference agents MB and RES, ranging from 93–96% at 25 μM. The presence of EWGs such as *p*-NO_2, *p*-F and 3,5-diF did not seem to affect their Aβ42 aggregation inhibition properties. The 24 h aggregation kinetic for a representative compound in this series **7b** is shown in Figure 80. This shows that **7b** was able to reduce the ThT fluorescence intensity along with increasing concentrations. The kinetic plot indicates that **7b** was able to reduce and prevent the growth phase in the Aβ42 fibrillogenesis pathway thereby reducing the formation of higher order aggregates. No clear SAR trend was seen due to the limited number of compounds tested. However the results obtained do suggest that these

compounds exhibit superior inhibition of Aβ42 aggregation compared to the *N*,4-diphenylthiazol-2-amine isomers discussed in Chapter 3. Further studies are required to confirm these findings.

Table 12. Inhibition data for *N*,2-diphenylthiazol-4-amine derivatives **7a-d**, and reference compounds toward Aβ42 aggregation, and their ClogP values.

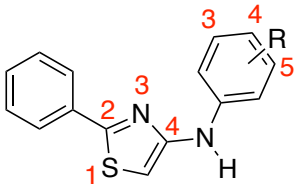

7

R = H, NO_2, F

Compound	R-group	% Inhibition for Aβ42 [a]				ClogP [b]
		1 μM	5 μM	10 μM	25 μM	
7a	*H*	42	26	49	93	3.87
7b	*p-NO₂*	18	44	95	96	2.64
7c	*p*-F	28	55	62	95	4.01
7d	*3,5-diF*	14	NA	23	95	4.15
MB	-	87	97	97	99	3.62
RES	-	81	94	95	98	2.83

[a]Percent aggregation inhibition values were average ± SD < 10% (n = 3) for three independent experiments. NA – Not Active. [b]ClogP values were determined using ChemDraw 19.1.

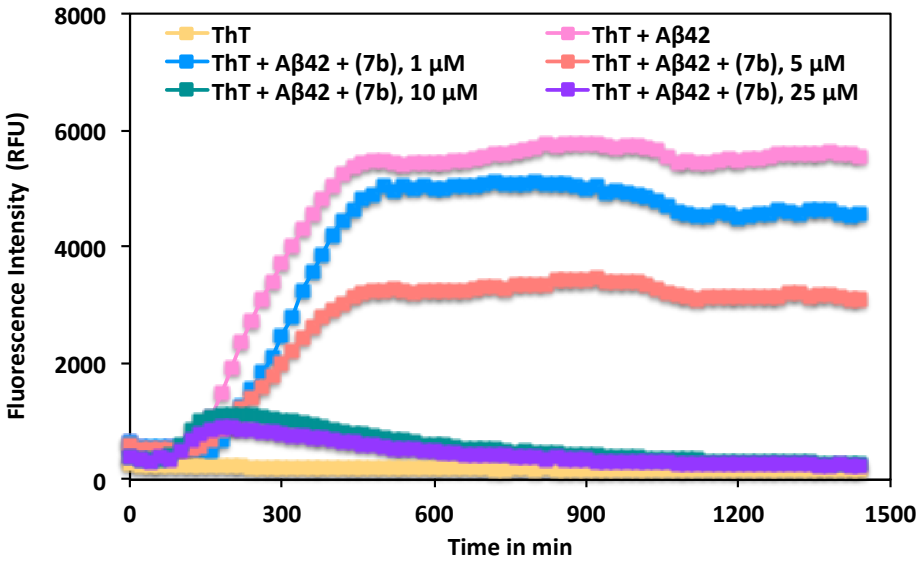

Figure 80. ThT-monitored 24 h aggregation kinetics of Aβ42 (5 μM) in the presence of 1, 5, 10, and 25 μM of *N*,4-diphenylthiazol-2-amines (**7b**) at pH 7.4, 37 °C in phosphate buffer. Aggregation kinetics were monitored by ThT-fluorescence spectroscopy (excitation = 440 nm, emission = 490 nm). Results are average ± SD of three independent experiments (n = 3).

7.3.3 Computational Modeling Studies

The binding interactions of most potent *N*,2-diphenylthiazol-4-amine derivatives was investigated by conducting molecular docking studies using the solved structures of Aβ40 and Aβ42 peptides.[212,213] Docking studies were carried out using the dimer assemblies of both Aβ40 and Aβ42 peptides as they represent the early forms of Aβ in solution. In the *N*,2-diphenylthiazol-4-amine series, compound **7a** (*N*,2-diphenylthiazol-4-amine) was identified as the most potent inhibitor of Aβ40 aggregation in the ThT-based fluorescence assay (67% inhibition at 25 μM). Figure 81 Panel A, shows the predicted binding mode of **7a** in the Aβ40-dimer model. This compound was interacting in the KLVFFA region at the N-terminal and with Val36 at the C-terminal. The central thiazole underwent couple of π-π T-shaped interactions with Phe19 and Phe20 aromatic rings (distance < 5 Å). It was interesting to note that in this regioisomer, the central thiazole ring (*N*,2-diphenylthiazol-4-amine) was involved in Aβ40 dimer binding which

was not seen previously in the thiazole-2-amine regioisomer (*N*,4-diphenylthiazol-2-amine). Furthermore, similar to the *N*,4-diphenylthiazol-2-amine regioisomer binding, the NH group in compound **7a** was involved in forming hydrogen bond with Val18 backbone, whereas the phenyl ring underwent π-alkyl interaction with Val18. At this point it is not clear if *N*,2-diphenylthiazol-4-amine isomers would exhibit better inhibition of Aβ40 aggregation relative to the corresponding *N*,4-diphenylthiazol-2-amine isomers. Additional SAR studies will be required to investigate this. Nevertheless, it appears that compound **7a** can bind and prevent Aβ40 aggregation.

In the *N*,2-diphenylthiazol-4-amine series, compound **7b** (*N*-(4-nitrophenyl)-2-phenylthiazol-4-amine) was identified as the most potent inhibitor of Aβ42 aggregation in the ThT-based fluorescence assay (96% inhibition at 25 μM). Figure 81 Panel B, shows the predicted binding mode of **7b** in the Aβ42-dimer model. This compound was bound in the KLVFFA pocket where the 4-nitrophenyl ring was close to Lys16, Val18 and Ala21. The nitro group underwent polar interactions with Lys16 side chain, and the phenyl ring underwent hydrophobic interactions with Val18 and Ala21 side chains (distance < 5 Å). The central thiazole ring was also in contact with Ala21 whereas the NH formed hydrogen-bonding interaction with backbone of Ala21 (distance = 2.3 Å) and the C2 phenyl ring underwent cation interaction with Lys16 side chain (distance < 3 Å). All these suggest that *N*,2-diphenylthiazol-4-amine series hold promise as novel class of Aβ aggregation inhibitors.

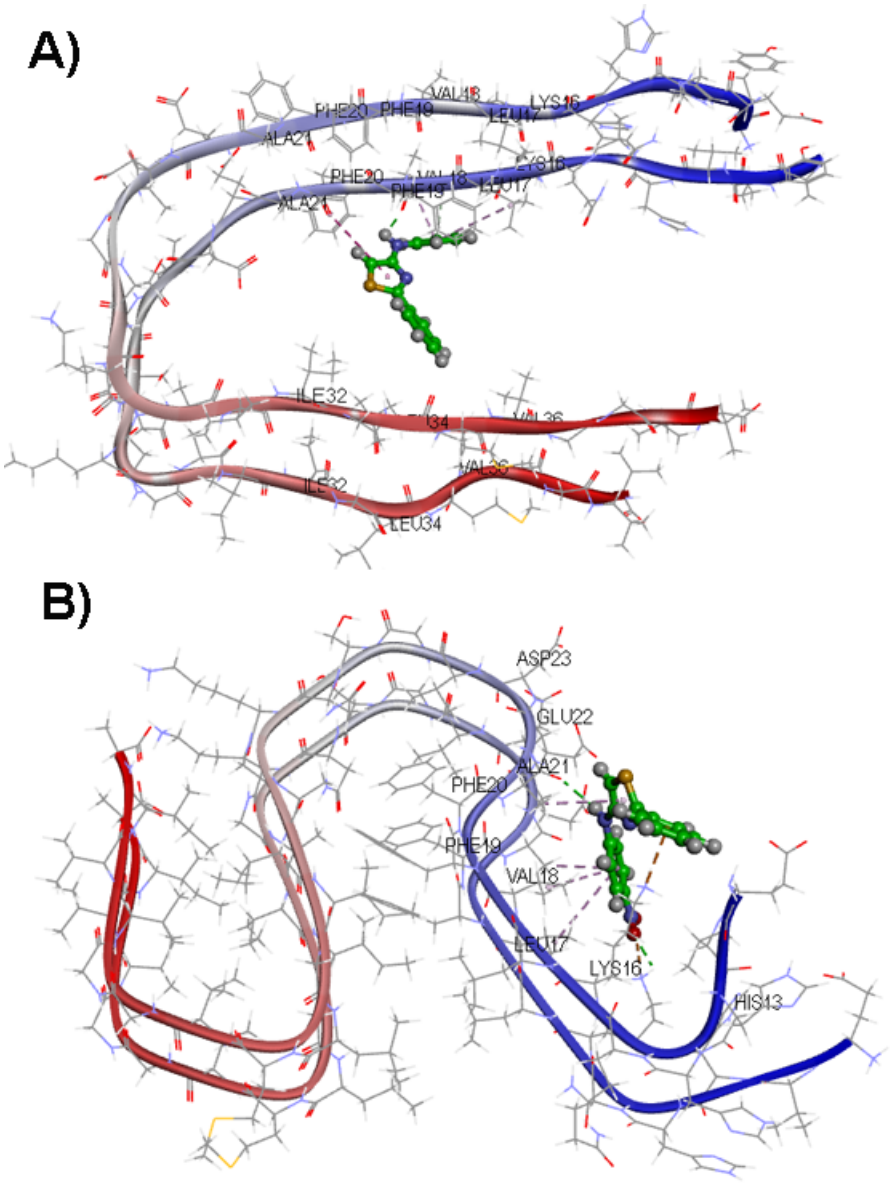

Figure 81. Panel A: Predicted binding mode of **7a** (ball and stick cartoon) in the Aβ40-dimer model (ribbon diagram, pdb id: 2LMN, CDOCKER energy = –8.90 kcal/mol; CDOCKER interaction Energy = –18.95 kcal/mol). Panel B: Predicted binding mode of **7b** (ball and stick cartoon) in the Aβ42-dimer model (ribbon diagram, pdb id: 5KK3, CDOCKER energy = –8.81 kcal/mol; CDOCKER interaction energy = –23.40 kcal/mol).

7.3.4 Transmission Electron Microscopy (TEM) Studies

The amyloid morphology of the *N*,2-diphenylthiazol-4-amine derivatives was conducted using **7a** as a representative example. As observed in Figure 82, co-incubation

of Aβ40 with **7a** (5 μM, Panel A) and Aβ42 with **7a** (5 μM, Panel B) led to a reduction in the formation of Aβ40/42 fibrils. This validated the anti-aggregation properties observed in the *N*,2-diphenylthiazol-4-amine derivative.

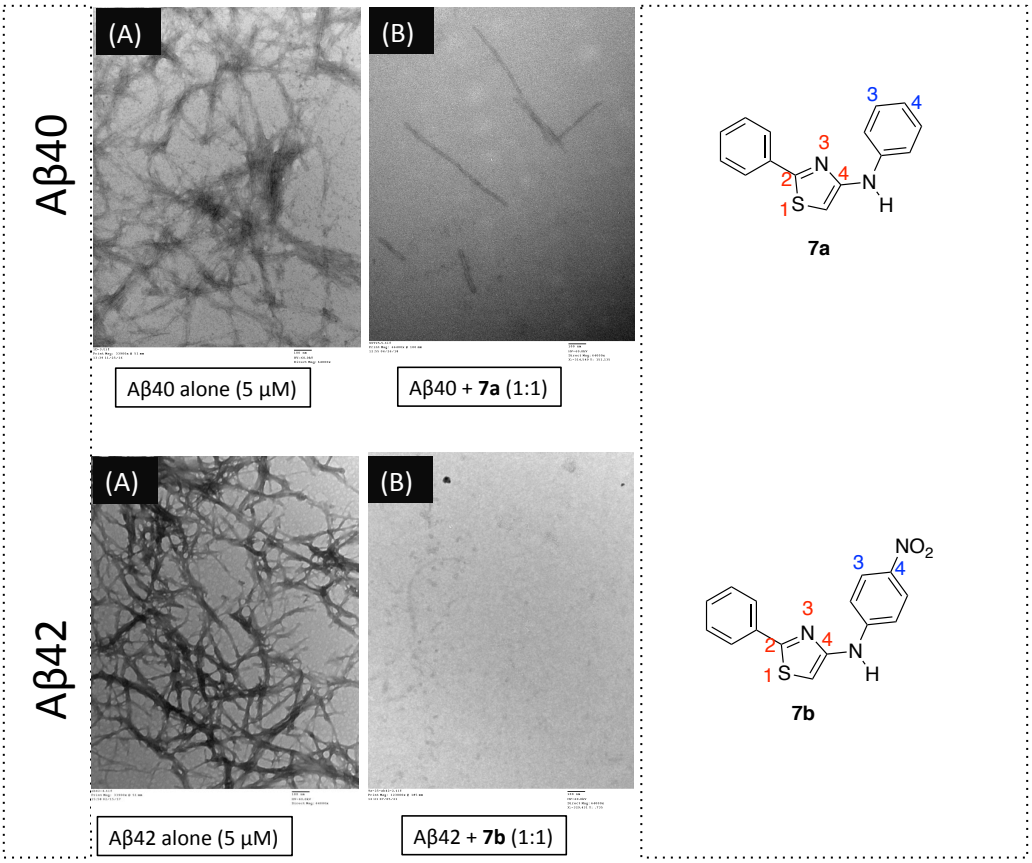

Figure 82. TEM images of Aβ40 and Aβ42 aggregation. Top: Panel A: Aβ40 control (5 μM). Panel B: Aβ40 + **7a** (5 μM). Bottom: Panel A: Aβ42 control (5 μM). Panel B: Aβ42 + **7b** (5 μM). Scale bars represent 100 nm.

7.3.5 Cell Viability Assay

The neuroprotective effect of *N*,2-diphenylthiazol-4-amines **7a-d** was evaluated by investigating the cell viability in HT22 hippocampal derived-cells exposed to Aβ40 (5 μM). The results are summarized in Figure 83. In the presence of Aβ40 alone the cell viability reduced to 63%. Strikingly, in the presence of 10 μM of **7a** or **7b**, there was

remarkable neuroprotection with cell viability ranging from 82-100% (Figure 83). Compound **7c** (R = *p*-F) was not effective in reducing Aβ40 induced cytotoxicity (cell viability 64%) whereas compound **7a** (R = H, cell viability >99%) was identified as the best compound from this group.

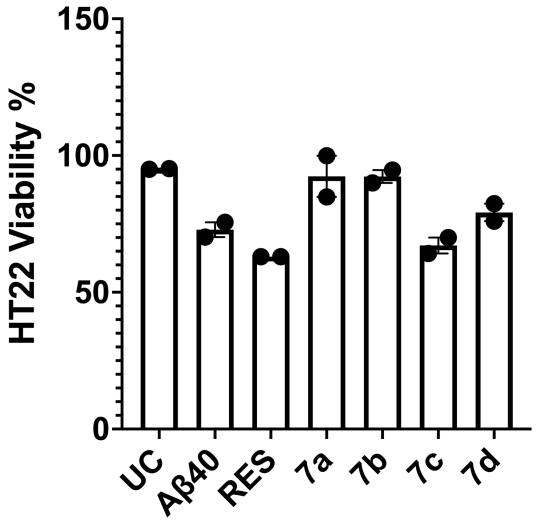

Figure 83. Percentage viability of the *N*,2-diphenylthiazol-4-amine derivatives **7a-d** and RES (10 μM) in HT22 cells treated with Aβ40 was assessed by MTT assay after 24 h incubation at 37 °C. The results were given as average of two independent experiments (n = 3). UC = untreated cells, RES = resveratrol.

The neuroprotective effect of *N*,2-diphenylthiazol-4-amines **7a-d** was evaluated by investigating the cell viability in HT22 hippocampal derived-cells exposed to Aβ42 (5 μM). The results are summarized in Figure 84. In the presence of Aβ42 alone the cell viability reduced 50%. Strikingly, all the tested compounds were able to offer excellent neuroprotection toward Aβ42 mediated cytotoxicity with cell viability ranging from 72-87% (Figure 84). Compound **7d** (R = 3,5-diF) was identified as the best compound from this set (cell viability = 87%).

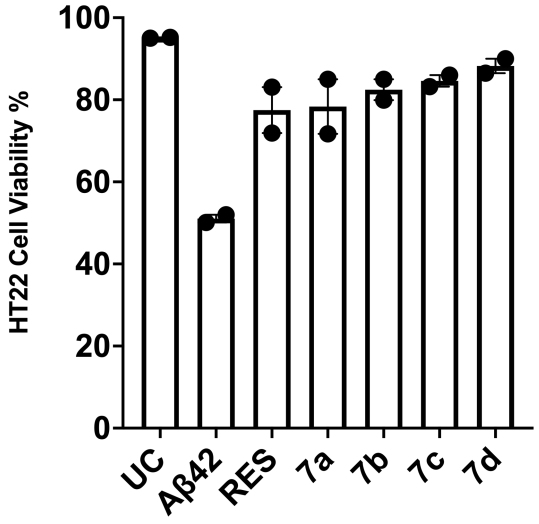

Figure 84. Percentage viability of the *N*,4-diphenylthiazol-2-amine derivatives **7a-d** and RES (10 μM) in HT22 cells treated with Aβ42 was assessed by MTT assay after 24 h incubation at 37 °C. The results were given as average of two independent experiments (n = 3). UC = untreated cells, RES = resveratrol.

7.4 Summary

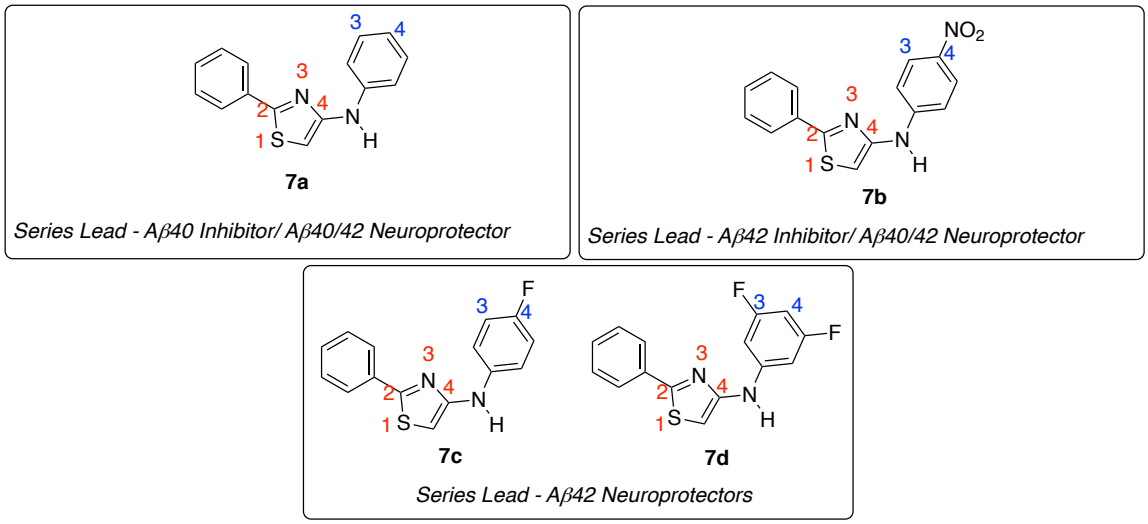

Figure 85. Cumulative chapter summary of *N*,2-diphenylthiazol-4-amines (**7**).

The anti-Aβ activity of *N*,2-diphenylthiazol-4-amines **7a-d** was evaluated in vitro by ThT-based fluorescence spectroscopy, TEM studies, computational modeling and cell culture studies. The results from these studies demonstrate that *N*,2-diphenylthiazol-4-

amines which are the regioisomers of corresponding *N*,4-diphenylthiazol-2-amines demonstrate promising activity toward both Aβ40 and Aβ42 aggregation inhibition with activity ranging from 18–96% at 25 μM. The unsubstituted *N*,2-diphenylthiazol-4-amine **7a** exhibited a good combination of Aβ40 and Aβ42 aggregation inhibition activity (67% and 93% inhibition at 25 μM). Compounds in this series were also able to demonstrate their neuroprotective activity in cell culture studies. In summary, we have demonstrated the potential of *N*,2-diphenylthiazol-4-amines as novel candidates which can target the amyloid cascade in AD. Further SAR optimization would be required to understand their anti-Aβ activity and SAR.

7.5 Experimental

7.5.1 Chemistry

7.5.1.1 Materials and Methods

General information. All the reagents and solvents were purchased from various vendors (Sigma-Aldrich, Oakwood Chemical, Matrix Scientific, TCI Chemicals, Aablocks, and Ark Pharm Inc.) with a minimum purity of 95% and were used without further purification. Melting points (mp) were determined using a Fisher-Johns apparatus and are uncorrected. Compound purification was carried out using Merck 230-400 mesh silica gel 60. All derivatives showed single spot on thin-layer chromatography (TLC) performed on Merck 60 F254 silica gel plates (0.2 mm) using variety of solvent systems and TLC spots were visualized with the handheld UV lamp 254/365 nm. ^{1}H NMR and ^{13}C NMR spectra were analyzed using a Bruker Avance 300 MHz series spectrometer in deuterated solvents. Data was analyzed using the Bruker TOPSPIN 3.6.1 software. Coupling constant (*J* values) were recorded in hertz (Hz) and the following abbreviations

were used for multiplicity of NMR signals: s = singlet, d = doublet, t = triplet, m = multiplet, br = broad. Compound purity and low resolution mass (LRMS) were evaluated using an Agilent 6100 series single quad LCMS equipped with an Agilent 1.8 μM Zorbax Eclipse Plus C18 (2.1 x 50 mm) running 30:70 Water:ACN with 0.1% FA at a flow rate of 0.5 mL/min. All the final compounds were > 95% pure as determined by calculating the peak area by LCMS (UV detector, 254 nm). High-resolution mass spectrometry data were obtained by carrying out a positive ion electrospray (ESI) experiments on using a Thermo Scientific Q-Exactive hybrid mass spectrometer, Department of Chemistry, University of Waterloo. Accurate mass determinations were performed at a mass resolution of 70,000 (@m/z200) with lock mass correction. All samples were injected at 10 mL/min in a 1:1 MeOH/H_2O + 0.1% formic acid.

7.5.1.2 General procedure for the synthesis of N,2-diphenylthiazol-4-amine derivatives (7a-d).[231]

The appropriate 2-chloro-*N*-phenylacetamide (0.50 g, 2.43 mmol) was dissolved in DMF (25 mL), and to this solution, thiobenzamide (0.34 g, 2.48 mmol) was added under a gentle flow of argon. The reaction mixture was refluxed for 16 h at 80 °C. Then, the reaction was cooled to RT and washed three times with 20 mL brine solution. The aqueous layers were extracted with DCM (2 x 20 mL). The combined organic layers were dried over $MgSO_4$, filtered, and concentrated *in vacuo* to obtain the crude product, which was purified using the silica gel column chromatography with Hex:EtOAc (7:1) as the eluent. Yield ranged from 3 – 51%. The analytical data is given below:

*N,2-Diphenylthiazol-4-amine (**7a**)*.[200] Yield: 51%. m.p. 87-90 °C. ^{1}H NMR (300 MHz, DMSO-d_6) δ (ppm): 9.02 (s, 1H), 7.93 (dd, J = 1.87, 1.49 Hz, 2H), 7.54-7.47 (m, 3H),

7.31-7.21 (m, 4H), 6.84-6.78 (m, 1H), 6.71 (s, 1H). HRMS (ESI) m/z calcd for $C_{15}H_{13}N_2S_2$ $[M+H]^+$ 253.0794, found 253.0788. Purity: 95%.

*N-(4-Fluorophenyl)-2-phenylthiazol-4-amine (**7c**).* Yield: 3.3%. m.p. 146-148 °C. ^{1}H NMR (300 MHz, DMSO-d_6) δ (ppm): 9.00 (s, 1H), 7.92 (dd, *J* = 1.9, 1.7 Hz, 2H), 7.55-7.46 (m, 3H), 7.33-7.28 (m, 2H), 7.08 (t, *J* = 8.8 Hz, 2H), 6.64 (s, 1H). HRMS (ESI) m/z calcd for $C_{15}H_{12}N_2FS$ $[M+H]^+$ 271.0699, found 271.0704. Purity: 96%.

*N-(3,5-Difluorophenyl)-2-phenylthiazol-4-amine (**7d**).* Yield: 11%. m.p. 80-82 °C. ^{1}H NMR (300 MHz, DMSO-d_6) δ (ppm): 9.53 (s, 1H), 7.93 (dd, *J* = 1.8 Hz, 2H), 7.57-7.48 (m, 3H), 6.98-6.94 (m, 2H), 6.89 (s, 1H), 6.59-6.52 (s, 1H). HRMS (ESI) m/z calcd for $C_{15}H_{11}N_2F_2S$ $[M+H]^+$ 289.0605, found 289.0609. Purity: 98%.

7.5.2 Biological Screening

7.5.2.1 Amyloid-β (Aβ) Aggregation Assay

Thioflavin T (ThT) is a benzothiazole dye that was used to detect the formation of amyloid aggregates in solution. The excitation and emission properties of ThT changes when it binds to the β-sheet structures of Aβ40/Aβ42 oligomers and fibrils.[145] In this regard, the anti-Aβ aggregation activity of *N*,2-diphenylthiazol-4-amine based derivatives (**7a-d**) was evaluated using ThT-based fluorescence assays. These assays were conducted in Costar, black, clear-bottomed 384-well plates with frequent shaking at 730 cpm under constant heating at 37 °C for 24 h. The excitation and emission of ThT were recorded at 440 and 490 nm, respectively. Readings were taken every 5 min using a BioTek Synergy H1 microplate reader. Test compounds were prepared in 215 mM phosphate buffer at pH

7.4. 0.5 mg of Aβ•HFIP samples (AnaSpec, CA, USA) was dissolved in 1% ammonium hydroxide solution for Aβ40 or 10% ammonium hydroxide for Aβ42, sonicated at RT for 5 min, and diluted to 50 μM in phosphate buffer. A 15 μM ThT stock solution was prepared. To each ThT background well, 44 μL ThT, 35 μL phosphate buffer, and 1 μL DMSO were added. To the Aβ control wells, 44 μL ThT, 28 μL phosphate buffer, and 8 μL Aβ40/42 (5 μM final concentration) were added. To each test compound containing wells, 44 μL ThT, 20 μL phosphate buffer, 1 μL DMSO, and 8 μL test compound in various concentrations (1, 5, 10, and 25 μM), and 8 μL of Aβ were added. ThT interferences were taken before the addition of 8 μL of Aβ40 or Aβ42 stock solution (5 μM final concentration). Known Aβ40 and Aβ42 aggregation inhibitors MB and RES were also evaluated for comparison. Plates were sealed with a ThermoSeal film (Sigma Aldrich) before placing the plates in the reader. Data presented was an average of triplicate reading for two-three independent experiments.

7.5.2.2 Transmission Electron Microscopy (TEM) Studies

The Aβ40 and Aβ42 aggregate morphology was examined by performing TEM experiment in the presence and absence of test compounds. TEM samples were prepared in Costar, round-bottomed 384-well plates with test compounds (25 μM). To the Aβ control wells, 44 μL ThT, 28 μL phosphate buffer, and 8 μL Aβ40/42 (5 μM final concentration) were added. To each test compound containing well, 44 μL ThT, 20 μL phosphate buffer, 1 μL DMSO, and 8 μL of test compound (25 μM), and 8 μL of Aβ40/42 were added. The plates were incubated on a BioTek Synergy H1 microplate reader at 37 °C and shaken at 730 cpm for 24 h.

TEM grids were prepared by adding 20 μL test compound over the formvar-coated copper grids (400 mesh) *via* the use of a Pasteur pipette, which were then air-dried for 3 h or longer before washing them with 20 μL of ultrapure water (UPW) to remove any precipitated buffer salt. The sample grids were air-dried for 30 min. Once the grids were dry, they were stained with 20 μL of 2% phosphotungstic acid (PTA). The excess of PTA was removed by blotting with filter paper. The grids were allowed to dry overnight. Scanning of these grids was performed using a Philips CM10 TEM at 60 kV (Department of Biology, University of Waterloo), and micrographs were collected using a 14-megapixel AMT camera.

7.5.2.3 Computational Modeling Studies

Molecular docking studies of *N*,4-diphenylthiazol-2-amines derivatives with Aβ peptides were conducted *via* the computational chemistry Discovery Studio (DS) software – Structure-Based-Design (SBD), version 4.0 from BIOVA Inc. (San Diego, USA).[220] The *Small Molecules* module was used to build the *N*,2-diphenylthiazol-4-amine derivatives, which were in turn docked with Aβ40 and Aβ42 dimer models obtained from protein data bank (pdb id: 2LMN and 5KK3) using the CDOCKER algorithm in the *Receptor-Ligand Interactions* module in DS using CHARMm force field.[220,221] CDOCKER algorithm uses simulated annealing protocol to determine the best ligand binding modes. *N*,4-diphenylthiazol-2-amine derivatives were built in 3D using *Build Fragment* tool; energy minimization was applied for 1000 iterations using steepest descent and conjugate gradient minimizations, respectively. The ligands were minimized using the Smart Minimization protocol (200 steps, RMS gradient 0.1 kcal/mol),

CHARMm force field and a distance depended dielectric constant. For the docking of *N*,2-diphenylthiazol-4-amine derivatives in Aβ40 and Aβ42 dimer models, the binding site was defined by a 20 Å radius sphere. Molecular docking was carried out by the CDOCKER algorithm, which includes 2000 heating steps, 700 K target temperature, 300 K cooling temperature target with 5000 cooling steps. The docked poses obtained were ranked using the CDOCKER energy and CDOCKER interaction energy parameters (kcal/mol). The protein-ligand complexes were evaluated by examining various polar and nonpolar interactions, such as hydrogen bonding, electrostatic, van der Waal's, and hydrophobic interactions.

7.5.2.4 Cell Viability Assay

The HT22 hippocampal cells were plated at a density of 10,000 cells/100 μL in Nunclon Delta 96-well plates with complete growth media consisting of DMEM and Ham's F12 in a 1:1 ratio, supplemented with 10% fetal bovine serum (FBS) and 1% penicillin-streptomycin (10,000 U/mL) at 37 °C in 5% CO_2. The cells were incubated at 37 °C for 24 h. To each untreated well, 100 μL DMEM/F-12 was added. To the Aβ control wells, 85 μL DMEM/F-12, 10 μL PBS, and 5 μL Aβ40/42 (5 μM final concentration) were added. To each test compound containing wells, 85 μL DMEM/F-12, 10 μL filter-sterilized test compounds (**7a-d**, and RES) in concentration of 10 μM in triplicates (n = 3), and 5 μL of Aβ40/42 were added. These cells were then incubated at 37 °C for 24 h. The MTT reagent solution[222] made of thiazolyl blue tetrazolium bromide powder (Sigma Aldrich) in PBS to 5 mg/mL and filter-sterilized through a 0.22 μm filter was added in 10% of the culture medium volume (DMEM/F-12, HEPES, no phenol red) to each well and the cells were cultured for an additional 2-3 h. After incubation, the

resulting formazan crystals were solubilized with the solubilisation solution prepared from a mixture of IPA, 10% Triton X-100 and 1% HCl (12M). The absorbance was taken at 570 and 690 nm. All results were presented as a relative percent of (4,5-dimethylthiazol-2-yl)-2,5-diphenyl tetrazolium bromide (MTT) to untreated controls. Known Aβ aggregation inhibitor resveratrol (RES) was used as a reference agent for comparison.

CHAPTER 8 Conclusions and Future Directions

8.1 Introduction

Alzheimer's disease (AD) is a devastating neurodegenerative disorder, which is a growing concern all over the world due to an aging population and increased life expectancy (Alzheimer's Association USA, https://www.alz.org). For more than two decades, cholinesterase inhibitors and NMDA antagonists were the main stay in AD pharmacotherapy. However, this class of therapeutics provide only symptomatic relief. Later research led to the discovery of many other factors including the amyloid and tau cascade hypothesis and their role in AD pathophysiology. Past decade saw the development of several novel classes of molecules that can prevent the formation of neurotoxic Aβ-species. However, many novel drug candidates that target the Aβ-cascade failed at various stages of clinical trials. In a ground breaking discovery, US FDA recently approved the first anti-Aβ therapeutic known as aducanumab, which received accelerated approval to treat AD patients.[232] Aducanumab is the first approved therapy to treat AD in the last 17 years, which again highlights the challenges and complexities in AD therapeutic design. The launch of aducanumab heralds a new beginning in the discovery and development of novel AD therapeutics that target the amyloid cascade in AD.

The current thesis research is directly related to amyloid cascade, aiming to design and develop novel small molecules that can reduce and prevent the formation of two known Aβ peptides – Aβ40 and Aβ42 aggregation. The molecules are based on diphenylthiazolamine ring systems possessing a central thiazole-4-amine or thiazole-2-

amines. A library of 47 compounds were designed, synthesized and evaluated as inhibitors of both Aβ40 and Aβ42 aggregation. These compounds were synthesized by either 3-step or 5-step synthesis, which involved coupling *N*-phenylthiourea with 2-bromo-3' or 4'-substituted-acetophenones or cyclization of thiobenzamide with 2-chloro-*N*-phenylacetamides to afford the target compounds which were either reduced or alkylated or subjected to treatment with either sulfonyl chlorides or sulfamoyl chlorides to afford diphenylthiazolamine libraries **1a-j**, **2a**, **2b**, **3a-i**, **4a**, **4b**, **5a-j**, **6a-j** and **7a-d**. These libraries were purified and characterized by NMR, LCMS and HRMS analysis. Their anti-aggregation properties toward Aβ40 and Aβ42 was evaluated by (i) studying Aβ aggregation kinetics using ThT-based fluorescence assay; (ii) transmission electron microscopy (TEM) to study Aβ morphology; (iii) computational modeling to understand the binding interactions of diphenylthiazolamine derivatives with Aβ40 and Aβ42 models and (iv) investigating the neuroprotective effects of these compound libraries toward Aβ40 or Aβ42-induced cytotoxicity in HT22 hippocampal neuronal cells. The following sections provide a summary of findings from Chapters 3–7.

8.2 *N*,4-Diphenylthiazol-2-Amine Derivatives (Chapter 3)

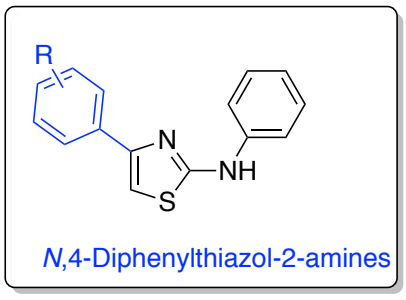

Figure 86. General structure of *N*,4-diphenylthiazol-2-amine derivatives in Chapter 3.

The SAR data obtained for a library of twelve *N*,4-diphenylthiazol-2-amine derivatives demonstrated that these compounds are capable of inhibiting the aggregation of both Aβ40 and Aβ42 (25–97% inhibition at 25 μM) and support our hypothesis that these series of compounds are capable of interacting with Aβ40 and Aβ42 dimers and prevent their aggregation into higher order structures. Computational modeling studies predict that these compounds can interact with both N- and C-terminal amino acids which can stabilize the dimer assembly, whereas in the Aβ42 dimer model, they bind in a cavity made up of amino acids KLVFFA closer to the N-terminal region which is known to be critical in the nucleation dependent aggregation process. Interaction of *N*,4-diphenylthiazole-2-amine derivatives in the KLVFFA region can reduce their aggregation into more toxic forms. Compounds in this series exhibited superior inhibition of Aβ42 aggregation relative to their Aβ40 inhibition profile. This suggests that these compounds exhibit greater binding affinity toward Aβ42 dimer, which was also supported by the protein-ligand complex energies (CDOCKER energy in kcal/mol). It was pleasing to see that compounds in this series were able to translate their anti-Aβ aggregation properties from the solution based in vitro experiments to cell culture studies in HT22 hippocampal neuronal cells, where they were able to reduce Aβ40 or Aβ42-induced cytotoxicity.

8.3 *N*-Methyl-*N*,4-Diphenylthiazol-2-Amine Derivative (Chapter 4)

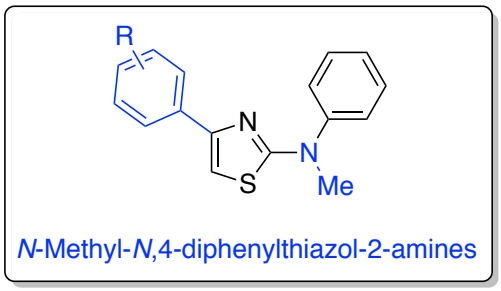

Figure 87. General structure of *N*-methyl-*N*,4-diphenylthiazol-2-amine derivatives in Chapter 4.

The SAR data obtained for a library of eleven *N*-methyl-*N*,4-diphenylthiazol-2-amine derivatives demonstrated that these compounds are capable of inhibiting the aggregation of both Aβ40 and Aβ42 (11–97% inhibition at 25 μM). As per our hypothesis, these series of compounds were able to inhibit both Aβ40 and Aβ42 aggregation which suggests their ability to bind to lower order structures such as Aβ40 and Aβ42 dimers and prevent their aggregation into higher order structures. Interestingly, the presence of N-methyl substituents, did reduce their inhibition activity toward Aβ40 aggregation compared to the corresponding *N*,4-diphenylthiazol-2-amines. Computational modeling studies, predict that the secondary amine NH present in *N*,4-diphenylthiazol-2-amine derivatives underwent a polar contact (H-bond) with Val18 backbone. The loss of this interaction in the N-methyl derivatives, might contribute to its weaker inhibition activity. This was further supported by the CDOCKER energy parameters for the ligand-protein complex which showed that the *N*,4-diphenylthiazol-2-amines exhibited superior binding toward Aβ40 dimer compared to the N-methyl derivatives. Amine derivatives in the KLVFFA region can reduce their aggregation into

more toxic forms. The presence of N-methyl substituent did not affect their activity toward inhibition of Aβ42 aggregation and furthermore several compounds in this series were able to translate their anti-Aβ aggregation properties from the solution based in vitro experiments to cell culture studies in HT22 hippocampal neuronal cells, where they were able to reduce both Aβ40 or Aβ42-induced cytotoxicity.

8.4 Alkysulfonamide and Sulfamide Substituted *N*,4-Diphenylthiazol-2-Amine Derivatives (Chapter 5)

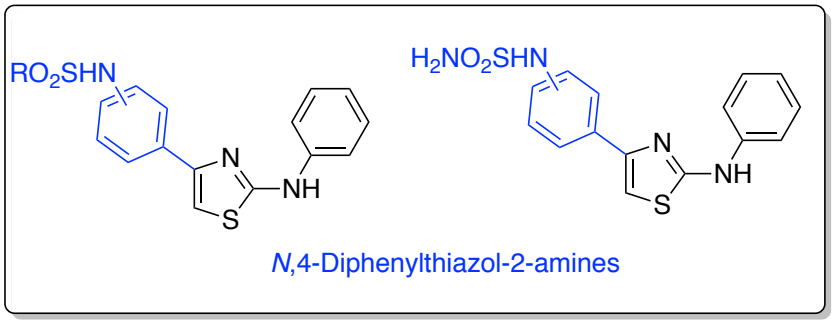

Figure 88. General structure of *N*,4-diphenylthiazol-2-amine derivatives in Chapter 5.

This series yielded compounds that demonstrated an excellent combination of inhibition the aggregation of both Aβ40 and Aβ42 peptides. The SAR data obtained for a library of ten alkylsufonamide or sulfamide containing *N*,4-diphenylthiazol-2-amine derivatives (Figure 88) demonstrated that these compounds are capable of inhibiting the aggregation of both Aβ40 and Aβ42 (43–95% inhibition at 25 μM). As per our hypothesis, these series of compounds were able to inhibit both Aβ40 and Aβ42 aggregation, which suggests their ability to bind to lower order structures such as Aβ40 and Aβ42 dimers and prevent their aggregation into higher order structures. Interestingly compounds in this series exhibited superior inhibition of Aβ40 aggregation compared to *N*,4-diphenylthiazol-2-amine and *N*-methyl derivatives described in Chapter 3 and 4,

whereas their activity toward Aβ42 aggregation inhibition was comparable to inhibition activity data seen for compounds from Chapter 3 and 4. These studies also suggest that presence of either alkylsufonamide or sulfamide substituents in *N*,4-diphenylthiazol-2-amine derivatives enhanced their anti-aggregation properties which was also supported by computational modeling studies that showed that the larger volumes of these compounds led to better interaction with Aβ40 and Aβ42 dimer models. Several compounds in this series were able to reduce both Aβ40 and Aβ42-induced cytotoxicity in HT22 cells. It was interesting to see that all the compounds in this series were able provide neuroprotection toward Aβ40-induced cytotoxicity in HT22 cells.

8.5 Alkylfulfonamide and Sulfamide Substituted *N*-Methyl-*N*,4-Diphenylthiazol-2-Amine Derivative (Chapter 6)

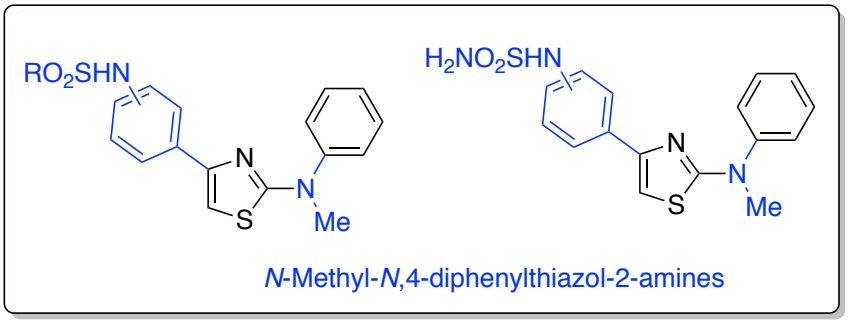

Figure 89. General structure of *N*-methyl-*N*,4-diphenylthiazol-2-amine derivatives in Chapter 6.

The SAR data obtained for a library of ten *N*-methyl-*N*,4-diphenylthiazol-2-amine derivatives containing alkylsufonamide or sulfamide substituents (Figure 89) exhibited dual inhibition of both Aβ40 and Aβ42 aggregation (43–95% inhibition at 25 μM). Contrary to our hypothesis *N*-methyl derivatives did not exhibit superior anti-aggregation activity compared to the corresponding alkylsulfonamide or sulfamide containing *N*,4-diphenylthiazol-2-amines, which suggests that *N*-methylation was not a major factor in

their anti-aggregation properties. Similar to the *N*,4-diphenylthiazol-2-amines in Chapter 5, several compounds in this series were able to reduce both Aβ40 and Aβ42-induced cytotoxicity in HT22 cells.

8.6 *N*,2-Diphenylthiazol-4-Amine Derivatives (Chapter 7)

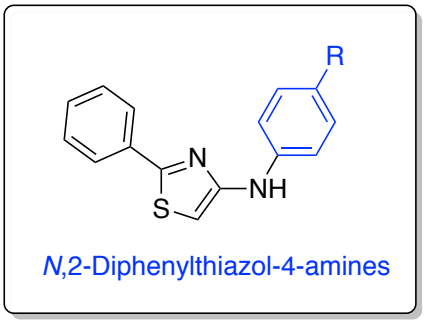

Figure 90. General structure of *N*,2-diphenylthiazol-4-amine derivatives in Chapter 7.

This small set of four compounds from the *N*,2-diphenylthiazol-4-amine derivatives (Figure 90), showed anti-aggregation properties toward both Aβ40 and Aβ42 (18–96% inhibition at 25 μM). Their anti-Aβ40 activity was weaker than the corresponding *N*,4-diphenylthiazole-2-amine derivatives. Computational studies also support this observation due to lower binding affinity of protein-ligand complex (CDOCKER energy) in the Aβ40-dimer model. Their activity toward Aβ42 aggregation inhibition was comparable to the corresponding thiazole-2-amine derivatives. Due to the evaluation of very limited number of compounds, we were not able to obtain complete SAR data. However, it was promising to note that compounds in this series were able to rescue HT22 cells from Aβ40 and Aβ42-induced cytotoxicity, which further supports their development. Planned studies include completing the SAR studies by evaluating *N*,2-diphenylthiazol-4-amines possessing EDGs and EWGs at the diphenyl ring positions,

N-methylation and incorporation of alkylsulfonamide and sulfamide substituents to investigate their effect on Aβ-aggregation inhibition and cytotoxicity in HT22 cells.

8.7 Limitations

The research outcomes described in Chapters 3–7 led to discovery of novel class of diphenylthiazole derivatives that possess anti-Aβ activity. However, there are some limitations in the current study. For example, the molecular mechanisms of anti-Aβ activity exhibited by diphenylthiazoles are not clear and needs to be investigated further which can enhance the quality of the data obtained and can be useful to carry out further SAR optimization. The in vitro ThT Aβ kinetics assay described in this thesis is generally useful to predict the ability of novel molecules to prevent the formation of Aβ fibrils. In this regard, carrying out immunoblotting experiments using Aβ-oligomer and Aβ-fibril specific antibodies[233] will provide mechanistic information on the ability of diphenylthiazole derivatives to prevent Aβ-oligomer and/or Aβ-fibril formation. Furthermore, thorough computational modeling experiments (*e.g*. molecular dynamics experiments) should be carried out using multiple forms of Aβ40 and Aβ42 species including dimers, pentamers, hexamers and fibrils to study the interactions of potent diphenylthiazole derivatives identified from the current study, to understand the key interactions involved in their anti-aggregation properties. Other studies to consider would be to investigate the effect of diphenylthiazole derivatives on preformed Aβ-oligomers and fibrils to determine their disaggregation properties. Therefore, combination of computational and immunoblotting experiments will provide concrete information on the

mechanisms of direct interactions of novel diphenylthiazole derivatives and their ability to bind and modulate Aβ-species and prevent their aggregation into toxic forms.

The cell viability and neuroprotection activity of diphenylthiazoles against Aβ-induced toxicity was carried out using MTT assay. It should be noted that MTT assay measures the metabolic activity of cells and may not account for the loss or reduction of cellular metabolic activity in the presence of Aβ. This can lead to false positive and errors in data interpretation. These issues can be avoided by conducting alternative cell viability assays based on measuring lactate dehydrogenase (LDH) and or adenosine triphosphate (ATP) based assays which can provide accurate data related to cell viability, membrane integrity and proliferation.[234] Other limitation of the current study includes the use of technical replicates during the cell culture experiments rather than the use of biological replicates, which can lead to errors or pseudoreplication during data interpretation.[235] These pitfalls can be avoided by conducting additional experiments using biological replicates to validate the study findings.

8.8 Future Directions

Our studies have identified novel diphenylthiazoleamine based small molecules which have the potential to bind to Aβ40 and Aβ42 peptides and prevent their self-assembly into neurotoxic species and hence reduce neurotoxicity in AD. As a logical next step, we aim to investigate the effect of these compounds on tau-aggregation and tau-induced neurotoxicity since this pathway is a major event in AD pathogenesis.[236] We anticipate challenges in this regard, since compared to Aβ40 or Aβ42 peptides, tau is a large protein made up of 441-amino acids.[237] Therefore, due to their small surface area,

small molecules may not be able to modulate their misfolding and aggregation into toxic forms. However, literature studies have shown that some small molecules are capable of reducing tau protein self-assembly into toxic forms.[238] In addition, tau-based hexapeptide segments such as VQIVYK and VQIINK are known to form neurotoxic steric-zipper assemblies.[239,240] We will first investigate the effect of diphenylthiazoleamine libraries in preventing or reducing tau-based hexapeptide steric-zipper assemblies in vitro, which will provide valuable insights on their potential in preventing tau-protein misfolding and aggregation.[241,242] To this end, a combination of computational modeling and in vitro studies will be carried out.

It should be noted that diphenylthiazoleamines synthesized in Chapter 5 and Chapter 6 possess sulfonamide ($-NHSO_2R_1$) or sulfamide ($-NHSO_2NH_2$) substituents. These types of substituents are known to be present in cyclooxygenase (COX) inhibitors such as nimesulide and celecoxib, which exhibit anti-inflammatory and analgesic activity.[243] This begs the intriguing question of developing multi-targeting agents which can prevent Aβ-aggregation and also exhibit anti-inflammatory activity since amyloid cascade itself can induce neuroinflammation in CNS.[244] Therefore, we will screen diphenylthiazoleamines possessing either sulfonamide ($-NHSO_2R_1$) or sulfamide ($-NHSO_2NH_2$) substituents to evaluate their COX-1 and COX-2 inhibition activity in vitro.

In the current work, we investigated the effect of a 5-membered thiazole containing diphenyl derivatives as inhibitors of Aβ aggregation. Computational modeling studies suggest that the electron deficient thiazole ring was interacting in the KLVFFA regions of the Aβ-dimer assemblies via nonpolar and polar interactions. This suggests

that other 5- and or 6-six member rings can be investigated to study their anti-aggregation properties. Most of the Aβ aggregation inhibitors reported to date posses planar, fused ring systems, whereas our study has shown that even diphenyl derivatives, possessing a central thiazole-amine ring possess anti-Aβ activity.[192] Other electron-rich and electron-deficient 5- and 6-membered rings such as a thiazole, oxazole, pyridine and pyranone can replace the thiazole ring as part of a broad SAR study (Figure 91). These proposed SAR studies can provide additional information on the structural requirements to design novel small molecules as chemical tools to study aggregation and as potential AD therapeutics.

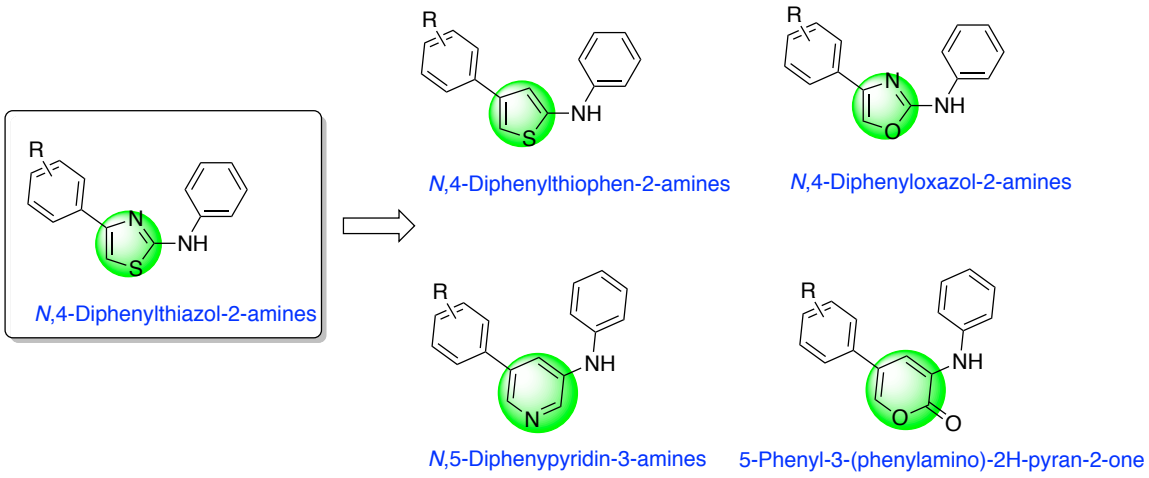

Figure 91. Suggested SAR strategies based on varying the central rings for future studies

In summary, our work led to the discovery of a novel class of diphenylthiazole-4-amine based small molecules as Aβ aggregation inhibitors. The significance of this study lies in the fact that several compounds from this class were able to prevent the aggregation of Aβ42, which is the more toxic form of Aβ. In addition, past research has demonstrated that developing inhibitors of Aβ42 is more challenging compared to developing Aβ40 aggregation inhibitors. Therefore, it was pleasing to see the

effectiveness of diphenylthiazol-4-amines toward Aβ42 aggregation. Significantly, there were also able to demonstrate their activity in cell culture model where they offered neuroprotection by preventing both Aβ40 and Aβ42 mediated cytotoxicity. The marketing of aducanumab, the first anti-Aβ therapy has given a new lease of life to the amyloid cascade hypothesis of AD pathogenesis. Under this scenario, our research will stimulate further research in discovering novel therapies for AD.

Letters of Copyright Permission

Letter of Copyright Permission for Figure 9

ELSEVIER LICENSE
TERMS AND CONDITIONS

Aug 26, 2021

This Agreement between Amy T. Pham ("You") and Elsevier ("Elsevier") consists of your license details and the terms and conditions provided by Elsevier and Copyright Clearance Center.

License Number	5103900120321
License date	Jul 07, 2021
Licensed Content Publisher	Elsevier
Licensed Content Publication	Drug Discovery Today
Licensed Content Title	Clearance of amyloid-beta in Alzheimer's disease: progress, problems and perspectives
Licensed Content Author	Yan-Jiang Wang,Hua-Dong Zhou,Xin-Fu Zhou
Licensed Content Date	Oct 1, 2006
Licensed Content Volume	11
Licensed Content Issue	19-20
Licensed Content Pages	8
Start Page	931
End Page	938
Type of Use	reuse in a thesis/dissertation
Portion	figures/tables/illustrations
Number of figures/tables/illustrations	1
Format	both print and electronic
Are you the author of this Elsevier article?	No
Will you be translating?	No
Title	PhD
Institution name	University of Waterloo
Expected presentation date	Aug 2021
Portions	1
Requestor Location	Dr. Amy Pham 10 Victoria St. South Kitchener, ON N2C5G1

Letter of Copyright Permission for Figure 12

SPRINGER NATURE LICENSE
TERMS AND CONDITIONS

Aug 26, 2021

This Agreement between Amy T. Pham ("You") and Springer Nature ("Springer Nature") consists of your license details and the terms and conditions provided by Springer Nature and Copyright Clearance Center.

License Number	5136510046956
License date	Aug 26, 2021
Licensed Content Publisher	Springer Nature
Licensed Content Publication	Nature Reviews Neuroscience
Licensed Content Title	Immune attack: the role of inflammation in Alzheimer disease
Licensed Content Author	Frank L. Heppner et al
Licensed Content Date	May 20, 2015
Type of Use	Thesis/Dissertation
Requestor type	academic/university or research institute
Format	print and electronic
Portion	figures/tables/illustrations
Number of	1

References

(1) Kirsch, R. E. (1993) Clinical research. *S. Afr. Med. J. 83*, 757–9.

(2) Trenchard, P. M., and Morgan, R. A. (1986) Sub-Ambient Aggregometry: A Tool for Examining Platelet Storage at any Temperature between 4–22 °C. *Pathophysiol. Haemost. Thromb. 16*, 352–361.

(3) Yang, H. D., Kim, D. H., Lee, S. B., and Young, L. D. (2016) History of Alzheimer's Disease. *Dement. Neurocognitive Disord. 15*, 115.

(4) (2020) 2020 Alzheimer's disease facts and figures. *Alzheimer's Dement. 16*, 391–460.

(5) Qiu, C., Kivipelto, M., and Von Strauss, E. (2009) Epidemiology of Alzheimer's disease: occurrence, determinants, and strategies toward intervention. *Dialogues Clin. Neurosci. 11*, 111–128.

(6) Pijnenburg, M. A. M., and Leget, C. (2007) Who wants to live forever? Three arguments against extending the human lifespan. *J. Med. Ethics 33*, 585–587.

(7) Red, U. S. D., Schnetzer, J. N., and Schnetzer, J. (2020) Dementia : Types , What They Are and How They Differ.

(8) Maia, M., and Sousa, E. (2019) BACE-1 and γ-Secretase as Therapeutic Targets for Alzheimer's Disease. *Pharmaceuticals 12*, 41.

(9) Yankner, B. A. (1996) Mechanisms of Neuronal Degeneration in Alzheimer's Disease. *Neuron 16*, 921–932.

(10) Ly, S., Altman, R., Petrlova, J., Lin, Y., Hilt, S., Huser, T., Laurence, T. A., and Voss, J. C. (2013) Binding of apolipoprotein E inhibits the oligomer growth of amyloid-β peptide in solution as determined by fluorescence cross-correlation spectroscopy. *J. Biol.*

Chem. 288, 11628–11635.

(11) Huang, Y. (2011) Roles of apolipoprotein E4 (ApoE4) in the pathogenesis of Alzheimer's disease: lessons from ApoE mouse models. *Biochem. Soc. Trans. 39*, 924–932.

(12) Safieh, M., Korczyn, A. D., and Michaelson, D. M. (2019) ApoE4: an emerging therapeutic target for Alzheimer's disease. *BMC Med. 17*, 64.

(13) Peron, E. P., Zimmerman, K. M., Crouse, E. L., Slattum, P. W., and Hobgood, S. E. (2020) Alzheimer Disease, in *Pharmacotherapy: A Pathophysiologic Approach, 11e* (DiPiro, J. T., Yee, G. C., Posey, L. M., Haines, S. T., Nolin, T. D., and Ellingrod, V., Eds.). McGraw-Hill Education, New York, NY.

(14) Viña, J., and Lloret, A. (2010) Why women have more Alzheimer's disease than men: Gender and mitochondrial toxicity of amyloid-β peptide. *J. Alzheimer's Dis. 20*, 527–533.

(15) Mielke, M., Vemuri, P., and Rocca, W. (2014) Clinical epidemiology of Alzheimer’s disease: assessing sex and gender differences. *Clin. Epidemiol. 6*, 37.

(16) Mielke, M. M. (2018) Sex and gender differences in Alzheimer disease dementia. *Psychiatr. Times 35*, 14–15.

(17) Beam, C. R., Kaneshiro, C., Jang, J. Y., Reynolds, C. A., Pedersen, N. L., and Gatz, M. (2018) Differences Between Women and Men in Incidence Rates of Dementia and Alzheimer's Disease. *J. Alzheimer's Dis. 64*, 1077–1083.

(18) Oveisgharan, S., Arvanitakis, Z., Yu, L., Farfel, J., Schneider, J. A., and Bennett, D. A. (2018) Sex differences in Alzheimer's disease and common neuropathologies of

aging. *Acta Neuropathol. 136*, 887–900.

(19) Anstey, K. J., Peters, R., Mortby, M. E., Kiely, K. M., Eramudugolla, R., Cherbuin, N., Huque, M. H., and Dixon, R. A. (2021) Association of sex differences in dementia risk factors with sex differences in memory decline in a population-based cohort spanning 20–76 years. *Sci. Rep. 11*, 1–10.

(20) Soreq, H. (2001) Acetylcholinesterase — new roles for an old actor. *Nat. Rev. Neurosci. 2*, 294–302.

(21) Dvir, H., Silman, I., Harel, M., Rosenberry, T. L., and Sussman, J. L. (2010) Acetylcholinesterase: From 3D structure to function. *Chem. Biol. Interact. 187*, 10–22.

(22) Sharma, K. (2019) Cholinesterase inhibitors as Alzheimer's therapeutics (Review). *Mol. Med. Rep. 20*, 1479–1487.

(23) Colovic, M. B., Krstic, D. Z., Lazarevic-Pasti, T. D., Bondzic, A. M., and Vasic, V. M. (2013) Acetylcholinesterase Inhibitors: Pharmacology and Toxicology. *Curr. Neuropharmacol. 11*, 315–335.

(24) Ehret, M. J., and Chamberlin, K. W. (2015) Current practices in the treatment of Alzheimer disease: where is the evidence after the phase III trials? *Clin. Ther. 37*, 1604–1616.

(25) Francis, P. T., Ramírez, M. J., and Lai, M. K. (2010) Neurochemical basis for symptomatic treatment of Alzheimer's disease. *Neuropharmacology 59*, 221–229.

(26) Nordberg, A., Ballard, C., Bullock, R., Darreh-Shori, T., and Somogyi, M. (2013) A review of butyrylcholinesterase as a therapeutic target in the treatment of Alzheimer's disease. *Prim. Care Companion J. Clin. Psychiatry 15*.

(27) Darvesh, S. (2016) Butyrylcholinesterase as a Diagnostic and Therapeutic Target for

Alzheimer's Disease. *Curr. Alzheimer Res. 13*, 1173–1177.

(28) Saxena, A., Redman, A. M. G., Jiang, X., Lockridge, O., and Doctor, B. P. (1999) Differences in active-site gorge dimensions of cholinesterases revealed by binding of inhibitors to human butyrylcholinesterase. *Chem. Biol. Interact. 119–120*, 61–69.

(29) Mushtaq, G., Greig, N., Khan, J., and Kamal, M. (2014) Status of Acetylcholinesterase and Butyrylcholinesterase in Alzheimer's Disease and Type 2 Diabetes Mellitus. *CNS Neurol. Disord. - Drug Targets 13*, 1432–1439.

(30) Caswell, M. D., Mok, S. S., Henry, A., Cappai, R., Klug, G., Beyreuther, K., Masters, C. L., and Small, D. H. (1999) The amyloid β-protein precursor of Alzheimer's disease is degraded extracellularly by a Kunitz protease inhibitor domain-sensitive trypsin-like serine protease in cultures of chick sympathetic neurons. *Eur. J. Biochem. 266*, 509–516.

(31) Conboy, L., Murphy, K. J., and Regan, C. M. (2005) Amyloid precursor protein expression in the rat hippocampal dentate gyrus modulates during memory consolidation. *J. Neurochem. 95*, 1677–1688.

(32) Bayer, T. A., Wirths, O., Majtényi, K., Hartmann, T., Multhaup, G., Beyreuther, K., and Czech, C. (2006) Key Factors in Alzheimer's Disease: β-amyloid Precursor Protein Processing, Metabolism and Intraneuronal Transport. *Brain Pathol. 11*, 1–11.

(33) Zhang, Y. W., Thompson, R., Zhang, H., and Xu, H. (2011) APP processing in Alzheimer's disease. *Mol. Brain 4*, 1–13.

(34) Menéndez-González, M., Pérez-Pinera, P., Martínez-Rivera, M., Calatayud, M. T., and Blázquez Menes, B. (2006) APP processing and the APP-KPI domain involvement in the amyloid cascade. *Neurodegener. Dis. 2*, 277–283.

(35) Chen, G., Xu, T., Yan, Y., Zhou, Y., Jiang, Y., Melcher, K., and Xu, H. E. (2017) Amyloid beta: structure, biology and structure-based therapeutic development. *Acta Pharmacol. Sin. 38*, 1205–1235.

(36) Cappai, R., Elise Needham, B., and Ciccotosto, G. D. (2007) The Function of the Amyloid Precursor Protein Family, in *Abeta Peptide and Alzheimer's Disease*, pp 37–51. Springer London, London.

(37) Cutler, N. R., and Sramek, J. J. (2013) Understanding Alzheimer's Disease (Zerr, I., Ed.). InTech.

(38) Caswell, M. D., Mok, S. S., Henry, A., Cappai, R., Klug, G., Beyreuther, K., Masters, C. L., and Small, D. H. (1999) The amyloid beta-protein precursor of Alzheimer's disease is degraded extracellularly by a Kunitz protease inhibitor domain-sensitive trypsin-like serine protease in cultures of chick sympathetic neurons. *Eur. J. Biochem. 266*, 509–516.

(39) Kepp, K. P. (2012) Bioinorganic chemistry of Alzheimer's disease. *Chem. Rev. 112*, 5193–5239.

(40) Barrow, C. J., and Small, D. H. (2007) Abeta Peptide and Alzheimer's Disease (Barrow, C. J., and Small, D. H., Eds.). Springer London, London.

(41) Mohamed, T., Shakeri, A., and Rao, P. P. N. (2016) Amyloid cascade in Alzheimer's disease: Recent advances in medicinal chemistry. *Eur. J. Med. Chem. 113*, 258–272.

(42) Murphy, M. P., and Levine, H. (2010) Alzheimer's Disease and the Beta-Amyloid Peptide. *J. Alzheimer's Dis. 19*, 1–17.

(43) Wolfe, M. S. (2014) Unlocking truths of γ-secretase in Alzheimer's disease: what is

the translational potential? *Future Neurol. 9*, 419–429.

(44) O'Brien, R. J., and Wong, P. C. (2011) Amyloid Precursor Protein Processing and Alzheimer's Disease. *Annu. Rev. Neurosci. 34*, 185–204.

(45) Ghosh, A. K., and Osswald, H. L. (2014) BACE1 (β-secretase) inhibitors for the treatment of Alzheimer's disease. *Chem. Soc. Rev. 43*, 6765–6813.

(46) Hampel, H., Vassar, R., De Strooper, B., Hardy, J., Willem, M., Singh, N., Zhou, J., Yan, R., Vanmechelen, E., De Vos, A., Nisticò, R., Corbo, M., Imbimbo, B. Pietro, Streffer, J., Voytyuk, I., Timmers, M., Tahami Monfared, A. A., Irizarry, M., Albala, B., Koyama, A., Watanabe, N., Kimura, T., Yarenis, L., Lista, S., Kramer, L., and Vergallo, A. (2020) The β-Secretase BACE1 in Alzheimer's Disease. *Biol. Psychiatry* 1–12.

(47) Vassar, R. (2014) BACE1 inhibitor drugs in clinical trials for Alzheimer's disease. *Alzheimers. Res. Ther. 6*, 89.

(48) Li, L., Darden, T. A., Bartolotti, L., Kominos, D., and Pedersen, L. G. (1999) An atomic model for the pleated β-sheet structure of Aβ amyloid protofilaments. *Biophys. J. 76*, 2871–2878.

(49) Landau, M., Sawaya, M. R., Faull, K. F., Laganowsky, A., Jiang, L., Sievers, S. A., Liu, J., Barrio, J. R., and Eisenberg, D. (2011) Towards a Pharmacophore for Amyloid. *PLoS Biol. 9*, 25–27.

(50) Schmidt, M., Sachse, C., Richter, W., Xu, C., Fandrich, M., and Grigorieff, N. (2009) Comparison of Alzheimer A (1-40) and A (1-42) amyloid fibrils reveals similar protofilament structures. *Proc. Natl. Acad. Sci. 106*, 19813–19818.

(51) Jan, A., Hartley, D. M., and Lashuel, H. A. (2010) Preparation and characterization of toxic Aβ aggregates for structural and functional studies in Alzheimer's disease

research. *Nat. Protoc. 5*, 1186–1209.

(52) Bruggink, K. A., Müller, M., Kuiperij, H. B., and Verbeek, M. M. (2012) Methods for analysis of amyloid-β aggregates. *J. Alzheimer's Dis. 28*, 735–758.

(53) Rodger, A. B. (2008) Unraveling the mystery. US Department of Health and Human Services.

(54) Sandoval, K. E., Witt, K. A., Crider, A. M., and Kontoyianni, M. (2014) Somatostatin Receptor-4 Agonists as Candidates for Treatment of Alzheimer's Disease, in *Drug Design and Discovery in Alzheimer's Disease*, pp 566–597. Elsevier.

(55) Wang, Y. J., Zhou, H. D., and Zhou, X. F. (2006) Clearance of amyloid-beta in Alzheimer's disease: progress, problems and perspectives. *Drug Discov. Today 11*, 931–938.

(56) Kumar, A., Singh, A., and Ekavali. (2015) A review on Alzheimer's disease pathophysiology and its management: an update. *Pharmacol. Reports 67*, 195–203.

(57) Rao, P. P. N., Pham, A. T., and Shakeri, A. (2020) Discovery of small molecules for the treatment of Alzheimer's disease, in *Small Molecule Drug Discovery*, pp 289–322. Elsevier.

(58) Shukla, V., Mishra, S. K., and Pant, H. C. (2011) Oxidative stress in neurodegeneration. *Adv. Pharmacol. Sci. 2011*.

(59) Bonda, D. J., Wang, X., Perry, G., Nunomura, A., Tabaton, M., Zhu, X., and Smith, M. A. (2010) Oxidative stress in Alzheimer disease: A possibility for prevention. *Neuropharmacology 59*, 290–294.

(60) Greenough, M. A., Camakaris, J., and Bush, A. I. (2013) Metal dyshomeostasis and oxidative stress in Alzheimer's disease. *Neurochem. Int. 62*, 540–555.

(61) Smith, M. a., Rottkamp, C. a., Nunomura, A., Raina, A. K., and Perry, G. (2000) Oxidative stress in Alzheimer's disease. *Biochim. Biophys. Acta - Mol. Basis Dis. 1502*, 139–144.

(62) Chauhan, V., and Chauhan, A. (2006) Oxidative stress in Alzheimer's disease. *Pathophysiology 13*, 195–208.

(63) Wang, X., Wang, W., Li, L., Perry, G., Lee, H., and Zhu, X. (2014) Oxidative stress and mitochondrial dysfunction in Alzheimer's disease. *Biochim. Biophys. Acta - Mol. Basis Dis. 1842*, 1240–1247.

(64) Du, X., Wang, X., and Geng, M. (2018) Alzheimer's disease hypothesis and related therapies. *Transl. Neurodegener. 7*, 1–7.

(65) Grimm, A., Friedland, K., and Eckert, A. (2016) Mitochondrial dysfunction: the missing link between aging and sporadic Alzheimer's disease. *Biogerontology 17*, 281–296.

(66) Querfurth, H. W., and LaFerla, F. M. (2010) Alzheimer's Disease. *N. Engl. J. Med. 362*, 329–344.

(67) Kayed, R., Head, E., Thompson, J. L., McIntire, T. M., Milton, S. C., Cotman, C. W., and Glabe, C. G. (2003) Common structure of soluble amyloid oligomers implies common mechanism of pathogenesis. *Science 300*, 486–489.

(68) Bitan, G., Kirkitadze, M. D., Lomakin, A., Vollers, S. S., Benedek, G. B., and Teplow, D. B. (2003) Amyloid-protein (Aβ) assembly: Aβ40 and Aβ42 oligomerize through distinct pathways. *Proc. Natl. Acad. Sci. 100*, 330–335.

(69) Hardy, J., and Selkoe, D. J. (2002) The amyloid hypothesis of Alzheimer's disease: progress and problems on the road to therapeutics. *Science 297*, 353–356.

(70) Roland, J. R., and Jacobsen, H. (2009) Alzheimer's disease: From pathology to therapeutic approaches. *Angew. Chemie - Int. Ed. 48*, 3030–3059.

(71) Haass, C., and Selkoe, D. J. (2007) Soluble protein oligomers in neurodegeneration: Lessons from the Alzheimer's amyloid β-peptide. *Nat. Rev. Mol. Cell Biol. 8*, 101–112.

(72) Miller, Y., Ma, B., and Nussinov, R. (2010) Polymorphism in alzheimer Aβ amyloid organization reflects conformational selection in a rugged energy landscape. *Chem. Rev. 110*, 4820–4838.

(73) Pithadia, A. S., and Lim, M. H. (2012) Metal-associated amyloid-β species in Alzheimer's disease. *Curr. Opin. Chem. Biol. 16*, 67–73.

(74) DeToma, A. S., Salamekh, S., Ramamoorthy, A., and Lim, M. H. (2012) Misfolded proteins in Alzheimer's disease and type II diabetes. *Chem. Soc. Rev. 41*, 608–621.

(75) Savelieff, M. G., Lee, S., Liu, Y., and Lim, M. H. (2013) Untangling amyloid-β, tau, and metals in Alzheimer's disease. *ACS Chem. Biol. 8*, 856–865.

(76) Hamley, I. W. (2012) The Amyloid Beta Peptide: A Chemist's Perspective. Role in Alzheimer's and Fibrillization. *Chem. Rev. 112*, 5147–5192.

(77) Perry, G., Cash, A. D., and Smith, M. A. (2002) Alzheimer Disease and Oxidative Stress. *J. Biomed. Biotechnol. 2*, 120–123.

(78) Smith, D. G., Cappai, R., and Barnham, K. J. (2007) The redox chemistry of the Alzheimer's disease amyloid β peptide. *Biochim. Biophys. Acta - Biomembr. 1768*, 1976–1990.

(79) Carrillo-Mora, P., Luna, R., and Colín-Barenque, L. (2014) Amyloid beta: Multiple mechanisms of toxicity and only some protective effects? *Oxid. Med. Cell. Longev. 2014*.

(80) Honda, K., Casadesus, G., Petersen, R. B., Perry, G., and Smith, M. A. (2004)

Oxidative Stress and Redox Active Iron in Alzheimer's Disease. *Ann. N. Y. Acad. Sci. 1012*, 179–182.

(81) Luque-Contreras, D., Carvajal, K., Toral-Rios, D., Franco-Bocanegra, D., and Campos-Peña, V. (2014) Oxidative Stress and Metabolic Syndrome: Cause or Consequence of Alzheimer's Disease? *Oxid. Med. Cell. Longev. 2014*, 497802.

(82) Wang, R., and Reddy, P. H. (2017) Role of Glutamate and NMDA Receptors in Alzheimer's Disease. *J. Alzheimer's Dis. 57*, 1041–1048.

(83) Parameshwaran, K., Dhanasekaran, M., and Suppiramaniam, V. (2008) Amyloid beta peptides and glutamatergic synaptic dysregulation. *Exp. Neurol. 210*, 7–13.

(84) Riederer, P., and Hoyer, S. (2006) From benefit to damage. Glutamate and advanced glycation end products in Alzheimer brain. *J. Neural Transm. 113*, 1671–1677.

(85) Hynd, M. R., Scott, H. L., and Dodd, P. R. (2004) Glutamate-mediated excitotoxicity and neurodegeneration in Alzheimer's disease. *Neurochem. Int. 45*, 583–595.

(86) Esposito, Z., Belli, L., Toniolo, S., Sancesario, G., Bianconi, C., and Martorana, A. (2013) Amyloid β, glutamate, excitotoxicity in alzheimer's disease: Are we on the right track? *CNS Neurosci. Ther. 19*, 549–555.

(87) Rego, A. C., and Oliveira, C. R. (2003) Mitochondrial dysfunction and reactive oxygen species in excitotoxicity and apoptosis: Implications for the pathogenesis of neurodegenerative diseases. *Neurochem. Res. 28*, 1563–1574.

(88) Louzada, P. R., Paula Lima, A. C., Mendonca-Silva, D. L., Noël, F., De Mello, F. G., and Ferreira, S. T. (2004) Taurine prevents the neurotoxicity of beta-amyloid and glutamate receptor agonists: activation of GABA receptors and possible implications for

Alzheimer's disease and other neurological disorders. *FASEB J. 18*, 511–518.

(89) Streit, W. J., Mrak, R. E., and Griffin, W. S. T. (2004) Microglia and neuroinflammation: A pathological perspective. *J. Neuroinflammation 1*, 1–4.

(90) Mosher, K. I., and Wyss-Coray, T. (2014) Microglial dysfunction in brain aging and Alzheimer's disease. *Biochem. Pharmacol. 88*, 594–604.

(91) Minter, M. R., Taylor, J. M., and Crack, P. J. (2016) The contribution of neuroinflammation to amyloid toxicity in Alzheimer's disease. *J. Neurochem. 136*, 457–474.

(92) Heppner, F. L., Ransohoff, R. M., and Becher, B. (2015) Immune attack: the role of inflammation in Alzheimer disease. *Nat. Rev. Neurosci. 16*, 358–372.

(93) Kinney, J. W., Bemiller, S. M., Murtishaw, A. S., Leisgang, A. M., Salazar, A. M., and Lamb, B. T. (2018) Inflammation as a central mechanism in Alzheimer's disease. *Alzheimer's Dement. Transl. Res. Clin. Interv. 4*, 575–590.

(94) Nasreddine, Z. S., Phillips, N. A., Bédirian, V., Charbonneau, S., Whitehead, V., Collin, I., Cummings, J. L., and Chertkow, H. (2005) The Montreal Cognitive Assessment, MoCA: A brief screening tool for mild cognitive impairment. *J. Am. Geriatr. Soc. 53*, 695–699.

(95) Sikkes, S. A. M., De Lange-De Klerk, E. S. M., Pijnenburg, Y. A. L., Scheltens, P., and Uitdehaag, B. M. J. (2009) A systematic review of Instrumental Activities of Daily Living scales in dementia: Room for improvement. *J. Neurol. Neurosurg. Psychiatry 80*, 7–12.

(96) Sarazin, M., Berr, C., De Rotrou, J., Fabrigoule, C., Pasquier, F., Legrain, S., Michel, B., Puel, M., Volteau, M., Touchon, J., Verny, M., and Dubois, B. (2007)

Amnestic syndrome of the medial temporal type identifies prodromal AD: A longitudinal study. *Neurology 69*, 1859–1867.

(97) Alves, L., Correia, A. S. A., Miguel, R., Alegria, P., and Bugalho, P. (2012) Alzheimer's Disease: A Clinical Practice-Oriented Review. *Front. Neurol. 3*, 1–20.

(98) McKhann, G. M., Knopman, D. S., Chertkow, H., Hyman, B. T., Jack, C. R., Kawas, C. H., Klunk, W. E., Koroshetz, W. J., Manly, J. J., Mayeux, R., Mohs, R. C., Morris, J. C., Rossor, M. N., Scheltens, P., Carrillo, M. C., Thies, B., Weintraub, S., and Phelps, C. H. (2011) The diagnosis of dementia due to Alzheimer's disease: Recommendations from the National Institute on Aging-Alzheimer's Association workgroups on diagnostic guidelines for Alzheimer's disease. *Alzheimer's Dement. 7*, 263–269.

(99) Briggs, R., Kennelly, S. P., and O'Neill, D. (2016) Drug treatments in Alzheimer's disease. *Clin. Med. (Northfield. Il). 16*, 247–253.

(100) Hori, Y., Ihara, N., Teramoto, N., Kunimi, M., Honda, M., Kato, K., and Hanakawa, T. (2015) Noninvasive Quantification of Cerebral Metabolic Rate for Glucose in Rats Using 18 F-FDG PET and Standard Input Function. *J. Cereb. Blood Flow Metab. 35*, 1664–1670.

(101) Berti, V., Vanzi, E., Polito, C., and Pupi, A. (2013) Back to the future: the absolute quantification of cerebral metabolic rate of glucose. *Clin. Transl. Imaging 1*, 289–296.

(102) J, R., G, O., and ER, S. (2006) Regulation of cerebral glucose metabolism.pdf. *Minerva Endocrinol. 31*, 149–158.

(103) Sharma, N., and Singh, A. N. (2016) Exploring biomarkers for Alzheimer's disease. *J. Clin. Diagnostic Res. 10*, KE01–KE06.

(104) Prvulovic, D., and Hampel, H. (2011) Amyloid β (Aβ) and phospho-tau (p-tau) as

diagnostic biomarkers in Alzheimer's disease. *Clin. Chem. Lab. Med. 49*, 367–374.

(105) Moussa-Pacha, N. M., Abdin, S. M., Omar, H. A., Alniss, H., and Al-Tel, T. H. (2020) BACE1 inhibitors: Current status and future directions in treating Alzheimer's disease. *Med. Res. Rev. 40*, 339–384.

(106) Cummings, J., Lee, G., Ritter, A., Sabbagh, M., and Zhong, K. (2019) Alzheimer's disease drug development pipeline: 2019. *Alzheimer's Dement. Transl. Res. Clin. Interv. 5*, 272–293.

(107) Samadi, H., and Sultzer, D. (2011) Solanezumab for Alzheimer's disease. *Expert Opin. Biol. Ther. 11*, 787–798.

(108) Das, B., and Yan, R. (2019) A Close Look at BACE1 Inhibitors for Alzheimer's Disease Treatment. *CNS Drugs 33*, 251–263.

(109) Coimbra, J. R. M., Marques, D. F. F., Baptista, S. J., Pereira, C. M. F., Moreira, P. I., Dinis, T. C. P., Santos, A. E., and Salvador, J. A. R. (2018) Highlights in BACE1 Inhibitors for Alzheimer's Disease Treatment. *Front. Chem. 6*, 1–10.

(110) Mohamed, T. (2016) Multi-Targeting Derivatives For Alzheimer ' s Disease : Utilization of Quinazoline Ring Scaffolds by Tarek Mohamed A thesis presented to the University of Waterloo in fulfillment of the thesis requirement for the degree of Doctor of Philosophy in © Tarek. University of Waterloo.

(111) Cummings, J., Lee, G., Ritter, A., and Zhong, K. (2018) Alzheimer's disease drug development pipeline: 2018. *Alzheimer's Dement. Transl. Res. Clin. Interv. 4*, 195–214.

(112) Xu, Y., Li, M., Greenblatt, H., Chen, W., Paz, A., Dym, O., Peleg, Y., Chen, T., Shen, X., He, J., Jiang, H., Silman, I., and Sussman, J. L. (2012) Flexibility of the flap in the active site of BACE1 as revealed by crystal structures and molecular dynamics

simulations. *Acta Crystallogr. Sect. D Biol. Crystallogr. 68*, 13–25.

(113) Meredith, J. E., Thompson, L. A., Toyn, J. H., Marcin, L., Barten, D. M., Marcinkeviciene, J., Kopcho, L., Kim, Y., Lin, A., Guss, V., Burton, C., Iben, L., Polson, C., Cantone, J., Ford, M., Drexler, D., Fiedler, T., Lentz, K. A., Grace, J. E., Kolb, J., Corsa, J., Pierdomenico, M., Jones, K., Olson, R. E., Macor, J. E., and Albright, C. F. (2008) P-Glycoprotein Efflux and Other Factors Limit Brain Amyloid β Reduction by β-Site Amyloid Precursor Protein-Cleaving Enzyme 1 Inhibitors in Mice. *J. Pharmacol. Exp. Ther. 326*, 502–513.

(114) De Strooper, B., and Chávez Gutiérrez, L. (2015) Learning by failing: ideas and concepts to tackle γ-secretases in Alzheimer's disease and beyond. *Annu. Rev. Pharmacol. Toxicol. 55*, 419–437.

(115) Doody, R. S., Raman, R., Farlow, M., Iwatsubo, T., Vellas, B., Joffe, S., Kieburtz, K., He, F., Sun, X., Thomas, R. G., Aisen, P. S., Siemers, E., Sethuraman, G., and Mohs, R. (2013) A Phase 3 Trial of Semagacestat for Treatment of Alzheimer's Disease. *N. Engl. J. Med. 369*, 341–350.

(116) Schor, N. F. (2011) What the halted phase III γ-secretase inhibitor trial may (or may not) be telling us. *Ann. Neurol. 69*, 237–239.

(117) Imbimbo, B. P. (2008) Alzheimer's disease: γ-secretase inhibitors. *Drug Discov. Today Ther. Strateg. 5*, 169–175.

(118) Postina, R. (2012) Activation of α-secretase cleavage. *J. Neurochem. 120*, 46–54.

(119) Mikulca, J. A., Nguyen, V., Gajdosik, D. A., Teklu, S. G., Giunta, E. A., Lessa, E. A., Tran, C. H., Terak, E. C., and Raffa, R. B. (2014) Potential novel targets for Alzheimer pharmacotherapy: II. Update on secretase inhibitors and related approaches. *J.*

Clin. Pharm. Ther. 39, 25–37.

(120) Uddin, M. S., Kabir, M. T., Jeandet, P., Mathew, B., Ashraf, G. M., Perveen, A., Bin-Jumah, M. N., Mousa, S. A., and Abdel-Daim, M. M. (2020) Novel anti-Alzheimer's therapeutic molecules targeting amyloid precursor protein processing. *Oxid. Med. Cell. Longev. 2020*.

(121) Macleod, R., Hillert, E. K., Cameron, R. T., and Baillie, G. S. (2015) The role and therapeutic targeting of α-, β-and γ-secretase in Alzheimer's disease. *Futur. Sci. OA 1*.

(122) Lichtenthaler, S. F., and Haass, C. (2004) Amyloid at the cutting edge: Activation of α-secretase prevents amyloidogenesis in an Alzheimer disease mouse model. *J. Clin. Invest. 113*, 1384–1387.

(123) Fahrenholz, F., and Postina, R. (2006) α-Secretase Activation – An Approach to Alzheimer's Disease Therapy. *Neurodegener. Dis. 3*, 255–261.

(124) Schallmey, M., Floor, R. J., Szymanski, W., and Janssen, D. B. (2012) 7.8 Hydrolysis and Reverse Hydrolysis: Halohydrin Dehalogenases, in *Comprehensive Chirality*, pp 143–155. Elsevier.

(125) Mangialasche, F., Solomon, A., Winblad, B., Mecocci, P., and Kivipelto, M. (2010) Alzheimer's disease: clinical trials and drug development. *Lancet Neurol. 9*, 702–716.

(126) Sevigny, J., Chiao, P., Bussière, T., Weinreb, P. H., Williams, L., Maier, M., Dunstan, R., Salloway, S., Chen, T., Ling, Y., O'Gorman, J., Qian, F., Arastu, M., Li, M., Chollate, S., Brennan, M. S., Quintero-Monzon, O., Scannevin, R. H., Arnold, H. M., Engber, T., Rhodes, K., Ferrero, J., Hang, Y., Mikulskis, A., Grimm, J., Hock, C., Nitsch, R. M., and Sandrock, A. (2016) The antibody aducanumab reduces Aβ plaques in Alzheimer's disease. *Nature 537*, 50–56.

(127) Wisniewski, T. (2012) Active immunotherapy for Alzheimer's disease. *Lancet Neurol. 11*, 571–572.

(128) Lannfelt, L., Relkin, N. R., and Siemers, E. R. (2014) Amyloid-ß-directed immunotherapy for Alzheimer's disease. *J. Intern. Med. 275*, 284–295.

(129) Morgan, D. (2011) Immunotherapy for Alzheimer's disease. *J. Intern. Med. 269*, 54–63.

(130) Rafii, M. S. (2015) Active Immunotherapy for Alzheimer's Disease: The Road Ahead. *J. Prev. Alzheimer's Dis. 2*, 78–79.

(131) Dolan, P. J., and Zago, W. (2018) Passive Immunotherapy in Alzheimer's Disease, in *Alzheimer's Disease - The 21st Century Challenge*, p 13. InTech.

(132) Pul, R., Dodel, R., and Stangel, M. (2011) Antibody-based therapy in Alzheimer's disease. *Expert Opin. Biol. Ther. 11*, 343–357.

(133) Loureiro, J. C., Pais, M. V., Stella, F., Radanovic, M., Teixeira, A. L., Forlenza, O. V., and de Souza, L. C. (2020) Passive antiamyloid immunotherapy for Alzheimer's disease. *Curr. Opin. Psychiatry 33*, 284–291.

(134) Hung, S. Y., and Fu, W. M. (2017) Drug candidates in clinical trials for Alzheimer's disease. *J. Biomed. Sci. 24*, 1–12.

(135) Crespi, G. A. N., Hermans, S. J., Parker, M. W., and Miles, L. A. (2015) Molecular basis for mid-region amyloid-β capture by leading Alzheimer's disease immunotherapies. *Sci. Rep. 5*, 2–6.

(136) Panza, F., Solfrizzi, V., Imbimbo, B. P., Giannini, M., Santamato, A., Seripa, D., and Logroscino, G. (2014) Efficacy and safety studies of gantenerumab in patients with Alzheimer's disease. *Expert Rev. Neurother. 14*, 973–986.

(137) Loeffler, D. A. (2020) AMBAR, an Encouraging Alzheimer's Trial That Raises Questions. *Front. Neurol. 11*, 1–7.

(138) Boada, M., López, O., Núñez, L., Szczepiorkowski, Z. M., Torres, M., Grifols, C., and Páez, A. (2019) Plasma exchange for Alzheimer's disease Management by Albumin Replacement (AMBAR) trial: Study design and progress. *Alzheimer's Dement. Transl. Res. Clin. Interv. 5*, 61–69.

(139) Robinson, S. R., Bishop, G. M., Lee, H. G., and Münch, G. (2004) Lessons from the AN 1792 Alzheimer vaccine: Lest we forget. *Neurobiol. Aging 25*, 609–615.

(140) Loeffler, D. A. (2013) Intravenous immunoglobulin and Alzheimer's disease: What now? *J. Neuroinflammation 10*, 1.

(141) Di Domizio, J., Zhang, R., Stagg, L. J., Gagea, M., Zhuo, M., Ladbury, J. E., and Cao, W. (2012) Binding with Nucleic Acids or Glycosaminoglycans Converts Soluble Protein Oligomers to Amyloid. *J. Biol. Chem. 287*, 736–747.

(142) Ahmed, M., Davis, J., Aucoin, D., Sato, T., Ahuja, S., Aimoto, S., Elliott, J. I., Van Nostrand, W. E., and Smith, S. O. (2010) Structural conversion of neurotoxic amyloid-B 1-42 oligomers to fibrils. *Nat. Struct. Mol. Biol. 17*, 561–567.

(143) Bieschke, J., Herbst, M., Wiglenda, T., Friedrich, R. P., Boeddrich, A., Schiele, F., Kleckers, D., Lopez del Amo, J. M., Grüning, B. A., Wang, Q., Schmidt, M. R., Lurz, R., Anwyl, R., Schnoegl, S., Fändrich, M., Frank, R. F., Reif, B., Günther, S., Walsh, D. M., and Wanker, E. E. (2012) Small-molecule conversion of toxic oligomers to nontoxic β-sheet–rich amyloid fibrils. *Nat. Chem. Biol. 8*, 93–101.

(144) Oz, M., Lorke, D. E., and Petroianu, G. A. (2009) Methylene blue and Alzheimer's disease. *Biochem. Pharmacol. 78*, 927–932.

(145) Biancalana, M., and Koide, S. (2010) Molecular mechanism of Thioflavin-T binding to amyloid fibrils. *Biochim. Biophys. Acta - Proteins Proteomics 1804*, 1405–1412.

(146) Xue, C., Lin, T. Y., Chang, D., and Guo, Z. (2017) Thioflavin T as an amyloid dye: fibril quantification, optimal concentration and effect on aggregation. *R. Soc. Open Sci. 4*, 160696.

(147) Sulatskaya, A. I., Maskevich, A. A., Kuznetsova, I. M., Uversky, V. N., and Turoverov, K. K. (2010) Fluorescence Quantum Yield of Thioflavin T in Rigid Isotropic Solution and Incorporated into the Amyloid Fibrils. *PLoS One* (Hofmann, A., Ed.) *5*, e15385.

(148) Stoothoff, W. H., and Johnson, G. V. W. (2005) Tau phosphorylation: physiological and pathological consequences. *Biochim. Biophys. Acta - Mol. Basis Dis. 1739*, 280–297.

(149) Gendron, T. F., and Petrucelli, L. (2009) The role of tau in neurodegeneration. *Mol. Neurodegener. 4*, 1–19.

(150) Mohamed, T., Gujral, S. S., and Rao, P. P. N. (2018) Tau Derived Hexapeptide AcPHF6 Promotes Beta-Amyloid (Aβ) Fibrillogenesis. *ACS Chem. Neurosci. 9*, 773–782.

(151) Noble, W., Hanger, D. P., Miller, C. C. J., and Lovestone, S. (2013) The importance of tau phosphorylation for neurodegenerative diseases. *Front. Neurol. 4*, 1–11.

(152) Mondragón-Rodríguez, S., Perry, G., Zhu, X., Moreira, P. I., Acevedo-Aquino, M. C., and Williams, S. (2013) Phosphorylation of Tau Protein as the Link between

Oxidative Stress, Mitochondrial Dysfunction, and Connectivity Failure: Implications for Alzheimer's Disease. *Oxid. Med. Cell. Longev. 2013*, 1–6.

(153) De Calignon, A., Polydoro, M., Su??rez-Calvet, M., William, C., Adamowicz, D. H., Kopeikina, K. J., Pitstick, R., Sahara, N., Ashe, K. H., Carlson, G. A., Spires-Jones, T. L., and Hyman, B. T. (2012) Propagation of Tau Pathology in a Model of Early Alzheimer's Disease. *Neuron 73*, 685–697.

(154) Kolarova, M., García-Sierra, F., Bartos, A., Ricny, J., and Ripova, D. (2012) Structure and pathology of tau protein in Alzheimer disease. *Int. J. Alzheimers. Dis. 2012*.

(155) Medina, M., and Avila, J. (2014) New perspectives on the role of tau in Alzheimer's disease. Implications for therapy. *Biochem. Pharmacol. 88*, 540–547.

(156) Sergeant, N., Delacourte, A., and Buée, L. (2005) Tau protein as a differential biomarker of tauopathies. *Biochim. Biophys. Acta - Mol. Basis Dis. 1739*, 179–197.

(157) Luna-Munoz, J., R., C., M., C., Flores-Rodriguez, P., Avila, J., R., S., la Cruz, F. De, Mena, R., A., M., and Floran-Garduno, B. (2013) Phosphorylation of Tau Protein Associated as a Protective Mechanism in the Presence of Toxic, C-Terminally Truncated Tau in Alzheimer's Disease, in *Understanding Alzheimer's Disease*, p 13. InTech.

(158) Martinez, A. (2010) Emerging Drugs and Targets for Alzheimer's Disease (Martinez, A., Ed.). Royal Society of Chemistry, Cambridge.

(159) Iqbal, K., Liu, F., Gong, C. X., del Alonso, A. C., and Grundke-Iqbal, I. (2009) Mechanisms of tau-induced neurodegeneration. *Acta Neuropathol. 118*, 53–69.

(160) Kocahan, S., and Doğan, Z. (2017) Mechanisms of Alzheimer's disease pathogenesis and prevention: The brain, neural pathology, N-methyl-D-Aspartate

receptors, tau protein and other risk factors. *Clin. Psychopharmacol. Neurosci. 15*, 1–8.

(161) Mohamed, T., and P.N. Rao, P. (2011) Alzheimer's Disease: Emerging Trends in Small Molecule Therapies. *Curr. Med. Chem. 18*, 4299–4320.

(162) Duan, Y., Dong, S., Gu, F., Hu, Y., and Zhao, Z. (2012) Advances in the Pathogenesis of Alzheimer's Disease: Focusing on Tau-Mediated Neurodegeneration. *Transl. Neurodegener. 1*, 1–7.

(163) Villard, V., Espallergues, J., Keller, E., Vamvakides, A., and Maurice, T. (2011) Anti-amnesic and neuroprotective potentials of the mixed muscarinic receptor/sigma 1 (σ 1) ligand ANAVEX2-73, a novel aminotetrahydrofuran derivative. *J. Psychopharmacol. 25*, 1101–1117.

(164) Dicko, A., Roh, M. E., Diawara, H., Mahamar, A., Soumare, H. M., Lanke, K., Bradley, J., Sanogo, K., Kone, D. T., Diarra, K., Keita, S., Issiaka, D., Traore, S. F., McCulloch, C., Stone, W. J. R., Hwang, J., Müller, O., Brown, J. M., Srinivasan, V., Drakeley, C., Gosling, R., Chen, I., and Bousema, T. (2018) Efficacy and safety of primaquine and methylene blue for prevention of Plasmodium falciparum transmission in Mali: a phase 2, single-blind, randomised controlled trial. *Lancet Infect. Dis. 18*, 627–639.

(165) Wood, H. (2016) Phase III trial of anti-tau drug generates mixed messages. *Nat. Rev. Neurol. 12*, 493–493.

(166) Novak, P., Zilka, N., Zilkova, M., Kovacech, B., Skrabana, R., Ondrus, M., Fialova, L., Kontsekova, E., Otto, M., and Novak, M. (2019) AADvac1, an Active Immunotherapy for Alzheimer's Disease and Non Alzheimer Tauopathies: An Overview of Preclinical and Clinical Development. *J. Prev. Alzheimer's Dis. 6*, 63–69.

(167) Mumtaz, A., Shoaib, M., Zaib, S., Shah, M. S., Bhatti, H. A., Saeed, A., Hussain, I., and Iqbal, J. (2018) Synthesis, molecular modelling and biological evaluation of tetrasubstituted thiazoles towards cholinesterase enzymes and cytotoxicity studies. *Bioorg. Chem. 78*, 141–148.

(168) Rahim, F., Javed, M. T., Ullah, H., Wadood, A., Taha, M., Ashraf, M., Qurat-Ul-Ain, Khan, M. A., Khan, F., Mirza, S., and Khan, K. M. (2015) Synthesis, molecular docking, acetylcholinesterase and butyrylcholinesterase inhibitory potential of thiazole analogs as new inhibitors for Alzheimer disease. *Bioorg. Chem. 62*, 106–116.

(169) Mishra, C. B., Kumari, S., and Tiwari, M. (2015) Thiazole: A promising heterocycle for the development of potent CNS active agents. *Eur. J. Med. Chem. 92*, 1–34.

(170) Slater, S. P. (2002) Product Class 17: Thiazoles, in *Category 2, Hetarenes and Related Ring Systems* (Schaumann, Ed.), pp 627–833. Georg Thieme Verlag, Stuttgart.

(171) Singh, I. P., Gupta, S., and Kumar, S. (2020) Thiazole Compounds as Antiviral Agents: An Update. *Med. Chem. (Los. Angeles). 16*, 4–23.

(172) Nora De Souza, M. V. (2005) Synthesis and biological activity of natural thiazoles: An important class of heterocyclic compounds. *J. Sulfur Chem. 26*, 429–449.

(173) Ayati, A., Emami, S., Asadipour, A., Shafiee, A., and Foroumadi, A. (2015) Recent applications of 1,3-thiazole core structure in the identification of new lead compounds and drug discovery. *Eur. J. Med. Chem. 97*, 699–718.

(174) Dincel, E. D., Gürsoy, E., Yilmaz-Ozden, T., and Ulusoy-Güzeldemirci, N. (2020) Antioxidant activity of novel imidazo[2,1-b]thiazole derivatives: Design, synthesis, biological evaluation, molecular docking study and in silico ADME prediction. *Bioorg.*

Chem. 103, 104220.

(175) Sun, Z. Q., Tu, L. X., Zhuo, F. J., and Liu, S. X. (2016) Design and discovery of Novel Thiazole acetamide derivatives as anticholinesterase agent for possible role in the management of Alzheimer's. *Bioorganic Med. Chem. Lett. 26*, 747–750.

(176) Banothu, J., Vaarla, K., Bavantula, R., and Crooks, P. A. (2014) Sodium fluoride as an efficient catalyst for the synthesis of 2,4-disubstituted-1,3-thiazoles and selenazoles at ambient temperature. *Chinese Chem. Lett. 25*, 172–175.

(177) Matsueda, K., Hongo, M., Tack, J., Aoki, H., Saito, Y., and Kato, H. (2010) Clinical trial: dose-dependent therapeutic efficacy of acotiamide hydrochloride (Z-338) in patients with functional dyspepsia - 100 mg t.i.d. is an optimal dosage. *Neurogastroenterol. Motil. 22*, 618-e173.

(178) Bennett, J. P., and Piercey, M. F. (1999) Pramipexole - A new dopamine agonist for the treatment of Parkinson's disease. *J. Neurol. Sci. 163*, 25–31.

(179) Storch, A., Burkhardt, K., Ludolph, A. C., and Schwarz, J. (2000) Protective effects of riluzole on dopamine neurons: Involvement of oxidative stress and cellular energy metabolism. *J. Neurochem. 75*, 2259–2269.

(180) Jimonet, P., Audiau, F., Barreau, M., Blanchard, J. C., Boireau, A., Bour, Y., Coléno, M. A., Doble, A., Doerflinger, G., Do Huu, C., Donat, M. H., Duchesne, J. M., Ganil, P., Guérémy, C., Honoré, E., Just, B., Kerphirique, R., Gontier, S., Hubert, P., Laduron, P. M., Blevec, J. Le, Meunier, M., Miquet, J. M., Nemecek, C., Pasquet, M., Piot, O., Pratt, J., Rataud, J., Reibaud, M., Stutzmann, J. M., and Mignani, S. (1999) Riluzole series. synthesis and in vivo "antiglutamate" activity of 6- substituted-2-benzothiazolamines and 3-substituted-2-imino-benzothiazolines. *J. Med. Chem. 42*,

2828–2843.

(181) Harnett, J. J., Roubert, V., Dolo, C., Charnet, C., Spinnewyn, B., Cornet, S., Rolland, A., Marin, J. G., Bigg, D., and Chabrier, P. E. (2004) Phenolic thiazoles as novel orally-active neuroprotective agents. *Bioorganic Med. Chem. Lett. 14*, 157–160.

(182) Avila, B., Roth, A., Streets, H., Dwyer, D. S., and Kurth, M. J. (2012) Triazolbenzo[d]thiazoles: Efficient synthesis and biological evaluation as neuroprotective agents. *Bioorganic Med. Chem. Lett. 22*, 5976–5978.

(183) Satoh, A., Nagatomi, Y., Hirata, Y., Ito, S., Suzuki, G., Kimura, T., Maehara, S., Hikichi, H., Satow, A., Hata, M., Ohta, H., and Kawamoto, H. (2009) Discovery and in vitro and in vivo profiles of 4-fluoro-N-[4-[6-(isopropylamino)pyrimidin-4-yl]-1,3-thiazol-2-yl]-N-methylbenzamide as novel class of an orally active metabotropic glutamate receptor 1 (mGluR1) antagonist. *Bioorg. Med. Chem. Lett. 19*, 5464–5468.

(184) Hong, S. P., Liu, K. G., Ma, G., Sabio, M., Uberti, M. A., Bacolod, M. D., Peterson, J., Zou, Z. Z., Robichaud, A. J., and Doller, D. (2011) Tricyclic thiazolopyrazole derivatives as metabotropic glutamate receptor 4 positive allosteric modulators. *J. Med. Chem. 54*, 5070–5081.

(185) Andurkar, S. V., Béguin, C., Stables, J. P., and Kohn, H. (2001) Synthesis and structural studies of aza analogues of functionalized amino acids: New anticonvulsant agents. *J. Med. Chem. 44*, 1475–1478.

(186) Collins, I., Wafford, K., Dawson, G. R., Moyes, C., Davey, W. B., Rowley, M., Bromidge, F. A., Quirk, K., Atack, J. R., McKernan, R. M., Thompson, S. A., Pike, A., Sohal, B., Tsou, N. N., Ball, R. G., and Castro, J. L. (2002) 3-Heteroaryl-2-pyridones: Benzodiazepine site ligands with functional selectivity for α2/α3-subtypes of human

GABAa receptor-ion channels. *J. Med. Chem. 45*, 1887–1900.

(187) Désaubry, L., Wermuth, C. G., Boehrer, A., Marescaux, C., and Bourguignon, J. J. (1995) Synthesis and anticonvulsant properties of BW A78U structurally-related compounds. *Bioorganic Med. Chem. Lett. 5*, 139–144.

(188) Lee, Y. S., Kim, H., Kim, Y. H., Roh, E. J., Han, H., and Shin, K. J. (2012) Synthesis and structure-activity relationships of tri-substituted thiazoles as RAGE antagonists for the treatment of Alzheimer's disease. *Bioorganic Med. Chem. Lett. 22*, 7555–7561.

(189) Andreani, A., Burnelli, S., Granaiola, M., Guardigli, M., Leoni, A., Locatelli, A., Morigi, R., Rambaldi, M., Rizzoli, M., Varoli, L., and Roda, A. (2008) Chemiluminescent high-throughput microassay applied to imidazo[2,1-b]thiazole derivatives as potential acetylcholinesterase and butyrylcholinesterase inhibitors. *Eur. J. Med. Chem. 43*, 657–661.

(190) Lagoja, I., Pannecouque, C., Griffioen, G., Wera, S., Rojasdelaparra, V. M., and Van Aerschot, A. (2011) Substituted 2-aminothiazoles are exceptional inhibitors of neuronal degeneration in tau-driven models of Alzheimer's disease. *Eur. J. Pharm. Sci. 43*, 386–392.

(191) Shiradkar, M. R., Akula, K. C., Dasari, V., Baru, V., Chiningiri, B., Gandhi, S., and Kaur, R. (2007) Clubbed thiazoles by MAOS: A novel approach to cyclin-dependent kinase 5/p25 inhibitors as a potential treatment for Alzheimer's disease. *Bioorganic Med. Chem. 15*, 2601–2610.

(192) Rao, P. P. N., Pham, A. T., and Shakeri, A. (2020) Discovery of small molecules for the treatment of Alzheimer's disease, in *Small Molecule Drug Discovery*, pp 289–

322. Elsevier.

(193) Varga, B., Csonka, Á., Csonka, A., Molnár, J., Amaral, L., and Spengler, G. (2017) Possible Biological and Clinical Applications of Phenothiazines. *Anticancer Res. 37*, 5983–5993.

(194) Tin, G., Mohamed, T., Gondora, N., Beazely, M. A., and Rao, P. P. N. (2015) Tricyclic phenothiazine and phenoselenazine derivatives as potential multi-targeting agents to treat Alzheimer's disease. *Medchemcomm 6*, 1930–1941.

(195) Darvesh, S., Darvesh, K. V., McDonald, R. S., Mataija, D., Walsh, R., Mothana, S., Lockridge, O., and Martin, E. (2008) Carbamates with Differential Mechanism of Inhibition Toward Acetylcholinesterase and Butyrylcholinesterase. *J. Med. Chem. 51*, 4200–4212.

(196) Mohamed, T., Zhao, X., Habib, L. K., Yang, J., and Rao, P. P. N. (2011) Design, synthesis and structure–activity relationship (SAR) studies of 2,4-disubstituted pyrimidine derivatives: Dual activity as cholinesterase and Aβ-aggregation inhibitors. *Bioorg. Med. Chem. 19*, 2269–2281.

(197) Mohamed, T., Yeung, J. C. K., Vasefi, M. S., Beazely, M. A., and Rao, P. P. N. (2012) Development and evaluation of multifunctional agents for potential treatment of Alzheimer's disease: Application to a pyrimidine-2,4-diamine template. *Bioorg. Med. Chem. Lett. 22*, 4707–4712.

(198) Mohamed, T., and Rao, P. P. N. (2017) 2,4-Disubstituted quinazolines as amyloid-β aggregation inhibitors with dual cholinesterase inhibition and antioxidant properties: Development and structure-activity relationship (SAR) studies. *Eur. J. Med. Chem. 126*, 823–843.

(199) Mohamed, T., Mann, M. K., and Rao, P. P. N. (2017) Application of quinazoline and pyrido[3,2-d]pyrimidine templates to design multi-targeting agents in Alzheimer's disease. *RSC Adv. 7*, 22360–22368.

(200) Warashina, M., Min, K. H., Kuwabara, T., Huynh, A., Gage, F. H., Schultz, P. G., and Ding, S. (2006) A synthetic small molecule that induces neuronal differentiation of adult hippocampal neural progenitor cells. *Angew. Chem. Int. Ed. Engl. 45*, 591–593.

(201) Graf, T., and Enver, T. (2009) Forcing cells to change lineages. *Nature 462*, 587–594.

(202) Schnürch, M., Waldner, B., Hilber, K., and Mihovilovic, M. D. (2011) Synthesis of 5-arylated N-arylthiazole-2-amines as potential skeletal muscle cell differentiation promoters. *Bioorg. Med. Chem. Lett. 21*, 2149–2154.

(203) Videnov, G., Kaiser, D., Kempter, C., and Jung, G. (1996) Synthesis of Naturally Occurring, Conformationally Restricted Oxazole- and Thiazole-Containing Di- and Tripeptide Mimetics. *Angew. Chemie Int. Ed. English 35*, 1503–1506.

(204) Kim, G. H., Halder, D., Park, J., Namkung, W., and Shin, I. (2014) Imidazole-based small molecules that promote neurogenesis in pluripotent cells. *Angew. Chemie - Int. Ed. 53*, 9271–9274.

(205) Halder, D., Kim, G.-H., and Shin, I. (2015) Synthetic small molecules that induce neuronal differentiation in neuroblastoma and fibroblast cells. *Mol. Biosyst. 11*, 2727–2737.

(206) Shidore, M., Machhi, J., Shingala, K., Murumkar, P., Sharma, M. K., Agrawal, N., Tripathi, A., Parikh, Z., Pillai, P., and Yadav, M. R. (2016) Benzylpiperidine-Linked Diarylthiazoles as Potential Anti-Alzheimer's Agents: Synthesis and Biological

Evaluation. *J. Med. Chem. 59*, 5823–5846.

(207) Cao, Q., Shin, W. S., Chan, H., Vuong, C. K., Dubois, B., Li, B., Murray, K. A., Sawaya, M. R., Feigon, J., Black, D. L., Eisenberg, D. S., and Jiang, L. (2018) Inhibiting amyloid-ß cytotoxicity through its interaction with the cell surface receptor LilrB2 by structure-based design. *Nat. Chem. 10*.

(208) Lipinski, C. A., Lombardo, F., Dominy, B. W., and Feeney, P. J. (2012) Experimental and computational approaches to estimate solubility and permeability in drug discovery and development settings. *Adv. Drug Deliv. Rev. 64*, 4–17.

(209) Makam, P., and Kannan, T. (2014) 2-Aminothiazole derivatives as antimycobacterial agents: Synthesis, characterization, in vitro and in silico studies. *Eur. J. Med. Chem. 87*, 643–656.

(210) Benz, M., and Prins, R. (1999) Kinetics of the reduction of aromatic nitro compounds with hydrazine hydrate in the presence of an iron oxide hydroxide catalyst. *Appl. Catal. A Gen. 183*, 325–333.

(211) Cellier, P. P., Spindler, J. F., Taillefer, M., and Cristau, H. J. (2003) Pd/C-catalyzed room-temperature hydrodehalogenation of aryl halides with hydrazine hydrochloride. *Tetrahedron Lett. 44*, 7191–7195.

(212) Paravastu, A. K., Leapman, R. D., Yau, W. M., and Tycko, R. (2008) Molecular structural basis for polymorphism in Alzheimer's β-amyloid fibrils. *Proc. Natl. Acad. Sci. U. S. A. 105*, 18349–18354.

(213) Colvin, M. T., Silvers, R., Ni, Q. Z., Can, T. V., Sergeyev, I., Rosay, M., Donovan, K. J., Michael, B., Wall, J., Linse, S., and Griffin, R. G. (2016) Atomic Resolution Structure of Monomorphic Aβ 42 Amyloid Fibrils. *J. Am. Chem. Soc. 138*, 9663–9674.

(214) Berridge, M. V., and Tan, A. S. (1993) Characterization of the Cellular Reduction of 3-(4,5-dimethylthiazol-2- yl)-2,5-diphenyltetrazolium bromide (MTT): Subcellular Localization, Substrate Dependence, and Involvement of Mitochondrial Electron Transport in MTT Reduction. *Arch. Biochem. Biophys. 303*, 474–482.

(215) Aslantürk, Ö. S. (2018) In Vitro Cytotoxicity and Cell Viability Assays: Principles, Advantages, and Disadvantages, in *Genotoxicity - A Predictable Risk to Our Actual World*, pp 137–144. InTech.

(216) Thompson, C. M., Poole, J. L., Cross, J. L., Akritopoulou-Zanze, I., and Djuric, S. W. (2011) Small molecule library synthesis using segmented flow. *Molecules 16*, 9161–9177.

(217) Co., T. P., and Ltd, A. T. L. W. (2021) Example 49 (2E)-4-(tert-Butylamino)-N-(2,6-difluoro-4-{8-[-methyl-6-(trifluoromethyl)-H-1,3-benzodiazol-5-yl]indolizine-3-carbonyl}phenyl}phenyl)but-2-enamide.

(218) Keshari, T., Kapoorr, R., and Yadav, L. D. S. (2015) Carbon tetrabromide mediated oxidative cyclocondensation of ketones and thioureas: an easy access to 2-aminothiazoles. *Tetrahedron Lett. 56*, 5623–5627.

(219) Ronco, C., Millet, A., Plaisant, M., Abbe, P., Hamouda-Tekaya, N., Rocchi, S., and Benhida, R. (2017) Structure activity relationship and optimization of N-(3-(2-aminothiazol-4-yl)aryl)benzenesulfonamides as anti-cancer compounds against sensitive and resistant cells. *Bioorganic Med. Chem. Lett. 27*, 2192–2196.

(220) Rao, P. P. N., Mohamed, T., Teckwani, K., and Tin, G. (2015) Curcumin Binding to Beta Amyloid: A Computational Study. *Chem. Biol. Drug Des. 86*, 813–820.

(221) Rao, P. P. N., Pham, A. T., Shakeri, A., El Shatshat, A., Zhao, Y., Karuturi, R. C.,

and Hefny, A. A. (2021) Drug Repurposing: Dipeptidyl Peptidase IV (DPP4) Inhibitors as Potential Agents to Treat SARS-CoV-2 (2019-nCoV) Infection. *Pharmaceuticals 14*, 44.

(222) Riss, T. L., Moravec, R. A., Niles, A. L., Duellman, S., Benink, H. A., Worzella, T. J., and Minor, L. (2013) Cell Viability Assays. *Assay Guid. Man. [Internet] 114*, 785–796.

(223) Apaydın, S., and Török, M. (2019) Sulfonamide derivatives as multi-target agents for complex diseases. *Bioorganic Med. Chem. Lett. 29*, 2042–2050.

(224) Bhat, M. A., Imran, M., Khan, S. A., and Siddiqui, N. (2005) Biological Activities of Sulfonamides. *Indian J. Pharm. Sci. 67*, 151–159.

(225) Chen, X., Hussain, S., Parveen, S., Zhang, S., Yang, Y., and Zhu, C. (2012) Sulfonyl Group-Containing Compounds in the Design of Potential Drugs for the Treatment of Diabetes and Its Complications. *Curr. Med. Chem. 19*, 3578–3604.

(226) Ning, X., Guo, Y., Ma, X., Zhu, R., Tian, C., Zhang, Z., Wang, X., Ma, Z., and Liu, J. (2013) Design, synthesis and pharmacological evaluation of (E)-3,4-dihydroxy styryl sulfonamides derivatives as multifunctional neuroprotective agents against oxidative and inflammatory injury. *Bioorganic Med. Chem. 21*, 5589–5597.

(227) Kwon, Y., Song, J., Lee, H., Kim, E. Y., Lee, K., Lee, S. K., and Kim, S. (2015) Design, Synthesis, and Biological Activity of Sulfonamide Analogues of Antofine and Cryptopleurine as Potent and Orally Active Antitumor Agents. *J. Med. Chem. 58*, 7749–7762.

(228) Holloway, M. K., Hunt, P., and McGaughey, G. B. (2009) Structure and modeling in the design of β- and γ-secretase inhibitors. *Drug Dev. Res. 70*, 70–93.

(229) MacMillan, K. S., Naidoo, J., Liang, J., Melito, L., Williams, N. S., Morlock, L., Huntington, P. J., Estill, S. J., Longgood, J., Becker, G. L., McKnight, S. L., Pieper, A. A., De Brabander, J. K., and Ready, J. M. (2011) Development of Proneurogenic, Neuroprotective Small Molecules. *J. Am. Chem. Soc. 133*, 1428–1437.

(230) Lis, R., and Marisca, A. J. (1987) Methanesulfonanilides and the Mannich reaction. *J. Org. Chem. 52*, 4377–4379.

(231) Makam, P., and Kannan, T. (2014) 2-Aminothiazole derivatives as antimycobacterial agents: Synthesis, characterization, in vitro and in silico studies. *Eur. J. Med. Chem. 87*, 643–656.

(232) Tolar, M., Abushakra, S., Hey, J. A., Porsteinsson, A., and Sabbagh, M. (2020) Aducanumab, gantenerumab, BAN2401, and ALZ-801 - The first wave of amyloid-targeting drugs for Alzheimer's disease with potential for near term approval. *Alzheimer's Res. Ther. 12*, 1–10.

(233) Tin, G., Mohamed, T., Shakeri, A., Pham, A. T., and Rao, P. P. N. (2019) Interactions of Selective Serotonin Reuptake Inhibitors with β-Amyloid. *ACS Chem. Neurosci. 10*, 226–234.

(234) Kamiloglu, S., Sari, G., Ozdal, T., and Capanoglu, E. (2020) Guidelines for cell viability assays. *Food Front. 1*, 332–349.

(235) Lazic, S. E., Clarke-Williams, C. J., and Munafò, M. R. (2018) What exactly is 'N' in cell culture and animal experiments? *PLOS Biol. 16*, e2005282.

(236) Götz, J., Halliday, G., and Nisbet, R. M. (2019) Molecular Pathogenesis of the Tauopathies. *Annu. Rev. Pathol. Mech. Dis. 14*, 239–261.

(237) Avila, J., Jiménez, J. S., Sayas, C. L., Bolós, M., Zabala, J. C., Rivas, G., and

Hernández, F. (2016) Tau Structures. *Front. Aging Neurosci. 8*, 1–10.

(238) Cisek, K., Cooper, G., Huseby, C., and Kuret, J. (2014) Structure and Mechanism of Action of Tau Aggregation Inhibitors. *Curr. Alzheimer Res. 11*, 918–927.

(239) Ganguly, P., Do, T. D., Larini, L., LaPointe, N. E., Sercel, A. J., Shade, M. F., Feinstein, S. C., Bowers, M. T., and Shea, J.-E. (2015) Tau Assembly: The Dominant Role of PHF6 (VQIVYK) in Microtubule Binding Region Repeat R3. *J. Phys. Chem. B 119*, 4582–4593.

(240) Seidler, P. M., Boyer, D. R., Rodriguez, J. A., Sawaya, M. R., Cascio, D., Murray, K., Gonen, T., and Eisenberg, D. S. (2018) Structure-based inhibitors of tau aggregation. *Nat. Chem. 10*, 170–176.

(241) Mohamed, T., Hoang, T., Jelokhani-Niaraki, M., and Rao, P. P. N. (2013) Tau-Derived-Hexapeptide 306 VQIVYK 311 Aggregation Inhibitors: Nitrocatechol Moiety as A Pharmacophore In Drug Design. *ACS Chem. Neurosci. 4*, 1559–1570.

(242) Silva, T., Mohamed, T., Shakeri, A., Rao, P. P. N., Soares da Silva, P., Remião, F., and Borges, F. (2019) Repurposing nitrocatechols: 5-Nitro-α-cyanocarboxamide derivatives of caffeic acid and caffeic acid phenethyl ester effectively inhibit aggregation of tau-derived hexapeptide AcPHF6. *Eur. J. Med. Chem. 167*, 146–152.

(243) Young, D. C. (2009) Pharmacophore Models, in *Computational Drug Design*, pp 161–169. John Wiley & Sons, Inc., Hoboken, NJ, USA.

(244) Blanco, A., Álvarez, S., Fresno, M., and Muñoz-Fernández, M. Á. (2010) Amyloid-β Induces Cyclooxygenase-2 and PGE2 Release in Human Astrocytes in NF-κ B Dependent Manner. *J. Alzheimer's Dis. 22*, 493–505.

Appendices

Appendix 1: Sample Spectra for Chapter 3

4-(3,4-Dimethoxyphenyl)-*N*-phenylthiazol-2-amine (1d)

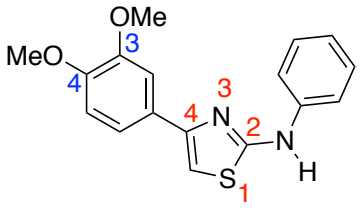

1d

BRUKER
10.226
7.716
7.689
7.499
7.471
7.366
7.340
7.315
7.209
7.023
6.996
6.985
6.959
6.935
3.837
3.787
3.341
2.1
ppm
0 1 2 3 4 5 6 7 8 9 10 11 12 13
6.00
1.99
0.94
2.06
2.02
2.02
0.96
ppm
7.0 7.1 7.2 7.3 7.4 7.5 7.6 7.7 7.8
1.99
0.94
2.06
2.02
2.02

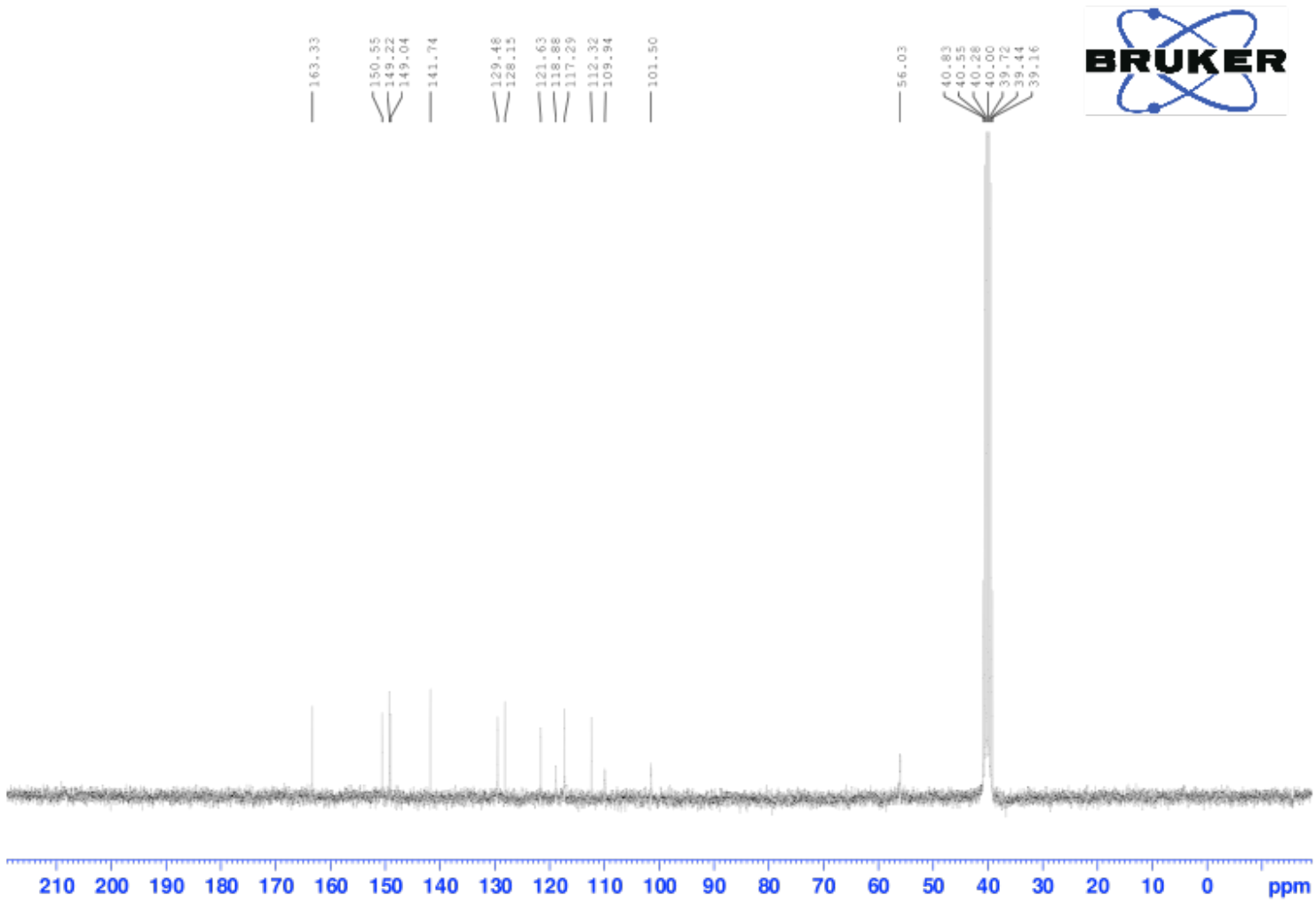
163.33
150.55
149.22
149.04
141.74
129.48
128.15
121.63
118.88
117.29
112.32
109.94
101.50
56.03
40.83
40.55
40.28
40.00
39.72
39.44
39.16
BRUKER
210 200 190 180 170 160 150 140 130 120 110 100 90 80 70 60 50 40 30 20 10 0 ppm

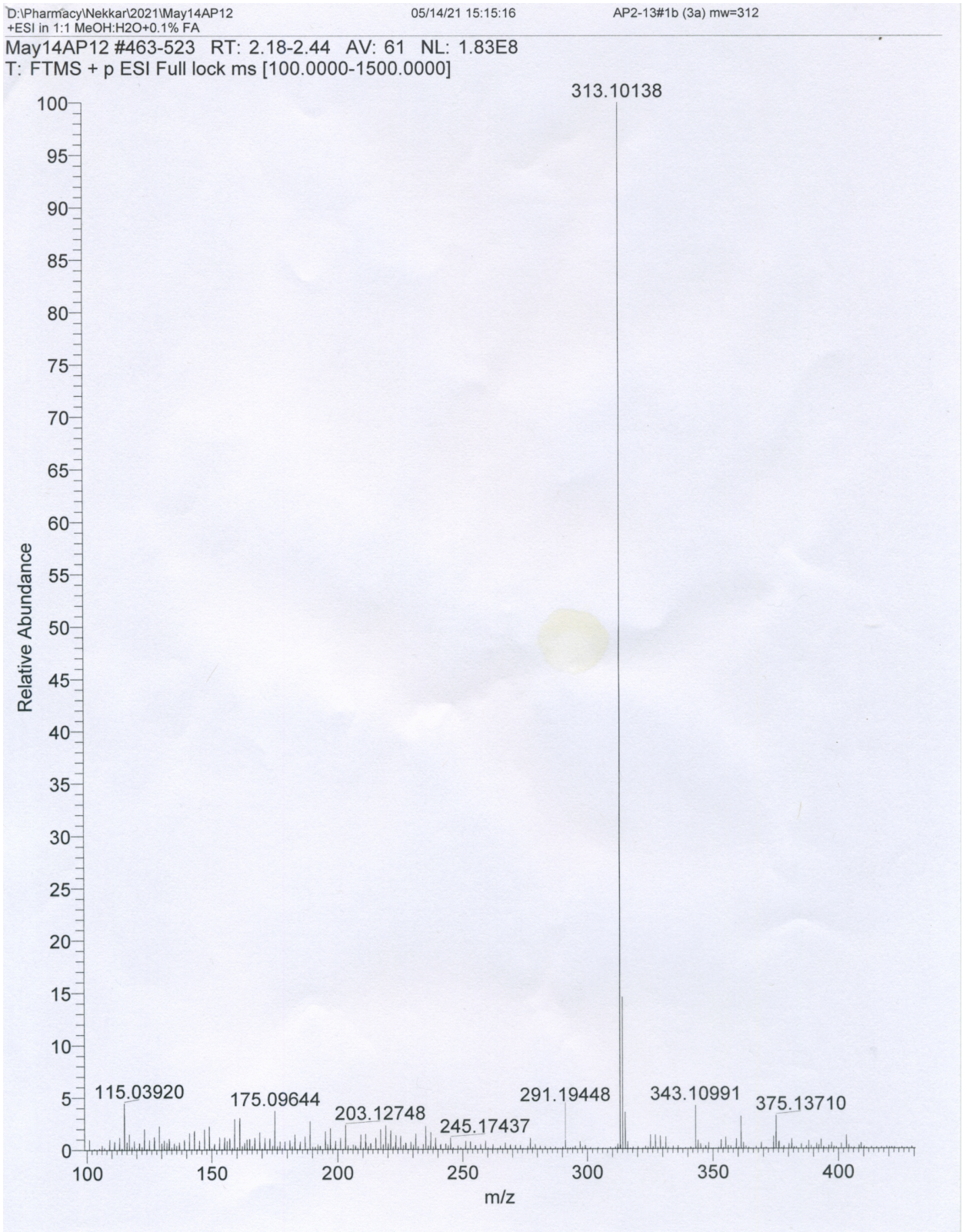
D:\Pharmacy\Nekkar\2021\May14AP12
05/14/21 15:15:16
AP2-13#1b (3a) mw=312
+ESI in 1:1 MeOH:H2O+0.1% FA
May14AP12 #463-523 RT: 2.18-2.44 AV: 61 NL: 1.83E8
T: FTMS + p ESI Full lock ms [100.0000-1500.0000]
313.10138
115.03920
175.09644
203.12748
245.17437
291.19448
343.10991
375.13710
Relative Abundance
m/z

4-(3-Nitrophenyl)-*N*-phenylthiazol-2-amine (1f)

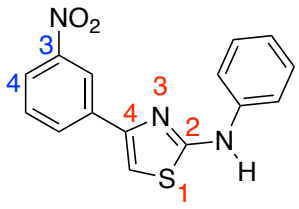

1f

BRUKER
2.509
3.331
10.378
8.699
8.376
8.350
8.170
8.143
7.759
7.732
7.715
7.688
7.676
7.388
7.362
7.337
7.018
6.993
6.969
ppm
1.02
2.07
4.20
1.03
1.04
1.03
1.00

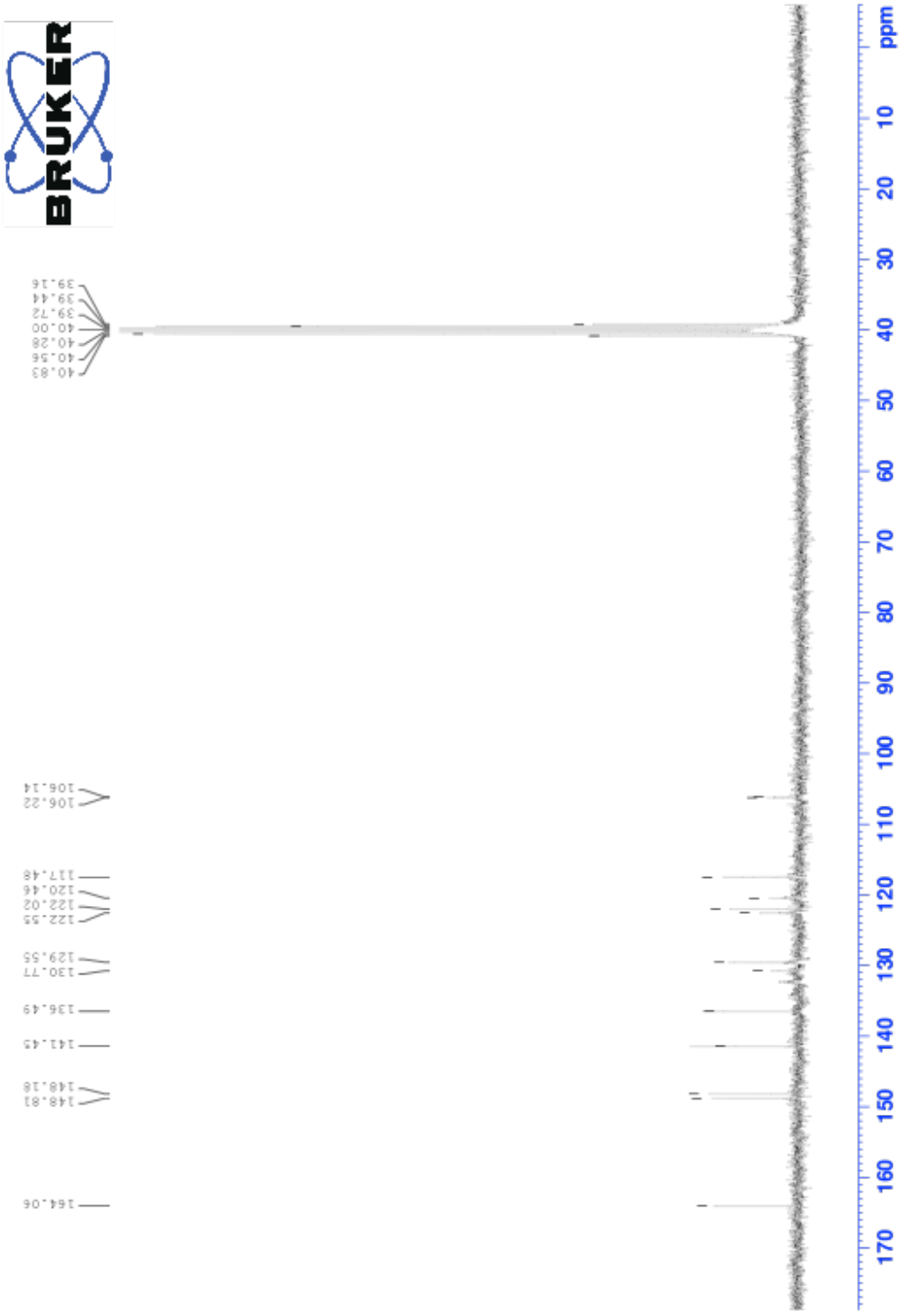
BRUKER
39.16
39.44
39.72
40.00
40.28
40.56
40.83
106.14
106.22
117.48
120.46
122.02
122.55
129.55
130.77
136.49
141.45
148.18
148.81
164.06
ppm
10
20
30
40
50
60
70
80
90
100
110
120
130
140
150
160
170

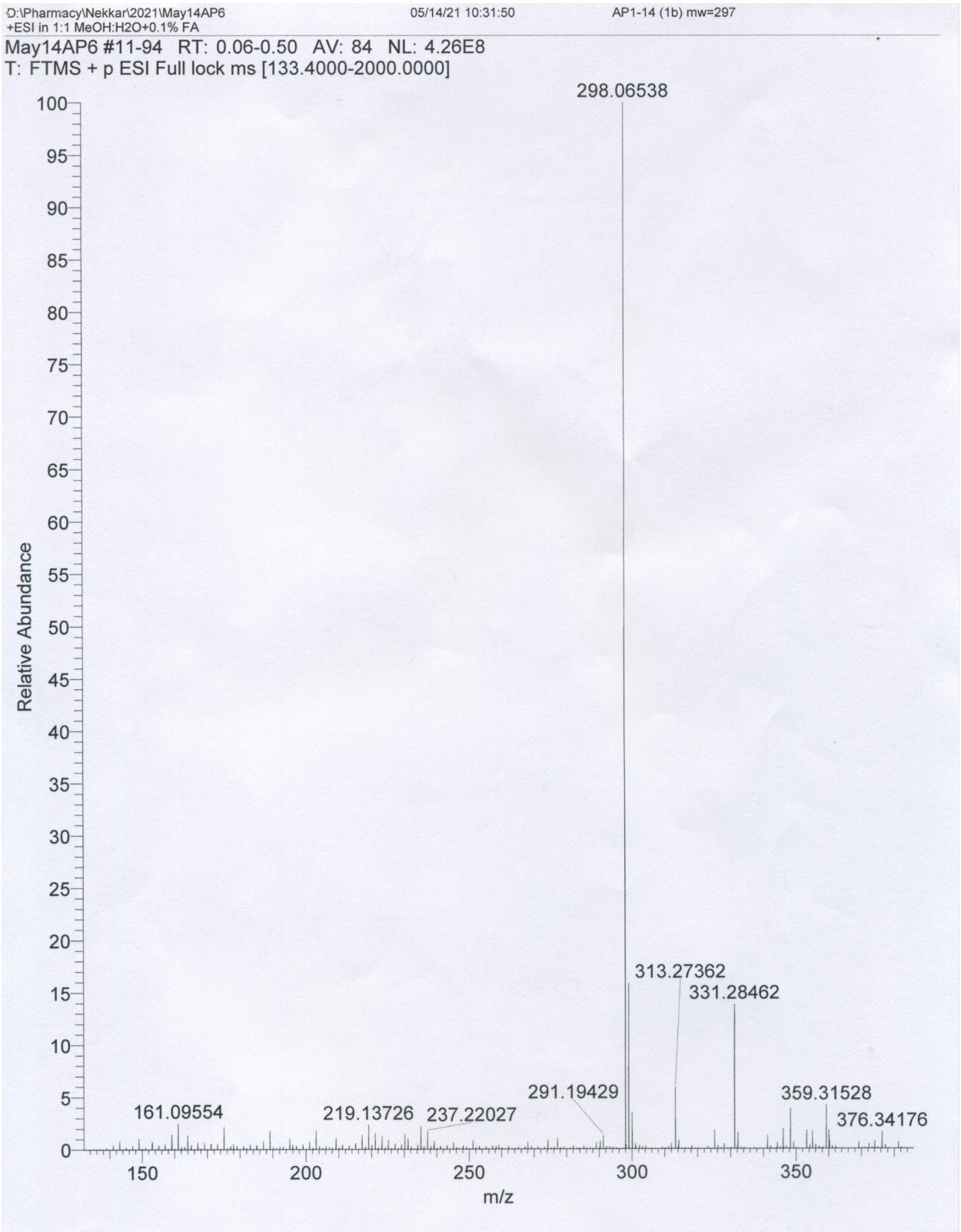
D:\Pharmacy\Nekkar\2021\May14AP6
+ESI in 1:1 MeOH:H2O+0.1% FA
05/14/21 10:31:50
AP1-14 (1b) mw=297
May14AP6 #11-94 RT: 0.06-0.50 AV: 84 NL: 4.26E8
T: FTMS + p ESI Full lock ms [133.4000-2000.0000]
298.06538
313.27362
331.28462
291.19429
359.31528
376.34176
161.09554
219.13726
237.22027
Relative Abundance
m/z
100
95
90
85
80
75
70
65
60
55
50
45
40
35
30
25
20
15
10
5
0
150
200
250
300
350

4-(3,4-Difluorophenyl)-*N*-phenylthiazol-2-amine (1j)

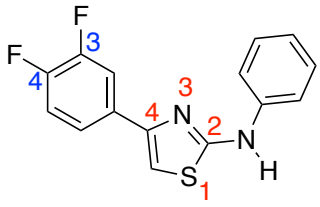

1j

BRUKER
10.297
7.955
7.928
7.921
7.914
7.888
7.785
7.770
7.757
7.715
7.688
7.537
7.505
7.474
7.432
7.374
7.348
7.323
6.993
6.969
6.945
3.337
2.507
1.04
2.12
2.14
2.09
1.06
1.04
1.00
ppm

BRUKER
104.56
114.79
114.94
117.37
118.19
118.33
121.84
122.88
129.52
132.68
141.51
148.37
163.78
ppm
40
50
60
70
80
90
100
110
120
130
140
150
160
170

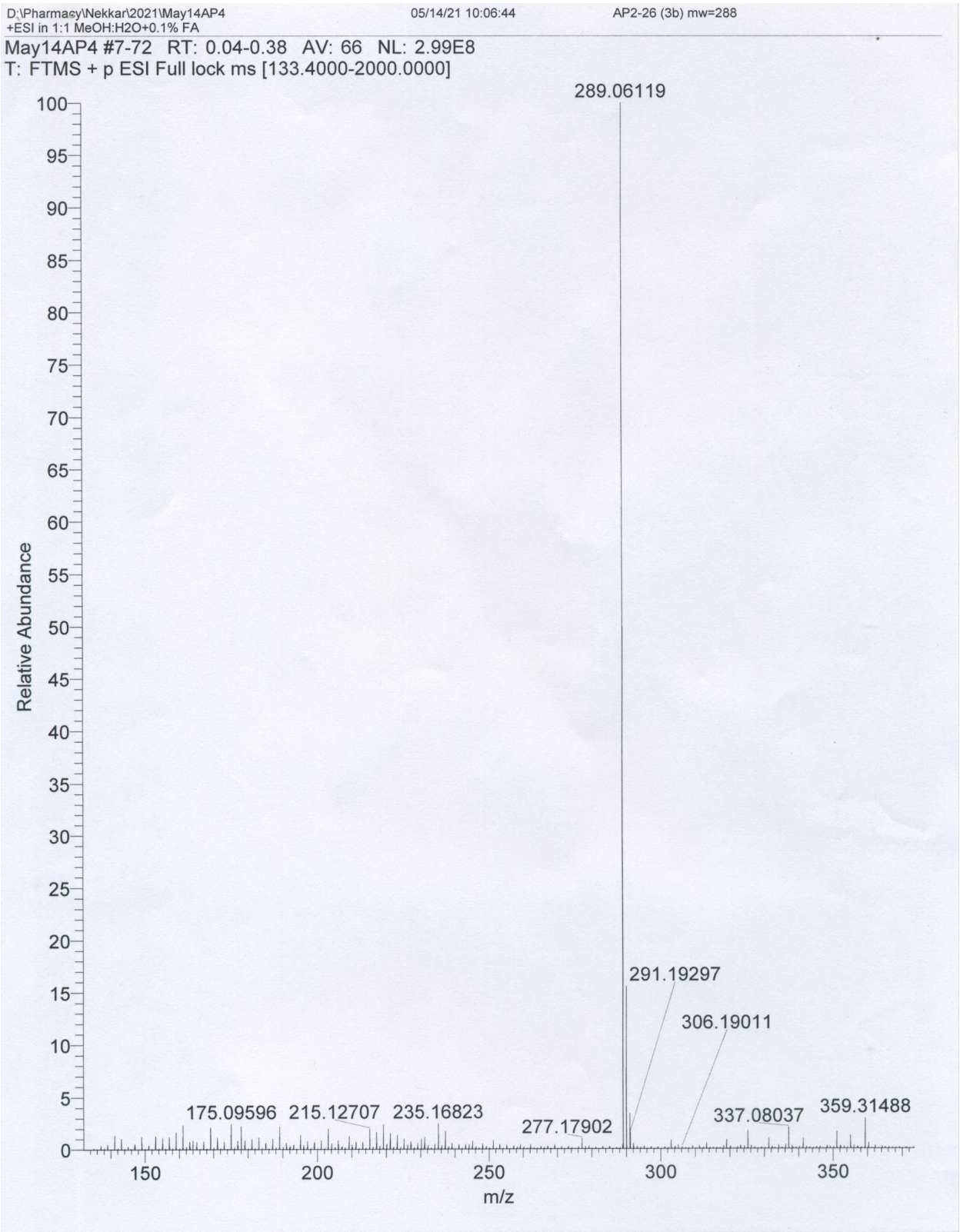
D:\Pharmacy\Nekkar\2021\May14AP4
+ESI in 1:1 MeOH:H2O+0.1% FA
05/14/21 10:06:44
AP2-26 (3b) mw=288
May14AP4 #7-72 RT: 0.04-0.38 AV: 66 NL: 2.99E8
T: FTMS + p ESI Full lock ms [133.4000-2000.0000]
289.06119
291.19297
306.19011
175.09596
215.12707
235.16823
277.17902
337.08037
359.31488
Relative Abundance
m/z
100
95
90
85
80
75
70
65
60
55
50
45
40
35
30
25
20
15
10
5
0
150
200
250
300
350

4-(4-Aminophenyl)-*N*-phenylthiazol-2-amine (2a)

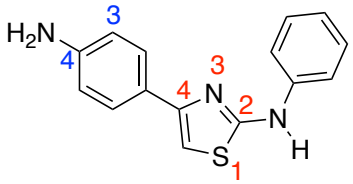

2a

BRUKER
2.508
3.383
5.158
6.522
6.536
6.543
6.558
6.935
6.959
6.984
7.060
7.076
7.087
7.171
7.313
7.339
7.365
7.722
7.749
10.205
ppm
0 1 2 3 4 5 6 7 8 9 10 11 12 13
1.66
0.95
1.01
2.84
0.97
1.98
1.96
1.00
7.7 7.6 7.5 7.4 7.3 7.2 7.1
1.96
1.98
0.97
2.84
1.01

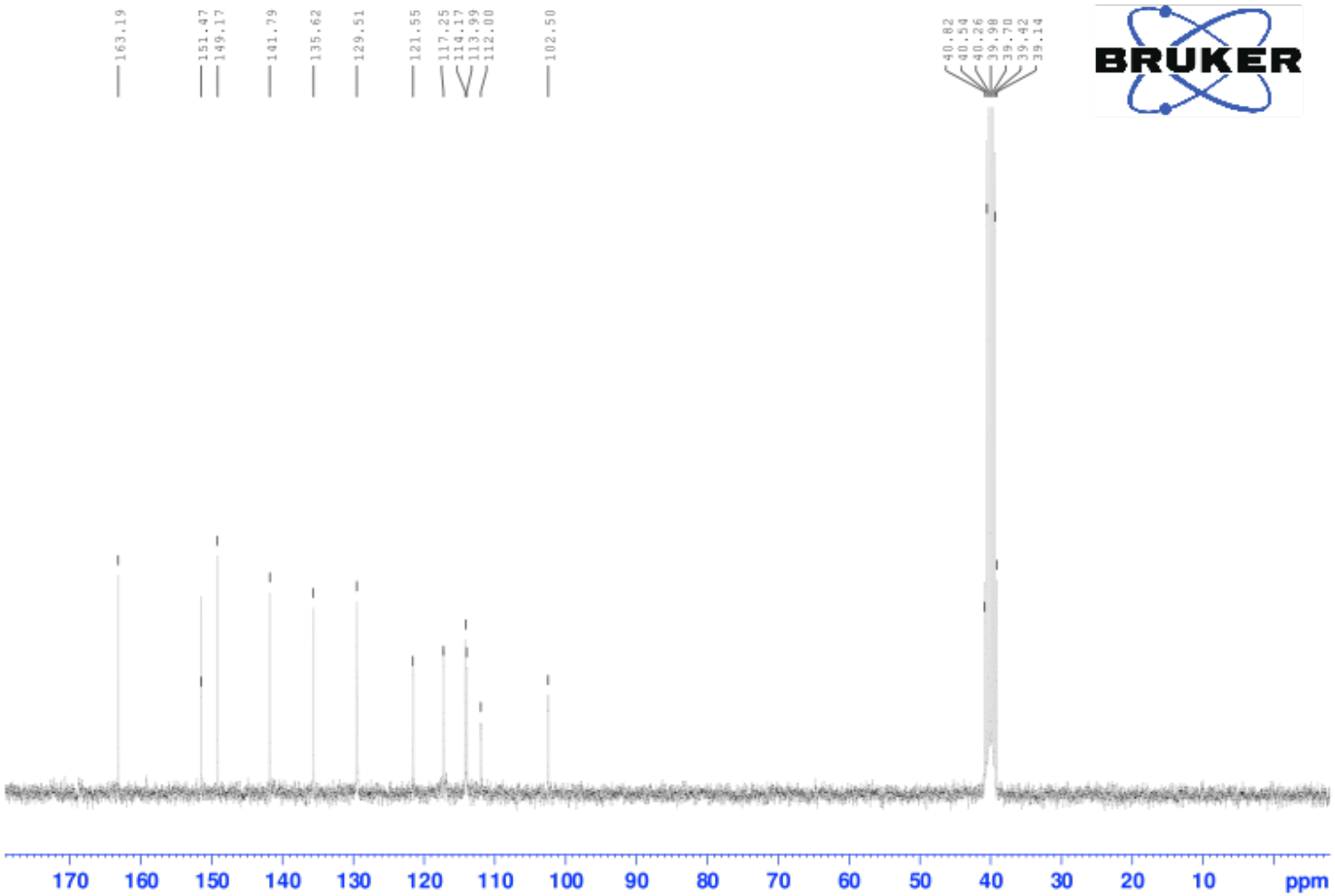
163.19
151.47
149.17
141.79
135.62
129.51
121.55
117.25
114.17
113.99
112.00
102.50
40.82
40.54
40.26
39.98
39.70
39.42
39.14
BRUKER
170
160
150
140
130
120
110
100
90
80
70
60
50
40
30
20
10
ppm

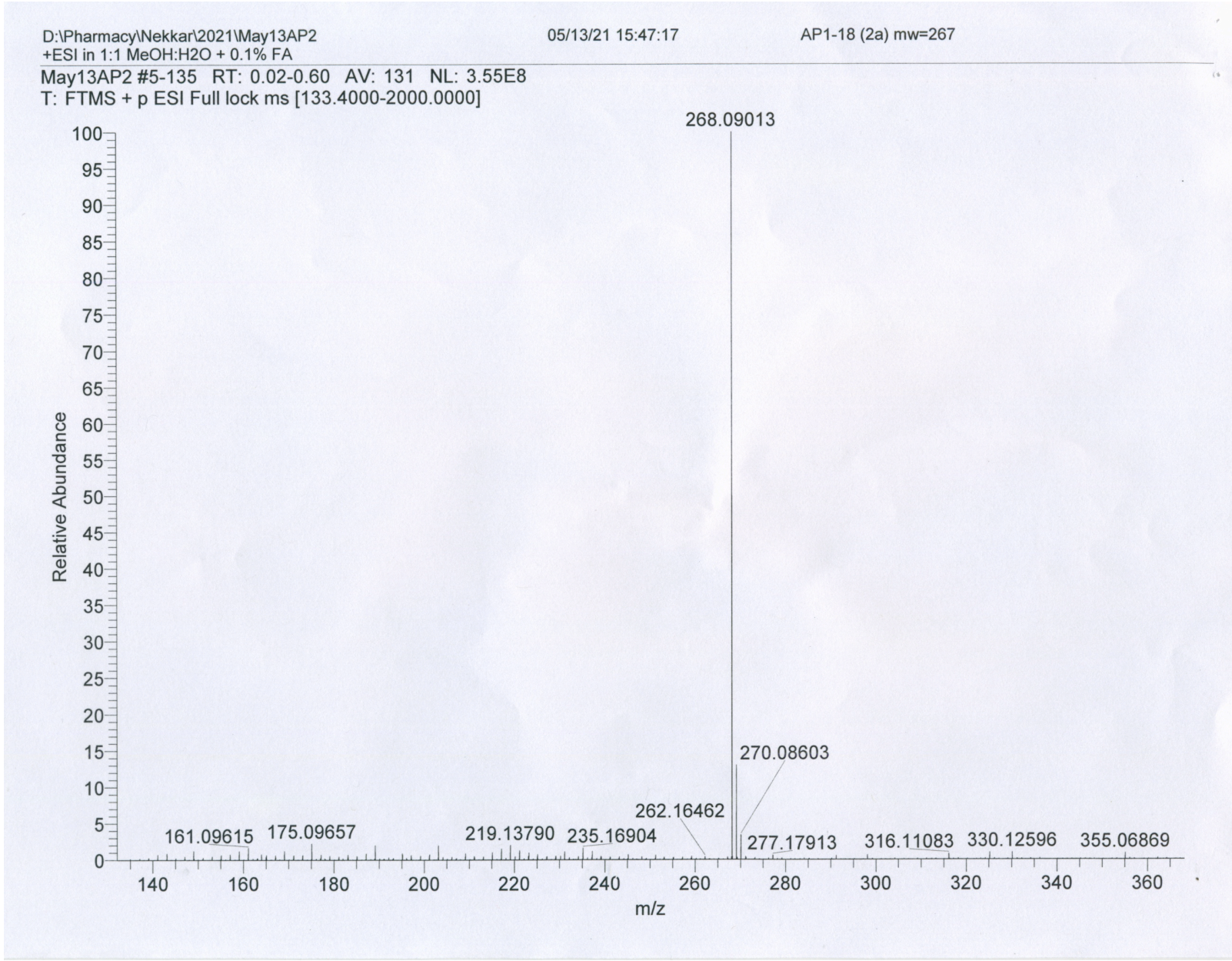
D:\Pharmacy\Nekkar\2021\May13AP2
+ESI in 1:1 MeOH:H2O + 0.1% FA
05/13/21 15:47:17
AP1-18 (2a) mw=267
May13AP2 #5-135 RT: 0.02-0.60 AV: 131 NL: 3.55E8
T: FTMS + p ESI Full lock ms [133.4000-2000.0000]
268.09013
270.08603
262.16462
161.09615
175.09657
219.13790
235.16904
277.17913
316.11083
330.12596
355.06869
Relative Abundance
m/z

Appendix 2: Sample Spectra for Chapter 4

N-Methyl-*N*-diphenylthiazol-2-amine (3a)

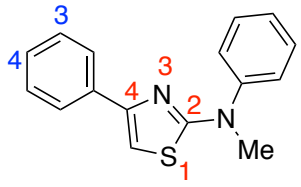

3a

BRUKER
2.499
3.336
3.540
7.886
7.861
7.542
7.515
7.498
7.473
7.446
7.421
7.396
7.371
7.313
7.289
7.265
7.198
ppm
1
2
3
4
5
6
7
8
9
10
2.93
1.98
6.35
2.03
0.97
ppm
7.3
7.4
7.5
7.6
7.7
7.8
7.9
0.97
2.03
6.35
1.98

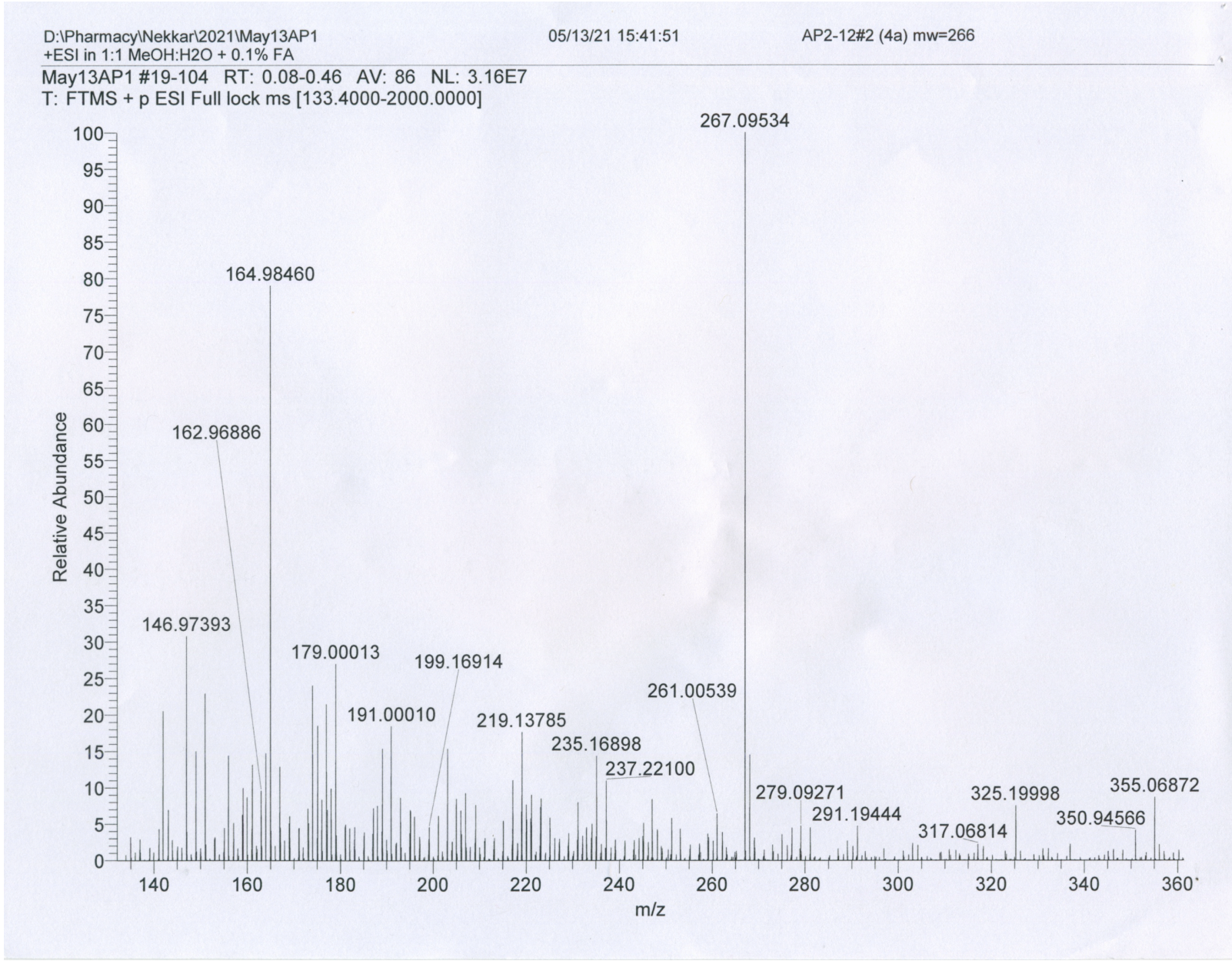
D:\Pharmacy\Nekkar\2021\May13AP1
+ESI in 1:1 MeOH:H2O + 0.1% FA
05/13/21 15:41:51
AP2-12#2 (4a) mw=266
May13AP1 #19-104 RT: 0.08-0.46 AV: 86 NL: 3.16E7
T: FTMS + p ESI Full lock ms [133.4000-2000.0000]
Relative Abundance
m/z
267.09534
164.98460
162.96886
146.97393
179.00013
199.16914
191.00010
219.13785
261.00539
235.16898
237.22100
279.09271
291.19444
325.19998
355.06872
350.94566
317.06814

4-(4-Methoxyphenyl)-*N*-methyl-*N*-phenylthiazol-2-amine (3c)

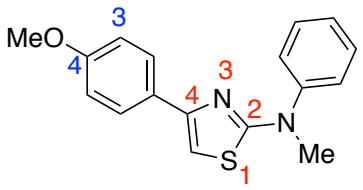

3c

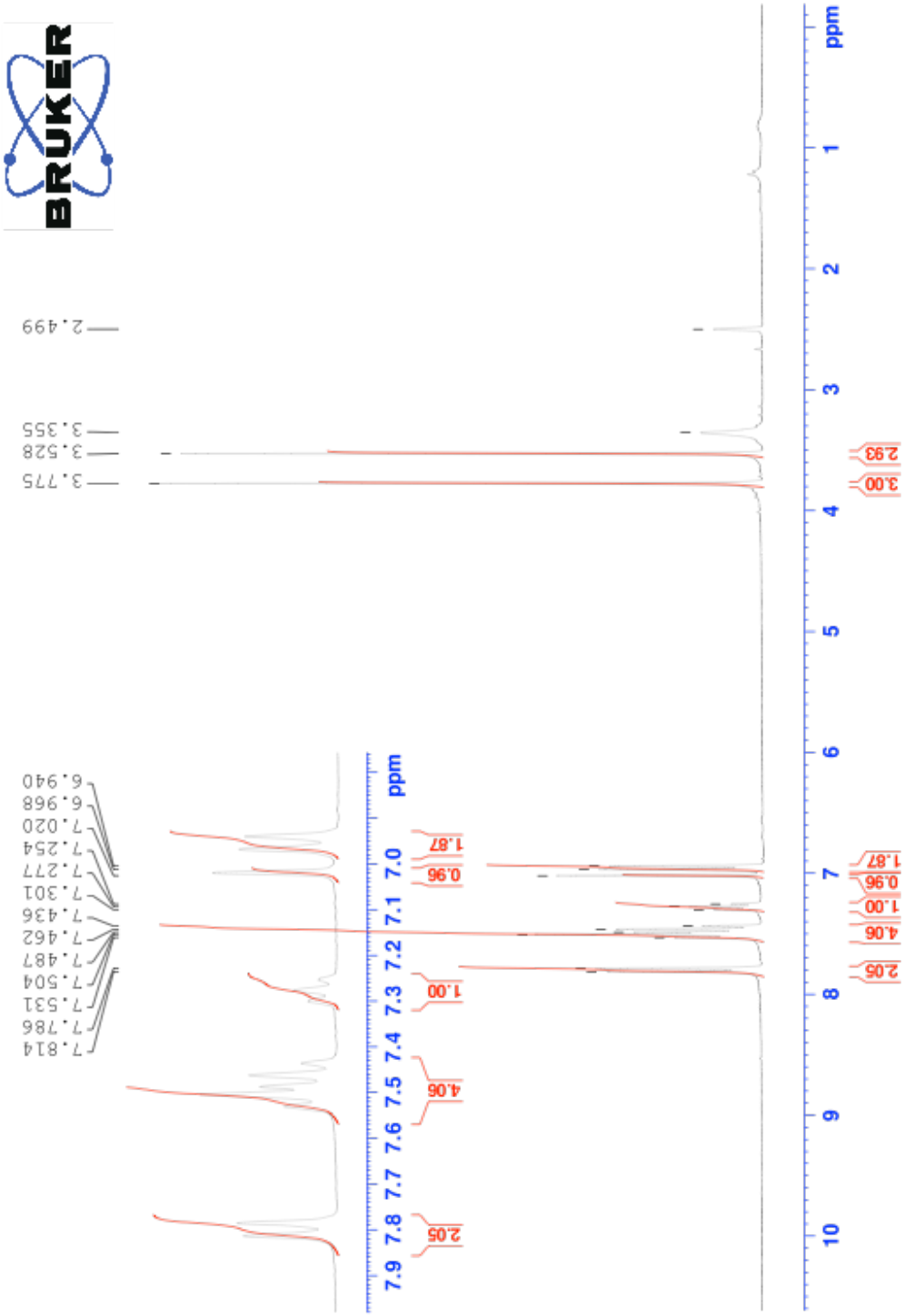
BRUKER
2.499
3.355
3.528
3.775
6.940
6.968
7.020
7.254
7.277
7.301
7.436
7.462
7.487
7.504
7.531
7.786
7.814
ppm
1.87
0.96
4.06
1.00
2.05
2.93
3.00

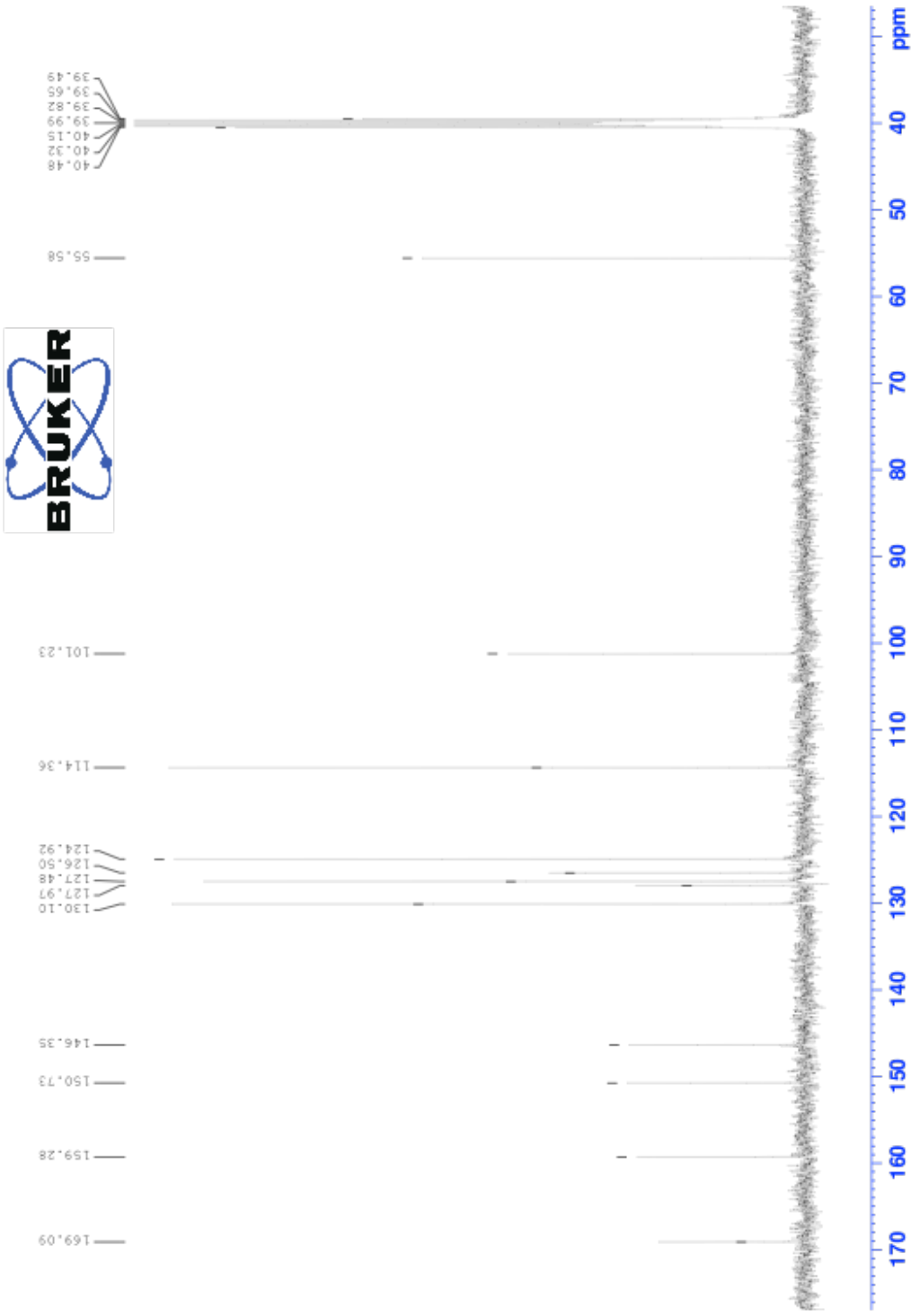
39.49
39.65
39.82
39.99
40.15
40.32
40.48
55.58
101.23
114.36
124.92
126.50
127.48
127.97
130.10
146.35
150.73
159.28
169.09
ppm
40
50
60
70
80
90
100
110
120
130
140
150
160
170

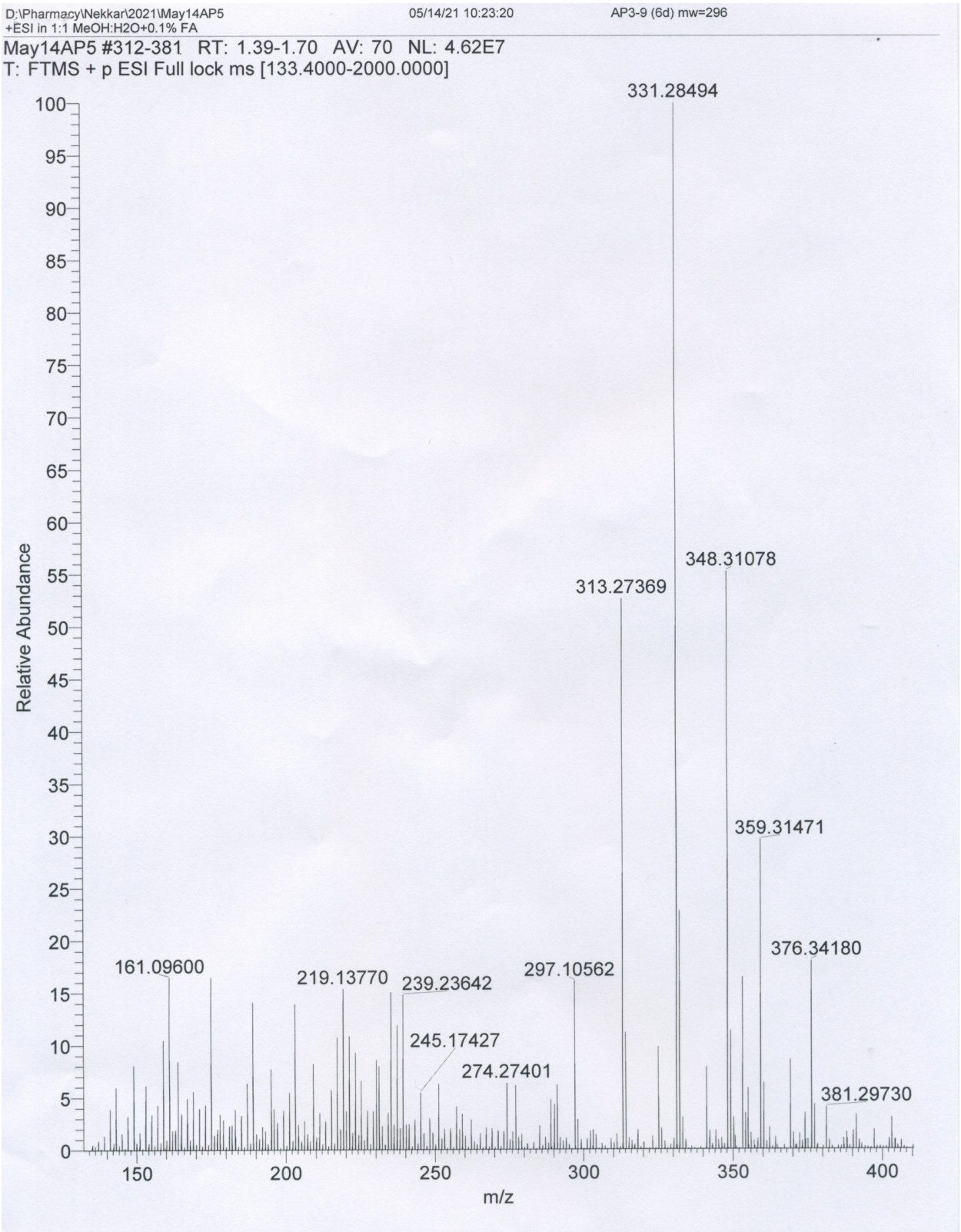
D:\Pharmacy\Nekkar\2021\May14AP5
+ESI in 1:1 MeOH:H2O+0.1% FA
05/14/21 10:23:20
AP3-9 (6d) mw=296
May14AP5 #312-381 RT: 1.39-1.70 AV: 70 NL: 4.62E7
T: FTMS + p ESI Full lock ms [133.4000-2000.0000]
331.28494
348.31078
313.27369
359.31471
376.34180
161.09600
219.13770
239.23642
297.10562
245.17427
274.27401
381.29730
Relative Abundance
m/z

4-(4-Chlorophenyl)-*N*-methyl-*N*-phenylthiazol-2-amine (3g)

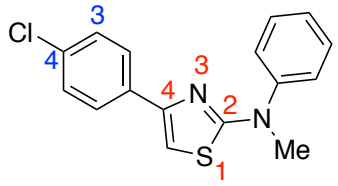

3g

BRUKER
2.499
3.332
3.535
7.275
7.299
7.323
7.441
7.470
7.478
7.503
7.512
7.538
7.877
7.905
ppm
0
1
2
3
4
5
6
7
8
9
10
11
12
13
3.00
2.33
6.17
1.97
ppm
7.3
7.4
7.5
7.6
7.7
7.8
7.9
2.33
6.17
1.97

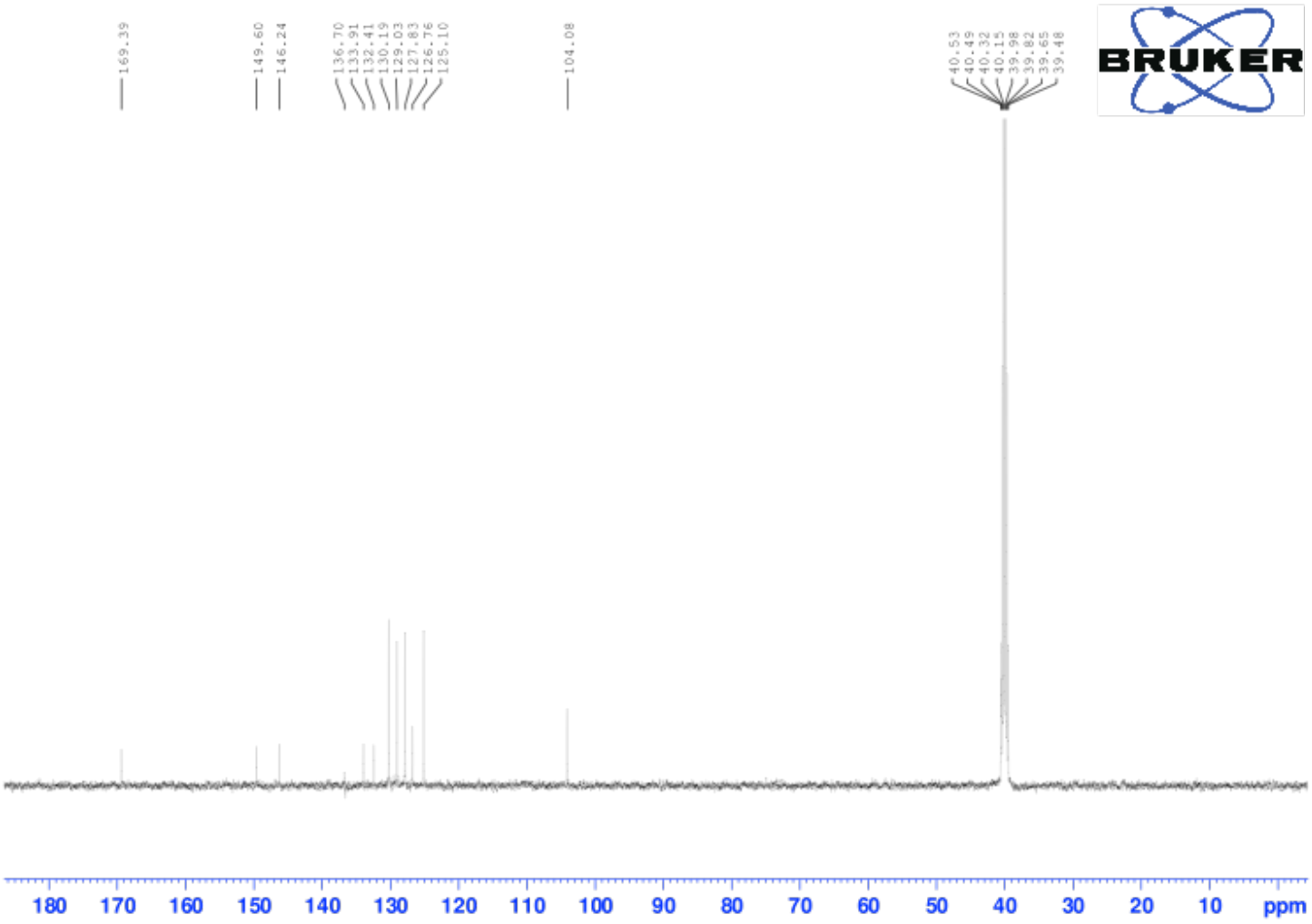
169.39
149.60
146.24
136.70
133.91
132.41
130.19
129.03
127.83
126.76
125.10
104.08
40.53
40.49
40.32
40.15
39.98
39.82
39.65
39.48
BRUKER
180
170
160
150
140
130
120
110
100
90
80
70
60
50
40
30
20
10
ppm

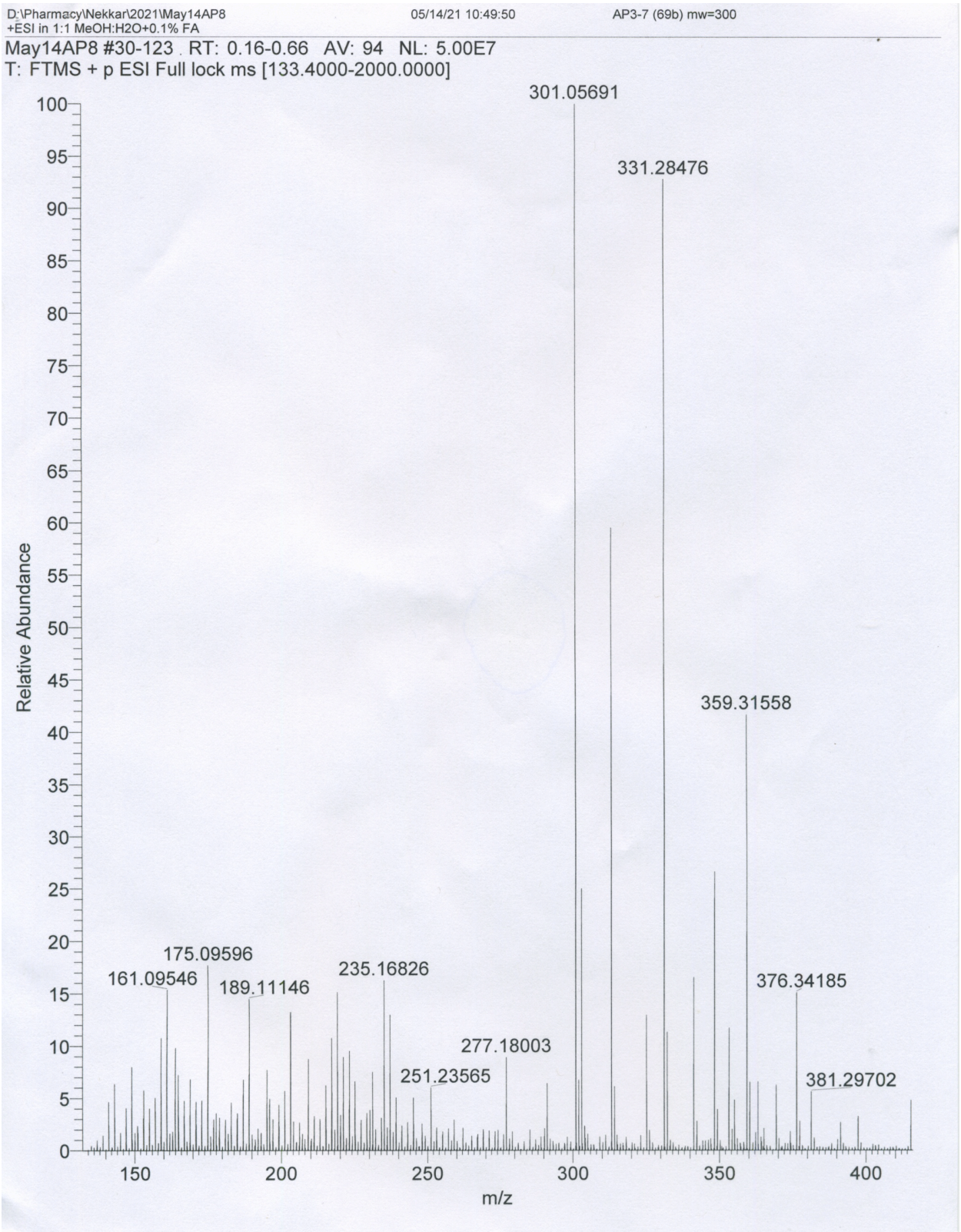
D:\Pharmacy\Nekkar\2021\May14AP8
+ESI in 1:1 MeOH:H2O+0.1% FA
05/14/21 10:49:50
AP3-7 (69b) mw=300
May14AP8 #30-123 RT: 0.16-0.66 AV: 94 NL: 5.00E7
T: FTMS + p ESI Full lock ms [133.4000-2000.0000]
301.05691
331.28476
359.31558
376.34185
381.29702
277.18003
251.23565
235.16826
175.09596
189.11146
161.09546
Relative Abundance
m/z
100
95
90
85
80
75
70
65
60
55
50
45
40
35
30
25
20
15
10
5
0
150
200
250
300
350
400

4-(3-Aminophenyl)-*N*-methyl-*N*-phenylthiazol-2-amine (4b)

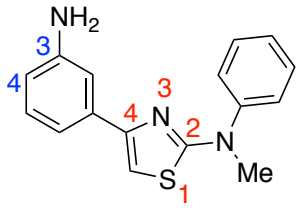

4b

BRUKER
2.499
3.330
3.510
5.227
6.553
6.579
6.779
7.236
7.259
7.283
7.426
7.452
7.477
7.493
7.524
7.552
ppm
1 2 3 4 5 6 7 8 9 10
3.00
1.97
6.26
1.07
0.97
2.07
ppm
6.6 6.7 6.8 6.9 7.0 7.1 7.2 7.3 7.4 7.5 7.6
2.07
0.97
1.07
6.26

BRUKER
39.16
39.44
39.72
40.00
40.28
40.55
40.83
98.63
114.12
123.37
124.80
126.29
127.21
130.04
146.46
148.82
151.88
168.72
ppm

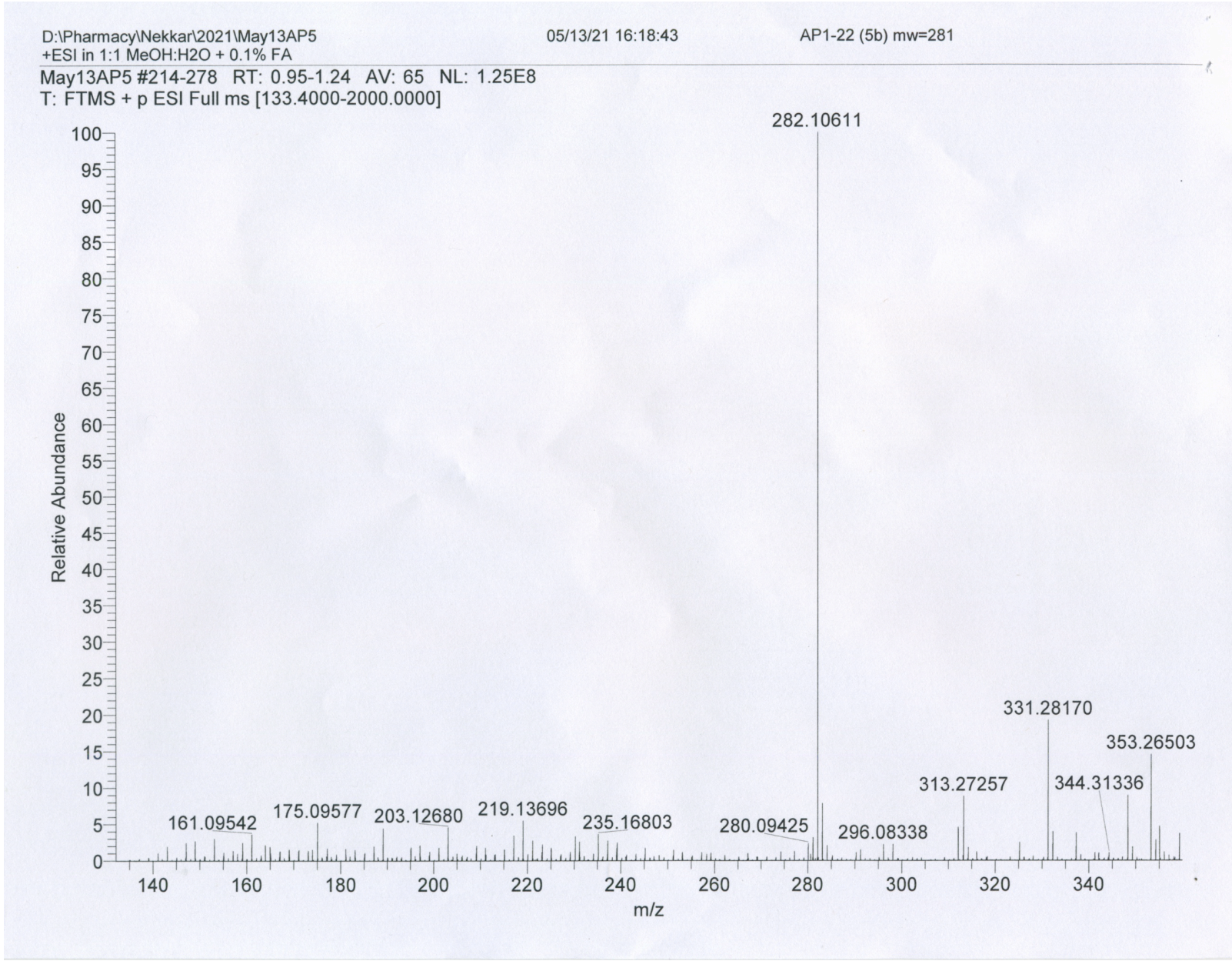
D:\Pharmacy\Nekkar\2021\May13AP5
+ESI in 1:1 MeOH:H2O + 0.1% FA
05/13/21 16:18:43
AP1-22 (5b) mw=281
May13AP5 #214-278 RT: 0.95-1.24 AV: 65 NL: 1.25E8
T: FTMS + p ESI Full ms [133.4000-2000.0000]
282.10611
331.28170
353.26503
313.27257
344.31336
161.09542
175.09577
203.12680
219.13696
235.16803
280.09425
296.08338
Relative Abundance
m/z

Appendix 3: Sample Spectra for Chapter 5

N-(4-(2-Phenylamino)thiazol-4-yl)phenyl)ethanesulfonamide (5c)

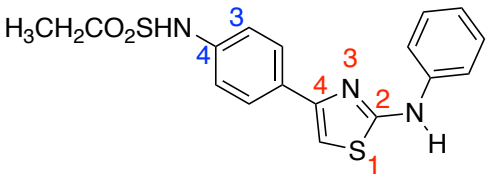

5c

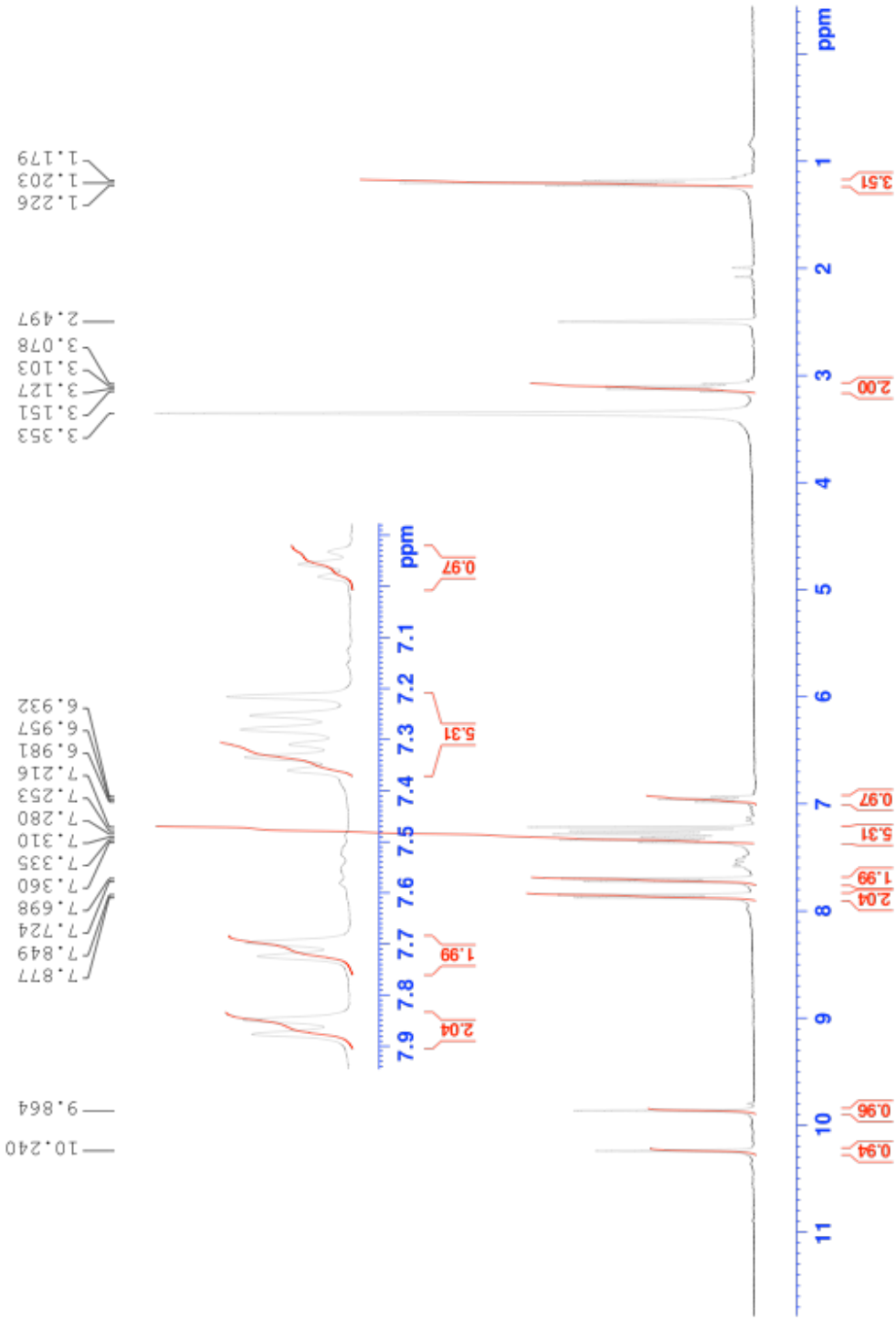
ppm
1
2
3
4
5
6
7
8
9
10
11
3.51
2.00
0.97
5.31
1.99
2.04
0.96
0.94
7.1
7.2
7.3
7.4
7.5
7.6
7.7
7.8
7.9
0.97
5.31
1.99
2.04
1.179
1.203
1.226
2.497
3.078
3.103
3.127
3.151
3.353
6.932
6.957
6.981
7.216
7.253
7.280
7.310
7.335
7.360
7.698
7.724
7.849
7.877
9.864
10.240

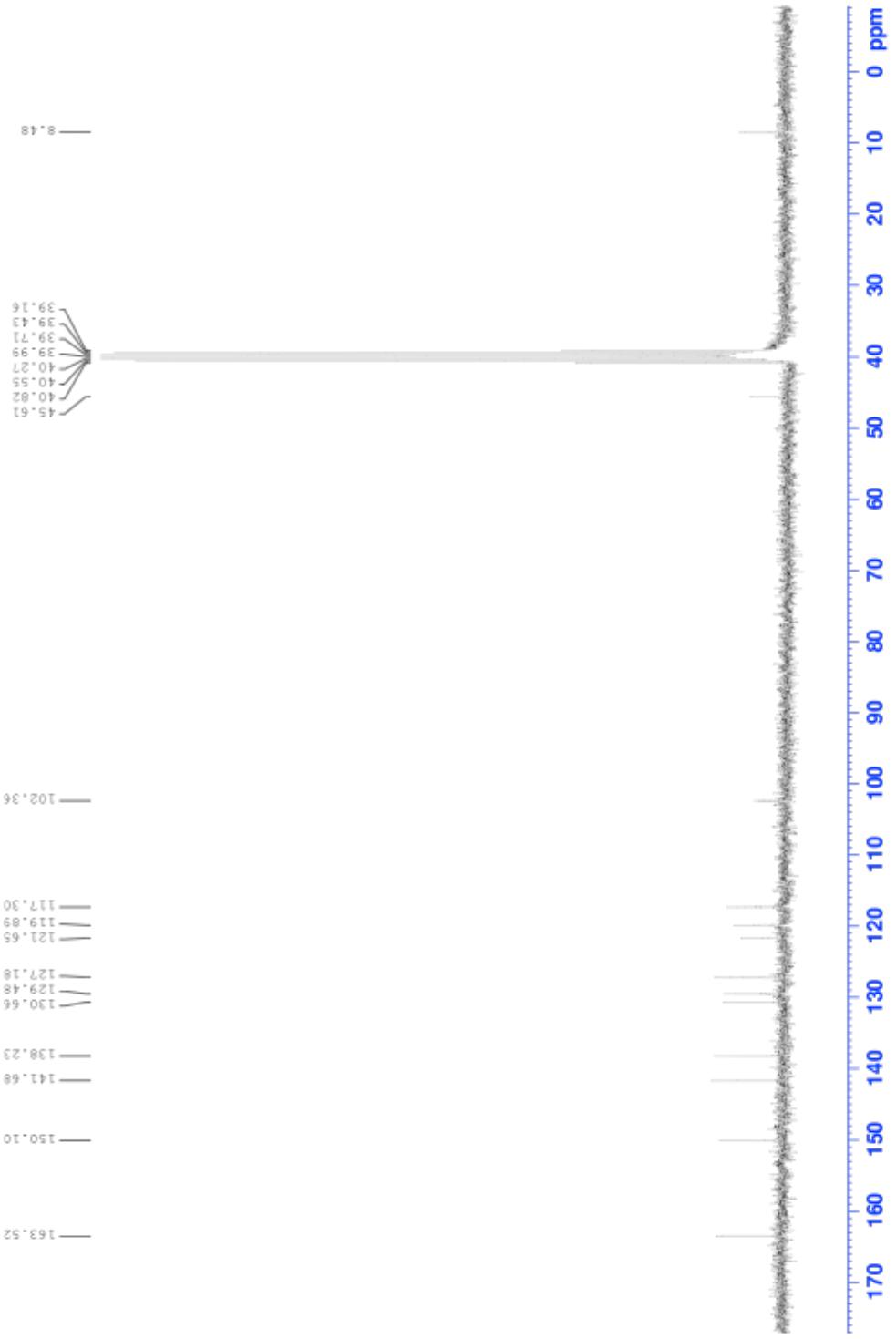
8.48
39.16
39.43
39.71
39.99
40.27
40.55
40.82
45.61
102.36
117.30
119.89
121.65
127.18
129.48
130.66
138.23
141.68
150.10
163.52
0 ppm
10
20
30
40
50
60
70
80
90
100
110
120
130
140
150
160
170

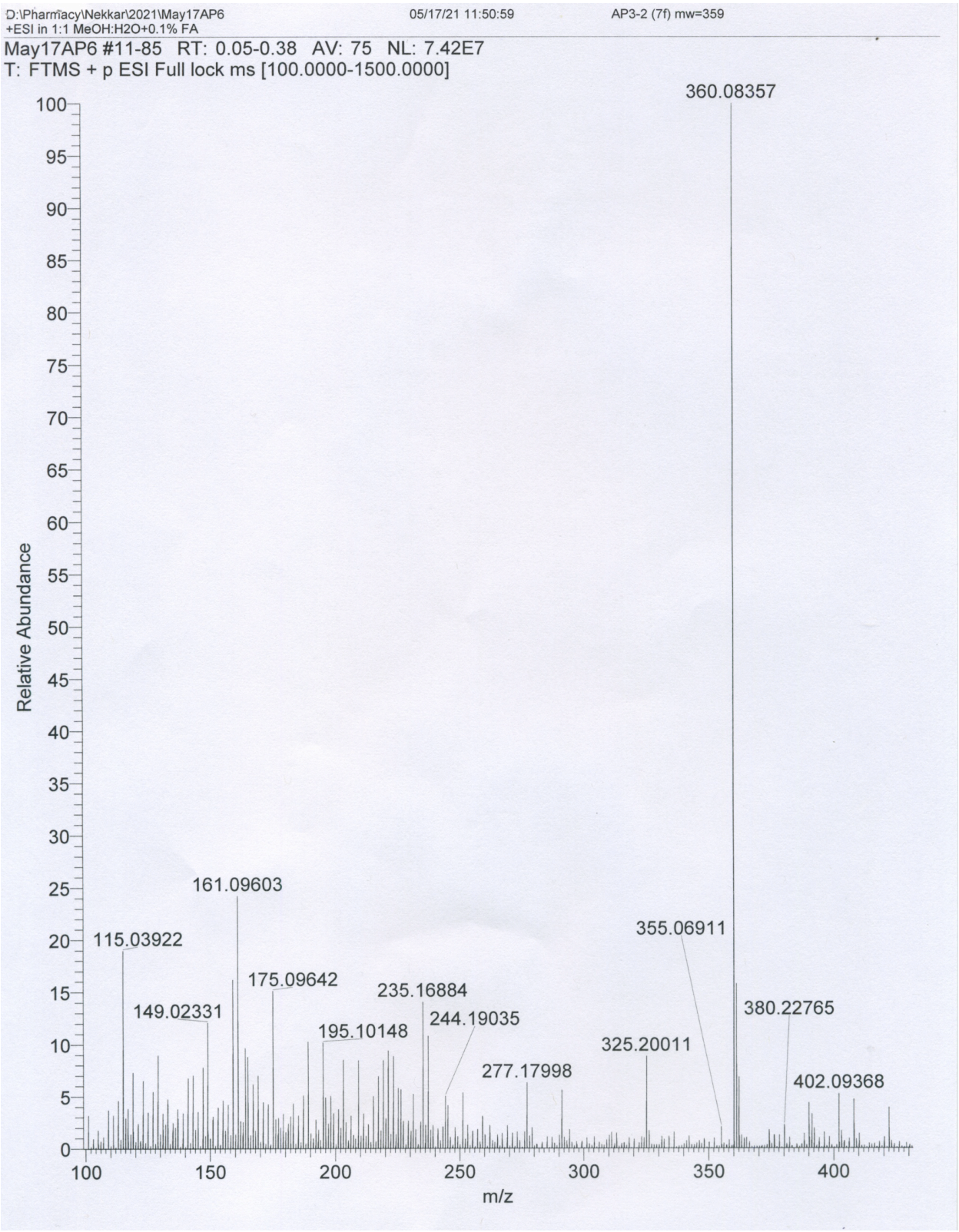
D:\Pharmacy\Nekkar\2021\May17AP6
+ESI in 1:1 MeOH:H2O+0.1% FA
05/17/21 11:50:59
AP3-2 (7f) mw=359
May17AP6 #11-85 RT: 0.05-0.38 AV: 75 NL: 7.42E7
T: FTMS + p ESI Full lock ms [100.0000-1500.0000]
360.08357
161.09603
115.03922
355.06911
175.09642
235.16884
149.02331
244.19035
380.22765
195.10148
325.20011
277.17998
402.09368
Relative Abundance
m/z

2,2,2-Trifluoro-*N*-(4-(2-(phenylamino)thiazole-4-yl)phenyl)-2-ethane-1-sulfonamide (5g)

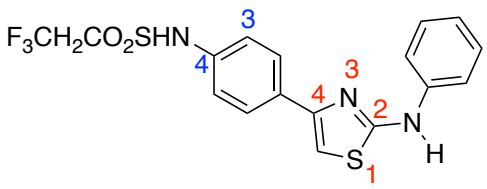

5g

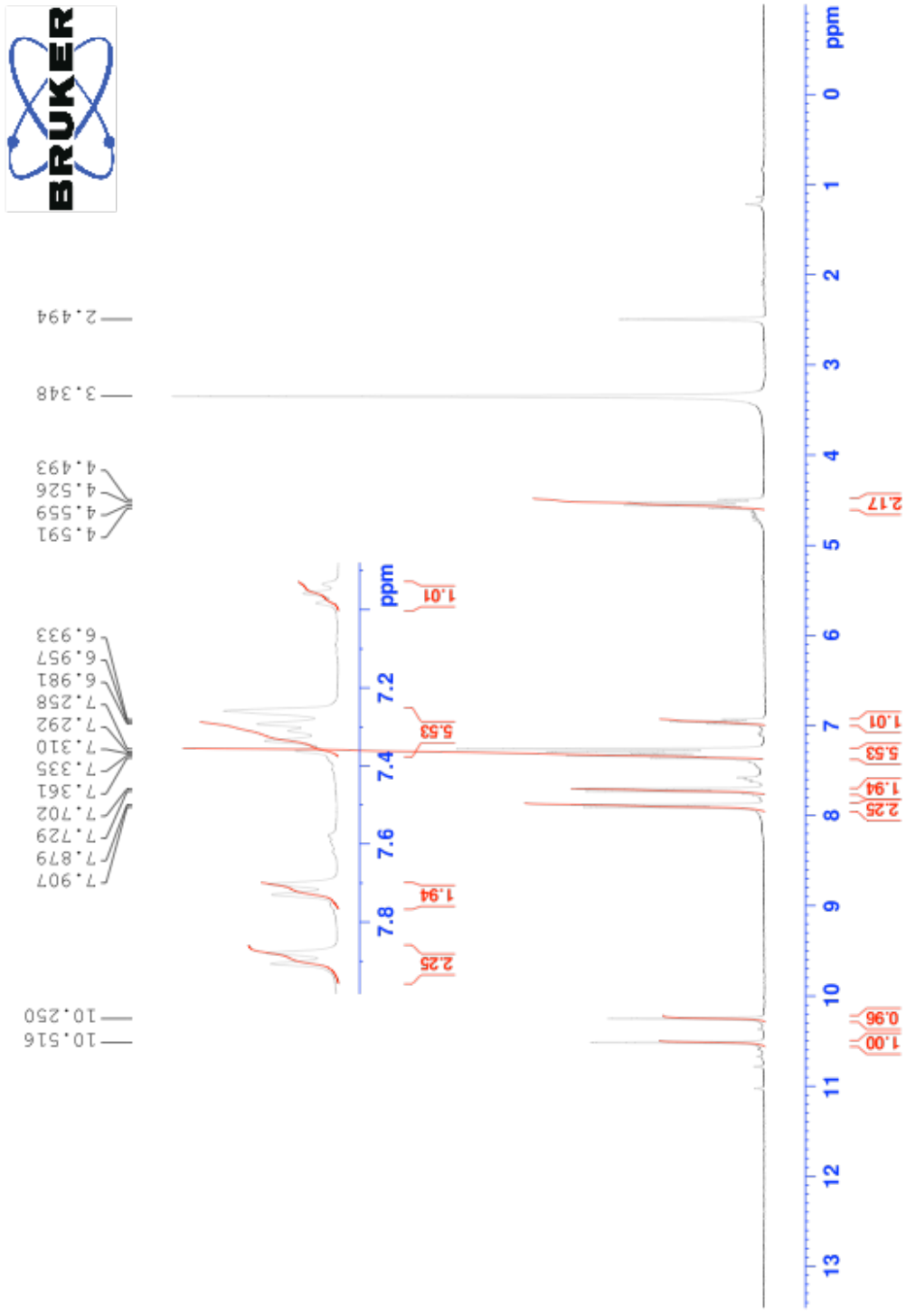
BRUKER
10.516
10.250
7.907
7.879
7.729
7.702
7.361
7.335
7.310
7.292
7.258
6.981
6.957
6.933
4.591
4.559
4.526
4.493
3.348
2.494
ppm
13
12
11
10
9
8
7
6
5
4
3
2
1
0
1.00
0.96
2.25
1.94
5.53
1.01
2.17
ppm
7.8
7.6
7.4
7.2
2.25
1.94
5.53
1.01

BRUKER
40.82
40.54
102.81
117.30
120.74
121.68
127.16
129.49
131.41
136.71
141.67
149.98
163.56
ppm

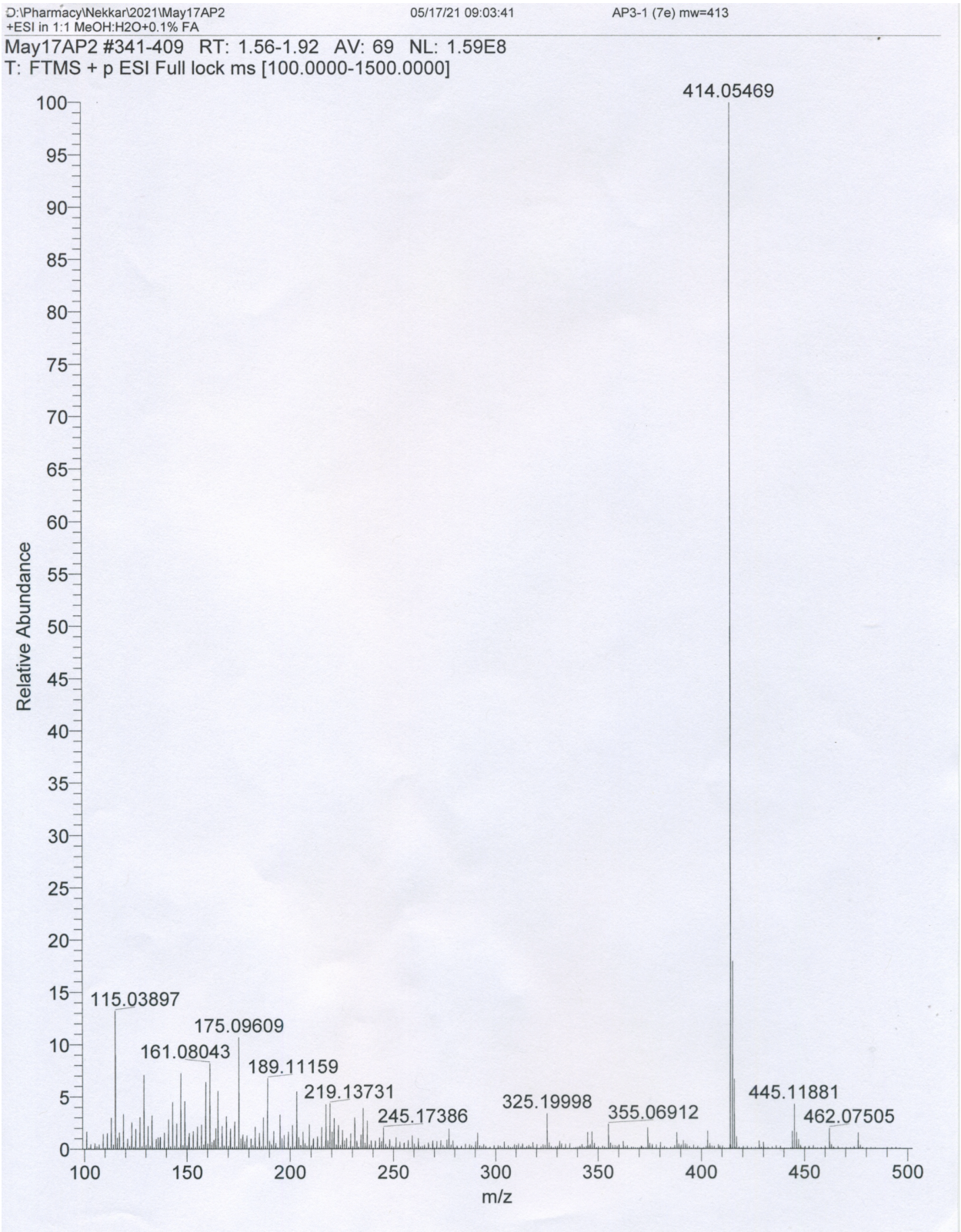
D:\Pharmacy\Nekkar\2021\May17AP2
+ESI in 1:1 MeOH:H2O+0.1% FA
05/17/21 09:03:41
AP3-1 (7e) mw=413
May17AP2 #341-409 RT: 1.56-1.92 AV: 69 NL: 1.59E8
T: FTMS + p ESI Full lock ms [100.0000-1500.0000]
414.05469
115.03897
175.09609
161.08043
189.11159
219.13731
245.17386
325.19998
355.06912
445.11881
462.07505
Relative Abundance
m/z

(4-(2-(Phenyl)amino)thiazole-4-yl)benzenesulfamide (5i)

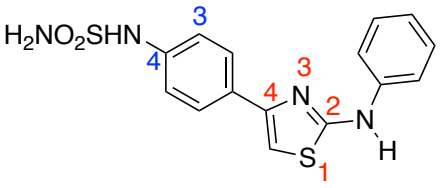

5i

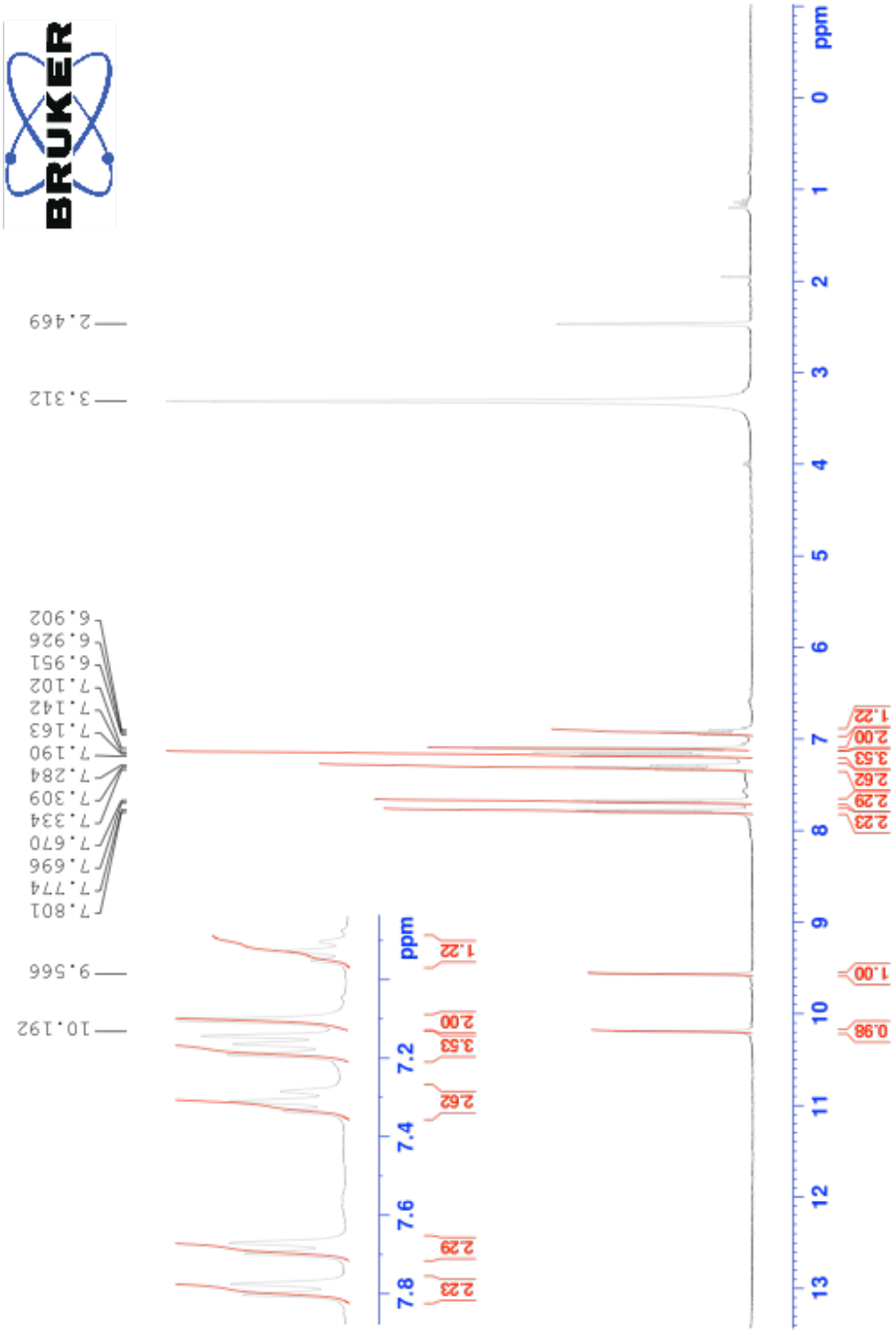
BRUKER
10.192
9.566
7.801
7.774
7.696
7.670
7.334
7.309
7.284
7.190
7.163
7.142
7.102
6.951
6.926
6.902
3.312
2.469
ppm
1.22
2.00
3.53
2.62
2.29
2.23
1.00
0.98

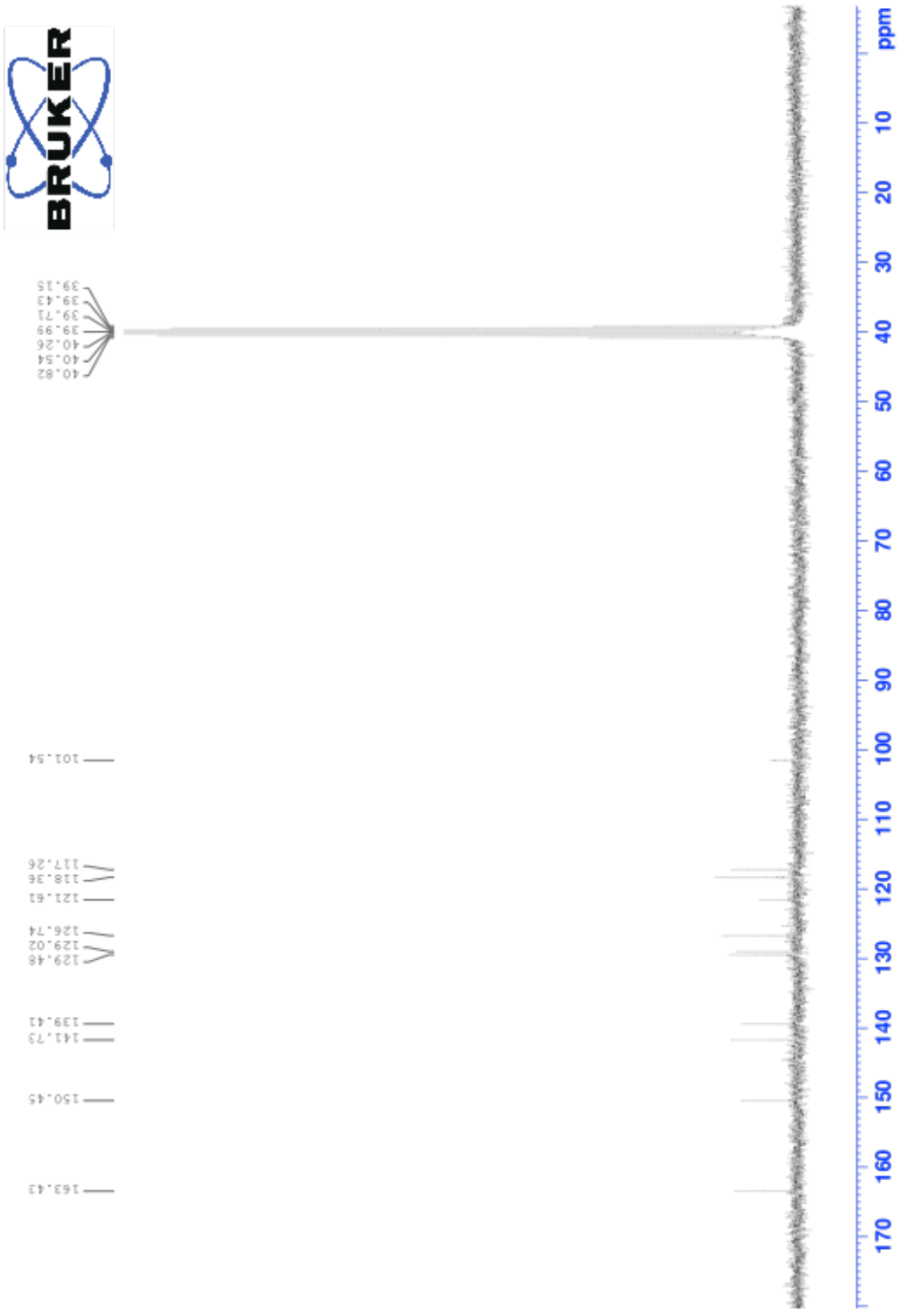
BRUKER
39.15
39.43
39.71
39.99
40.26
40.54
40.82
101.54
117.26
118.36
121.61
126.74
129.02
129.48
139.41
141.73
150.45
163.43
ppm
10
20
30
40
50
60
70
80
90
100
110
120
130
140
150
160
170

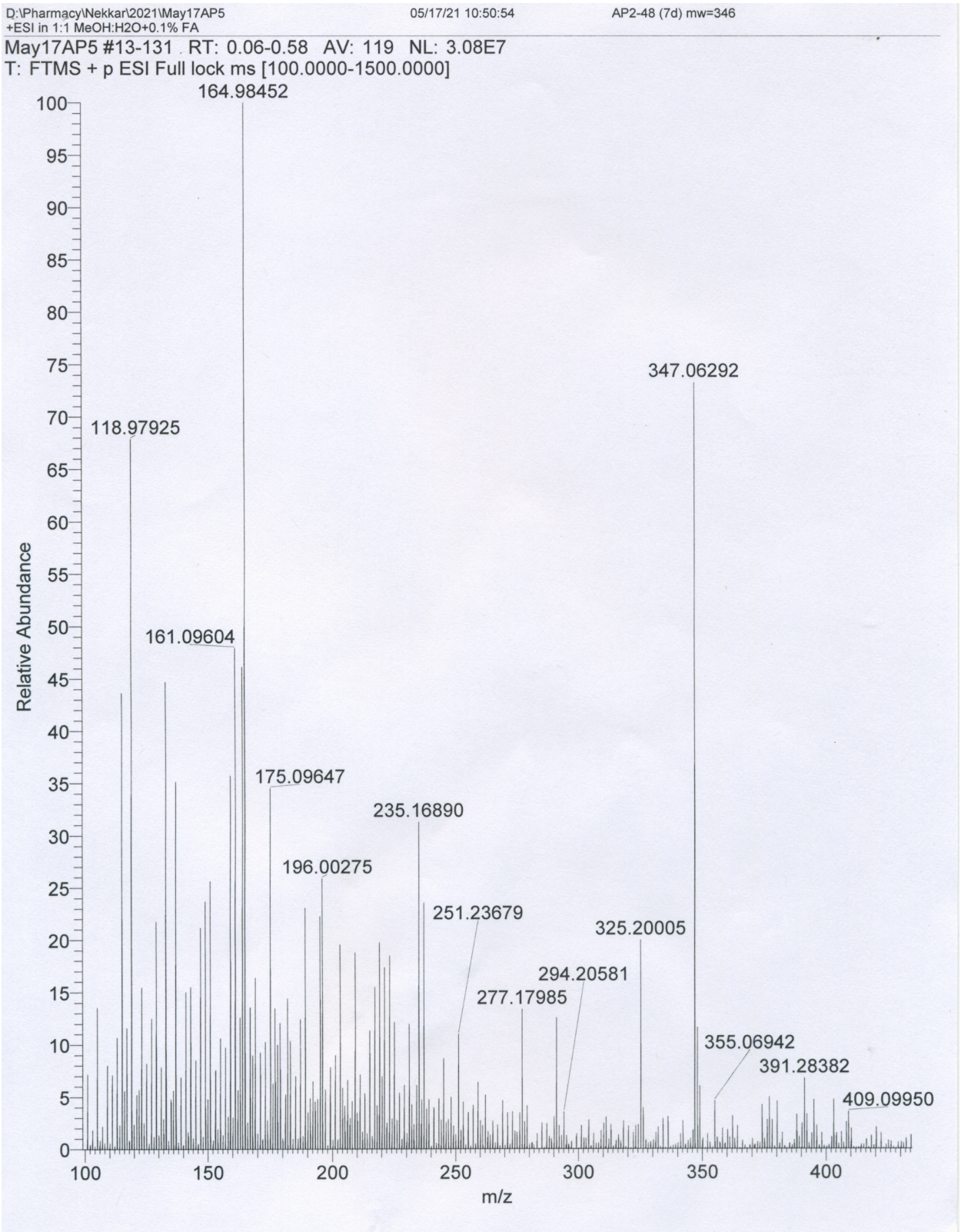
D:\Pharmacy\Nekkar\2021\May17AP5
+ESI in 1:1 MeOH:H2O+0.1% FA
05/17/21 10:50:54
AP2-48 (7d) mw=346
May17AP5 #13-131 RT: 0.06-0.58 AV: 119 NL: 3.08E7
T: FTMS + p ESI Full lock ms [100.0000-1500.0000]
164.98452
347.06292
118.97925
161.09604
175.09647
235.16890
196.00275
251.23679
325.20005
294.20581
277.17985
355.06942
391.28382
409.09950
Relative Abundance
m/z

Appendix 4: Sample Spectra for Chapter 6

N-(4-(2-(Methyl(phenyl)amino)thiazol-4-yl)phenyl)methanesulfonamide (6a)

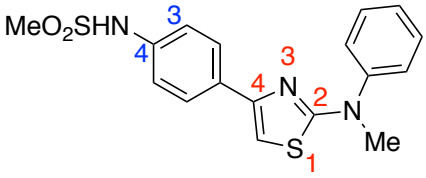

6a

2.996
2.999
3.376
3.525
7.098
7.211
7.237
7.255
7.281
7.303
7.439
7.464
7.490
7.504
7.531
7.803
7.830
9.790
ppm
2.92
3.10
1.02
3.23
4.47
2.09
1.00

BRUKER
39.12
39.40
39.68
39.96
40.24
40.52
40.79
102.51
120.22
124.98
126.58
127.15
130.15
130.88
138.15
146.28
150.38
169.22
ppm
10
20
30
40
50
60
70
80
90
100
110
120
130
140
150
160
170
180

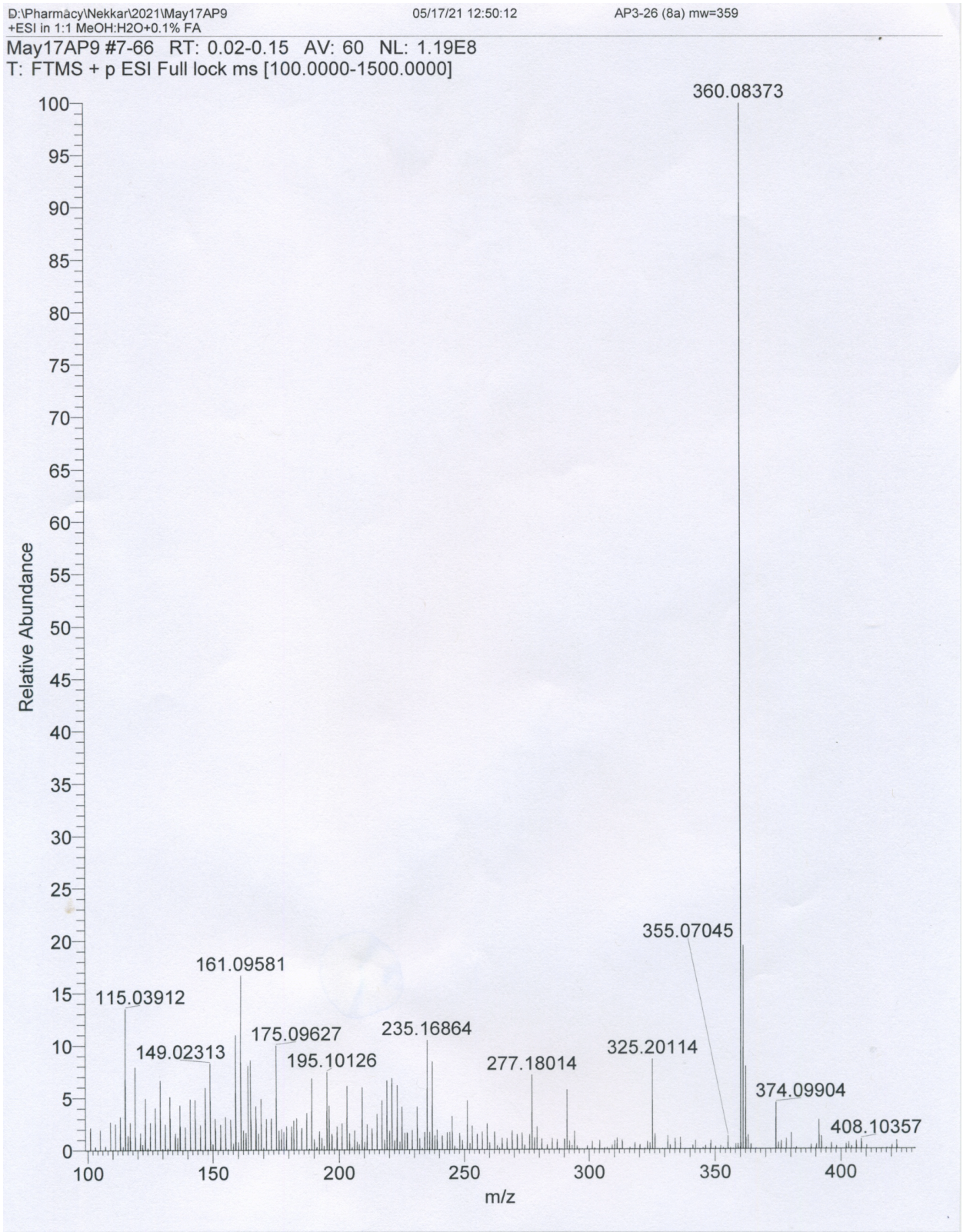
D:\Pharmacy\Nekkar\2021\May17AP9
+ESI in 1:1 MeOH:H2O+0.1% FA
05/17/21 12:50:12
AP3-26 (8a) mw=359
May17AP9 #7-66 RT: 0.02-0.15 AV: 60 NL: 1.19E8
T: FTMS + p ESI Full lock ms [100.0000-1500.0000]
360.08373
355.07045
161.09581
115.03912
175.09627
235.16864
149.02313
195.10126
277.18014
325.20114
374.09904
408.10357
Relative Abundance
m/z

***N*-(3-(2-(Methyl(phenylamino)thiazol-4-yl)phenyl)methanesulfonamide (6b)**

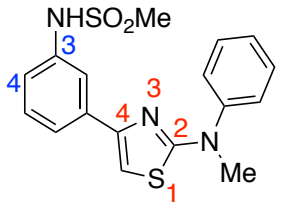

6b

BRUKER
9.764
7.739
7.603
7.576
7.551
7.526
7.502
7.478
7.450
7.377
7.351
7.324
7.318
7.294
7.270
7.172
7.167
7.152
3.542
3.318
3.003
ppm
0.90
3.05
3.07
1.83
1.93
5.00
0.95
ppm
1.83
1.93
5.00
0.95

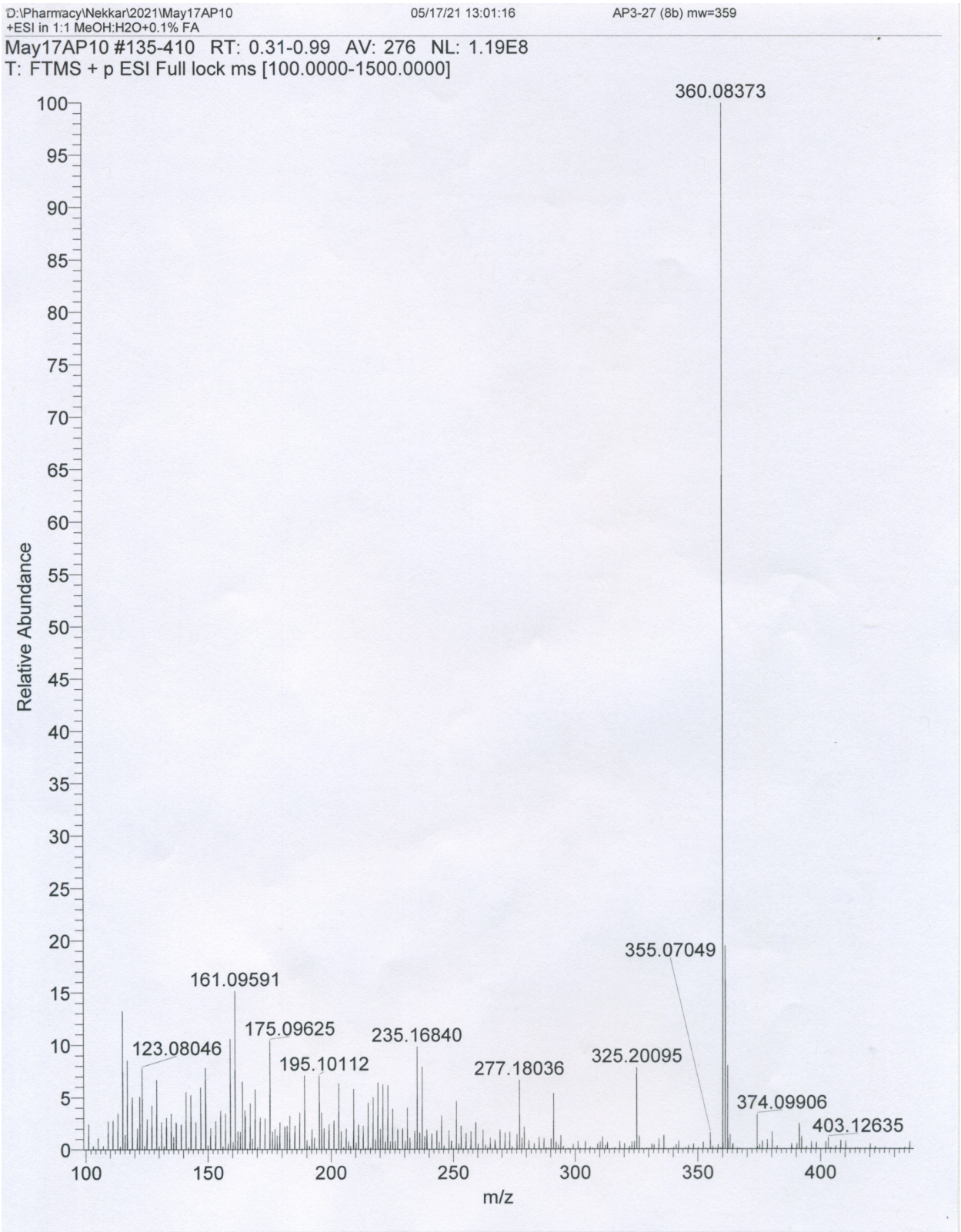
D:\Pharmacy\Nekkar\2021\May17AP10
05/17/21 13:01:16
AP3-27 (8b) mw=359
+ESI in 1:1 MeOH:H2O+0.1% FA
May17AP10 #135-410 RT: 0.31-0.99 AV: 276 NL: 1.19E8
T: FTMS + p ESI Full lock ms [100.0000-1500.0000]
360.08373
355.07049
161.09591
175.09625
235.16840
123.08046
195.10112
277.18036
325.20095
374.09906
403.12635
Relative Abundance
m/z

***N*-(4-(2-(Methyl(phenylamino)thiazol-4-yl)phenyl)propane-2-sulfonamide (6e)**

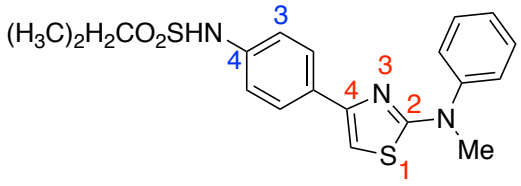

6e

9.808
7.809
7.780
7.537
7.512
7.495
7.471
7.443
7.308
7.285
7.264
7.236
7.087
3.529
3.454
3.294
3.271
3.249
3.226
1.257
1.234
1.066
1.043
BRUKER
ppm
0.79
2.00
4.22
2.97
0.92
6.26
1.15
3.06
2.00
4.22
2.97
0.92

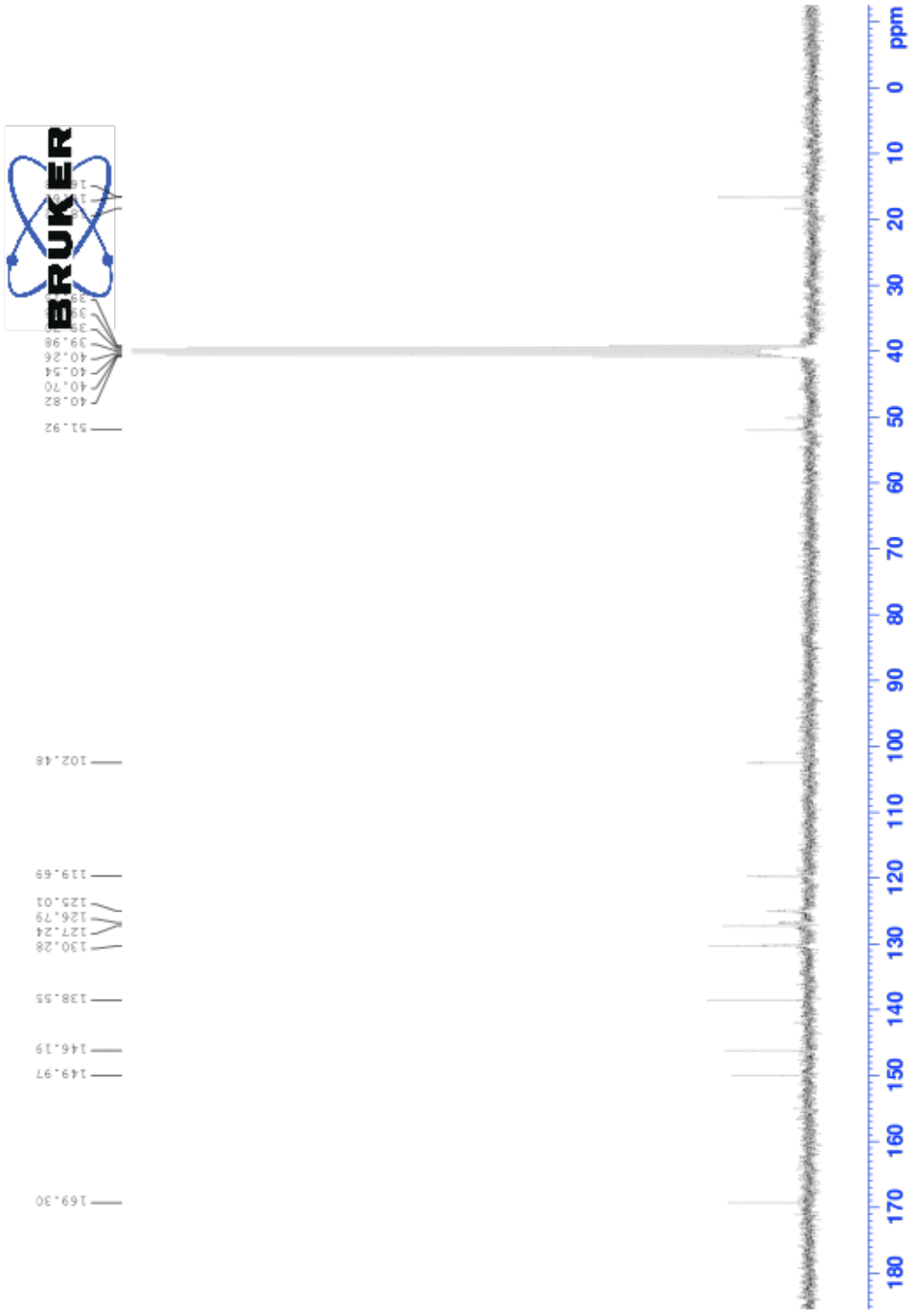
BRUKER
51.92
102.48
119.69
125.01
126.79
127.24
130.28
138.55
146.19
149.97
169.30
ppm

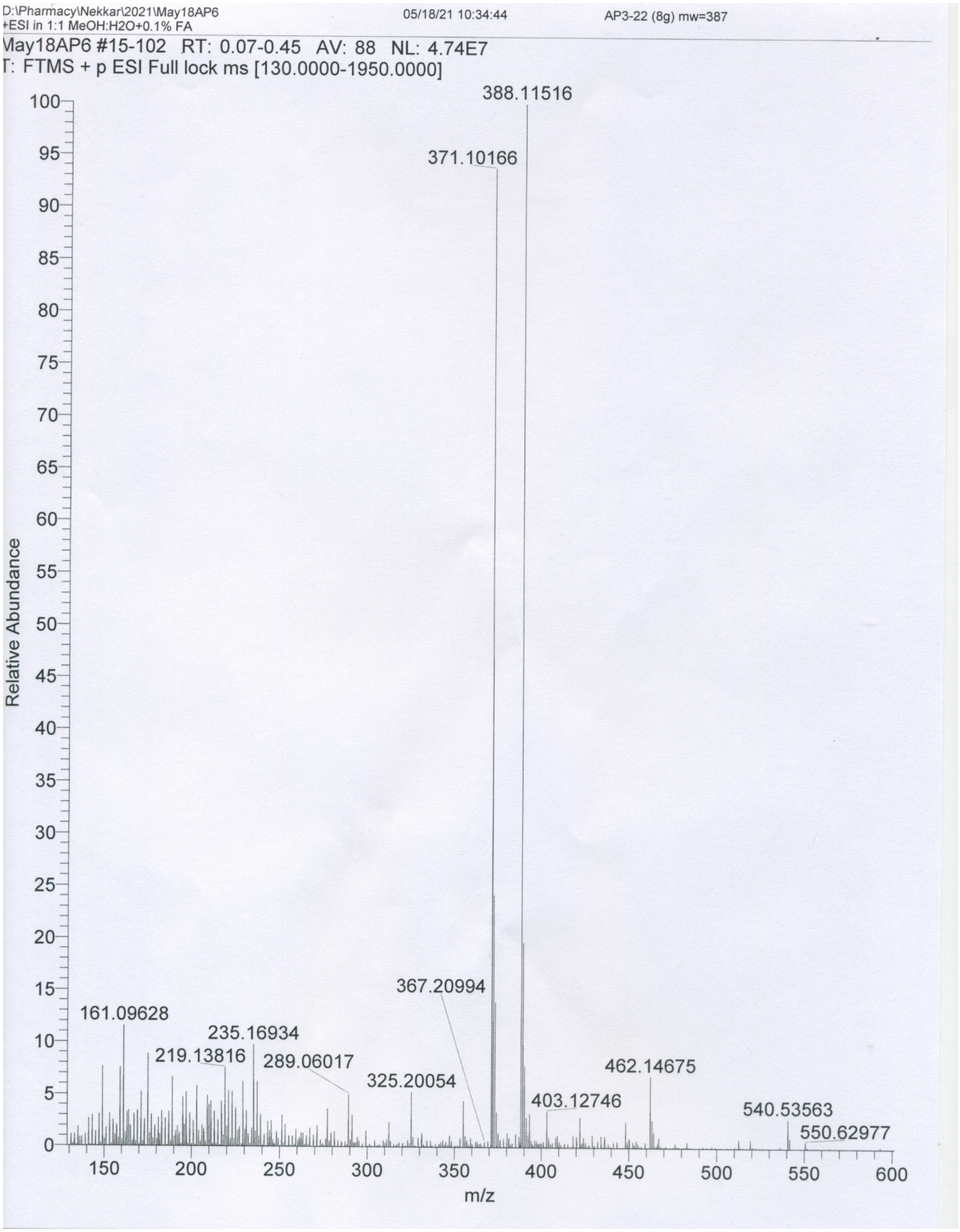
D:\Pharmacy\Nekkar\2021\May18AP6
+ESI in 1:1 MeOH:H2O+0.1% FA
05/18/21 10:34:44
AP3-22 (8g) mw=387
May18AP6 #15-102 RT: 0.07-0.45 AV: 88 NL: 4.74E7
T: FTMS + p ESI Full lock ms [130.0000-1950.0000]
388.11516
371.10166
367.20994
161.09628
235.16934
219.13816
289.06017
325.20054
462.14675
403.12746
540.53563
550.62977
Relative Abundance
m/z

2,2,2-Trifluoro-*N*-(3-(2-(methyl(phenylamino)thiazol-4-yl)phenyl)ethane-1-sulfonamide (6h)

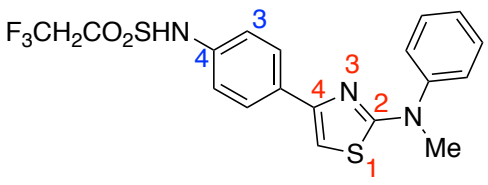

BRUKER
10.473
7.746
7.651
7.625
7.585
7.576
7.552
7.527
7.504
7.480
7.452
7.401
7.374
7.348
7.321
7.297
7.275
7.178
7.162
4.566
4.534
4.501
4.468
3.543
3.334
2.507
2.33
2.00
1.47
2.51
4.71
0.87
0.87
0.78
ppm
0
1
2
3
4
5
6
7
8
9
10
11
12
13
7.2
7.3
7.4
7.5
7.6
7.7

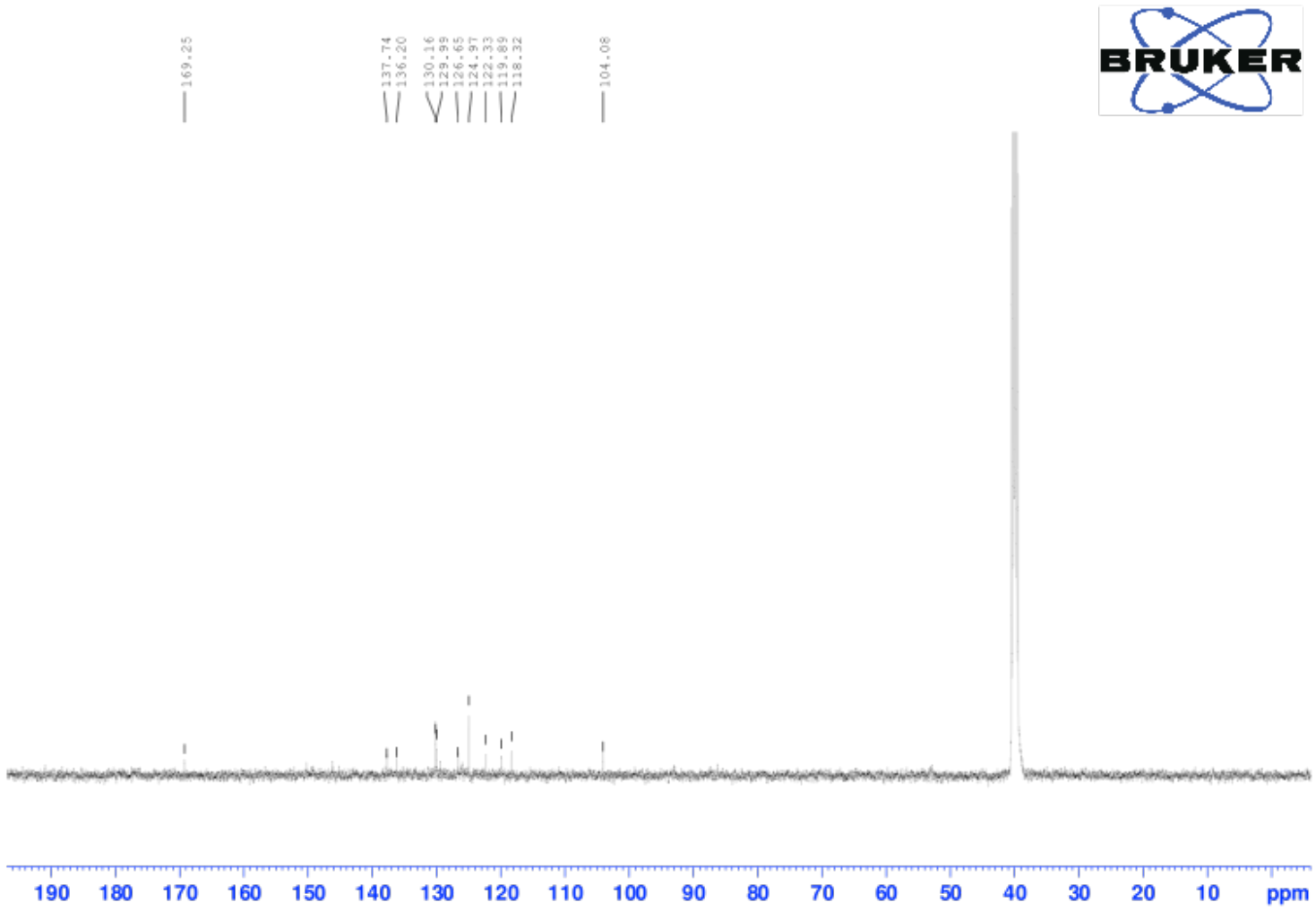
169.25
137.74
136.20
130.16
129.99
126.65
124.97
122.33
119.89
118.32
104.08
BRUKER
190 180 170 160 150 140 130 120 110 100 90 80 70 60 50 40 30 20 10 ppm

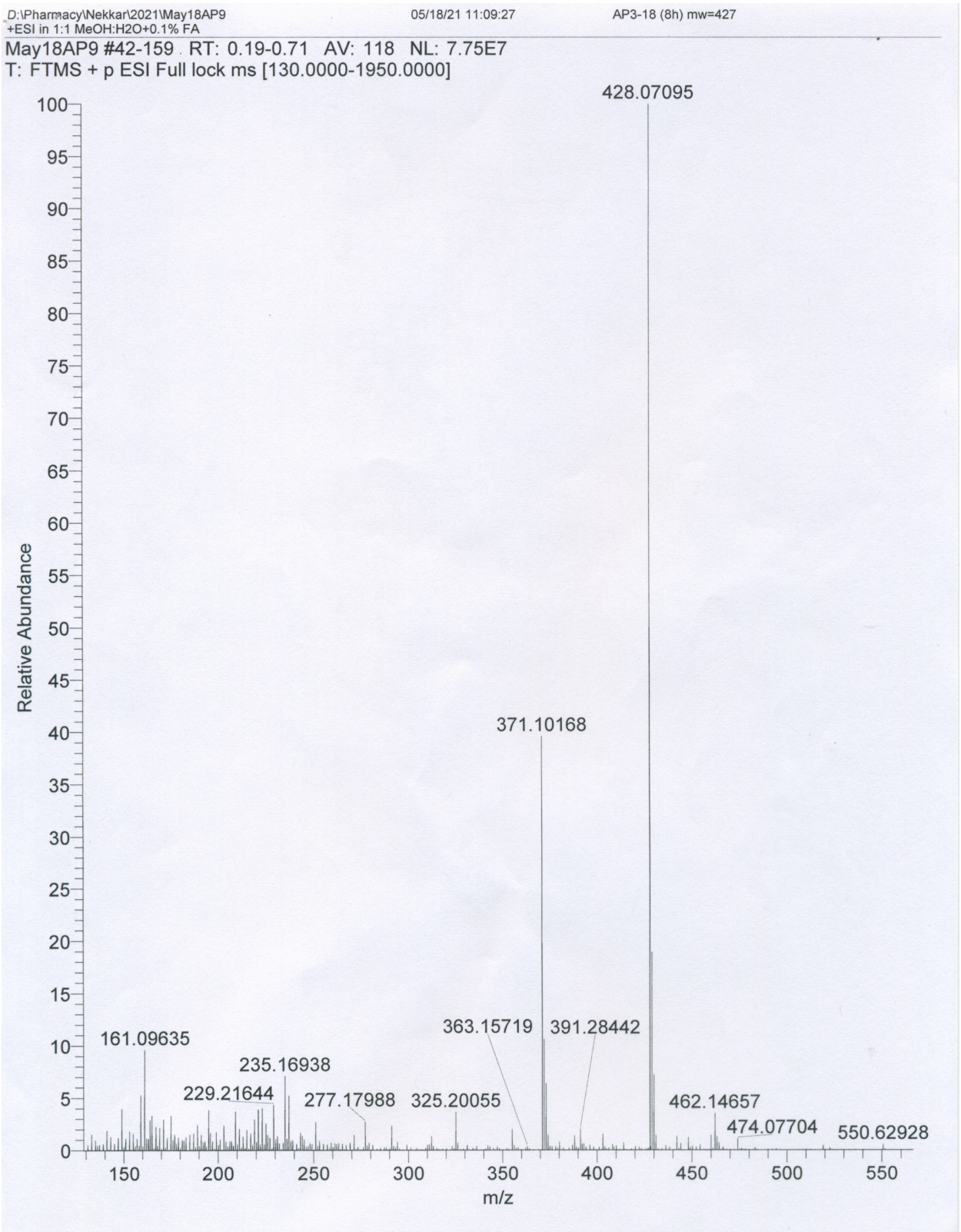
D:\Pharmacy\Nekkar\2021\May18AP9
05/18/21 11:09:27
AP3-18 (8h) mw=427
+ESI in 1:1 MeOH:H2O+0.1% FA
May18AP9 #42-159 RT: 0.19-0.71 AV: 118 NL: 7.75E7
T: FTMS + p ESI Full lock ms [130.0000-1950.0000]
428.07095
371.10168
363.15719
391.28442
161.09635
235.16938
229.21644
277.17988
325.20055
462.14657
474.07704
550.62928
Relative Abundance
m/z

Appendix 5: Sample Spectra for Chapter 7

N,2-Diphenylthiazol-4-amine (7a)

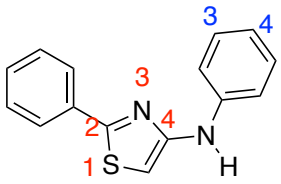

7a

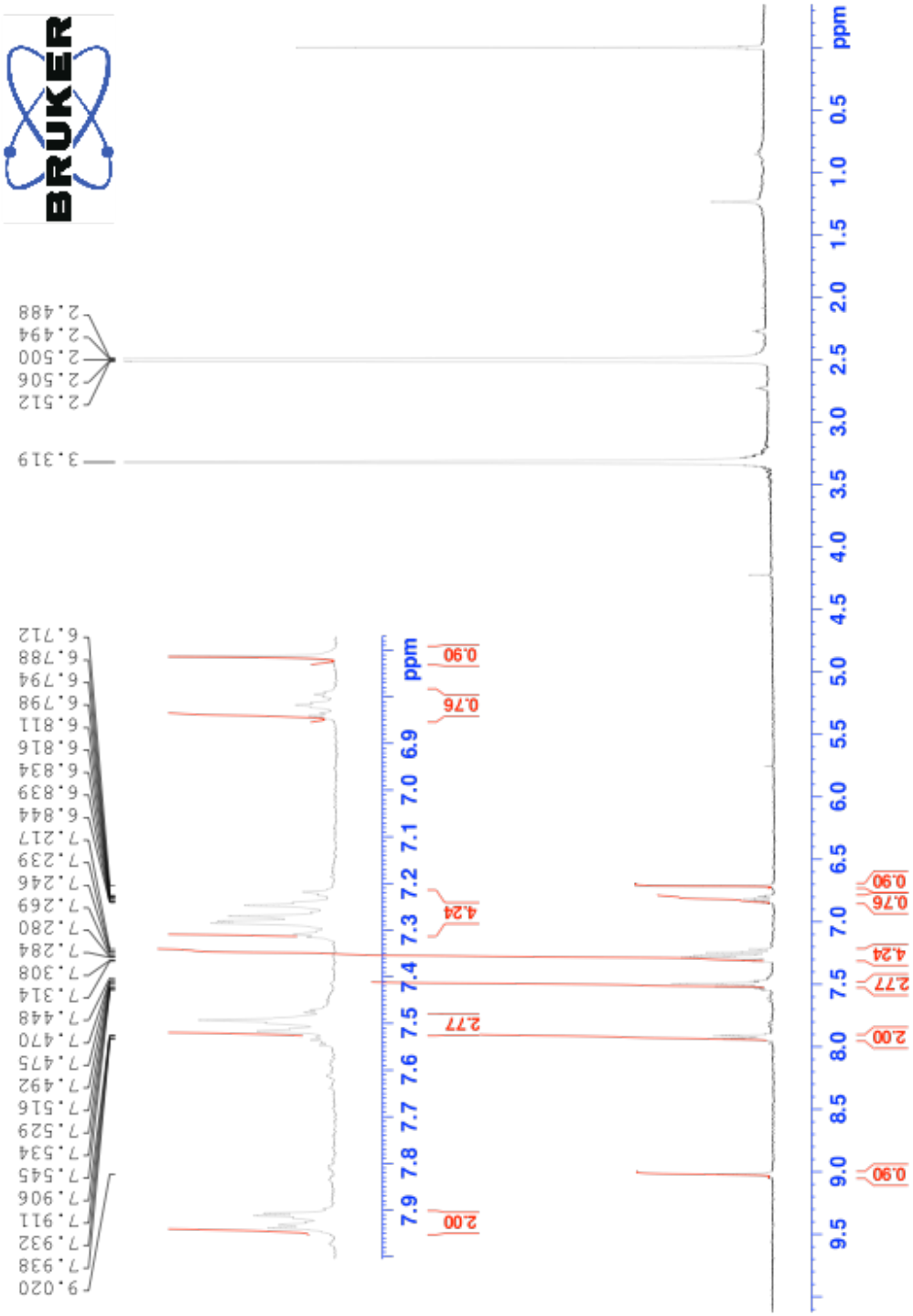

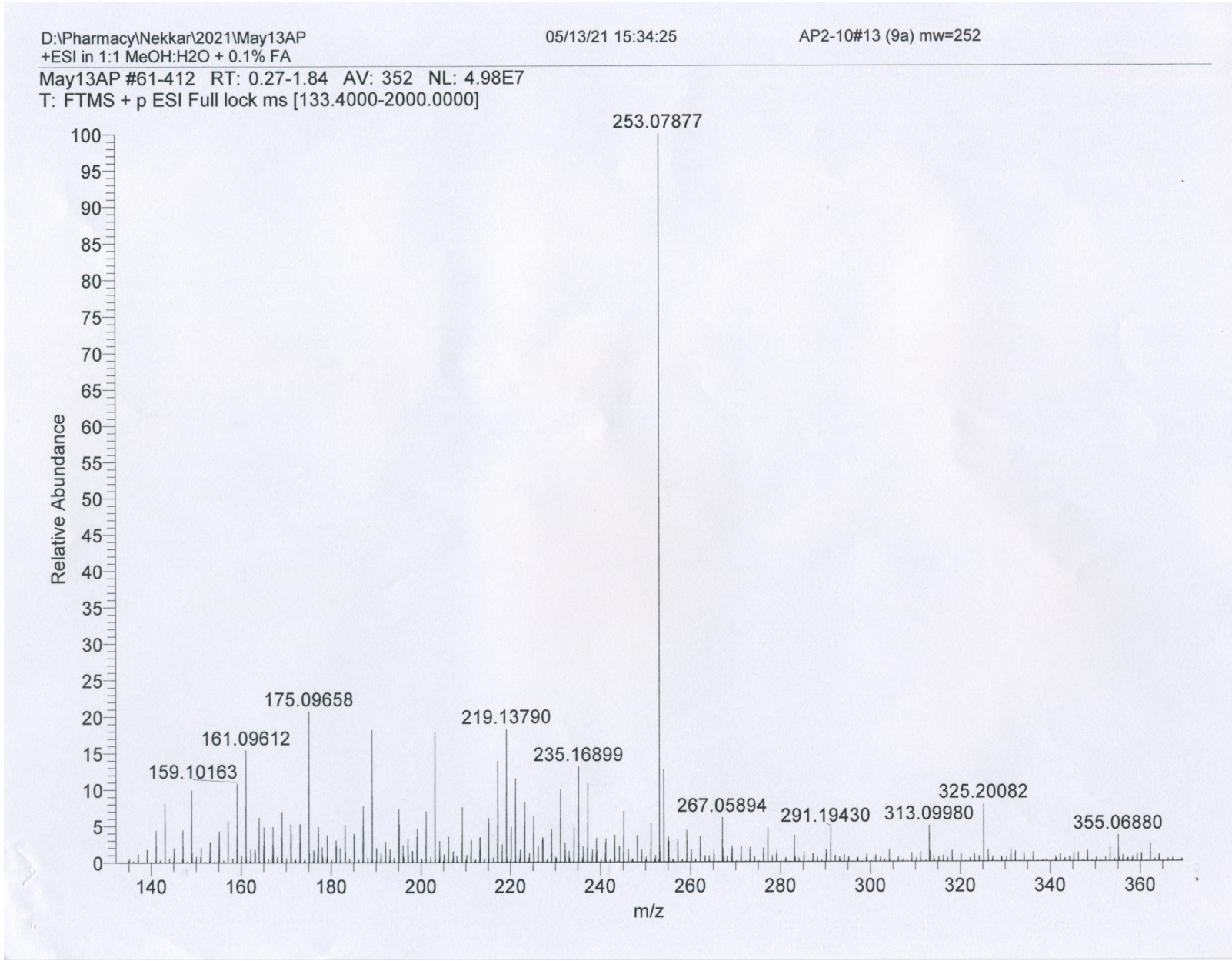
D:\Pharmacy\Nekkar\2021\May13AP
+ESI in 1:1 MeOH:H2O + 0.1% FA
05/13/21 15:34:25
AP2-10#13 (9a) mw=252
May13AP #61-412 RT: 0.27-1.84 AV: 352 NL: 4.98E7
T: FTMS + p ESI Full lock ms [133.4000-2000.0000]
Relative Abundance
m/z
253.07877
175.09658
219.13790
161.09612
235.16899
159.10163
267.05894
291.19430
313.09980
325.20082
355.06880

***N*-(4-Fluorophenyl)-2-phenylthiazol-4-amine (7c)**

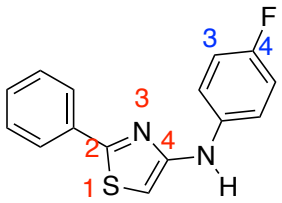

7c

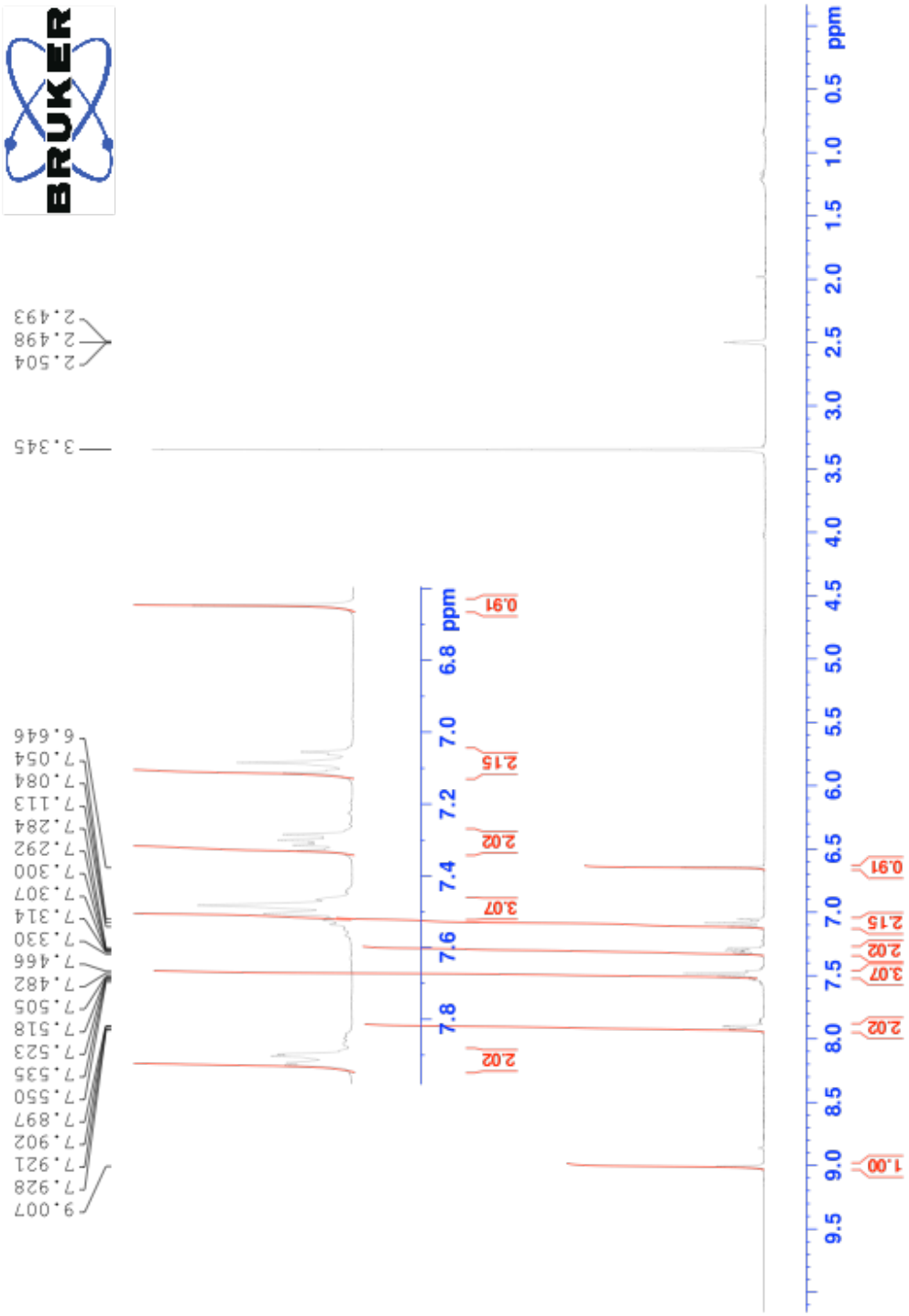
BRUKER
2.493
2.498
2.504
3.345
9.007
7.928
7.921
7.902
7.897
7.550
7.535
7.523
7.518
7.505
7.482
7.466
7.330
7.314
7.307
7.300
7.292
7.284
7.113
7.084
7.054
6.646
ppm
0.91
2.15
2.02
3.07
2.02
1.00
0.91
2.15
2.02
3.07
2.02

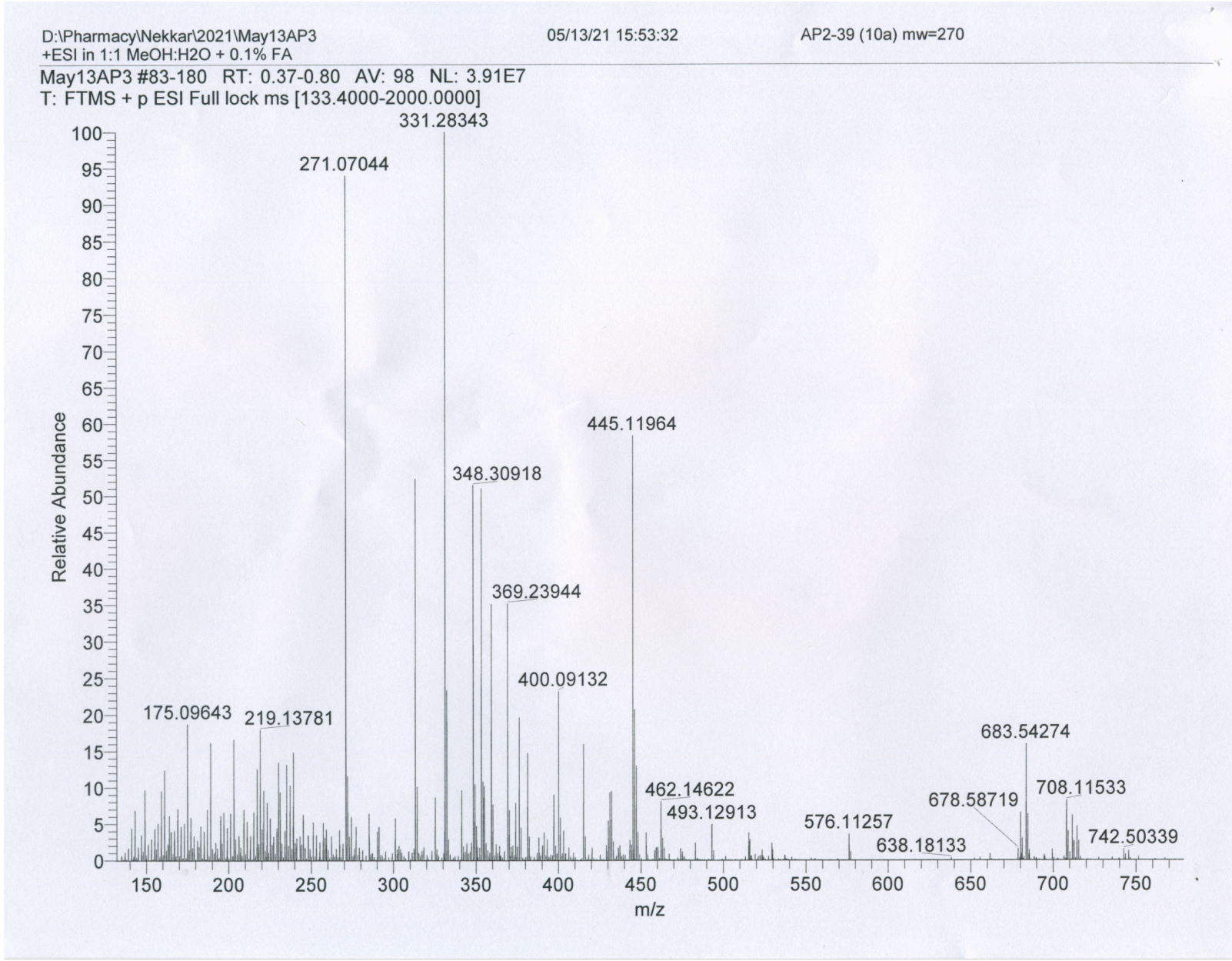
D:\Pharmacy\Nekkar\2021\May13AP3
+ESI in 1:1 MeOH:H2O + 0.1% FA
05/13/21 15:53:32
AP2-39 (10a) mw=270
May13AP3 #83-180 RT: 0.37-0.80 AV: 98 NL: 3.91E7
T: FTMS + p ESI Full lock ms [133.4000-2000.0000]
331.28343
271.07044
445.11964
348.30918
369.23944
400.09132
175.09643
219.13781
683.54274
462.14622
708.11533
678.58719
493.12913
576.11257
742.50339
638.18133
Relative Abundance
m/z

***N*-(3,5-Difluorophenyl)-2-phenylthiazol-4-amine (7d)**

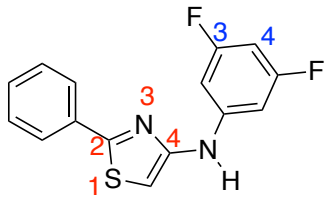

7d

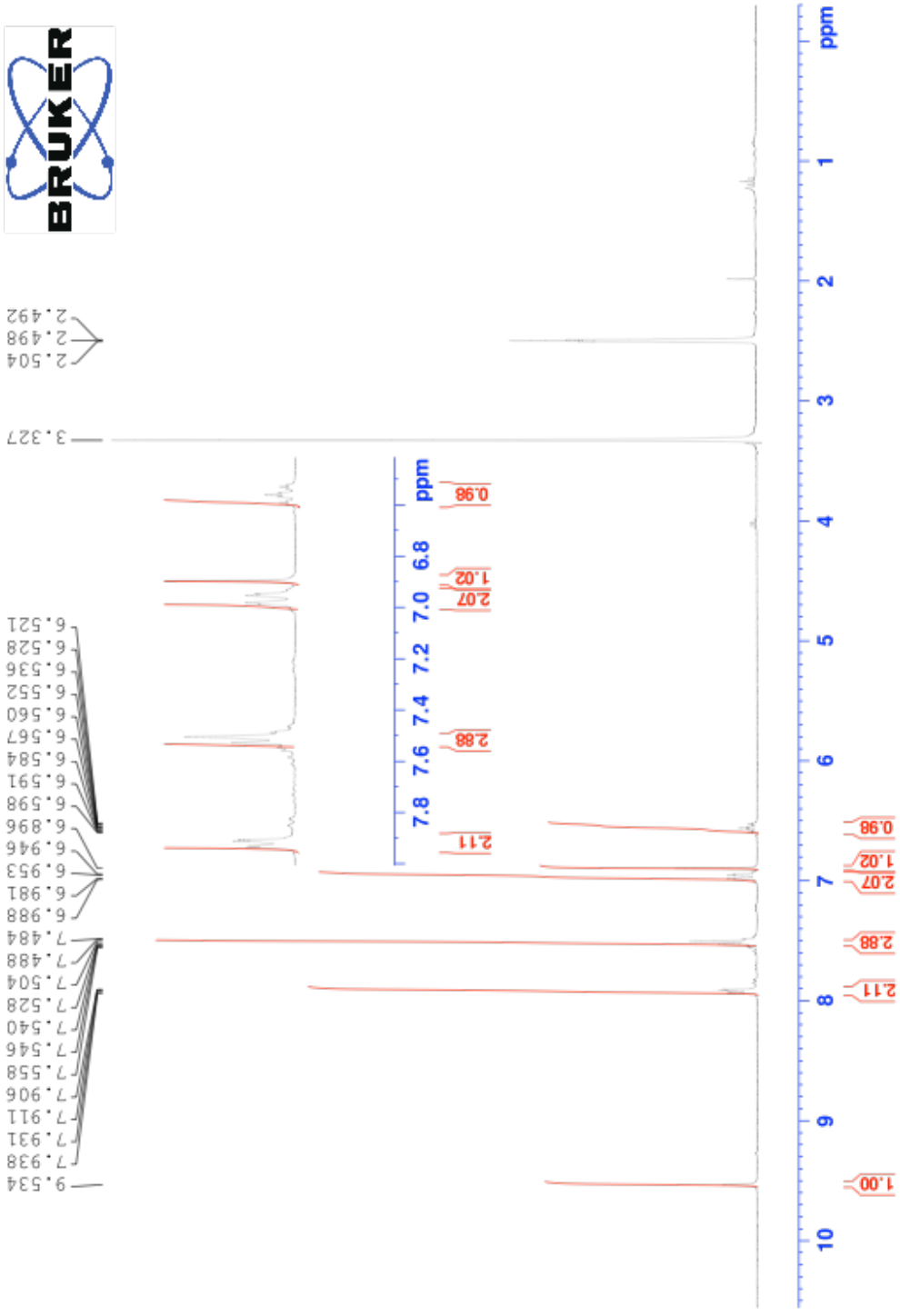
BRUKER
2.492
2.498
2.504
3.327
9.534
7.938
7.931
7.911
7.906
7.558
7.546
7.540
7.528
7.504
7.488
7.484
6.988
6.981
6.953
6.946
6.896
6.598
6.591
6.584
6.567
6.560
6.552
6.536
6.528
6.521
ppm
0.98
1.02
2.07
2.88
2.11
1.00

BRUKER
40.44
40.28
40.11
96.89
98.30
98.53
126.05
129.81
130.75
133.38
152.58
ppm

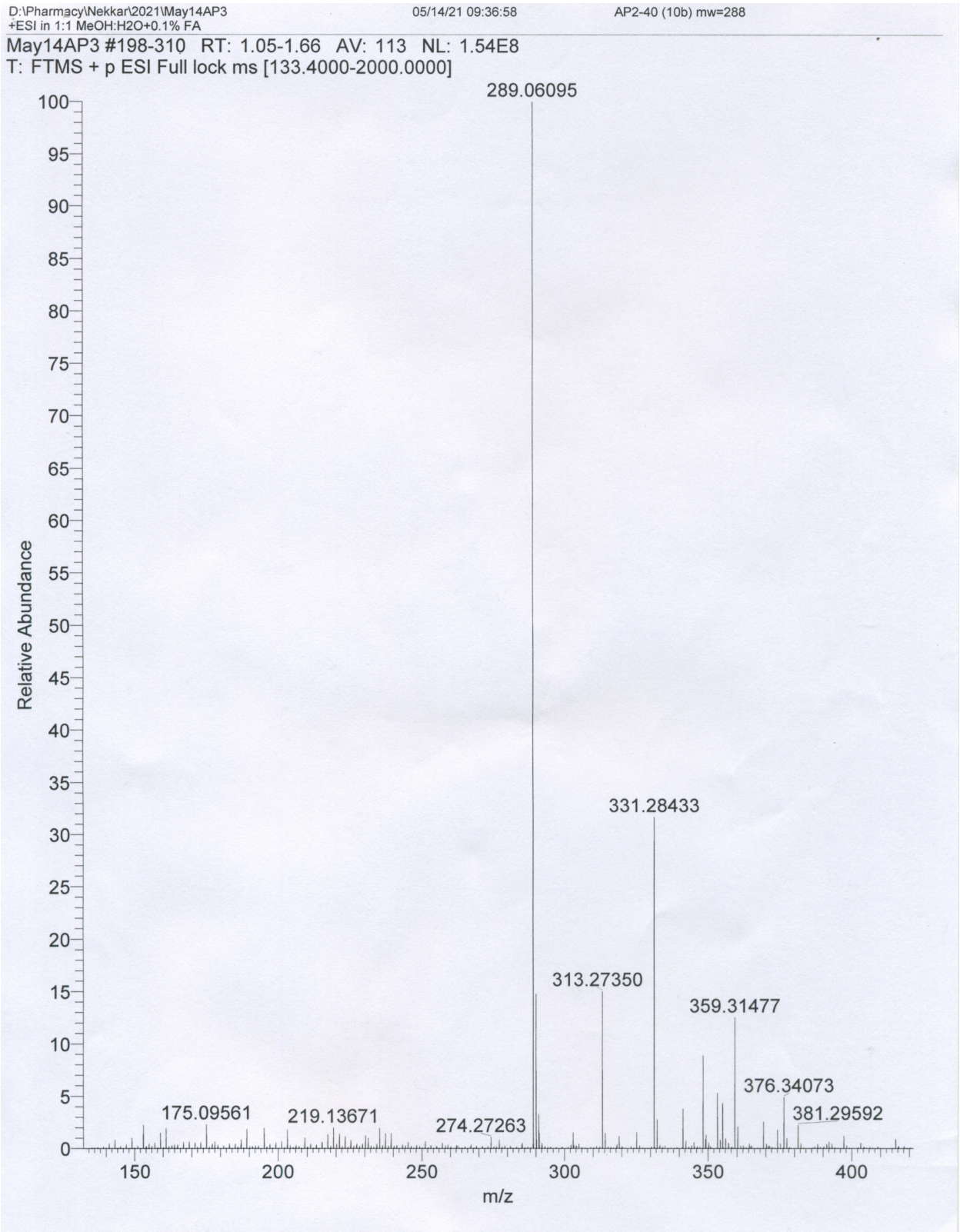
D:\Pharmacy\Nekkar\2021\May14AP3
+ESI in 1:1 MeOH:H2O+0.1% FA
05/14/21 09:36:58
AP2-40 (10b) mw=288
May14AP3 #198-310 RT: 1.05-1.66 AV: 113 NL: 1.54E8
T: FTMS + p ESI Full lock ms [133.4000-2000.0000]
289.06095
331.28433
313.27350
359.31477
376.34073
381.29592
175.09561
219.13671
274.27263
Relative Abundance
m/z
100
95
90
85
80
75
70
65
60
55
50
45
40
35
30
25
20
15
10
5
0
150
200
250
300
350
400

Cytotoxicity at 10 μM

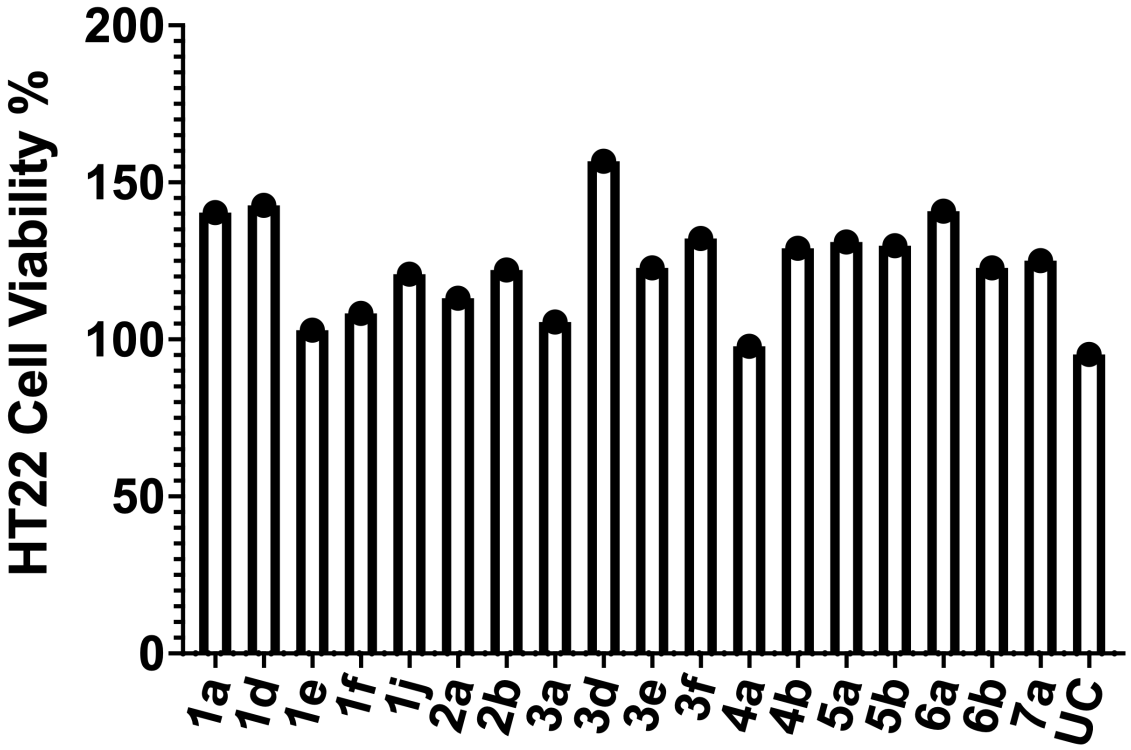

Figure 92. Percentage viability of the *N*,4-diphenylthiazol-2-amines and regioisomer (10 μM) in HT22 cells in the absence of Aβ was assessed by MTT assay after 24 h incubation at 37 °C.